Low-frequency Antennas, Transparent Ground Planes, and Transponders for Communication Enhancement in Unfavorable Environments

by

Mani Kashanianfard

A dissertation submitted in partial fulfillment
of the requirements for the degree of
Doctor of Philosophy
(Electrical Engineering)
in the University of Michigan
2018

Doctoral Committee:

Professor Kamal Sarabandi, Chair
Professor Carlos E. S. Cesnik
Professor Antony Grbic
Professor Eric Michielssen

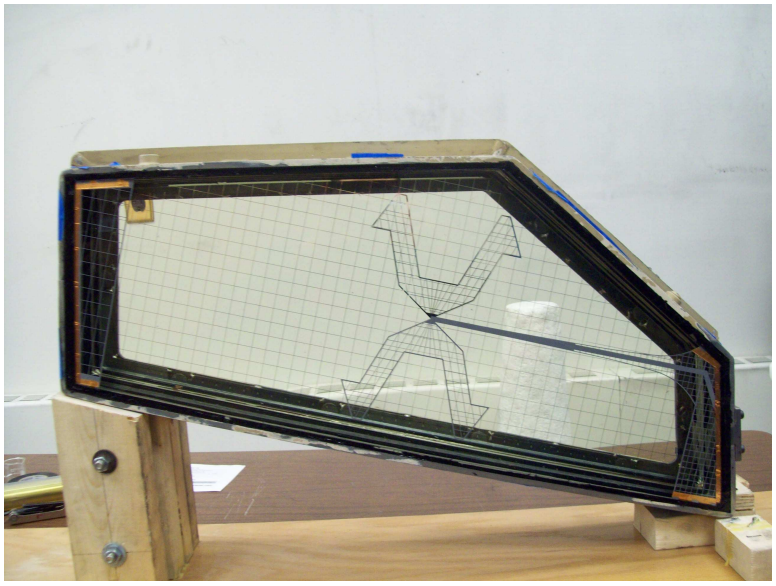

Mani Kashanianfard

manikafa@umich.edu

ORCID iD: 0000-0003-1549-4878

to my parents,

Katayoon and Ali

ACKNOWLEDGEMENTS

I would like to thank my advisor, Professor Kamal Sarabandi, for providing the opportunity to work with him, as well as his support and guidance in many aspects of my life during my graduate studies.

This work would not have been possible without the help of Dr. Adib Nashashibi, who helped me with the fabrication and measurement of the transparent antennas and the polarimetric radar calibrator.

Special thanks to Professor Carlos Cesink and Professor Anthony Grbic, for their support as members of my doctoral committee and also for generously agreeing to let me use their research equipment for fabrication. I would also like to thank Dr. Devesh Kumar for his help with the fabrication of transparent antennas.

I would like to thank Professor Eric Michielssen, for his continuous guidance through graduate courses and also as one of my committee members.

I would like to thank my friends and colleagues, Dr. Morteza Nick, Dr. Mariko Buergin, Dr. Meysam Moallem, Dr. Mehrnoosh Vahidpoor, Dr. Adel El-Sherbini, Dr. Jackie Vitaz, Dr. Amit Patel, Dr. Fikadu Dagefu, Michael Benson, Dr. Young Jun Song, Dr. Michael Thiel, Dr. Jessie Duan, Seyed Mohammad Amjadi, Dr. Amr Alaa Eldin Ibrahim, Mohammad Mousavi, Menglou Rao, Behzad Yektakhah, Mostafa Zaky, Dr. Armin Jam, Dr. Jihun Choi, Dr. Hatim Bukhari, Dr. Jiangfeng Wu, and Dr. Sangjo Choi.

Finally, I would like to thank my friends at The University of Michigan Tango Club.

TABLE OF CONTENTS

LIST OF FIGURES

LIST OF TABLES

ABSTRACT

The communication environment has a major influence on the performance of wireless networks. Unlike antennas, receivers, processors, and other components of a typical wireless system, the designer has almost no control over the communication channel. Therefore, it is imminent that the adverse effects of the communication channel such as path-loss, multipath, lack of a clear line of sight, and interference are among the most limiting factors in designing and operating wireless networks. Recent investments in infrastructures such as cell-phone towers, communication satellites, routers, and networking devices have been aimed at reducing the aforementioned adverse effects. However, wireless ad hoc networks (WANET) cannot rely on pre-existing infrastructures such as access points or routers.

In this thesis, a number of solutions are presented to enhance communication and navigation in harsh environments. 1) At lower frequencies, the defects of the communication channel are less prominent, which has led militaries to use UHF and VHF frequency bands for communication. A number of optically transparent UHF antennas are developed and embedded in the windows of military vehicles to reduce their visual signature. 2) Direction finding at low frequencies using baseline method results in an exorbitantly large array of sensors. However, a vector sensor consisting of three orthogonal two-port loop antennas can be used. A simple and accurate circuit model for the two-port loop antenna is developed for the first time that can be used for direction of arrival estimation over a wide range of frequencies and angles. 3) Using a conventional radio repeater with ad-hoc systems requires a communication protocol and decreases the throughput by a factor of two for every repeater in the chain. A full-duplex repeater, capable of simultaneously transmitting and receiving at the same frequency, is developed for the 2.4 GHz ISM band.

CHAPTER 1

Introduction

1.1 Background

The communication environment has a major influence on the performance of wireless networks. Unlike antennas, receivers, processors, and other components of a typical wireless system, the designer has almost no control over the communication channel. Moreover, the communication environment is often shared between myriads of independent devices and networks. Therefore, it is imminent that the adverse effects of the communication channel such as path-loss, multi-path, lack of a clear line of sight, and interference are among the most limiting factors in designing and operating wireless networks. Although in most cases the communication channel cannot be altered to improve connectivity, the network design can be tailored to accommodate the shortcomings of the communication channel. Recent investments in infrastructures such as cell-phone towers, communication satellites, routers, and networking devices have been aimed at reducing the aforementioned adverse effects.

Cell-phone towers and wireless access points serve as interfaces between wireless and wired networks. These devices typically have a limited range due to power constraints, obstacles, or reuse of the frequency band by multiple users in adjacent or neighboring cells. In situations where access points or cell sites cannot be used due to their cost or their dependency on additional infrastructures such as wired data links and power lines, radio repeaters may be used. Radio repeaters receive a signal from one side of the communication link,

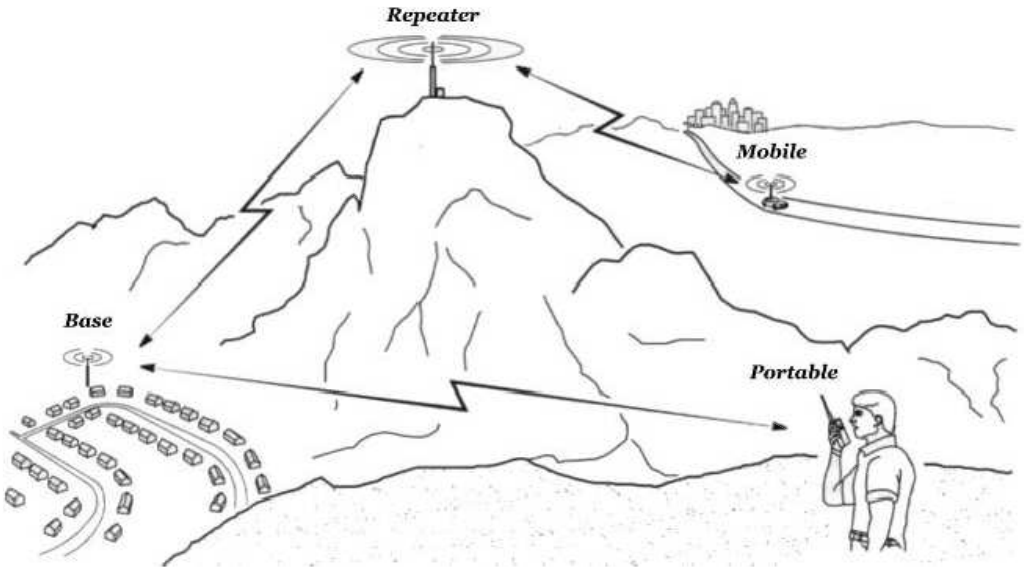

Figure 1.1: A radio repeater can help establish a line of sight between two devices. Photo by hamslife.com http://www.hamslife.com/the-first-ham-radio-repeater/

recondition and retransmit to the other side of the link. The most commonly used types of repeaters receive and transmit the desired data in packages. As the repeater is receiving each package, it down-converts, demodulates and decodes the signal to retrieve the original digital data that is communicated through the link. For this reason, a communication protocol is needed to facilitate the data transmission and reception between the repeaters and the two ends of the link. The repeater then encodes, modulates and retransmits the signal with a much higher amplitude than what was received which allows for communication with nodes that were otherwise too far to be able to receive the original signal. In addition, if a direct line of sight between the transmitter and receiver does not exist, a radio repeater can help establish a line of sight between the two, as shown in Fig.1.1.

The down-conversion and up-conversion processes are necessary because the radio repeaters use a single antenna or two closely spaced antennas as transmit and receive antennas. Therefore, the energy that is coupled from the transmit antenna of the repeater to its own receive antenna is much greater than the signal arrived from the base station. Moreover, the coupled energy from the transmit antenna creates a positive feedback and cause

the repeater to go to oscillation. For these reasons, the repeaters cannot transmit and receive simultaneously over the same frequency band and need to store the data to be transmitted at a later time and/or different frequency.

Radio repeaters are used for a variety of other applications ranging from small repeaters that are used to establish a line of sight with obstructed or shadowed regions in indoor environments to communications satellites that are used for television, telephone, radio, internet and military applications. However, the basics of operation of all these repeaters are more or less the same.

In addition to using radio repeaters, in complex environments where the multi-path effects are significant, advanced methods of increasing the capacity of the radio link such as the multiple input, multiple output (MIMO) technology can be used. In recent years there has been extensive research on different methods of exploiting multipath effects using MIMO techniques [1–5]. These methods use a combination of precoding, spatial multiplexing, and diversity coding to increase the capacity of the channel using multiple transmit and receive antennas [6]. Depending on the methods used, some knowledge of the communication channel, or the channel state information (CSI) might be required for successful implementation of these methods.

The aforementioned techniques and devices cannot be utilized for all applications. Specifically, wireless ad hoc networks (WANET) cannot rely on pre-existing infrastructures such as access points or routers [7, 8]. Instead, each node participates in routing the data to the other nodes. Because of their flexibility and reliability, ad hoc networks are the preferred choice for many applications such as battlefield communications, emergency situations, or short range communication devices using Bluetooth or similar technologies [9]. An ad hoc network allows the military personnel to maintain communication on the battlefield where the infrastructure does not exist or cannot be relied upon. Similarly, in emergency situations such as disaster relief, a reliable communication system between rescue teams, firefighters, medics, etc. is crucial.

In the absence of infrastructure, the adverse effects of the communication channel due to the obstacles in the communication path become more critical. These effects are especially limiting at higher frequencies because electromagnetic waves with shorter wavelengths are much more easily scattered and/or absorbed by most common obstacles in the communication channel. In view of this fact, ad hoc communication networks operate at lower frequencies whenever feasible, given the bandwidth requirements and available frequency band allocation. As an example, militaries use communication systems that operate at longer wavelengths (UHF and VHF) for ground communication between the vehicles. Moreover, radio waves at frequencies below 50 MHz can benefit from the ionosphere to extend their range to intercontinental distances [10]. At these frequencies, the ionosphere reflects a portion of the incident field back towards the earth and can be used as a scatterer to redirect the electromagnetic waves and establish a line of sight with destinations that were otherwise shadowed by the curvature of the earth. The frequencies between 3 MHz to 30 MHz are often referred to as the HF (high frequency) band. The HF band is used for many applications including government and military, international shortwave broadcasting, aviation communication, weather stations, and amateur radio and citizens band services.

In addition to its applications in communications, the HF band is used by over-the-horizon (OTH) radars which are ground-based radars capable of detecting targets at ranges between hundreds to thousands of kilometers [11, 12]. Fig.1.2 shows an OTH radar consisting of an array of monopole antennas. The array transmits a pulse almost parallel to the ground at the location of the radar. Similar to communication devices at the HF band, the OTH radar exploits the ionosphere's reflection properties to extend its range beyond the curvature of the earth.

Because of the common usage of the HF band in military radar and communications applications, there is a great interest in direction finding and source tracking at these frequencies. Traditionally, source tracking is performed using an array of receiving antennas

Figure 1.2: An over-the-horizon radar consisting of a long array of monopole antennas. Photo courtesy of the US Navy, https://commons.wikimedia.org/w/index.php?curid=9766600

with each element receiving a scalar value related to the intensity of the field incident upon the element. The magnitude and phase of the received signals are then used to estimate the angle of arrival and location of the source(es). Alternatively, if vector sensors are used, each array element measures all six components of the incident field (three electric field components and three magnetic field components) [13]. These so-called vector networks can consist, for example, of three orthogonal loop antennas and three orthogonal dipole antennas [14].

In situations where a high bit-rate is required or lower carrier frequencies cannot be used because of interference or size limitations, the adverse effects of the communication channel can be mitigated to some extent using full-duplex low-power repeaters. These types of repeaters generally consist of a transmit and receive antenna and a low-power amplifier. In these repeaters, the down conversion and up conversion processes are eliminated

and the transmit and receive antennas share the same bandwidth and operate simultaneously. To achieve this a very high level of isolation is needed between the transmit and receive antennas.

1.2 Ad-hoc Communication at UHF and VHF Frequencies

As mentioned earlier, militaries use ground communication systems that operate at longer wavelengths (UHF and VHF) to increase their range and reduce the adverse effects of the communication channel. In addition, because of the issues related to near-earth wave propagation of horizontally polarized waves, vertical polarization is the preferred choice [15, 16]. However, operation in vertical polarization at lower frequencies requires placement of large vertical monopoles or dipoles on vehicles. A commonly used military vehicle, MATV is depicted in Fig.1.3. As shown in the image, the vehicle carries multiple vertical antennas for communication purposes. Such antennas create air drag, increase visibility, and in situations where multiple channels or space diversity are needed, the proximity of multiple antennas can result in co-site interference due to their omnidirectional radiation pattern.

To circumvent such problems, the focus has shifted towards finding methods of embedding radar and communication antennas within or around the body of the platforms. The windows are of particular interest for antenna placement because they cover a relatively large surface area and are well above the ground level. However, for a window embedded antenna, optical transparency becomes an important requirement. A transparent conducting layer can be fabricated by depositing a very thin layer of metal, oxide or semiconductor on a transparent substrate and has been used to fabricate transparent antennas at frequencies above 2GHz [17–19]. Fig.1.4 shows a commercially available transparent film coated with a transparent conductor.

Figure 1.3: Military vehicles carry multiple vertical monopole or dipole antennas for ground communication purposes. Such antennas create air drag and increase visibility.

Figure 1.4: A commercially available transparent conductor. Photo by 3M, inc. https://www.element14.com/community/docs/DOC-29008/l/3m-transparent-conductors

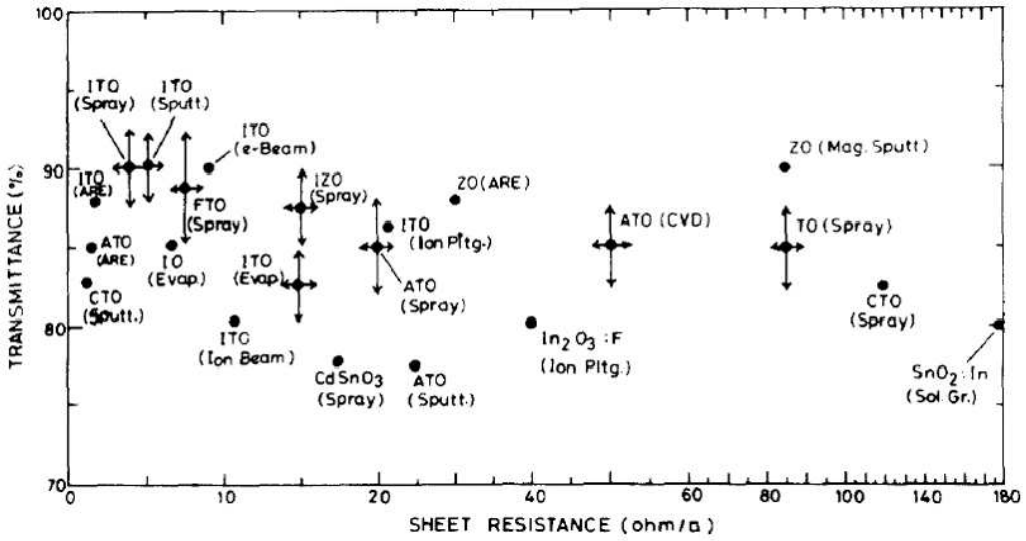

Figure 1.5: Different values of optical transmittance and sheet resistance can be achieved based on the deposition methods and materials used. Photo courtesy of K. L. CHOPRA [23]

In addition to the antenna application, the conducting film can be etched to achieve a certain filtering behavior while maintaining optical transparency [20–22]. Increasing the thickness of the conductive layer increases its conductivity but reduces its optical transparency, hence a trade-off must be found between the two [23]. Fig.1.5 compares the optical transparency and sheet resistance of transparent conductors made of different materials. Different values of optical transmittance and sheet resistance can be achieved based on the deposition methods and materials used. However, in order to achieve an optical transparency of 85% or higher, the thickness of the conductive layer has an upper limit of a few tens of nanometers, which is two to three orders of magnitude less than the skin depth of conductors at VHF and UHF bands. For this reason, transparent conductors are not effective at the frequency range of interest. The limitations of using transparent conductors for antenna fabrication have been studied rigorously in recent years [24–27].

Alternatively, wire antennas can be used to provide the desired optical transparency. Window embedded wire antennas have been introduced at FM frequencies for low-power or receive-only applications [28–31]. The power transmitted by the military radios at VHF and UHF frequencies can exceed tens of watts. At these power levels, it is important to

isolate the interior of the vehicle from the antenna radiation. Moreover, isolating the cabin eliminates the effects of the cabin interior and passengers on the antenna input impedance and radiation pattern. Therefore a transparent ground plane is needed behind the radiating element to reduce the radiation inside the vehicle and at the same time increase the directivity of the antenna. A meshed patch antenna on a mesh ground plane can provide the required isolation with the cabin interior [32,33]. However, because of the sub-wavelength dimensions of the armored windows at VHF and UHF frequencies, a patch antenna, if feasible, cannot provide the one-octave bandwidth required by the army radios.

Wire grids are commonly used as reflectors for many applications where a metallic sheet is unwanted due to its weight, cost or other constraints such as transparency requirements [34]. Fig.1.6 shows a parabolic reflector made of a wire grid to reduce its cost, weight, and wind load. A periodic wire grid screen, with a periodicity much smaller than a wavelength, essentially acts as a high pass filter to an incoming wave and therefore can be used as an equivalent ground plane at frequencies much below its cutoff frequency [35]. Obviously, a wire grid screen is a perfect ground plane at DC (zero frequency) and its RF transmissivity is increased monotonically with frequency. However, antennas have a specific band of operation and a reflecting screen needs to act as a perfect ground plane only over the bandwidth of the antenna which incidentally does not extend to DC. Hence a band-selective ground plane design seems to be more appropriate for antenna applications. For example, screens made of specific types of frequency selective surfaces(FSS) can show perfect reflectivity at certain frequencies.

Conventional frequency selective surfaces are periodic structures consisting of metallic unit cells whose dimensions are comparable to a wavelength [36–38]. Fig.1.7 shows two common types of band-stop frequency selective surfaces. In addition to their primary stop-band, these structures have several harmonic stop bands when the circumference of their unit cell is close to a multiple of the wavelength. Moreover, these structures show their filtering behavior when many unit cells are present and the response of such surfaces are very

Figure 1.6: Wire grids are commonly used as replacement for full-metal reflectors to reduce the cost and weight of the reflectors or provide optical transparency. Photo courtesy of rfhamdesign http://www.rfhamdesign.com/products/parabolicdishkit/45meterdishkit/index.php

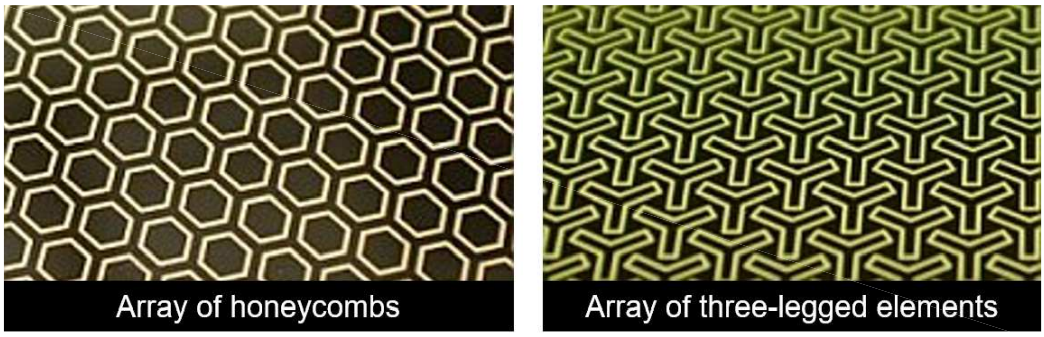

Figure 1.7: Conventional band-stop frequency selective surfaces are usually made up of a planar array of resonant elements.

sensitive to the incidence angle and the curvature of the incident wave phase front [39]. It is possible to reduce the unit cell size of the FSS to some extent by altering the shape of the unit cells [40]. However, this miniaturization does not result in an improvement in the angle dependency or harmonic behavior of the FSS. Recently, a new class of FSS structures with subwavelength unit cells, miniaturized element frequency selective surfaces(MEFSS), is introduced [41] to alleviate the aforementioned drawbacks of the traditional FSS structures.

Fig.1.8 shows one of the simplest forms of MEFSSs with a bandpass behavior. The structure consists of an array of metallic patches fabricated on a substrate that is backed by a wire-mesh grid. Unlike traditional FSSs, each unit cell of MEFSS is not resonant over the operational frequency band. Instead, the filtering behavior results from the interaction of the elements with each other and the incoming electromagnetic field. Fig.1.9 shows individual layers of the structure and their interaction with the incoming field. The incoming radiation induces surface currents on the metallic parts of the surfaces in a direction perpendicular to the incoming magnetic field. Because of their small size, the unit cells of the structure can be modeled as lumped elements: the adjacent edges of the metallic patches form capacitors and the wires on the wire mesh grid form inductors. The induced surface currents are affected by the lumped element behavior of the unit cells and are also coupled to the incoming and scattered electromagnetic field through boundary conditions.

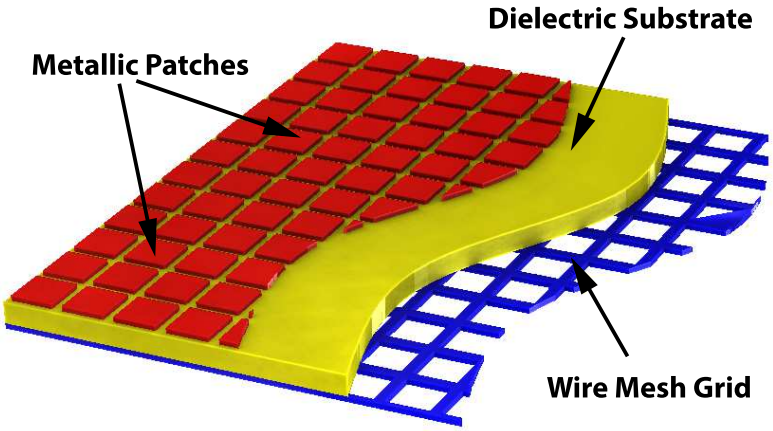

Figure 1.8: A commonly used bandpass MEFSS consisting of an array of sub-wavelength metallic patch elements and a wire mesh grid.

It is conventional to model the propagation of plane waves in free space using transmission lines. The same convention can be carried out to model the field interaction with MEFSSs. The thickness of the substrate is usually extremely small compared to the wavelength ($\approx \lambda/100$). Therefore, the structure can be modeled as a parallel L-C circuit as shown in Fig.1.10.

Because each individual element is not resonant at the operational band of the MEFSS, the structure does not show harmonic behavior in its frequency response. In addition, because the structure can be modeled using lumped elements, the frequency response of the structure is almost independent of the angle of arrival. These properties of MEFSSs make them much better suited for transparent ground planes for antenna applications than the traditional FSSs. The antenna can be smaller or comparable to the wavelength and is placed in close proximity of the equivalent ground plane. MEFSS structures, designed as a stop-band filter and tuned at the center frequency of the antenna, are ideal as a transparent replacement for reflective ground planes. Moreover, the flexibility in the design of MEFFS structures allows for high-order, wideband, and/or multi-band surfaces with a sharp roll off.

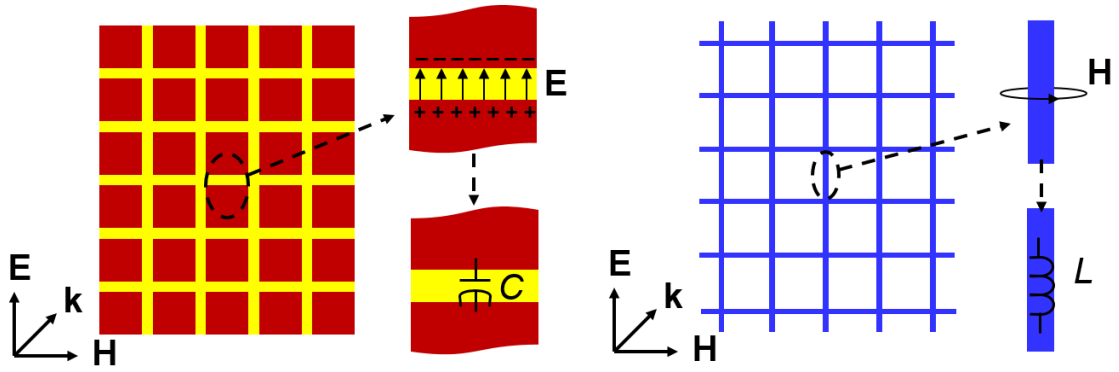

Figure 1.9: The patch array and the wire grid interact with the incoming electromagnetic field. This interaction can be modeled as capacitance (patch array) and inductance (wire grid)

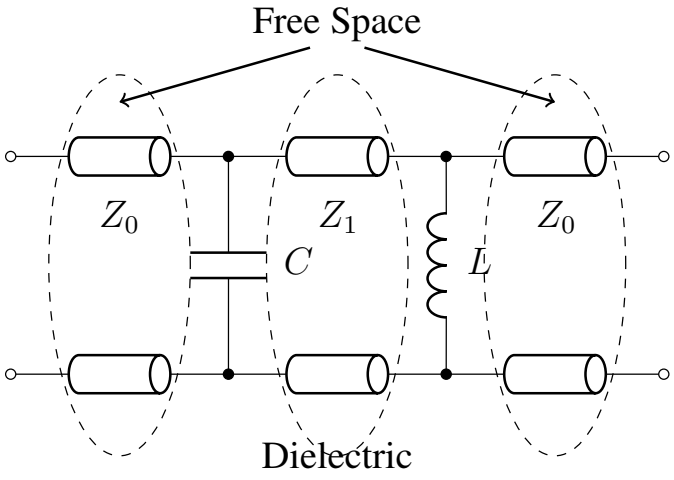

Figure 1.10: The equivalent circuit model of the patch-wire MEFSS. The structure acts like a first order band-pass filter

1.3 RF Boosters, Repeaters, and Transponders

Radio repeaters are commonly used to enhance the radio connectivity in harsh communication environments where the effects of the communication channel such as multi-path, attenuation, and none-line-of-sight have an adverse impact on the connectivity of the channel. A radio repeater can assist reestablishing the line of sight between the transmitter and receiver in such environments. [42–46] In addition, a radio repeater can be used to extend the communication range by amplifying and retransmitting the signal along a desired direction.

Most radio repeaters down-convert the signal and then up-convert and retransmit at a different frequency or time slot [47, 48]. The advantage of using this theme is that the transmit (Tx) and receive (Rx) channels are isolated through the system diplexer. As a result, a very high gain repeater can be realized. However, since transmission and reception are done at different frequencies or time slots, for every repeater added to the chain, the throughput available to the end device is cut by half. This significantly hinders the performance of such repeater systems especially if a long repeater chain is required. Furthermore, a significant portion of the power used by these systems is devoted to down-conversion, decoding, encoding and up-conversion and only a small fraction of the consumed power is radiated. Another disadvantage is that such repeaters must rely on a communication protocol to manage the allocated spectrum for each user and thus the complexity is increased substantially.

Alternatively, a protocol independent low power repeater that consists only of Tx and Rx antennas and a low power high gain amplifier can be used. [49, 50] Using this theme, all communications from multiple users and different modulation schemes in the frequency band of the repeater can be supported simultaneously. This way no protocol for routing the data packets of different users is needed be and the full bandwidth can be utilized without reducing throughput and with high power efficiency. These features of full-duplex repeater systems make them a compelling alternative to half-duplex repeaters especially for ad-

hoc communication networks where a single communication protocol is not defined and infrastructures may not be available to provide external power to the network devices.

The main challenge in implementing this configuration pertains to the coupling level between the adjacent Tx and Rx antennas operating at the same frequency band. The mutual coupling between the two antennas creates a feedback which if higher than the reciprocal of the amplifier gain, can cause the system to go to oscillation. This coupling imposes a restriction on how high the amplifier gain can be chosen. Several approaches have been proposed to decrease the mutual coupling between the antennas. These approaches include modifying the currents on the ground plane on which the antennas are fabricated [51–54], using engineered electromagnetic structures such as electromagnetic band gaps(EBG) [55–58], or creating destructive interference between the two antennas [59]. The defected ground structures improve the isolation but degrade radiation polarization and pattern. EBG structures usually require periodic geometry and large dimensions. Destructive interference between the antennas requires an odd multiple of half wavelength distance between the two Tx antennas as well as accurate, nonsymmetric power distribution between the two Tx antennas.

Recently a protocol independent omnidirectional radio repeater for ad-hoc communications at ISM band was introduced [60]. While omnidirectional repeaters provide good coverage in all directions and can handle forward and backward links simultaneously, they are not beneficial if the path loss in the channel is not significant as will be shown later in this paper. Moreover, as will be shown in this paper, the signal level must decrease by 10dB every time the signal passes through a repeater if a 20dB signal to noise ratio throughout the communication path is desired.

In addition to their use in communication devices and satellites, full-duplex transponders can be used as accurate active calibration targets for a variety of radar applications including polarimetric syntectic aperture radars (SAR). SARs are important remote sensing tools for the acquisition of quantitative information about the earth's environment. The

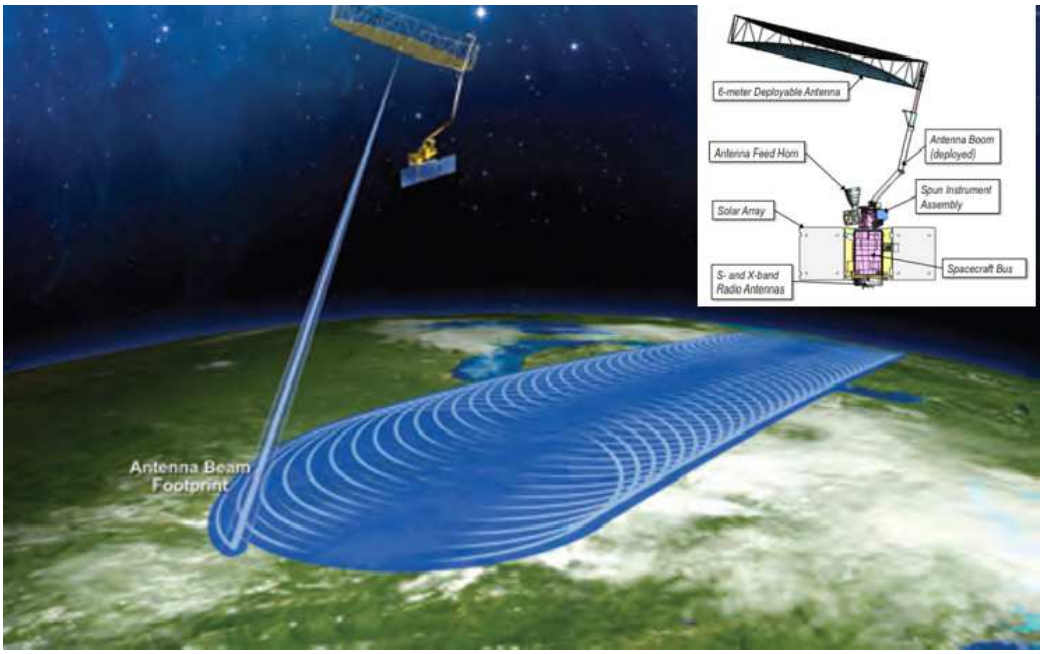

Figure 1.11: SMAP polarimetric radar scans the entire surface of the earth once every three days and measures the moisture content to soil as well as its freeze, thaw state. External calibration is crucial for producing accurate soil moisture data.

NASA SMAP (Soil Moisture Active Passive) mission utilizes an L-band radiometer and an imaging SAR to provide high accuracy global maps of soil moisture and net ecosystem exchange of carbon [61]. The SMAP radar consists of a 6m diameter mesh reflector antenna that conically scans the surface of the earth with a surface incident angle of approximately 40°. The 3 dB beamwidth footprint of the antenna provides a 40km spatial resolution. The resolution is further increased in range using pulse compression and in azimuth using Doppler discrimination. Because of its unique scanning path, the maximum available resolution varies between 230m $\times$ 360m to 230m $\times$ 1.1km for different points on the swath. Fig.1.11 shows the SMAP satellite and its swath.

A variety of internal calibration hardware and algorithms, as well as external calibration procedures, are needed to ensure accurate calibration of a spaceborne radar. With a direct external calibration, not only different polarimetric channels can be calibrated with respect to each other, but radiometric calibration and radar stability can be assessed throughout the

radar's life. Many of the most popular and effective external calibration methods [62–64] involve the use of point calibration targets with known scattering matrix elements. These targets are placed on the surface of the earth and are imaged by the radar as it flies over the terrain. There are also other techniques based on distributed targets that can be used for radiometric calibration of SAR systems [65–67]. A point calibration target must have a number of attributes to be suitable for external calibration of the radar: 1) large radar cross section that can provide a high signal-to-clutter ratio for all channels, 2) relatively wide RCS pattern to eliminate errors due to slight misalignment that may be present between the satellite and the target, 3) stable scattering matrix for the duration of the mission, and 4) a relatively small size for portability and ease of deployment. The data obtained during the fly-by is used with the known characteristics of the target to calibrate the SAR.

In particular, the calibration target must generate a clean signal that is well above the noise or clutter that is expected in the scene. Assuming the worst case scenario, the SMAP radar has a ground resolution of 230m by 1.1Km at the 150Km near-range of the swath. Based on a careful measurement of different terrestrial targets such as bare surfaces, crops, and trees [68–71], an upper bound of about -10 dB for the co-polarized backscatter coefficient is obtained. This corresponds to, on average, an RCS of 44 dBsm for one ground pixel. Therefore, the calibration target must at least have an RCS that is 20 dB above the clutter, or 65 dBsm, to be effective.

Passive point targets, such as corner reflectors, that can provide RCS levels on the order of 65 dBsm are prohibitively large [72]. Because of the large RCS needed for a reasonably small size target, an active calibration target must be used. To increase the RCS of an active radar calibrator either the amplifier gain or the antenna gain, or both, must be increased. The amplifier gain is mainly limited by two factors: (1) the isolation between the receiver and transmitter, and (2) the amplifier stability requirements. The antenna gain is also limited by two factors: (1) beamwidth requirements, and (2) size and weight limitations. At low frequencies, such as L-band, size and weight considerations become the

dominant limiting factors. To avoid the problems that occur when the transmit antenna is in the proximity of the receive antenna, including pattern asymmetry and amplitude and phase ripple, the antennas must be outside of the near-field zone of each other. Increasing the gain of the antenna expands its near-field zone which means the transmitter and receiver antennas have to be placed on separate panels, which would then cause pointing uncertainty and deployment issues.

To mitigate the difficulties of mounting the transmitter and receiver antennas on separate panels, a single dual-polarized antenna design has been introduced [73] that functions much like a full-duplex repeater. In this design, a high cross-polarization isolation is achieved over a wide bandwidth using a square horn antenna with a waveguide orthomode transducer (OMT). The OMT isolation was measured to be better than 35 dB with the common port short-circuited. The isolation improves to about 55 dB when the common port is connected to the antenna, provided that the antenna has more than 20 dB return loss. Several other OMT configurations have been introduced with the isolation between the two ports ranging from 35 dB to 50 dB [74–78]. However, to achieve a stable RCS of 65-75 dBSm a much higher isolation between the two antennas (75 dB) is desired. In the following chapters, the design and fabrication of an active calibration target with an RCS of more than 80dBsm are presented.

1.4 Direction of Arrival Estimation at the HF Band.

Short dipole and small loop antennas are the oldest radiating elements whose applications appeared in the first set of experiments designed by Henrich Hertz in 1887 in support of James Clerk Maxwell's mathematical theory of 1873. Since then these antennas and their variations have appeared in myriads of different configurations for many applications. One such application has been in the area of source tracking and direction finding. In the receiving mode, these elements can be used as electric and magnetic field probes. That is,

under high impedance termination, the voltage at the antenna terminal, V_{OC} can be used to determine the intensity of the field components at a given orientation. Multiple probes in different orientations are needed to measure all field components which can then be used for direction finding [79]. Neglecting the multi-path effects, five independent field components (e.g. three components of the electric field and two components of the magnetic field) are required to uniquely determine the field direction of arrival; however, in multi-path environments, more field components will be needed.

Small loops and dipoles are commonly used for direction finding in the HF band within the frequency range of 1MHz to 10MHz [80]. At these frequencies, the size of the probes is relatively large (1m-5m). Therefore placing multiple dipoles and loop antennas close to each other would require a large space. In addition, accurate direction finding requires all field components to be measured at the same point which means the probes need be co-located. Due to physical constraints and interference effects, co-locating loops and dipoles that are oriented in different directions is impractical.

To mitigate the aforementioned problems, two-port loop antenna configuration is proposed [81]. This antenna is configured to have two ports and is capable of simultaneously measuring one component of electric and magnetic fields. Three such probes are sufficient to measure all six field components provided that the two-port loops are placed orthogonal to each other at the same location. Such arrangement also provides minimal mutual coupling. The two-port loop antenna has been studied in the past and approximate solutions using integral equations are provided [82–86]. Many empirical and physics-based circuit models have been proposed for loop antennas and dipoles with different configurations [87–91]. However, a simple and accurate circuit model for the two-port loop antenna does not exist. In the following chapters, a circuit model consisting of lumped elements for the two-port loop antenna will be presented.

1.5 Chapter Outline

1.5.1 Chapter 1: Introduction

In Chapter 1, the main problems and ideas addressed in this research are presented. A brief review of the past and recent research for improving wireless communication in harsh environments especially for ad hoc wireless systems is provided. The ideas are divided into subsections dealing with ad hoc communication in UHF and VHF bands and transparent antenna solutions, RF boosters, repeaters, and transponders, and direction of arrival estimation at HF frequencies. Following the introduction section, the novel ideas that deal with the challenges raised in this research are presented. A brief description of these ideas is listed below.

1.5.2 Chapter 2: Transparent Window Embedded Antennas

As mentioned earlier, because of the problems related to the use of vertical dipole and monopole antennas on military vehicles, the focus has shifted towards finding ways to embed the antennas within the body of the vehicles. In Chapter 2, the design and fabrication of window-embedded optically transparent antennas for a few commonly used military vehicles are presented. Each vehicle has three different windows with irregular shapes and a unique multilayered glass stack-up. The antennas are fabricated on the outermost layer of the windows and the innermost layers are covered by a wire-mesh ground plane. With this configuration, the window acts like a cavity behind the radiating element. The shape and size of the cavity have a major influence on the radiation characteristics of the antenna, which means each window requires its own independent antenna design.

The irregular shape of the windows has negative effects on bandwidth and beam steering of the antenna. These challenges are addressed in this chapter and novel solutions are provided. Different methods of meshing the antennas to create a transparent antenna are considered and an optimal mesh based on the density and direction of surface currents on

the antenna is generated.

1.5.3 Chapter 3: Transparent Ground Planes for Automotive Applications

In Chapter 3, the idea of replacing the existing wire mesh ground planes with a more flexible alternative, miniaturized element frequency selective surfaces, is investigated. Frequency selective surfaces can provide higher isolation than the wire mesh of the same opacity because they can show band-stop behavior as opposed to the high-pass behavior exhibited by a wire-mesh grid. In addition to this advantage, MEFSS structures can provide high order filtering behavior that can be used for applications where a bandpass behavior is required in a frequency band relatively close to the stop-band of the MEFSS. However, the main drawback of using high-order MEFSS structures has been the need to increase the thickness of the substrate linearly with the number of poles in the response of the MEFSS. Increasing the thickness of the MEFSS increases its weight, cost, and also the angle dependency of its frequency response as will be shown Chapter 3. In the first part of the chapter, first order bandstop MEFSS structures are considered and several novel ideas to improve their isolation, bandwidth, and transparency are presented. Following that part, a multilayered MEFSS with high order response is presented. This novel design allows for a high order response with a substrate thickness almost independent of the number of elements.

1.5.4 Chapter 4: A Full-duplex Repeater for the 2400 MHz ISM Band

Chapter 4 deals with the design, fabrication, and analysis of a full-duplex directional repeater system with a large isolation between the transmit and receive antennas. The isolation improvement is achieved by separating the antennas by a ground plane in between and also creating a polarization mismatch between the two antennas. This technique exploits

the fact that most mobile platforms that use the ISM band to communicate are designed to be able to transmit and receive in both vertical and horizontal polarizations. In addition, a two-element receiver array is proposed that further decreases the coupling using a novel near-field cancellation technique. Following that section, a performance analysis of full-duplex repeaters placed in complex environments as well as free space situations is provided and the key properties of directional and omnidirectional repeaters are discussed. Finally, the fabricated repeater is tested in a number of scenarios and its performance is evaluated.

1.5.5 Chapter 5: A High-gain Transponder for Radar Calibration of SMAP

In Chapter 5, the same design concept as what was used for the SIR-C mission is revisited with the aid of modern computational tools, namely ANSYS HFSS, and the design and fabrication processes are improved to achieve a much higher isolation than what was reported in 1994. The details of the OMT design was not provided in the previous paper but are improved and included here. There are a number of other improvements using perturbation and leakage cancellation techniques to increase the isolation between the two ports to about 75dB over the desired band of 1.22GHz to 1.32GHz. Finally, a stable gain amplifier system with the ability to compensate for temperature and aging drifts in the system is included. The RCS of the fabricated PARC is measured in the field and reported as well as the radar image of the area created by the SMAP radar.

1.5.6 Chapter 6: An Accurate Circuit Model for the Two-port Loop Antenna

The two-port loop antenna has been studied in the past and approximate solutions using integral equations are provided [82–86]. Many empirical and physics-based circuit models

have been proposed for loop antennas and dipoles with different configurations [87–91]. However, a simple and accurate circuit model for the two-port loop antenna does not exist. In chapter 6, a simple circuit model applicable for a wide frequency range is presented for which the values of the lumped elements are related to the physical parameters (i.e. size and shape) of the split-loop. Numeric values of the circuit components are found using a full wave simulation of the loop's passive Z-parameters. This model also provides a more accurate lumped element circuit model for the conventional loop antennas simply by short-circuiting one of the two ports of the split-loop model. The circuit model is also used to predict the gain pattern of the antenna very accurately. The received voltage due to the transverse dipole mode currents as well as the transmission line mode currents is taken into account. The accuracy of this model is examined for loops with circumferences up to 1.1λ and is compared with the commonly used parallel L-C model and the transmission line model [89]

1.5.7 Chapter 7: Conclusion

In chapter 7, a summary of important contributions from this research is provided and directions for further work on the presented ideas are discussed.

CHAPTER 2

Transparent Armored Window Embedded Antennas

2.1 Introduction

The development of compact, low profile, and power-efficient antennas capable of operating over a wide range of frequencies is of great practical importance in a number of army applications. Survivability and lethality in battlefield environments significantly depend on reliable communication and situational awareness. This mandates equipping war fighters with a wide range of communication devices operating over different frequency bands and wireless sensors for battlefield situation awareness, surveillance, and target detection. As mentioned earlier, militaries use ground communication systems that operate at long wavelengths (UHF and VHF) in vertical polarization which allows them to mitigate the adverse effects of the communication channel while maximizing the communication range. However, operation in vertical polarization at lower frequencies requires placement of large vertical monopoles or dipoles on vehicles. Such antennas create air drag, increase visibility, and in situations where multiple physical channels or space diversity are needed, the proximity of multiple antennas can result in co-site interference due to their omnidirectional radiation pattern. An optically transparent window-embedded antenna is a compelling alternative that can mitigate the aforementioned shortcomings of the existing antennas.

Table .2.1 lists a number of commonly used army radios and their corresponding fre-

Table 2.1: Existing military radios and their frequency bands

Radio	Frequency band
SINCGARS AN/VRC-90	VHF low: 30-90 MHz VHF high: 90-224.999 MHz UHF: 225-512 MHz UHF SATCOM: 243-270 MHz and 292-318 MHz
AN/VRC-103, AN/PSC-5, or AN/PRC-117	VHF: 30-90 MHz, 116-150 MHz, and 225-400 MHz UHF SATCOM: 243-270 MHz and 292-318 MHz VHF/UHF: 30-512 MHz
EPLRS RT-1720	420-450 MHz

quency bands. Most of the radios utilize an extremely wide frequency range to support a frequency hopping spread spectrum (FHSS) communication scheme [92]. FHSS enabled radios to change the carrier frequency rapidly within the band in a predetermined pattern. As a result, the communication is more resistant to narrow-band jamming or interception [93]. For this reason, the radios are capable of operating over a fraction of the allocated band. The existing antennas typically operate at the low VHF band from 30 MHz to 80 MHz or the UHF band from 225 MHz to 450 MHz. These antennas offer a voltage standing wave ratio (VSWR) of better than 3.5 to 1 which corresponds to an input reflection coefficient of lower than -5.1 dB. The antennas are broadband monopole and dipole antennas whose bandwidth is often increased at the expense of reducing their efficiency. Therefore the antennas offer passive gains in the range of -8 dBi to -1 dBi.

In this chapter, first a monopole bow-tie antenna backed by a cavity (armored window) is discussed. A transparent ground plane is placed on the innermost layer of the window to prevent RF radiation from entering the cabin. Because of the small thickness of the window glass ($\lambda_0/18$), the radiation element and the transparent ground plane are placed very close to each other. Consequently, the gain or bandwidth of the antenna is compromised. As a

trade-off, the minimum return loss requirement for the antenna is reduced to $5.1dB$ which is compatible with the existing radios and in line with the specifications of the existing antennas. It should also be noted that simple and power efficient external matching can be used to further enhance this level of return loss. The antenna is intended for a slanted windshields with a tilt angle as high as 15°. Therefore, the main beam of the antenna needs to be tilted away from boresight. However, because of the small size of the window, phased array schemes cannot be implemented to steer the beam. Alternatively, a monopole antenna implemented over a finite-size ground plane can be used to steer the beam in the desired direction as will be shown here. In addition, unlike a dipole antenna, the proposed monopole antenna can be directly connected to an unbalanced radio output and does not require a balun.

Following the monopole bow-tie design, a dipole bow-tie antenna is proposed for a slightly larger window. The antenna requires a balanced feed which means a balun must be used with the antenna. Two separate antennas based on a transformer balun and a microstrip tapered balun are designed. The tapered balun based antenna is capable of handling the transmitted power by the commonly used radios (up to 100 watts). In addition to the mentioned antennas, a two-element phased array and a single element bow-tie dipole antenna are proposed for the windshield and side windows of Mine Resistant Ambush Protected All Terrain Vehicle (MATV) respectively. The windows of this vehicle have irregular shapes which makes the antenna design particularly challenging as the main beam of the antenna tends to steer in different directions at different frequencies due to the field formations inside the window cavity. A simple technique based on cavity mode management is proposed to stabilize the beam direction as a function of frequency. In addition, the antenna shape and position within the window are optimized to further improve the performance.

After discussing the original design concepts, different methods of meshing the antennas for minimizing their opacity are considered and an optimal mesh based on the direction and density of the surface currents on the antenna is presented. All four antennas are fab-

ricated using a uniquely developed fabrication technique that consists of metal deposition on glass, chemical etching and bonding the glass layers containing the antenna with several other glass and polycarbonate layers to form a stack that mimics the stack-up of the existing windows. Finally, the performance of the fabricated antennas is evaluated in a number of indoor and outdoor tests including a full test with four identical antennas mounted on a demonstration vehicle.

2.2 Monopole Antenna Design

Fig.2.1 shows the geometry of an armored window and an embedded monopole bow-tie antenna. A bow-tie configuration is considered as it can provide a wide bandwidth and generates a magnetic field around the antenna that is mainly parallel to the antenna surface. This is important as we intend to place a ground plane parallel and near the antenna element. The window is made of several layers of glass and polycarbonate with the effective dielectric constant of 4.5. The window is rectangular with dimensions of $W_h = 30cm$ and $W_w = 61cm$. The glass and polycarbonate layers are stacked together to form a slab with the thickness of $W_t = 7.6cm$. The antenna and the reflecting ground plane are placed on the opposite sides of the slab as shown. In practical scenarios, the windshield is tilted with respect to the vertical direction as shown in Fig.2.2. The ground plane is connected to the metallic enclosure that is holding the glass in place, and the enclosure is in turn connected to the metallic body of the vehicle.

The window-embedded antenna is modeled and simulated using a finite element based full-wave solver, ANSYS HFSS 2014. The height, Ah and width, Aw of the antenna are designed to maximize the bandwidth of the antenna, assuming a minimum acceptable return loss based on the commonly used radio specifications. The optimized design parameters are found to be $Ah = 18.3cm$ and $Aw = 57.9cm$. The gain in the horizontal direction (15° from boresight), and the input reflection coefficient of the optimized monopole antenna are

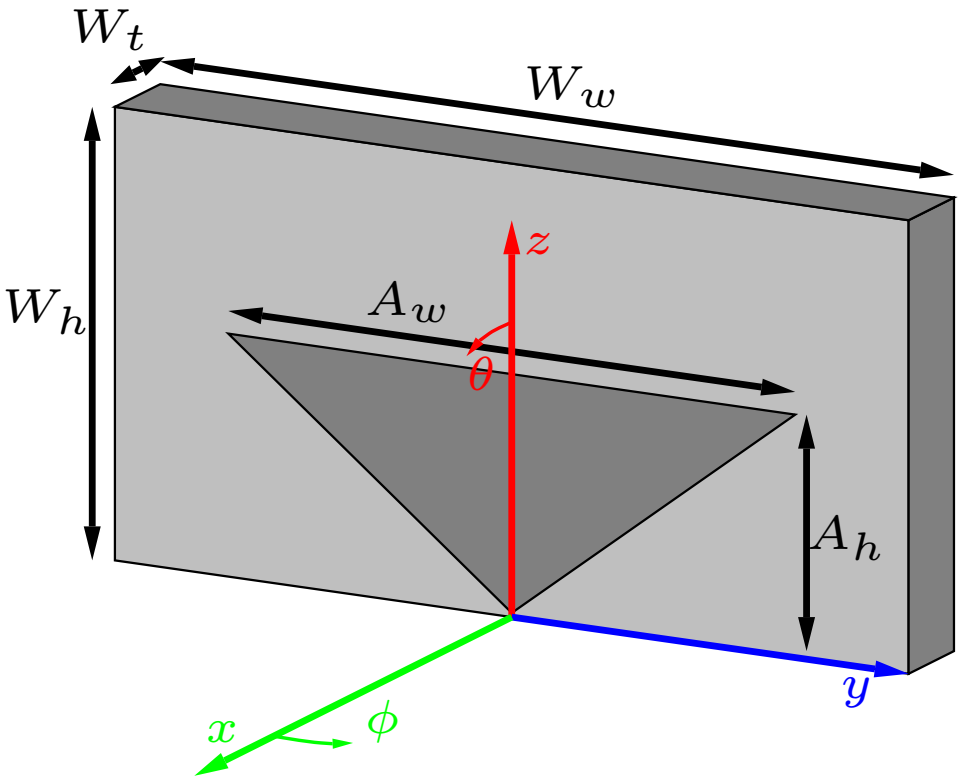

Figure 2.1: The geometry and design parameters of the monopole bow-tie and the armored window. A ground plane is placed on the backside of the window to provide cabin isolation and increase the directivity of the antenna.

plotted in Fig.2.3. The simulation results indicate that this antenna is not a good radiator at frequencies below 320MHz.

The reason for the poor performance of the antenna at lower frequencies is best explained by studying the different resonances that result in the wide-band behavior of the antenna. The simulated input impedance of the bow-tie antenna is plotted in Fig.2.4. As seen in the graph, the antenna has a sharp resonance at 255MHz. The currents on the edges of the bow-tie antenna, produced by the circulating magnetic field, establish a standing pattern at a frequency inversely proportional to the edge length. The real part of the input impedance of the antenna is extremely large at this resonant frequency as a result of a null current at the input. The wide-band response of the antenna starts well above the first resonant frequency. For this reason, the antenna must be designed such that the first resonance occurs well below the desired frequency band. This can be achieved by increasing

Figure 2.2: The placement of the monopole antenna in the windshield with a 15° tilt. The ground plane is fabricated on the inside of the window glass and in electrically attached to the metallic body of the vehicle.

the edge length of the antenna. However, the maximum size of the antenna is limited by the window dimensions and cannot be chosen arbitrarily. Alternatively, the first resonant frequency can be reduced by making the edges of the bow-tie convex, as shown in Fig.2.5, which increases the side length without increasing the overall dimensions of the antenna. Fig.2.5 depicts the response of the antenna for $Bw = 6.1cm$, $Bh = 10.7cm$, $Ah = 18.3cm$ and $Aw = 57.9cm$. The simulation results confirm that bending the sides of the bow-tie antenna results in a 30MHz decrease in the first resonant frequency.

As seen in Fig.2.5, making the sides of the bow-tie convex results in a poor impedance matching over the operational band of the bow-tie. The impedance matching is improved by making the top side of the bow-tie convex as well. Moreover, two stub-like extensions are added at the ends of the mentioned edges of the bow-tie to enhance the input impedance matching further as shown in Fig.2.6. The design parameters are optimized to improve the matching. The frequency response of the optimized shape is shown in Fig.2.7. As is evident from the graph, a return loss of higher than $5.1dB$ and $5dBi$ to $7dBi$ gain in the horizontal direction are achieved over the desired bandwidth (275MHz-550MHz). The optimized design parameters are $Bw = 32.0cm$, $Bh = 4.6cm$, $Ah = 15.8cm$, $Aw = 55.2cm$,

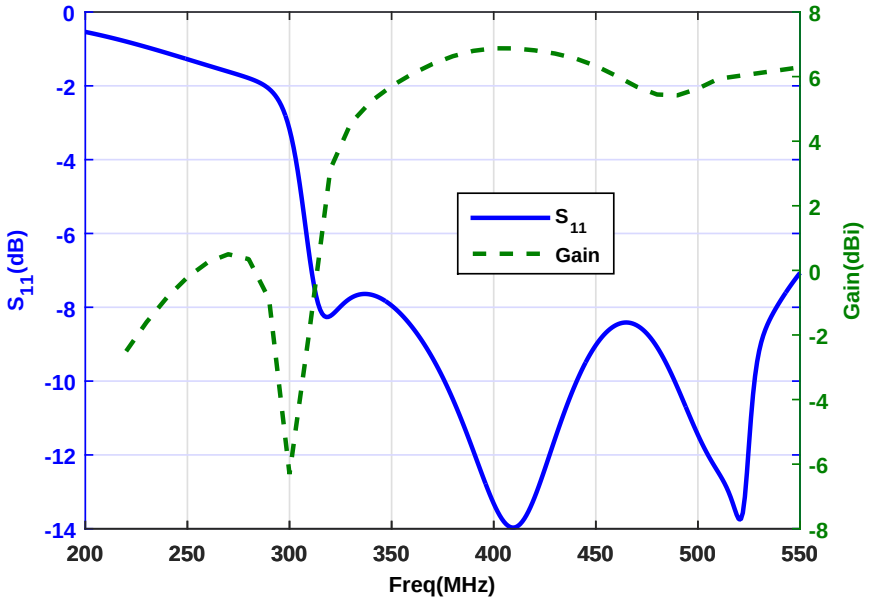

Figure 2.3: The input reflection coefficient and gain of a generic monopole bow-tie placed in the window. The width and height of the antenna are optimized to maximize the bandwidth. The antenna is not an efficient radiator at frequencies below 320MHz.

$Eh = 3.7cm$, $Ew = 32.8cm$, $Sh = 13.0cm$ and $Sw = 2.7cm$.

Since the window is slanted $15°$ with respect to the vertical direction, the main beam of the antenna needs to be tilted to achieve maximum radiation towards the horizontal direction. Because of the small dimensions of the window, it is not possible to embed a phased array in the window. However, it is well-known that the main beam of a monopole antenna, in the absence of an infinite ground plane, is not exactly perpendicular to the antenna and is tilted upwards. The tiled beam property of monopole antennas can be exploited to achieve the desired radiation pattern without the need to implement a phased array. Moreover, because the antenna is embedded in the window frame, its radiation pattern is restricted by the waveguide modes that are supported by the frame. Fig.2.8 shows a few of these waveguide modes and their corresponding radiation patterns in vertical polarization. As seen in the graph, exciting TE_{10} or TE_{20} alone does not result in a tilted beam in E plane. The lowest order mode that is capable of supporting a tilted beam is TE_{11}. Note that TE_{01} and TM_{11} radiate in horizontal polarization and are not included in the analysis. This study shows

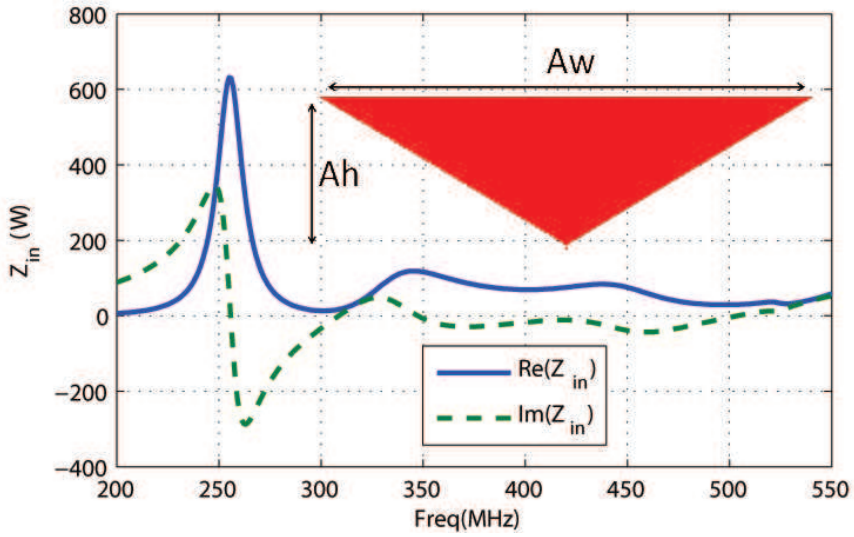

Figure 2.4: The input impedance of the Generic monopole bow-tie antenna. The antenna has one resonant frequency around 250MHz with a very high radiation resistance. The first resonant frequency must be decreased to reduce the lower limit of the radiation band of the antenna.

that the antenna must excite TE_{11} or higher order modes to create a tilted beam. However, the cutoff frequency of TE_{11} in our structure is 330MHz. The wave number along the depth of the window is very small at frequencies slightly above the cut-off, and the depth of the window is less than $\lambda_0/12$. Therefore, regardless of the shape of the antenna, TE_{11} can only be efficiently excited at frequencies well above 330MHz. Because of its asymmetry, a monopole antenna is inherently capable of exciting TE_{11} when allowed by the mentioned geometrical restrictions. Fig.2.9 shows the radiation patterns of the window embedded monopole antenna in the E-plane. As expected, the beam is only slightly tilted at 375MHz, but a significant upwards shift is observed at 475MHz. In Fig.2.10, the far-field radiation patterns of the first two fundamental waveguide modes are plotted. The far-field of any antenna placed in the window can be closely represented as a linear combination of the radiation patterns of individual waveguide modes. Fig.2.11 shows the gain of the window embedded monopole antenna both at boresight and horizontal direction (15° angle). The simulation results show that the antenna has a higher gain at the horizontal direction compared to boresight towards the end of the frequency band.

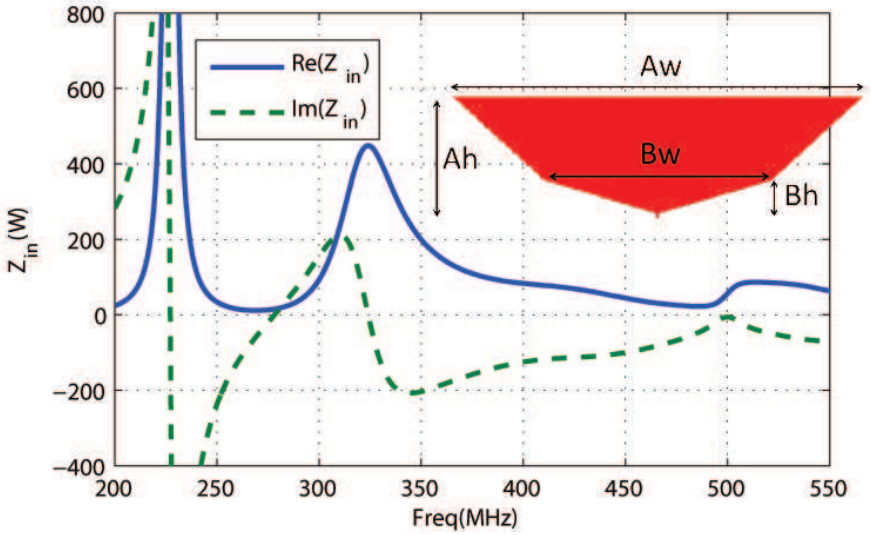

Figure 2.5: The input impedance of the monopole bow-tie antenna with convex edges. The first resonant frequency is decreased but the matching at higher frequencies is compromised.

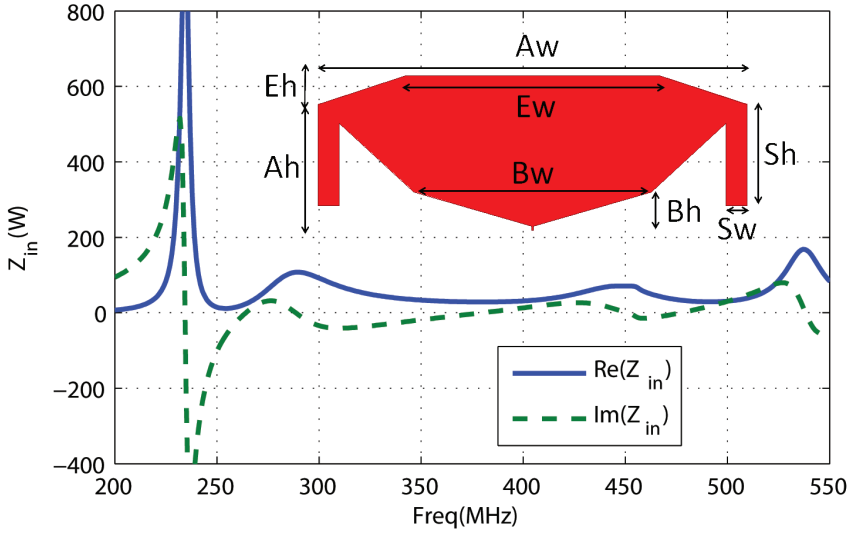

Figure 2.6: The input impedance of the modified monopole bow-tie antenna. Stub-like extensions are added at the two corners of the bow-tie antenna to further push back the lowest resonant frequency and improve the matching at higher frequencies.

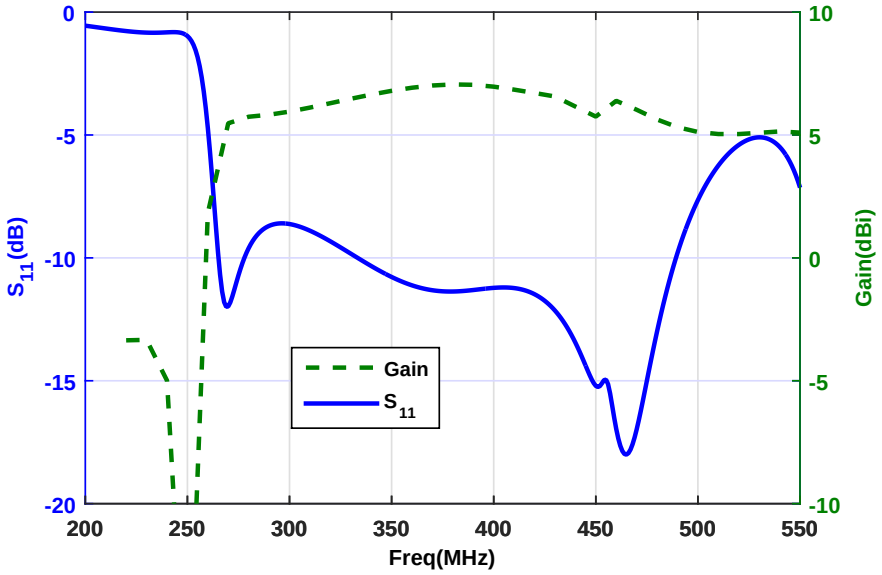

Figure 2.7: The input reflection coefficient and gain of the modified monopole bow-tie antenna placed in the window. The lower limit of the operation band is decreased to 270MHz as a result of modifying the shape of the antenna.

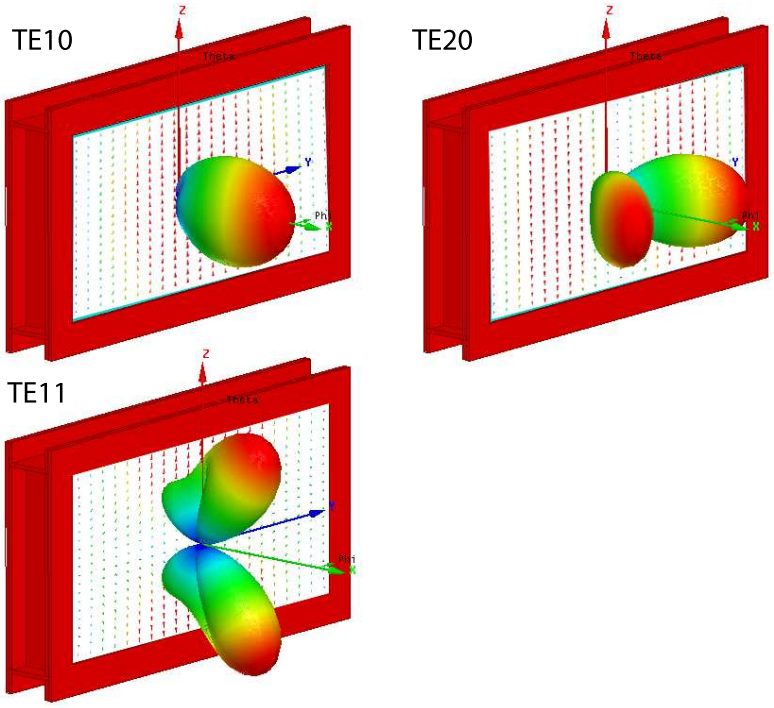

Figure 2.8: Electric field distribution and radiation pattern of the different waveguide modes in the antenna. These results correspond to a theoretical excitation of individual modes. The field of a realistic antenna can have components from all modes.

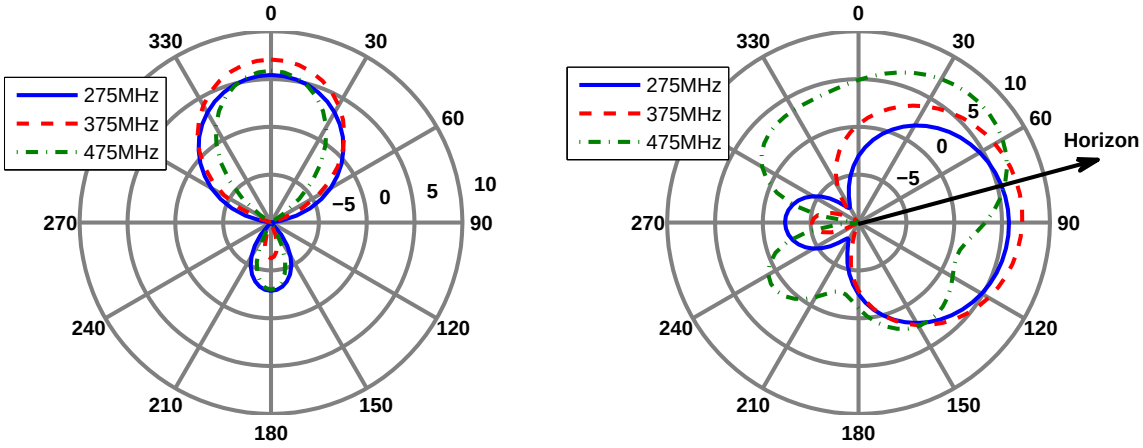

(a) H-plane (b) E-plane

Figure 2.9: Simulated radiation patterns of the antenna in E- and H-planes. The H-plane pattern is plotted versus ϕ and the E-plane pattern is plotted versus θ. A titled beam is achieved in E-plane at higher frequencies.

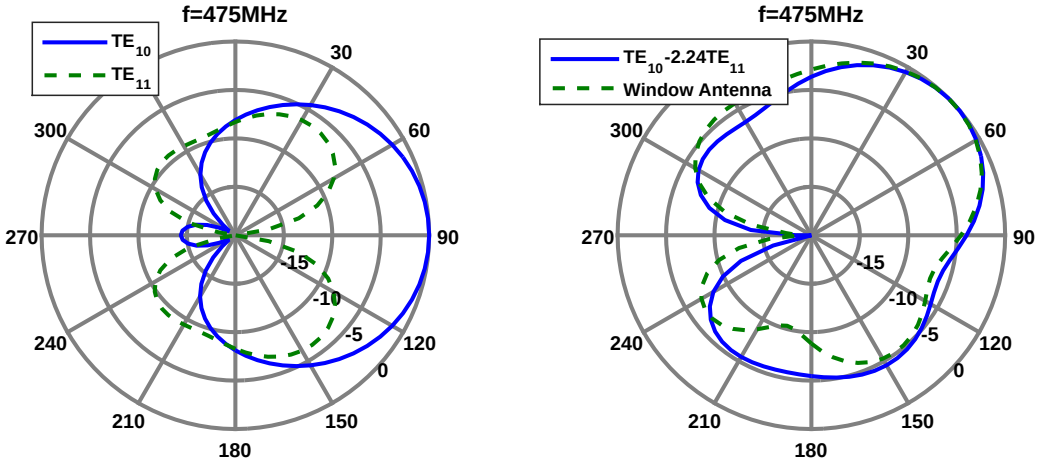

(a) H-plane (b) E-plane

Figure 2.10: Simulated radiation patterns of the first two modes of the waveguide (left) and the radiation pattern of the antenna (right). The far-field of any antenna placed in the window can be approximated by a linear combination of the far fields of individual waveguide modes.

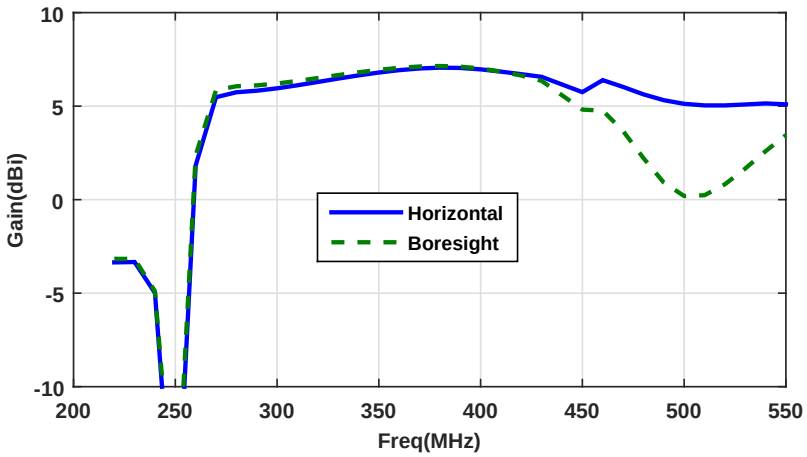

Figure 2.11: The gain of the monopole antenna at 15° and boresight. The main beam of the antenna is tilted at higher frequencies to compensate for the 15° windshield angle. At lower frequencies the beam is wider and s tilt in the beam is not necessary.

2.3 Dipole Antenna Design

In the previous section a monopole antenna was discussed as the radiating element in a relatively small and slanted window. The advantages of the monopole antenna include its small size, simplicity of feeding structure, and the possibility of achieving a tilted beam required for slanted windows. However, a dipole antenna usually offers a wider bandwidth and better radiation pattern than a monopole antenna and therefore is a better choice if a tilted beam is not required and the window dimensions are large enough to accommodate a dipole antenna. In this section the design of a dipole bow-tie antenna for the back window of MATV, a commonly used armored vehicle, is presented. The back window of MATV is not slanted and therefore does not require a tilted beam. The main difficulty in using a dipole antenna is that it requires a balanced feed. For this reason, a balanced feed line such as a twin-wire transmission line is sometimes used along with a differential amplifier to feed dipole antennas, particularly in receive only applications with short cable lengths. However, coaxial cables offer much better power handling, lower loss, and far superior shielding compared to balanced transmission lines. For these reasons, coaxial cables are almost always the preferred choice for feeding antennas. In order to connect an unbalanced line such as a coaxial cable to a balanced antenna, a device commonly known as a balun is needed [88]. Due to the large bandwidth and high power requirement of armored window embedded antennas, a tapered microstrip balun is most suited for this application. The balun design is discussed in detail later in this chapter.

The antenna design is performed through full-wave simulation using an ideal lumped feed. The antenna placement in the window is shown in Fig.2.12. The effects of adding the balun are included after the initial optimization of the antenna parameters are done. Similar to the monopole antenna, a generic bow-tie dipole antenna was placed in the window and its height and width was optimized to maximize the bandwidth of the antenna. In order to increase the bandwidth towards the lower frequencies, the sides and top of the bow-tie are bent similar to the monopole antenna design. Because of the larger window size, further

miniaturization using stub-like extensions was not necessary.

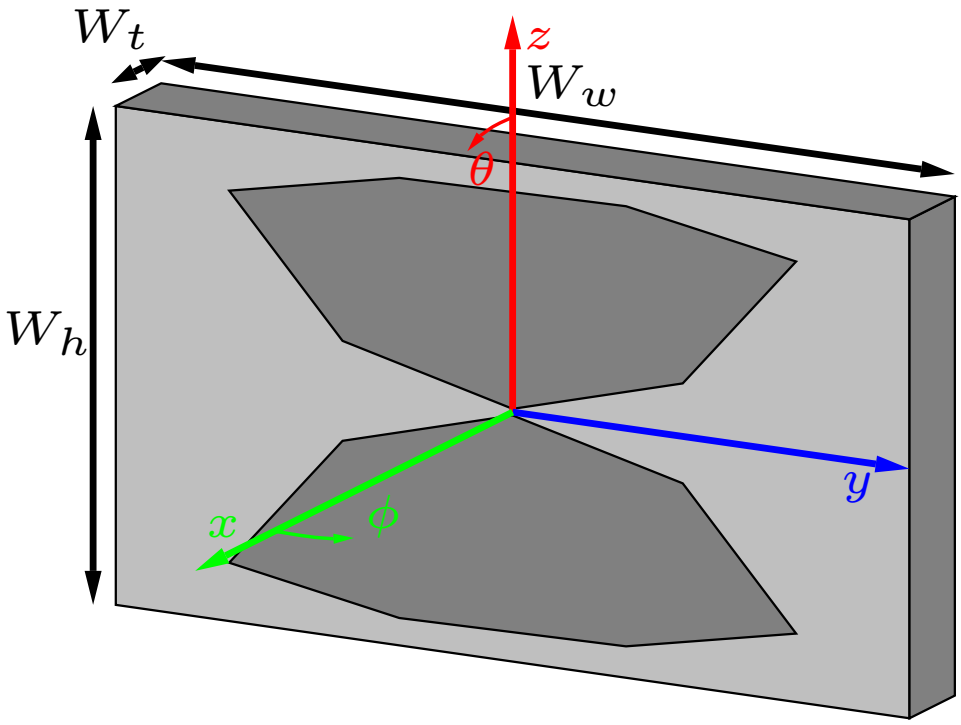

Figure 2.12: The geometry and design parameters of the monopole bow-tie and the armored window. A ground plane is placed on the backside of the window to provide cabin isolation and increase the directivity of the antenna.

Fig.2.13 shows the antenna shape and its design parameters. The antenna parameters were optimized to maximize the bandwidth of the antenna. The window dimensions and design parameters are $W_w = 686mm$, $W_h = 381mm$, $A_w = 285mm$, $A_h = 112mm$, $B_w = 83mm$, $B_h = 23mm$, $E_w = 129mm$, and $E_h = 78mm$. The input reflection coefficient of the optimized design and its gain along boresight are plotted versus frequency in Fig.2.14. Fig.2.15 shows the radiation pattern of the designed antenna in E and H planes. The gain of the antenna in the frequency range of 225-450 MHz varies between 5.4 dBi and 7.6 dBi with its maximum and minimum at 425 MHz and 225 MHz respectively.

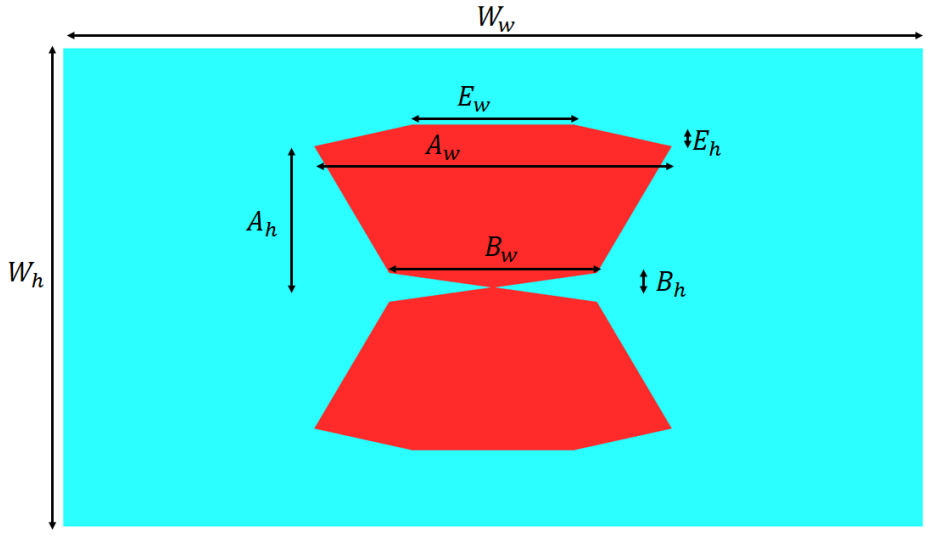

Figure 2.13: The geometry and design parameters of the modified bow-tie dipole antenna. The sides are bent to reduce the lower end of the operational bandwidth.

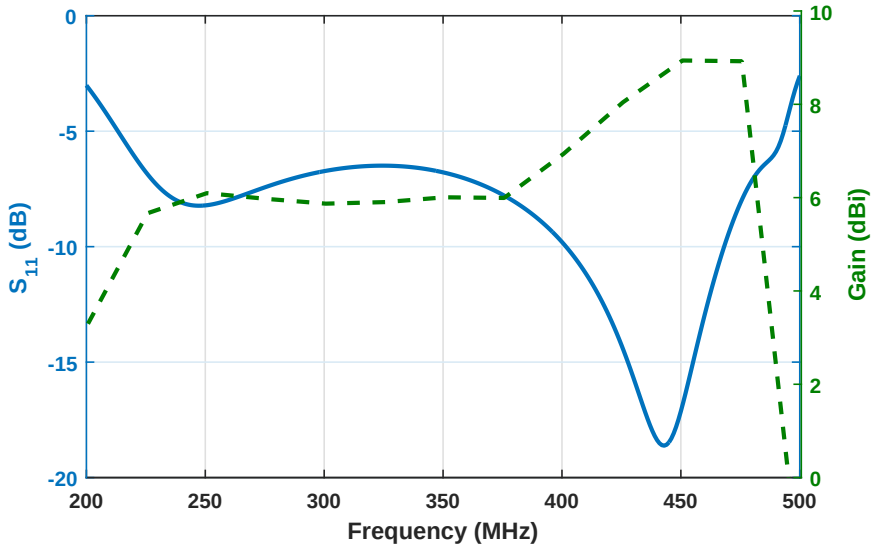

Figure 2.14: The input reflection coefficient and gain along the boresight of the modified dipole bow-tie antenna. The antenna has acceptable performance from 225 MHz to 475 MHz.

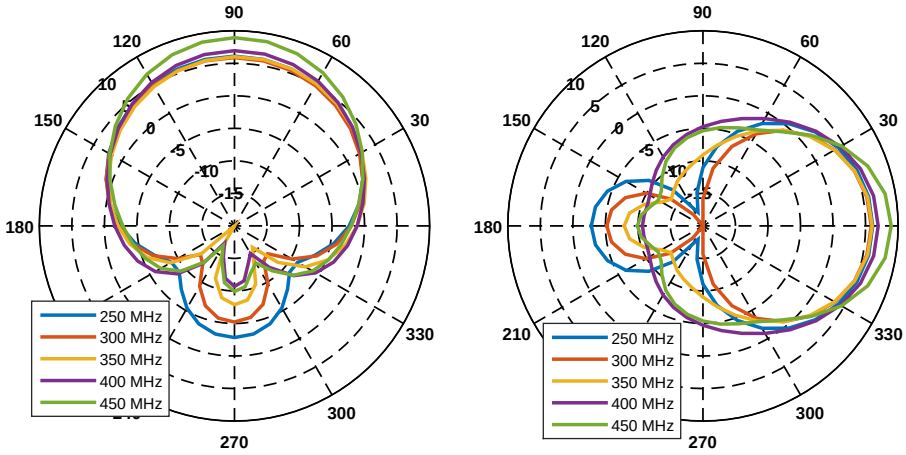

(a) E-plane (b) H-plane

Figure 2.15: he radiation pattern of the modified dipole bow-tie antenna in E and H planes. The direction of maximum radiation is along the boresight for all frequencies..

2.4 Irregular Shape Windows

Fig.2.16 shows a typical MATV with a number of monopole antennas mounted on the body of the vehicle. The antennas are designed for use with multiple radios carried by the vehicle for different purposes including satellite and ground communication. In this section, window embedded antennas are presented that are specifically designed for the side window and the windshield of this vehicle. The window embedded antennas are to replace the existing antennas and supersede their performance in terms of gain, cabin isolation, co-site interference, visibility, and air drag.

Figure 2.16: The transparent antennas replace the commonly used monopole antennas and improve their performance. The windshield and side windows of MATV are good candidates for antenna placement.

The cross section views of the windshield and side windows of the vehicle are depicted in Fig.2.17. The windows are made of several glass and polycarbonate layers with dielectric constants of 7.25 and 2.8 respectively. The overall thickness of the stack-up is 10.2 cm. To minimize passenger exposure to the RF radiation from the antenna, a transparent ground plane must be placed on one the side of the stack-up that faces the inside of the cabin and

the antenna is placed on the outer side of the slab. Therefore, the window glass and ground plane form a cavity behind the radiating element.

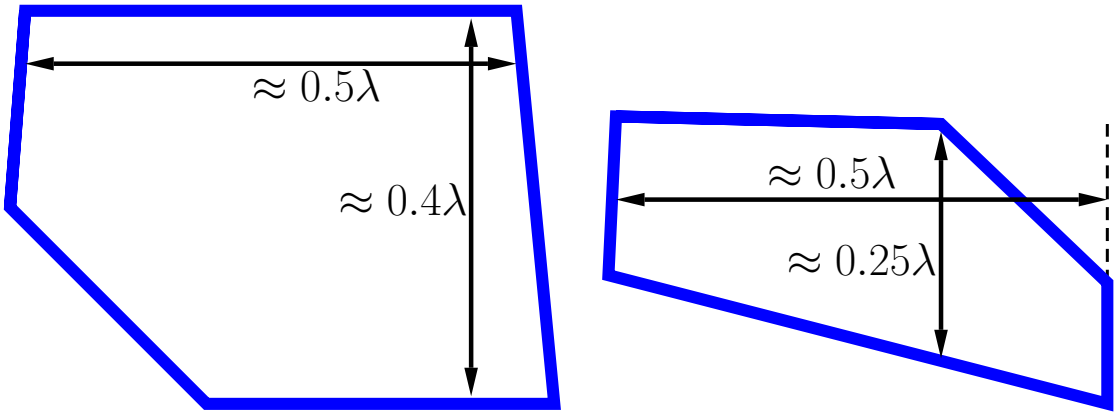

(a) Windshield (b) Side window

Figure 2.17: The cross section of the windshield and side windows of MATV. The windows have irregular shapes which makes it tricky for antenna design due to various asymmetric waveguide modes allowed by the structure.

The radiation pattern of the antenna is severely influenced by the shape of the window opening. The cavity opening can be viewed as a cross section of a waveguide and because of the boundary conditions on the walls, only certain field distributions (modes) are allowed on the window opening. The radiated field of the antenna can be found knowing only the field distribution on the window opening which can be expressed as a linear combination of the individual modes. Therefore, the radiation pattern of the antenna as a whole is closely approximated by a linear combination of the radiation patterns of individual waveguide modes. Because of the asymmetry of the window frame, the field distribution of the waveguide modes in the window is asymmetrical. Therefore, unlike the dipole antenna that was designed in a rectangular waveguide, the high order modes in the window can be excited even if the shape of the antenna is symmetrical. As a result, the main beam of the antenna can be steered to different directions unwontedly. Moreover, since the amplitudes of different waveguide modes that are excited by the antenna in the window are change with frequency, the direction of maximum radiation of the antenna can vary as a function of frequency. The behavior of the beam can be controlled to some extent by changing the

position of the antenna in the window. However, full-wave simulation results show that a stable beam over the entire frequency range of operation cannot be achieved.

In order to stabilize the beam of the antenna, the field distribution on the aperture of the window must be altered. This can be achieved by placing metallic sheets on the aperture of the window to force new boundary conditions on the aperture and therefore change the field distribution. The area covered by the metallic sheets can be chosen in such a way as to increase the symmetry of the antenna aperture and therefore that of the field distribution. Metalizing the aperture reduces the area of the window opening and increases the cuf-off frequencies of the modes and therefore can hinder the performance of the antenna particularly at lower frequencies. In addition, covering the aperture increases the opacity of the overall design. Therefore it is important to minimize the area covered by metal as much as possible. Fig.2.18 shows the numerically calculated field distribution of the first few waveguide modes in the window in the presence and the absence of the metallic covers. The simulation results confirm that the metallic covers can help increase the symmetry of the higher order waveguide modes and therefore reduce their contribution when a symmetric antenna is used. Fig.2.19 shows the radiation pattern of a generic bow-tie antenna placed in the window frame for different frequencies. As seen in the graphs, the main beam of the antenna steers in different directions in the absence of metallic covers especially at higher frequencies. However, the radiation pattern is much more stable when the metallic covers are added to the window aperture.

.

The windshield of MATV makes a 50° angle with ground which means the main beam of the antenna needs to tilted by 40° with respect to the boresight of the antenna. This tilt can be achieved placing a two element phased array in the antenna aperture instead of a single element antenna. Fig.2.20 shows a two element bow-tie array placed in the window and the S-parameters of its equivalent two-port network are depicted in Fig.2.21. Similar to the single antenna excitation, the radiation pattern of the two element array can

be expressed as a linear combination of the radiation patterns of the individual modes. The aperture field distribution of the dominant mode has a vertical symmetry with respect to the boresight of the antenna. Therefore is cannot produce a tilted beam. In order to generate a tilted beam, the higher order modes mist be excited by the antenna. The cut-off frequency of the lowest order mode that exhibits a vertical asymmetry is about 250 MHz. Therefore this mode cannot be exited at frequencies below 250 MHz and as a result, independent of the shape of the radiating element, a tilted beam cannot be achieved at frequencies blow 250 MHz.

In order to achieve a tilted beam, a phase shift between the excitation of the two elements is required. Fig.2.22 shows the radiation pattern of the antenna when the two elements are excited individually with a phase shift equivalent to a true time delay between the two elements. In this configuration, the phase shift between the two antenna excitations varies linearly with frequency. As seen in the graph, a tilted beam is achieved above 250 MHz and the tilt angle for higher frequencies is relatively stable with respect to the frequency. Moreover, ss seen in the graph, the directivity of the antenna is significantly higher than its gain at frequencies below 300 MHz. The reason for the drop in gain is the high mutual coupling between the two antennas. Some of the accepted energy by each antenna is coupled to the other antenna and is therefore absorbed by the matched terminal placed at the input of the antenna.

In practice, the required phase shift between the two array elements can be established using an asymmetric feed network consisting of an equal-split power divider and two transmission lines of different lengths, L_1 and L_2, which are used to connect the power divider outputs to the individual array elements. The difference between L_1 and L_2 determines the phase shift between the two elements and sets the tilt angle of the beam. The exact values of L_1 and L_2 are optimized to achieve the best impedance matching for the combined array. The power divider can be fabricated by simply splitting a 50ohm transmission line into two 100ohm lines (T-junction). This configuration is shown in Fig.2.23. The in-

put reflection coefficinet of the array is shown in fig.2.24. As seen in the graph, the input impedance matching of the array is much better than that of the individual elements. Here, the relatively hight mutual coupling of the antennas is exploited to improve the impedance matching. However, this mutual coupling has adverse effects on the performance of the array as will be discussed here.

The T-junction divider is wide-band, easy to design and integrate within the window, and can handle the high power requirements of our application. However, the performance of the T-junction divider is adversely affected by any impedance mismatch at the antenna terminals as well as coupling between the two elements. For this reason, at frequencies below 300 MHz where the bow-tie elements have poor impedance matching, the beam is not properly steered and therefore a gain drop in the 40° direction is observed compared to the case where individual elements are fed separately. The radiation pattern and the gain in the 40° direction of the array fed using the power divider is plotted in Fig.2.25 and compared with the ideally fed array. As seen in the graph, the feed network is not capable of creating a tilted beam at lower frequencies.

In view of the mentioned difficulties in fabricating an effective feed network for the two element array, an alternative approach for feeding the array is proposed. Our simulation results show a strong coupling between the two array elements especially for the lower end of the frequency band. The coupling along with the impedance mismatches of individual elements are the main reasons for the failure of the T-junction feed network. However, with proper design, the coupling between the two antennas can be exploited to reduce the complexity of the feed network. Full-wave simulation confirms that it is possible to feed only one element and use the coupling between the two elements to parasitically feed the second element. The relative distance of the two antennas plays a role in the amount of coupling between the two elements and can be optimized to achieve the required beam tilt. The shape of the elements is altered to improve the impedance matching. The shape of the modified element and the design parameters are shown in Fif.2.26. The optimal

design parameters are $A_h = 114mm$, $A_w = 152mm$, $B_h = 76mm$, $E_h = 25mm$, $E_w = 76mm$, and $D = 228mm$. The input impedance matching, gain in horizontal direction, and radiation pattern of the antenna array with one parasitically fed element are plotted in Fig.2.27, Fig.2.29, and Fig.2.28 respectively. The simulation results confirm a tilted beam and good impedance matching over the desired band.

The mode management technique discussed above is also applied to the side window of MATV. However, the side window is much smaller than the windshield which reduces the directivity and efficiency of the antenna. As a result, covering much of the area of the window opening to stabilize the beam severely hinders the performance of the antenna. For this reason, the area that is covered by metallic sheets is kept to a minimum at the expense of allowing a small unwanted beam steering at higher frequencies. Fig.2.30 shows the metallic covers and a dipole bow-tie antenna in the window. Similar to the previous designs, the sides of the bow-tie antenna are bent to increase the bandwidth.

The shape of the antenna can be optimized further to reduce the surface area of the antenna and therefore increase its transparency. Fig.2.31 shows the surface current density on the antenna at a few different frequencies. The simulation results show that most of the current flows on the sides of the bow-tie and there is hardly any current on the top and middle parts of the bow-tie. Therefore a large portion of the antenna can be removed without a significant effect on the current distribution on the surface of the antenna. Similar to the previously discussed designs, stub-like extensions can be attached to the bow-tie to improve the impedance matching. Fig.2.32 shows the geometry and the design parameters of the optimized antenna. The design parameters are $A_h = 114mm$, $A_w = 114mm$, $B_h = 76mm$, $B_w = 114mm$, $C_w = 152mm$, $D_w = 95mm$, $E_h = 25mm$, $E_w = 76mm$, $F_w = 38mm$, and $F_h = 38mm$. As seen in the graph, a large portion of the antenna is removed to improve the transparency of the antenna. The input reflection coefficient, absolute gain in boresight, and radiation pattern of the antenna are plotted in Fig.2.33, Fig.2.34 and Fig.2.31 respectively.

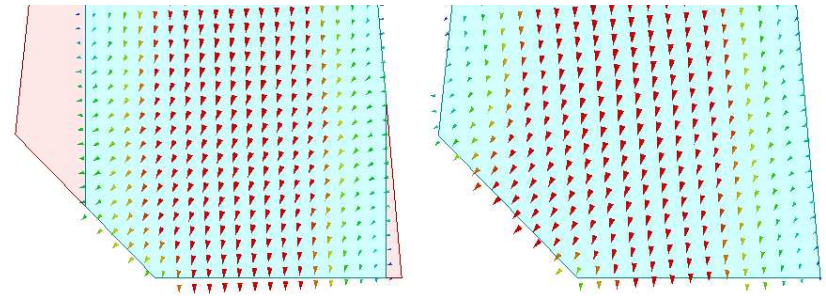

(a) Lowest order mode

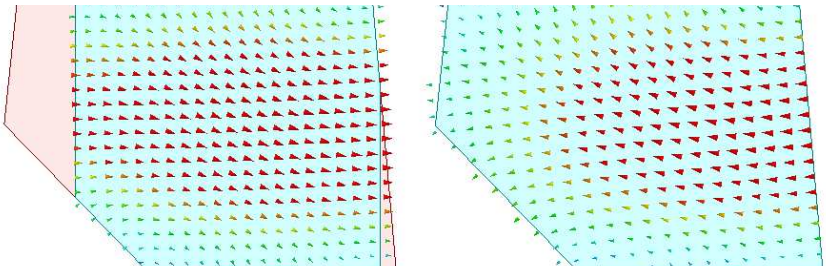

(b) Second mode

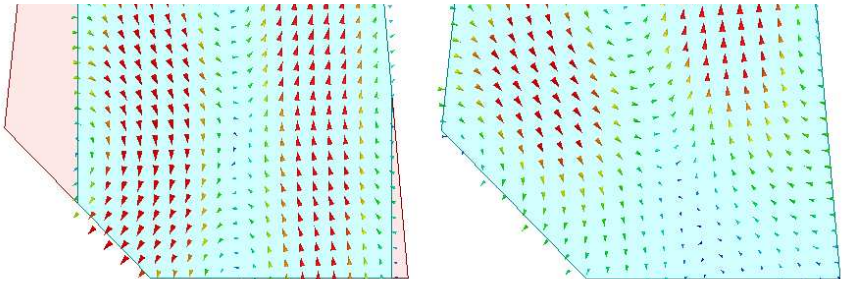

(c) Third mode

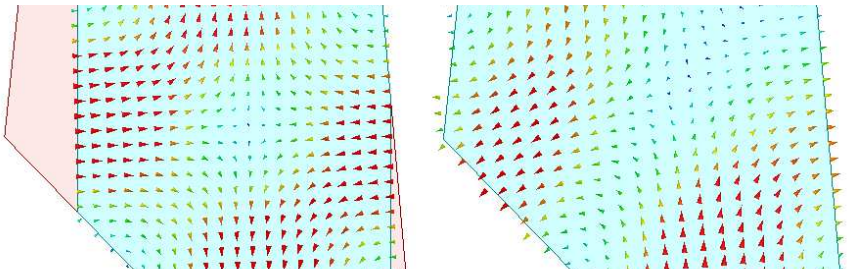

(d) Fifth mode

Figure 2.18: The field distribution of the waveguide modes supported by the windshield structure. The metallic covers increase the symmetry of the field distribution and help stabilize the radiation pattern over the operating frequency band.

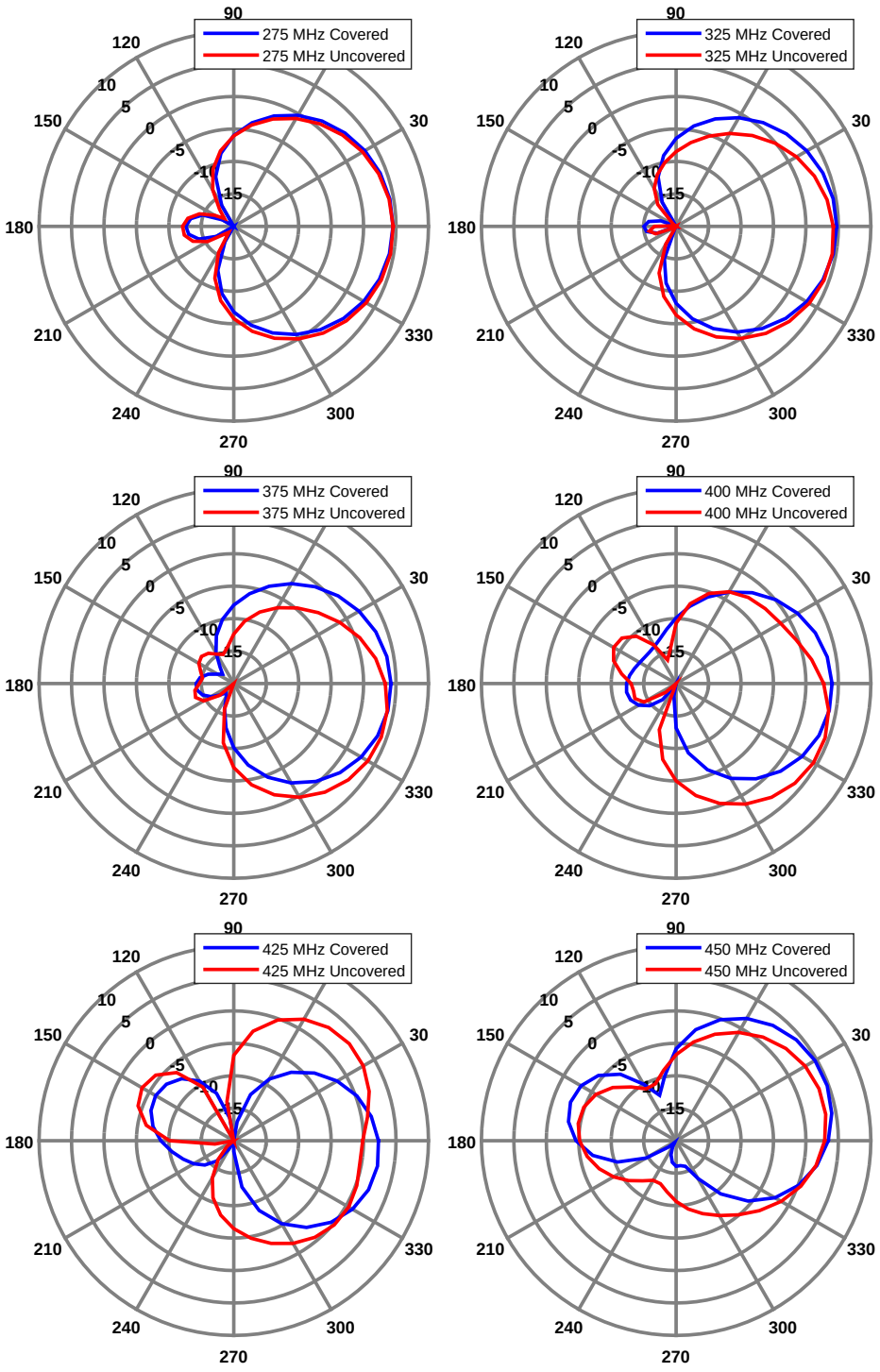

Figure 2.19: The radiation pattern of the antenna in the H-plane for different frequencies. The beam of the antenna steers in different directions as a result of the irregular shape of the window. The beam can be stabilized by covering some of the aperture using metallic sheets.

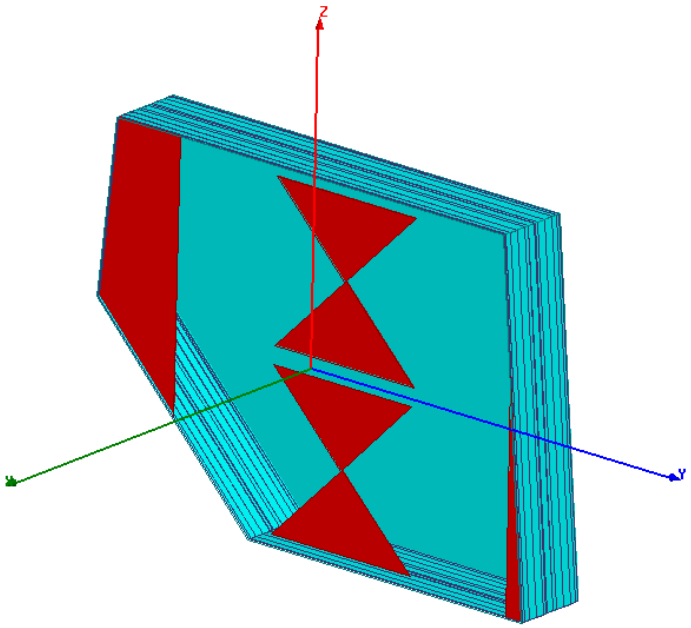

Figure 2.20: The geometry of a two element array placed in the windshield. The height and width of the antenna are optimized to improve the impedance matching.

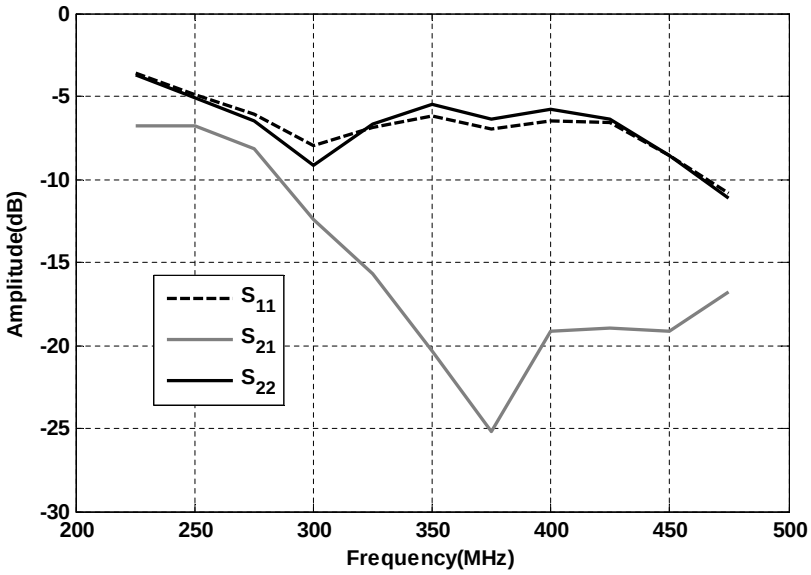

Figure 2.21: The S-paremeters of a two-element array placed in the windshield. There is a high degree of mutual coupling between the two antennas specially at low frequencies which can hinder the performance of the array.

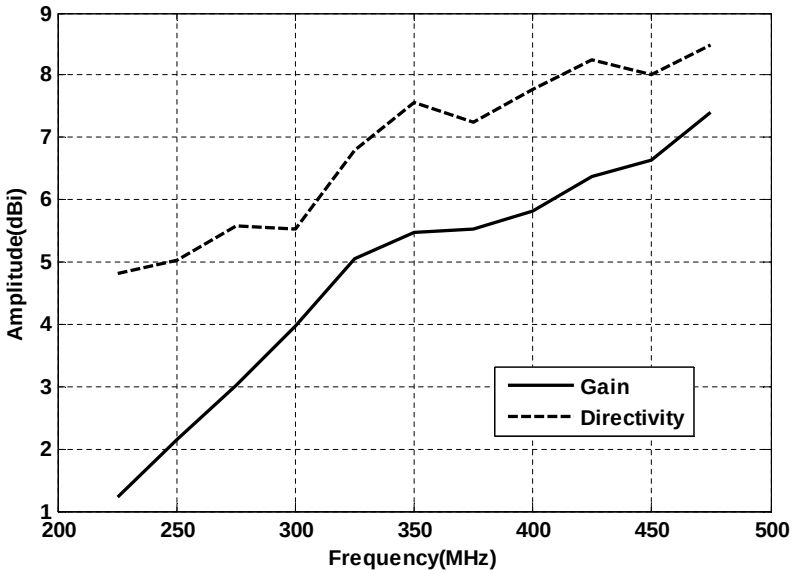

(a) Gain and directivity of the antenna in the horizontal direction ($45°$ from boresight)

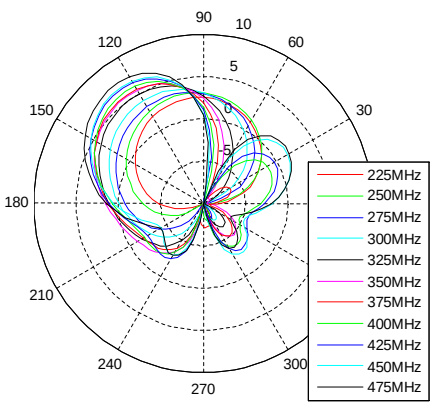

(b) E-plane radiation pattern

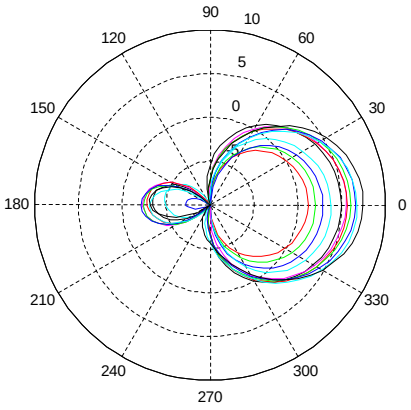

(c) H-plane radiation pattern

Figure 2.22: The gain, directivity and radiation pattern of the two-element array antenna embedded in the windshield of the MATV. A tilted beam is achieved at frequencies above 250 MHz.

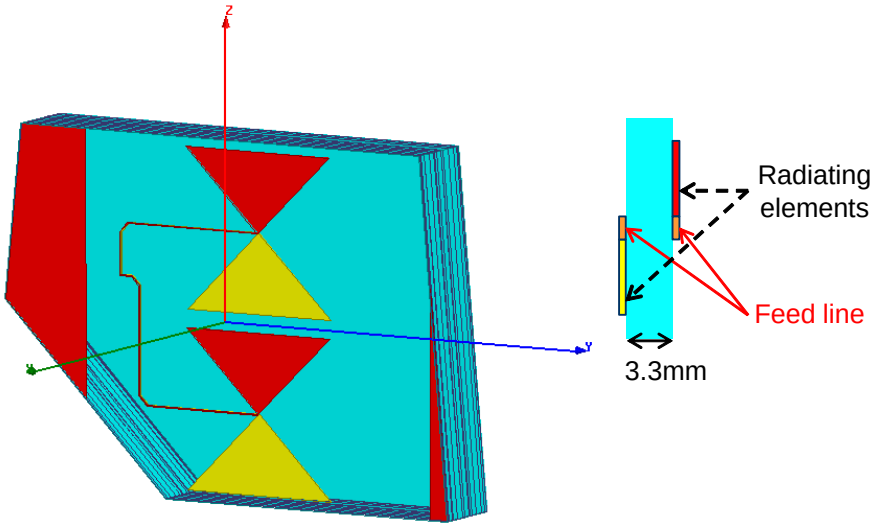

Figure 2.23: The geometry of the feed network based on a T-junction power divider. The feed line and antennas are fabricated on the front (red) and back (yellow)sides of a glass slab.

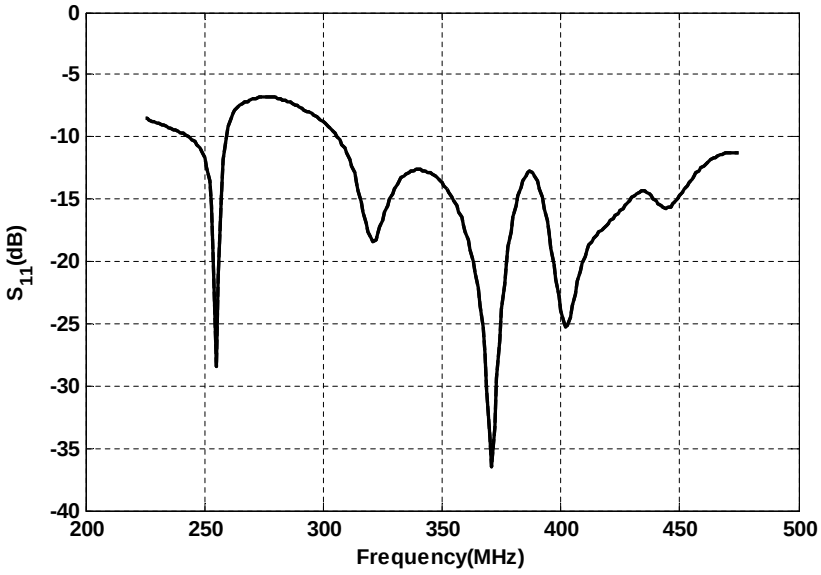

Figure 2.24: The input reflection coefficient of a two element array placed in the windshield and fed using a T-junction power divider.

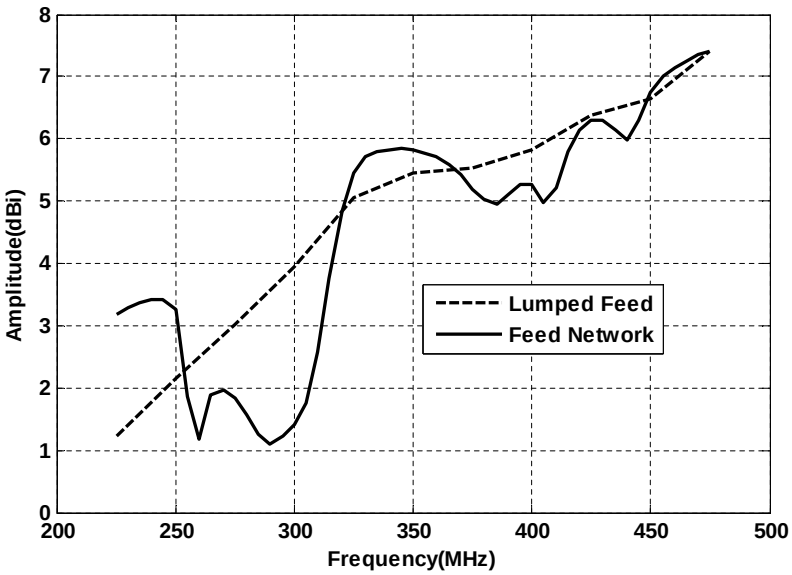

(a) Gain in 40° from boresight

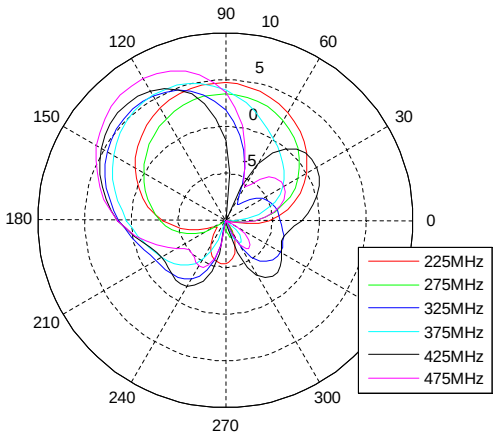

(b) E-plane

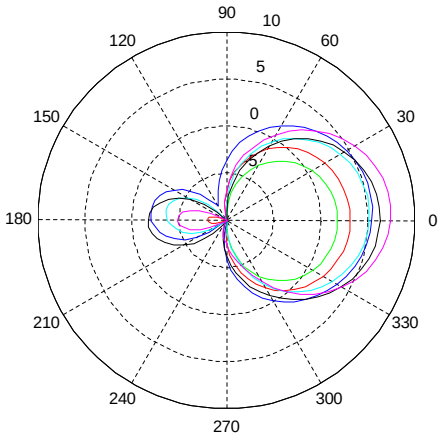

(c) H-plane

Figure 2.25: The gain and radiation pattern of the two element array fed using the designed feed network. The feed network is not capable of creating a tilted beam at the lower frequency range because of the poor impedance matching and hight mutual coupling between the antennas.

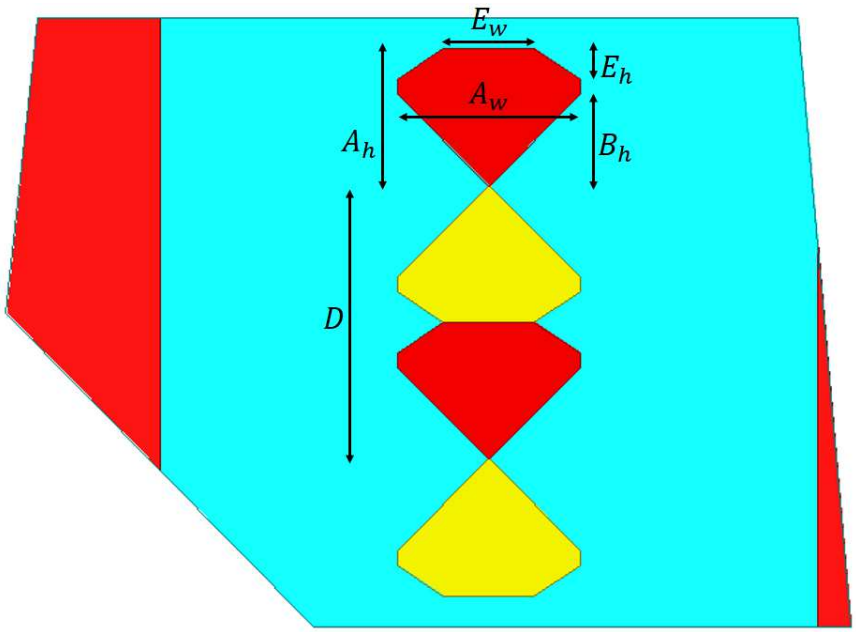

Figure 2.26: The optimized parasitically fed array antenna and the design parameters. Only the top radiating element is externally excited.

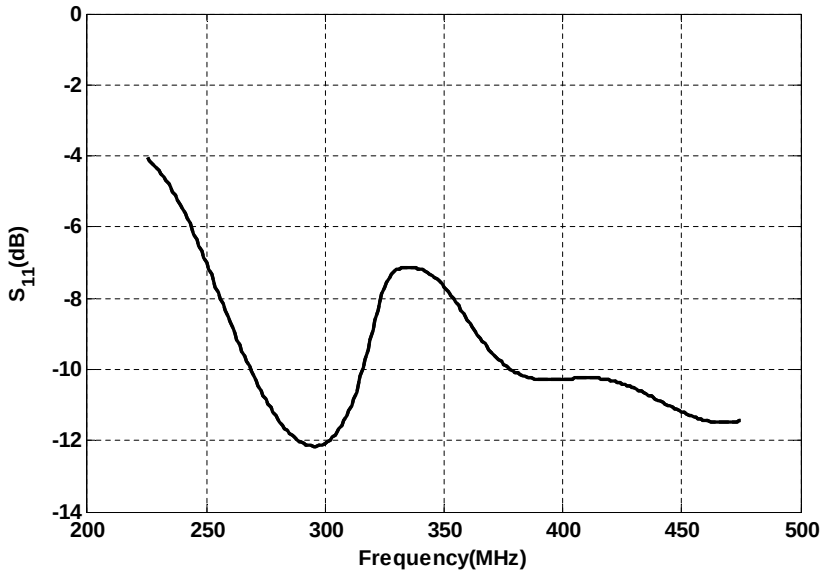

Figure 2.27: The input impedance matching of the array with one parasitically fed element. The shape of the elements and the spacing between them are optimized to maximize the gain in the desired direction and minimize the input impedance mismatch.

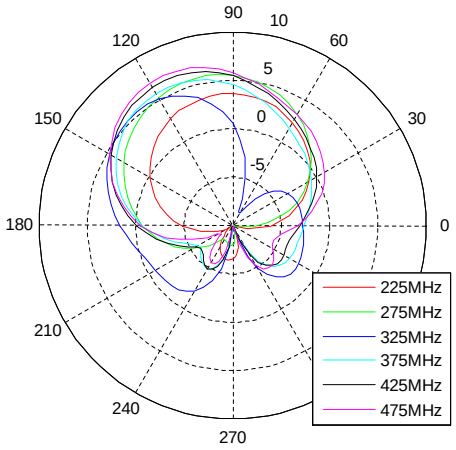

Figure 2.28: E-plane radiation pattern of the array with one parasitically fed element. A tilted beam is achieved at frequencies above 250 MHz.

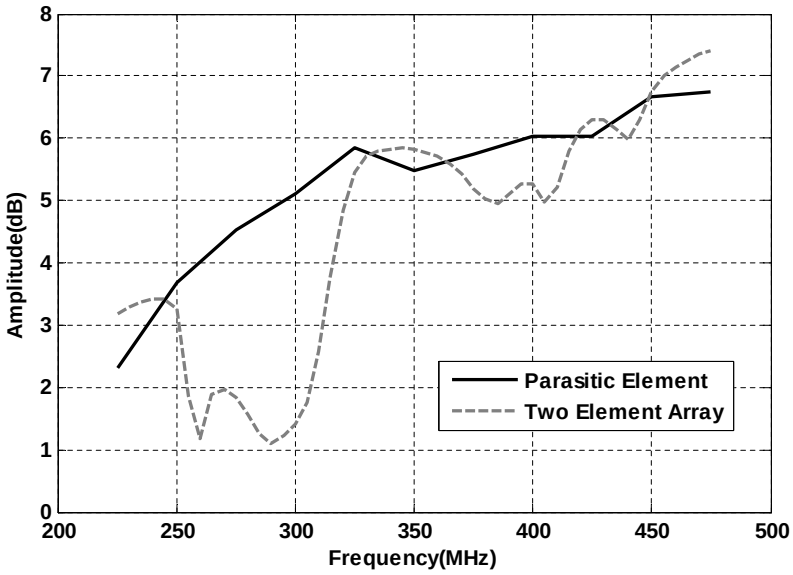

Figure 2.29: The gain of the two element array antenna with one parasitically fed element at 40°from boresight. This design outperforms the ideally fed two element array as well as the two element array fed using the designed feed network.

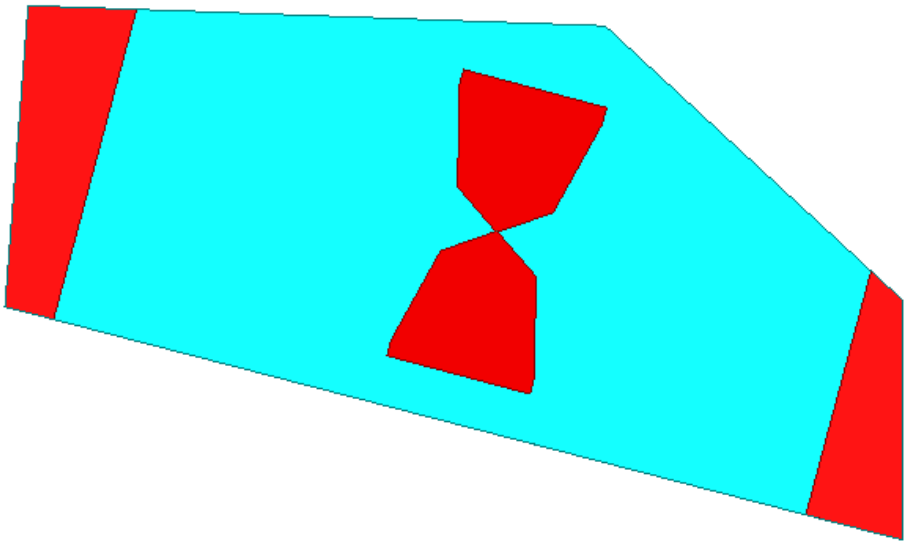

Figure 2.30: Geometry and positioning of a modified dipole bow-tie antenna placed in the side window of the MATV. The bent sides help reduce the lower bound of the operational frequency band.

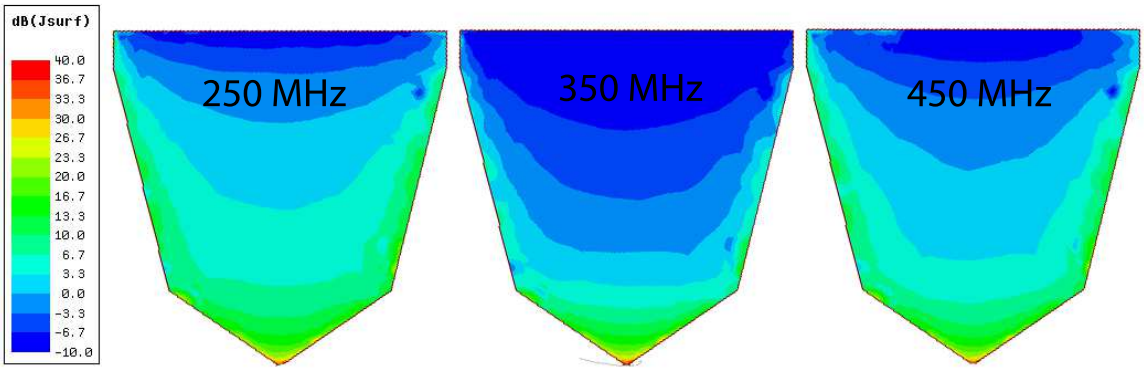

Figure 2.31: Surface current distribution on the antenna at different frequencies.

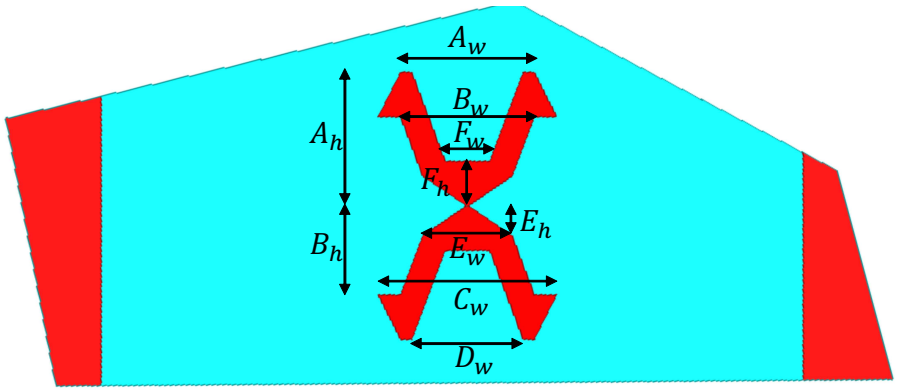

Figure 2.32: The geometry and design parameters of the optimized antenna for the side window of the MATV.

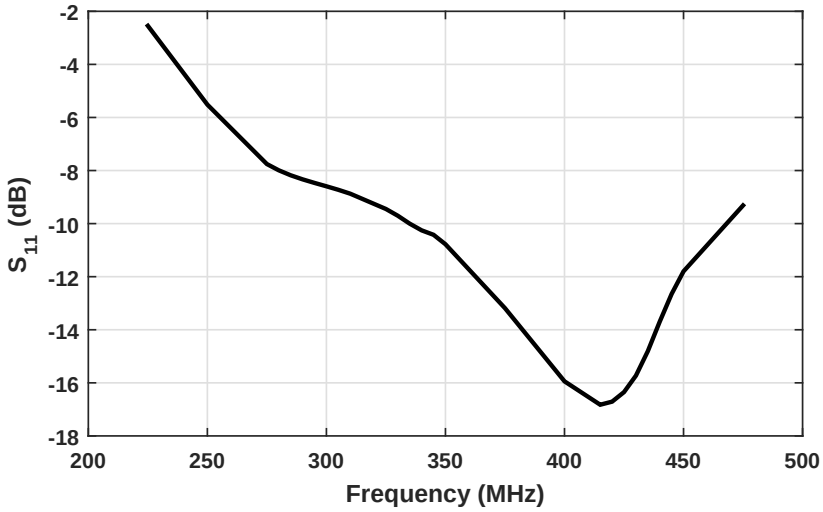

Figure 2.33: The input impedance matching of the antenna designed for the side window of the MATV. The antenna performs well from 250 MHz to 475 MHz

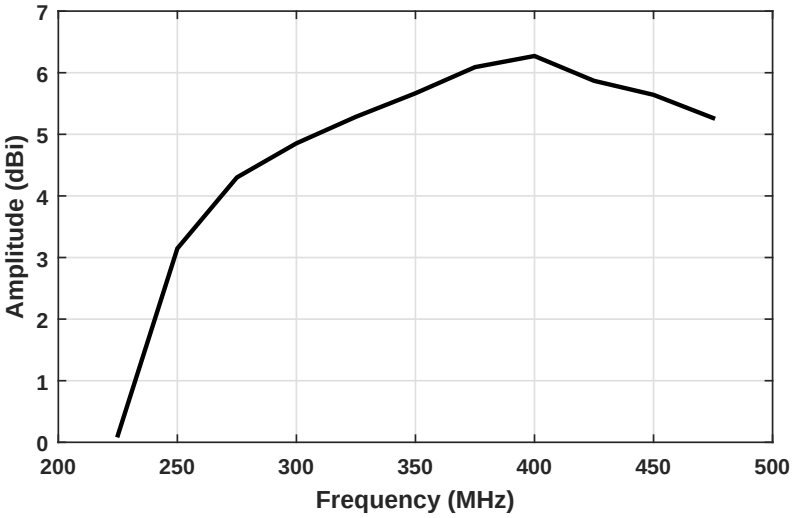

(a) Gain along boresight

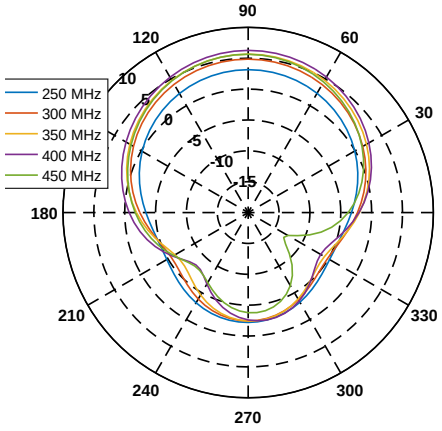

(b) E-plane

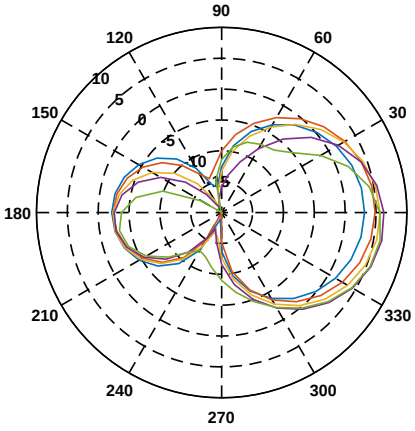

(c) H-plane

Figure 2.34: The gain and radiation pattern of the antenna designed for the side window of MATV. A 3 dBi to 6 dBi gain is achieved from 250 MHz to 475 MHz.

2.5 Transparent Antenna

Optically transparent conductors cannot be used to fabricate antennas at UHF frequencies because of their extremely small thickness compared to the skin depth. However, the antenna can be replaced by a fine wire-mesh without a significant change in its gain and input impedance. This option is explored for all the designed antennas and the results are presented in this section.

As a starting point, the metallic surface of the monopole antenna is replaced by a uniform square wire mesh while the outer shape of the antenna is kept intact. The square mesh consists of $1mm$ wide wires and has a mesh pitch of $18.3mm$. Using this configuration, only about 10% of the entire window surface is covered with metallic traces, and therefore the window can still serve its optical purposes. However, the opacity can be reduced further by recognizing the fact that the magnitude and direction of the currents on the antenna are not uniform and the mesh density can be varied accordingly. Fig.2.35 shows the magnitude and direction of surface currents on the antenna for different frequencies. Assuming a single frequency excitation, the direction and magnitude of the surface current at any point on the antenna change with time. In the most general case, $\vec{J_s}(t)$ sweeps a complete ellipse every period. However, for resonant structures such as the monopole antenna presented here, the surface currents are polarized and therefore the mentioned ellipse is highly eccentric. The arrows in Fig.2.35 represent the direction of the large axis of the $\vec{J_s}(t)$ ellipse. Ideally, the wire mesh is designed to be in line with the direction of the currents so that the currents are not heavily disturbed by the mesh. As seen in the graph, the surface currents are stronger along the edges of the bow-tie, and the current directions in these regions do not change significantly with frequency. In the regions where the directions of the currents vary considerably with frequency, the current direction corresponding to the frequency with the highest current magnitude is chosen.

Fig.2.36 shows the alternate mesh geometry. In this design, a finer mesh is used in the areas with greater surface current density, and the mesh direction is altered to be in line

with the direction of currents on the antenna. This design uses the same wire width as the uniform mesh design. However, its opacity is reduced to 6% by using coarser mesh in the areas with lower current density. Fig.2.37 shows the surface currents on the wire mesh geometry. As seen in the graph, currents are forced to flow along the direction of the mesh. Fig.2.38 compares the input reflection coefficient of the two designs. As seen in the graph, the modified mesh shows a closer electrical performance to the solid metal antenna in addition to a 40% reduction in opacity.

Similar to the monopole antenna, the dipole bow-tie can be replaced by a transparent mesh. Two different feeding mechanisms are used for the dipole antenna, one based on a balun transformer and one based on a microstrip tapered balun. The balun transformer is used to connect a balanced twin-wire line fabricated on the surface of the glass to a coaxial line that is used to connect the antenna to the radio. The meshed antenna with twin-wire transmission line is shown in Fig.2.39. The transformer balun has a 2 to 1 turn ratio with one side having a center wire that can be grounded to ensure a balanced output. Therefore, the transformer balun provides impedance matching between the 100Ω twin-wire and 50Ω coaxial line as well as mode matching between the two lines.

The antenna and the twin-wire feed line are placed on a single layer which simplifies the fabrication process compared to a tapered microstrip balun. However, the balun transformer introduces 1 to 2 dB additional loss in the path of the signal and also is not capable of handling tens of watts of power transmitted by the radio. Therefore the transformer balun is only suitable for receive-only antennas. Alternatively, a balun transformer design can be used to connect the antenna to the coaxial line. For this design, the top and bottom sides of the antenna are placed on the opposite sides of a 3mm thick slab of glass as shown in Fig.2.40. The microstrip balun consists of two linearly tapered metallic strips placed on the opposite sides of the slab and each connected to one side of the dipole antenna. The strips have the same width at the antenna feed point, thereby forming a balanced transmission line. The balanced side of the strips have a width of 3.83 mm while the unbalanced sides

are 1.7 mm and 11.5 mm wide respectively. The balun taper is curved to increase the length of the cable and allow for a smoother transition. The tapered balun and transparent antenna are modeled together with the window frame in a full-wave simulation setup. The input reflection coefficient of the complete design is plotted in Fig.2.41.

The linear taper is easy to implement but is not the most efficient taper in terms of impedance matching performance and taper length. A better performance can be achieved by dividing the mictrostrip taper into two parts: a mode-matching taper and an impedance matching taper. The mode-matching taper connects the balanced antenna feed to an unbalanced mictrostrip line. Throughout the length of this taper, only the ground side of the microstrip line changes its width to match that of the signal strip by the end of the taper. The signal strip width is designed to have a 100Ω impedance at the balanced side. Instead of linearly changing the width of the ground side, a Klopfenstein taper [94] is used to achieve the best performance for a given taper length. The resulting impedance at the unbalanced end of the mode-matching section is close to 65Ω. The Klopfenstein taper is continued, this time only changing the width of the signal strip to match the impedance to a 50Ω. Fig.2.42 shows the tapered balun geometry. The taper performance is verified using full-wave simulation and the results are shown in Fig.2.42. A better than 15 dB return loss at each port and less than 0.5 dB insertion loss is achieved over the entire band.

The tapered mictrostrip balun is integrated with the antenna designed for the front window of the MATV. The antenna consists of a dipole bow-tie that is fed by the balun and an identical antenna that is excited parasitically. The antennas are meshed radially which provides a higher mesh density close to the feed point where the surface current density is maximum. The mesh density is also increased close to the sides of the antenna and wider wires are used on the circumference of the antenna, where most of the current flows. In addition to the antennas, the mictrostrip balun and the metallic covers on the surface of the window are also meshed. Fig.2.44 shows the completed design. The input reflection coefficient and radiation pattern of the antenna are plotted in Fig.2.45.

A microstrip balun based on the same principle discussed above is designed for the side window of the MATV. However, the optimum input impedance for the side antenna is 70Ω as opposed to 100Ω for the front window. The surface area of the antenna is drastically reduced by removing metal from the top and middle parts of the antenna, where the surface currents are negligible. The remaining metallic parts of the antenna are meshed to further improve the transparency of the design. Similar to the front window, the balun and metallic covers are also meshed. The complete design is shown in Fig.2.46 and the full wave simulation results are plotted in Fig.2.47.

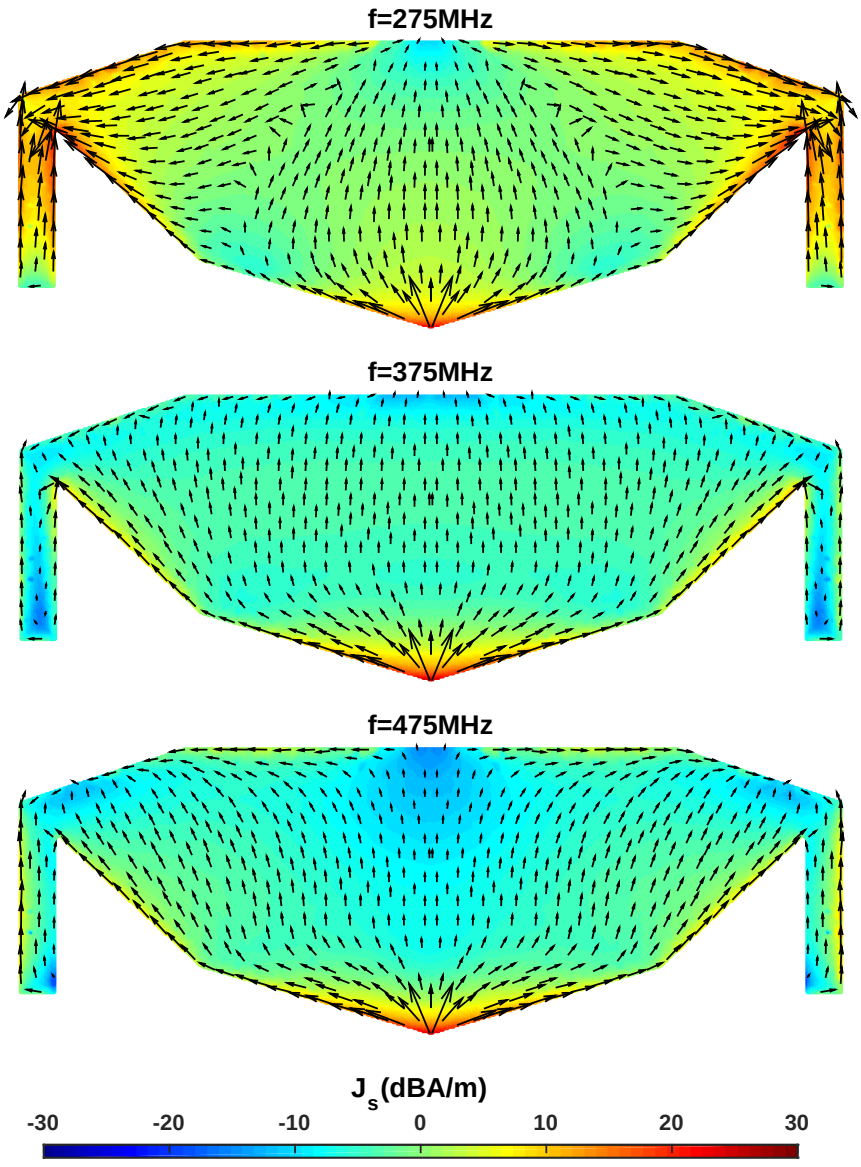

Figure 2.35: Surface current density and direction for different frequencies. A non-uniform mesh that follows the direction of the currents and is denser where the currents are stronger performs better than a uniform mesh.

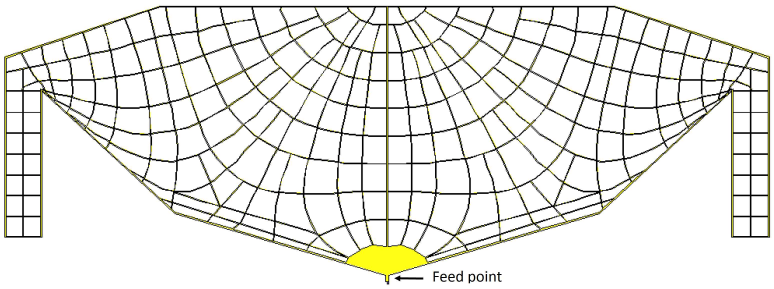

Figure 2.36: The modified wire mesh geometry. The direction of the mesh follows that of the surface currents on the full-metal antenna and the mesh is finer where the currents are stronger. If the current direction varies with frequency for a specific point, the direction corresponding to the frequency with the strongest surface current at that point is selected.

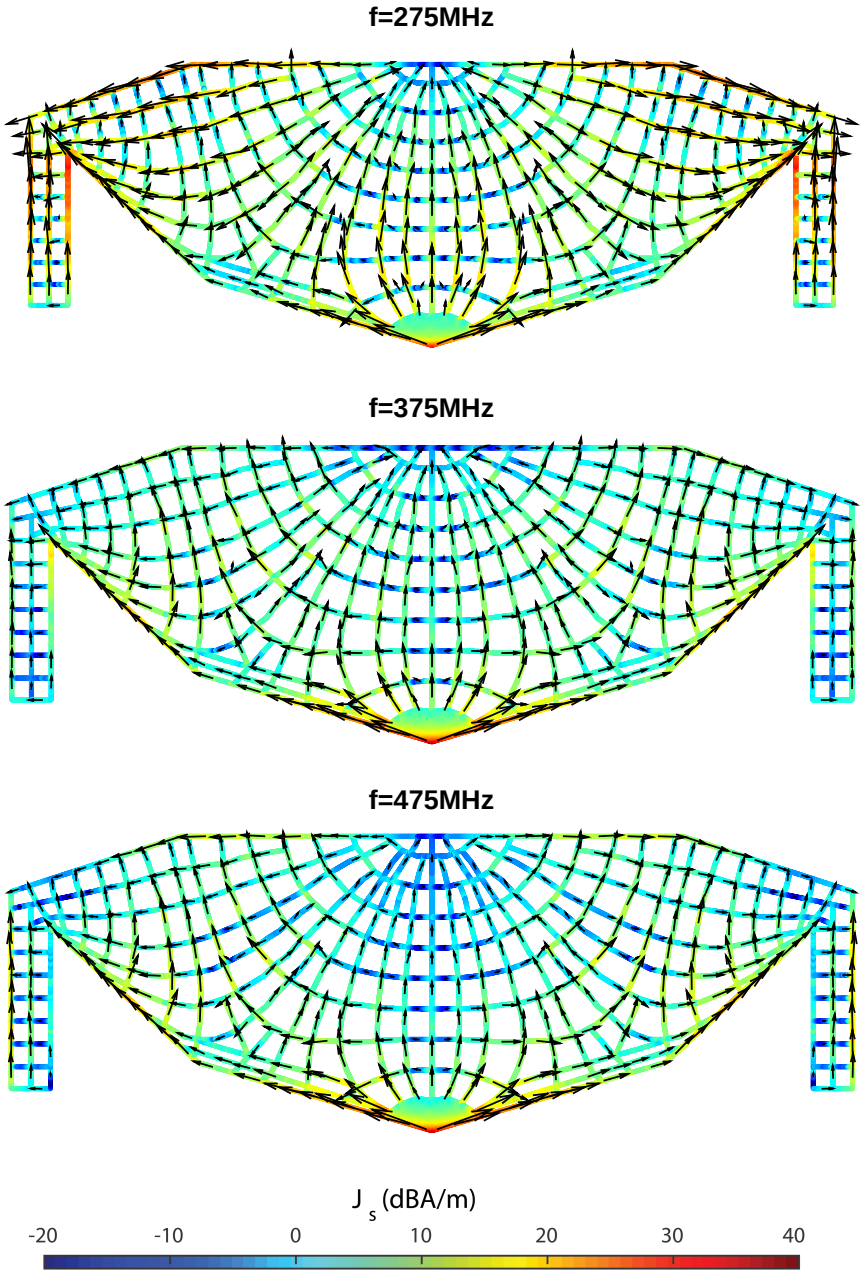

Figure 2.37: Surface current density and current flow direction on the modified mesh for different frequencies. The currents are forced to flow along the mesh wires.

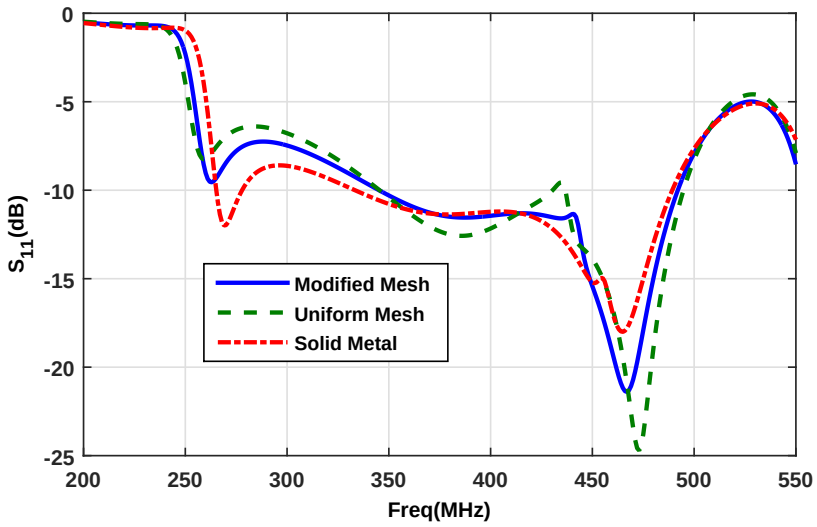

Figure 2.38: The input reflection coefficient of the uniform and modified wire meshes. The modified mesh performs closer to the full-metal antenna in addition to having less opacity than the uniform mesh.

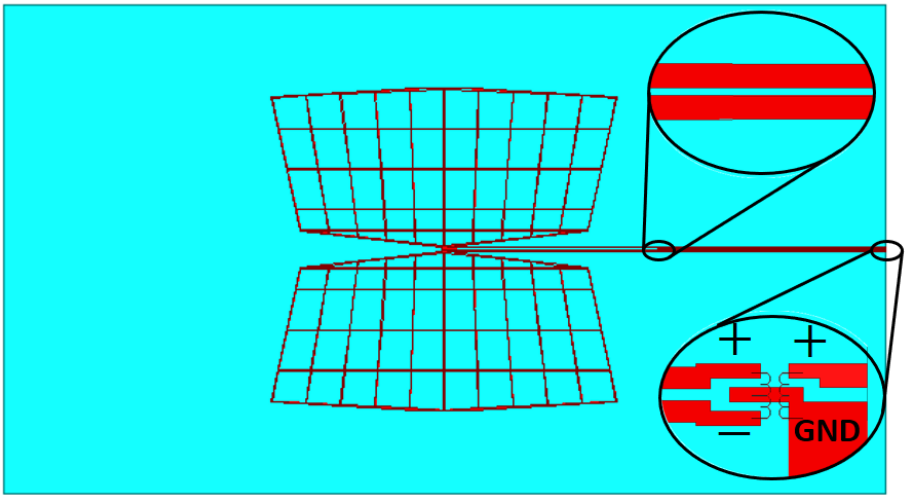

Figure 2.39: The meshed dipole window in the window frame. A transformer balun is used to connect the 100Ω twin-wire transmission line to a 50Ω coaxial line.

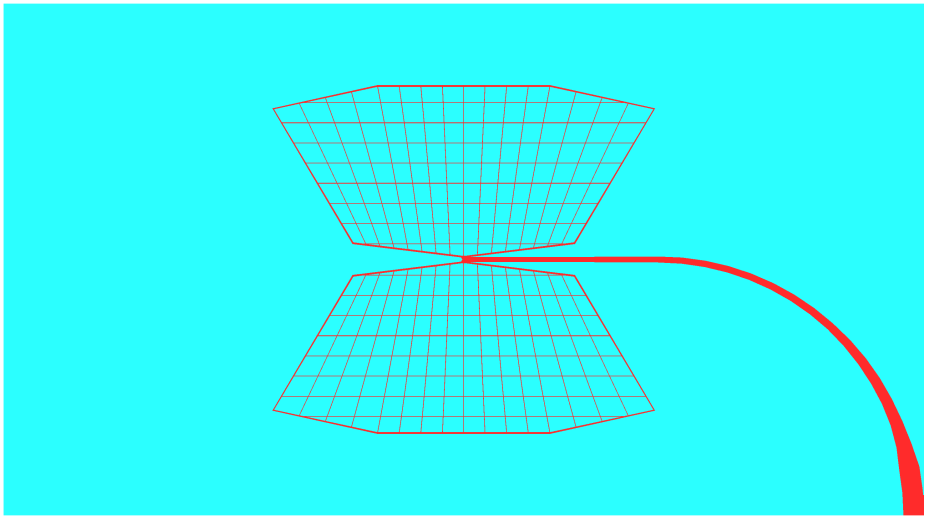

Figure 2.40: The meshed dipole antenna fed using a microchip tapered balun.

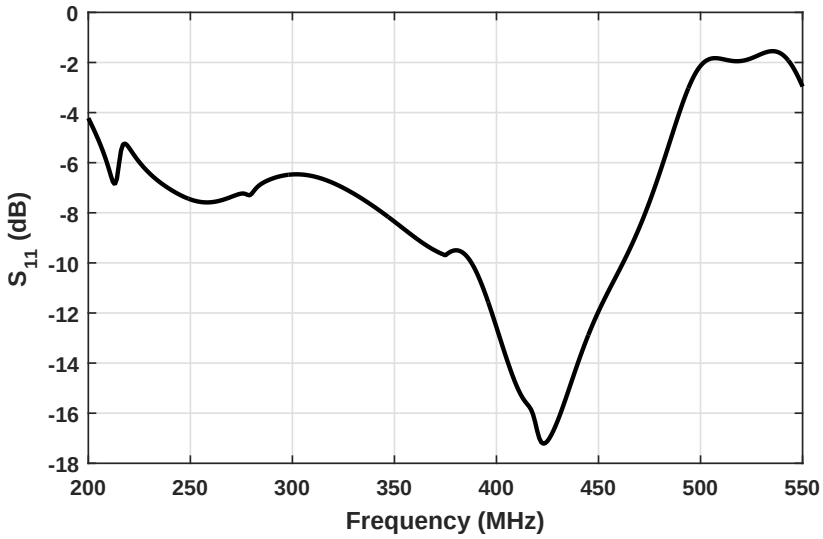

Figure 2.41: The input reflection coefficient of the meshed antenna with the tapered balun. The antenna has acceptable return loss between 225 MHz and 475 MHz.

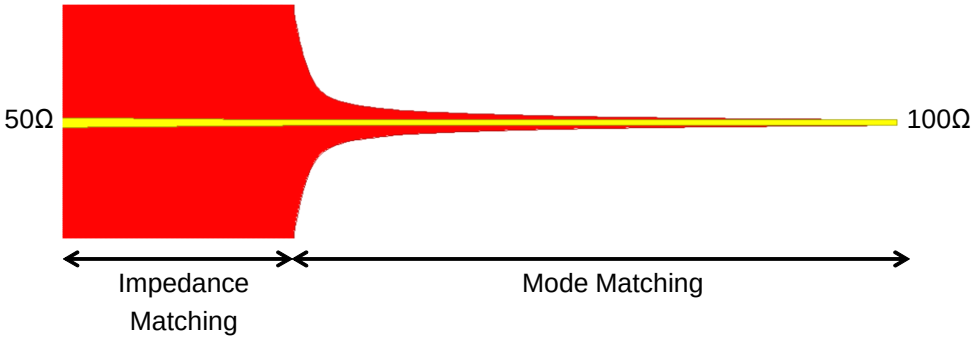

Figure 2.42: The taper is divided into a mode-matching and an impedance matching part. two. Each part uses a Klopfenstein taper to achieve the best performance for a given taper length.

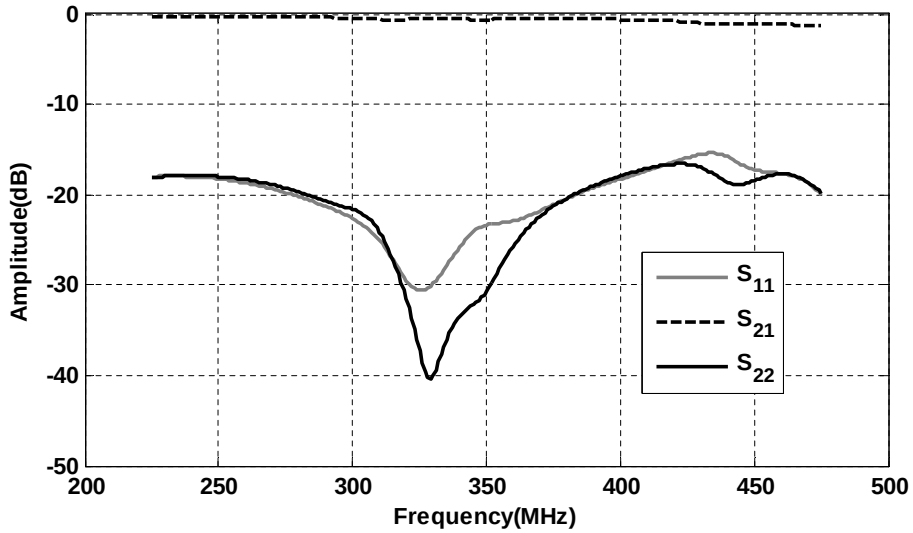

Figure 2.43: The full-wave simulation results of the tapered balun alone. A better than 15 dB return loss is achieved for both ports over the entire band.

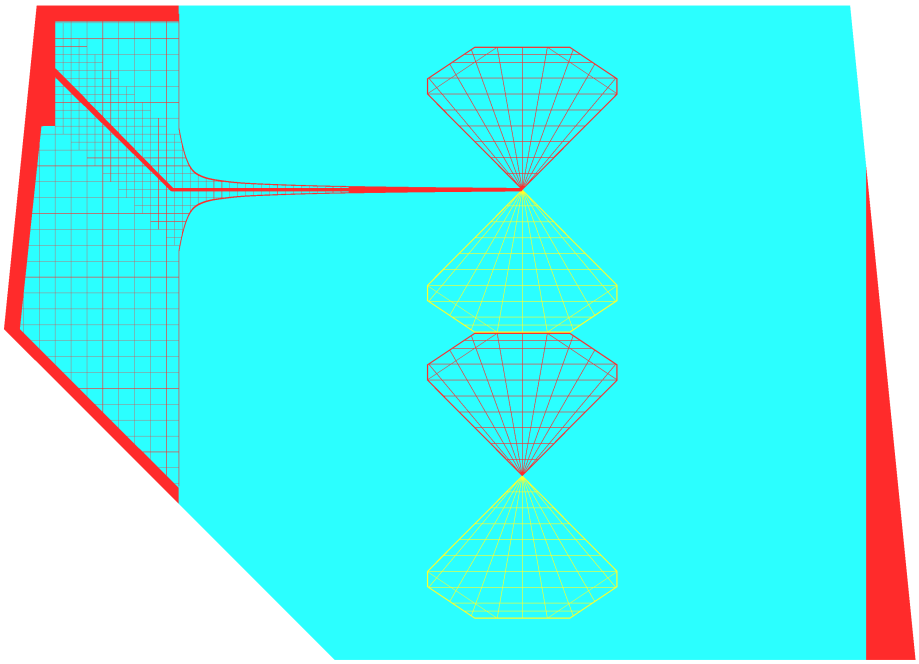

Figure 2.44: The meshed windshield antenna is fed using a tapared balun. The balun and the metallic covers are meshed as well. The antenna is meshed radially to increase the mesh density close to the feed point where the surface currents are stronger.

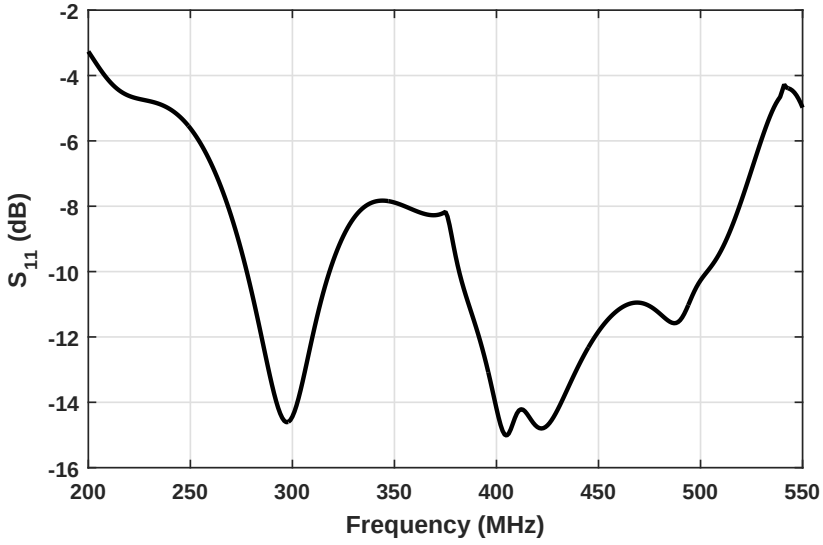

Figure 2.45: The input reflection coefficient of the meshed windshield antenna.

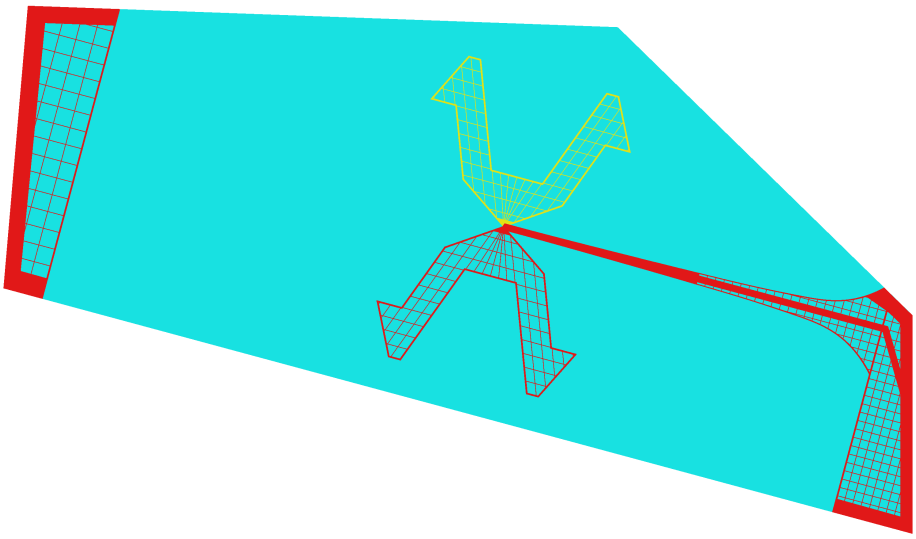

Figure 2.46: The meshed antenna designed for the side window of the MATV. The antenna uses a tapered microchip balun.

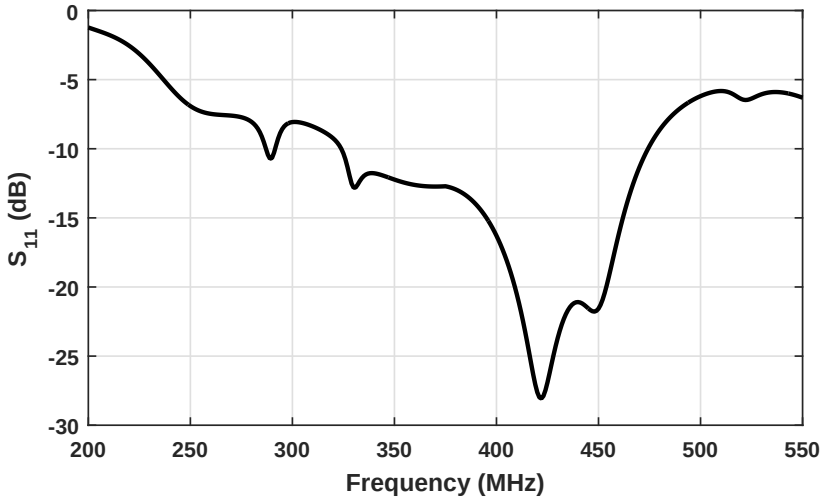

Figure 2.47: The input reflection coefficient of the meshed side window of the MATV.

2.6 Fabrication of Transparent Traces

An important part of fabricating transparent antennas made up of a wire mesh is the process of fabricating metallic traces on a transparent substrate. The conventional methods of fabricating printed circuit boards involve using an adhesive layer to attach a layer of copper to the substrate. Since the adhesive layer used is normally opaque or translucent, the fabricated printed circuit board will not be transparent even if the substrate on which the copper layer is attached is transparent. Despite this fact, the standard copper deposition techniques can be altered to achieve a transparent circuit board. However, the copper clad has to be custom ordered and manufacturers are unwilling to provide this service in small quantities. Although this method may be suitable for mass production, the price of fabricating one prototype is beyond what can be afforded for this project. Therefore, alternative methods of metal deposition on a transparent substrate are explored and summarized in this section.

The first method that is considered is a process commonly referred to as electro-less plating, during which a sub-micron layer of nickel is first deposited on a transparent plastic such as polycarbonate. The thickness of the nickel layer is much less than the skin depth of most metals at UHF and VHF frequencies (a few microns). Therefore the nickel layer is not adequate for operation at UHF and VHF frequencies. However, the nickel layer is conductive and can act as a base for depositing a thicker layer of copper using conventional electroplating. Fig.2.48 shows a few sheets of polycarbonate with the thickness of 0.062 that are covered by a $32\mu m$ layer of copper using the mentioned technique. Once copper is successfully deposited, chemical etching can be used to create the desired pattern on the substrate. Fig.2.49 shows the fabricated transparent monopole antenna and meshed ground plane. As seen in the pictures, the fabricated sheets are translucent. The polycarbonate sheets were transparent prior to nickel deposition. However, it is essential to treat the surface of the polycarbonate sheets with chemicals to increase the surface roughness and therefore increase the adhesion between the nickel layer and the polycarbonate sheets. As a result of this increase in the surface roughness, the polycarbonate sheets become

translucent

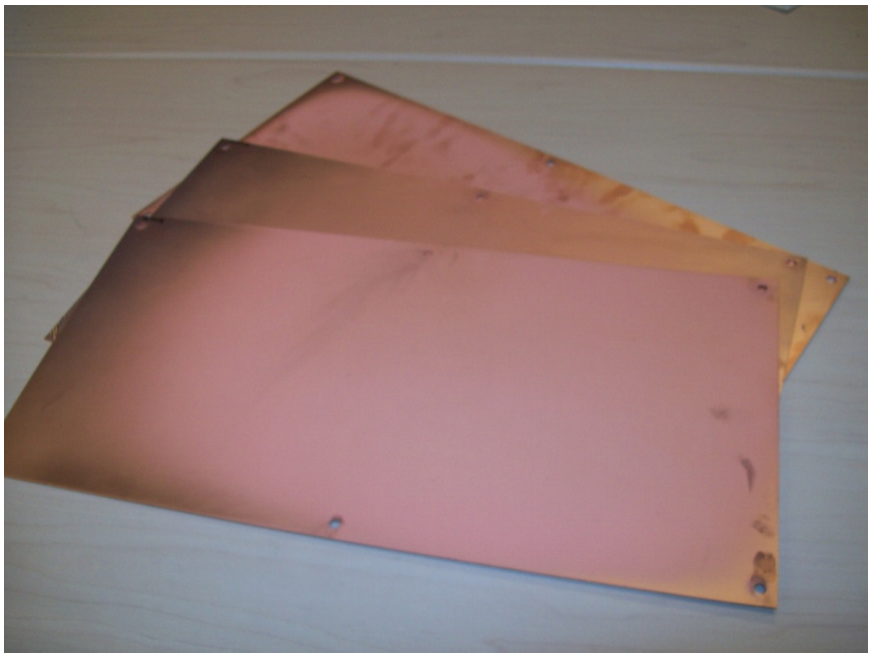

Figure 2.48: polycarbonate sheets metalized using electro-less plating

If the original surface smoothness of the polycarbonate substrate can be restored without damaging the metallic traces, the polycarbonate sheets can be made transparent. It may be possible to achieve this during the final process of fabricating the armored windows. The armored windows are made of multiple layers of glass and polycarbonate. A thin layer of polyurethane is used as an adhesive between different layers. In order to bond all the layers, the whole stack-up is treated with a very high pressure and temperature which causes the polyurethane layers to melt and bond the other layers together. The stack-up is placed in a sealed bag and vacuumed prior to increasing the temperature to prevent air bubbles from forming inside the stack-up. There are several types of polycarbonate with slightly different refractive indexes. Therefore it is possible to fabricate the antenna on a polycarbonate slab with the same dielectric constant as that of the polyurethane layer used in the bonding process. The polyurethane will then melt and fill in the imperfections on the surface of the polycarbonate, creating a transparent slab. While this technique can be explored further and perfected for commercial fabrication of transparent antennas, a simple

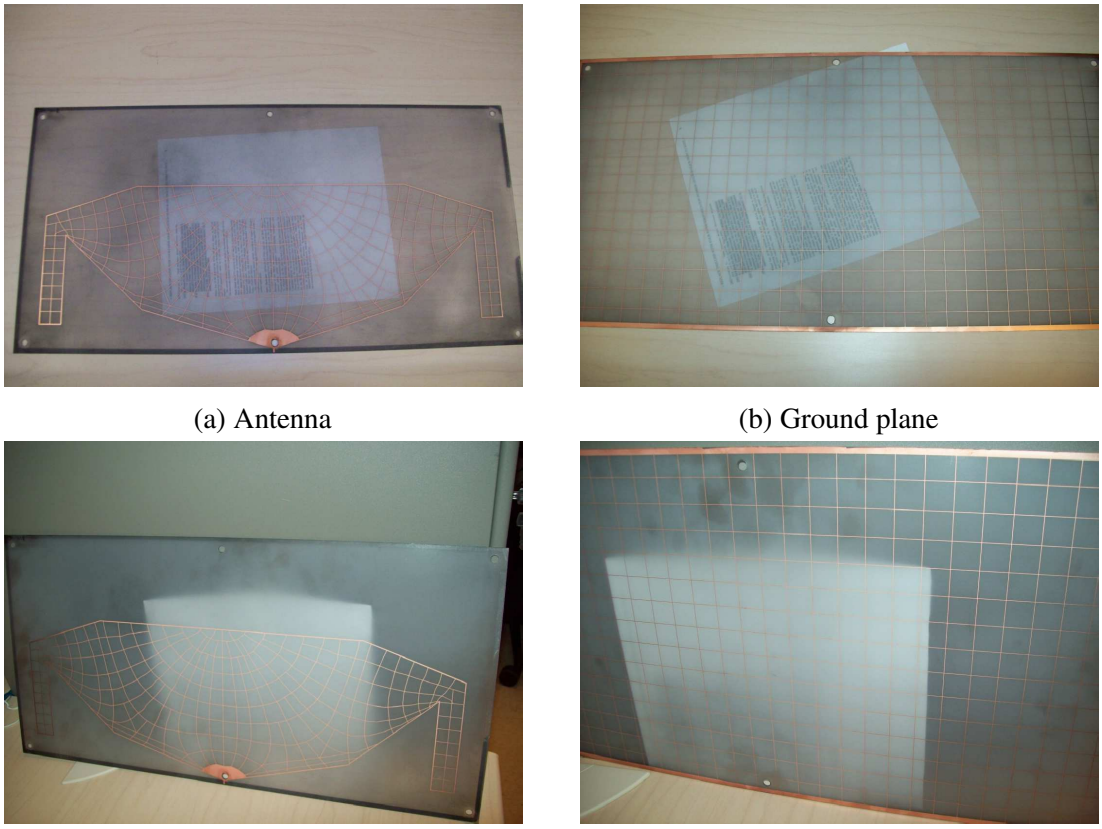

(a) Antenna (b) Ground plane

(c) Antenna (d) Ground plane

Figure 2.49: Fabricated translucent antennas on polycarbonate. Objects are clearly visible if they are attached to the back of the slab (a and b), but become blurry if they are placed at a distance (c and d).

and low-cost alternative must be used for fabricating a prototype transparent antenna.

Several other fabrication methods were considered including parylene deposition on a sheet of copper and polyester-copper lamination. In the first technique, a thin layer of parylene (approximately 100μ) is deposited on copper foil and in the second technique, copper and polyester foils are attached together using heat, pressure and a solvent as the bonding agent. Both of these methods require the copper to be chemically etched after the initial laminate is created. The surface of the transparent substrate that is facing the copper foil, takes its shape. Therefore, depending on the surface roughness of the copper foil, the surface of the substrate under copper may not be smooth enough to allow for the light to pass without distortion. As a result, a translucent surface may be created similar to

what was observed with electro-less printing. In the case of polyester lamination, a second layer of polyester can be laminated to the first layer after the chemical etching is done, to restore the smooth surface of the laminate. Fig.2.50 shows samples fabricated using these techniques. As seen in the images, both methods perform better than electro-less printing. The parylene layer is transparent but it is not perfectly clear as a result of roughnesses in its surface. The polyester laminate in Fig.2.50a is fabricated using the mentioned laminate, etch, laminate technique. The fabricated sample is transparent and clear but distorts the image due to wrinkles and air bubbles that are present between the two polyester foils. It should be noted that this sample was laminated manually because of its small size. The manufacturer claimed the imperfections could be eliminated if their automated process was to be used.

(a) Copper polyester laminate

(b) parylene deposited copper

Figure 2.50: Transparent printed circuit boards fabricated by parylene deposition and lamination. The fabricated PCBs are transparent but they are not clear due to surface roughnesses created in the fabrication process.

In collaboration with Motson Graphics, a robust procedure for fabricating conductive traces on glass using silk printing was developed. In this method, a conductive ink consisting of extremely small silver particles is used to print the metallic traces directly on the surface of the glass. The advantage of this method over metal coating is that the conductive ink is applied only to the places where it is needed. Therefore there is no need for etching the metallic coating to create the desired metallic traces. Fig.2.51 shows the fabricated

transparent monopole antenna and meshed ground plane using conductive silk printing.

Physical vapor deposition[] ia another method commonly used to deposit a layer of metal on different substrates. A thin layer of metal, typically a few hundred nanometers, can be deposited on transparent substrates such as glass, polycarbonate or polyester. This technique involves vaporizing the metal in vacuum and guiding the vapor towards the target surface. The advantage of this method over chemical deposition methods or electro-less plating is that the surface roughness of the transparent material does not change. Therefore the substrate remains transparent after the metal layer is etched to form the desired metallic traces. A variety of different metals including gold, silver, aluminum and chrome can be deposited using this method. Because of its simplicity, const effectiveness, and excellent performance, this method was chosen to fabricate the transparent antennas and ground planes. A 16μ layer of aluminum was first deposited on glass and the traces were created by chemically etching the aluminum. The fabricated transparent antennas and ground planes for the back window, side window and windshield of MATV are depicted in Fig.2.52, Fig.2.53, and Fig.2.54 respectively.

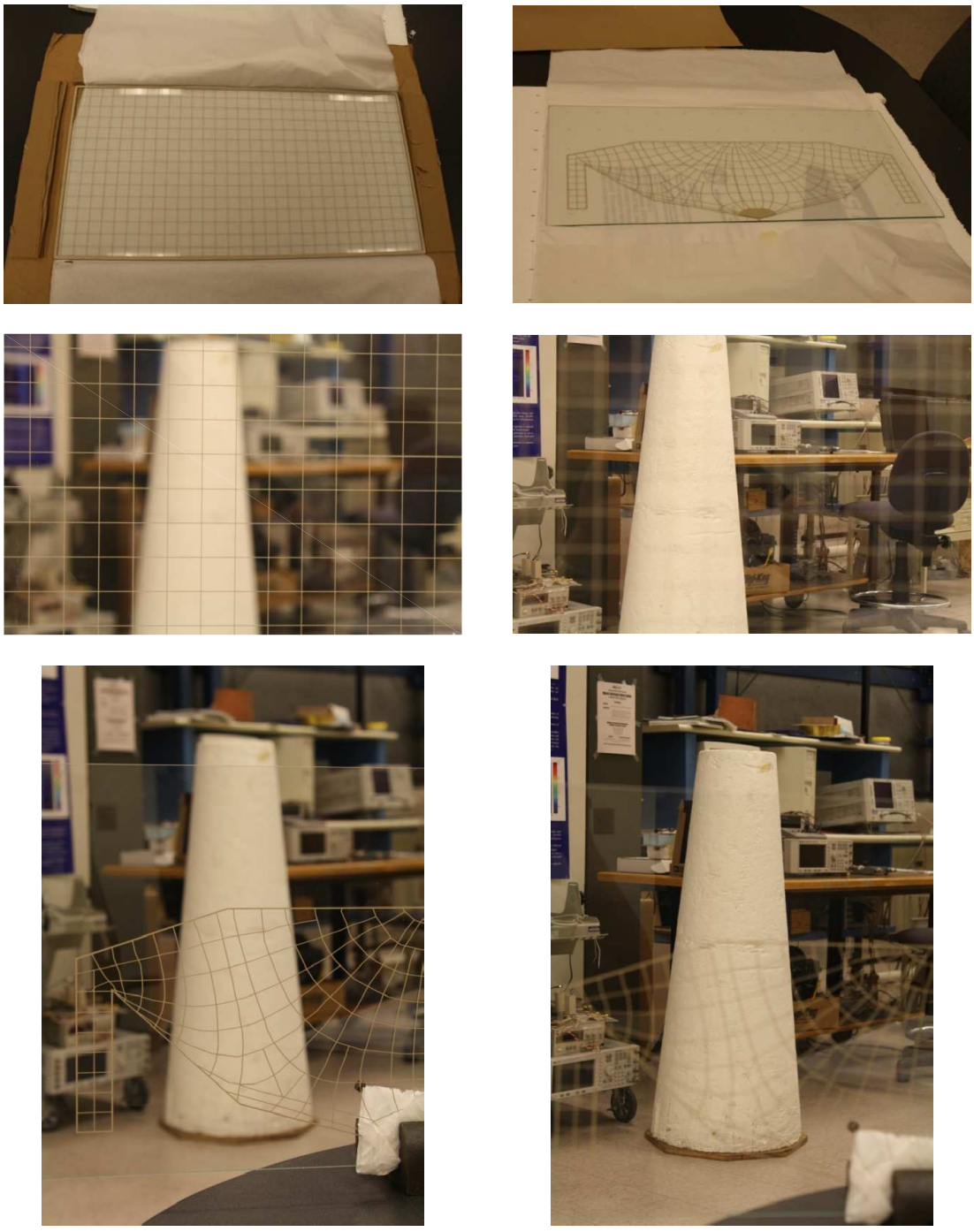

Figure 2.51: Fabricated meshed monopole antenna and meshed ground plane using conductive paint silk printing.

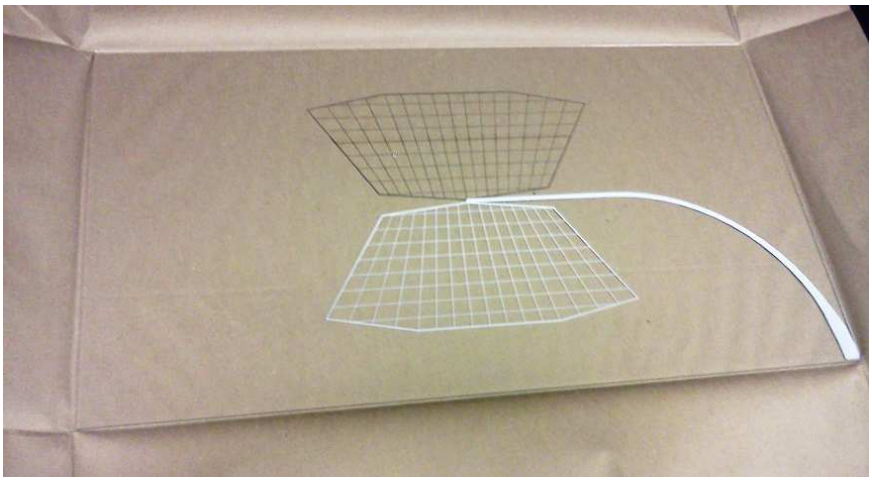

Figure 2.52: Fabricated dipole antenna with microstrip taper using physical vapor deposition of aluminum and chemical etching.

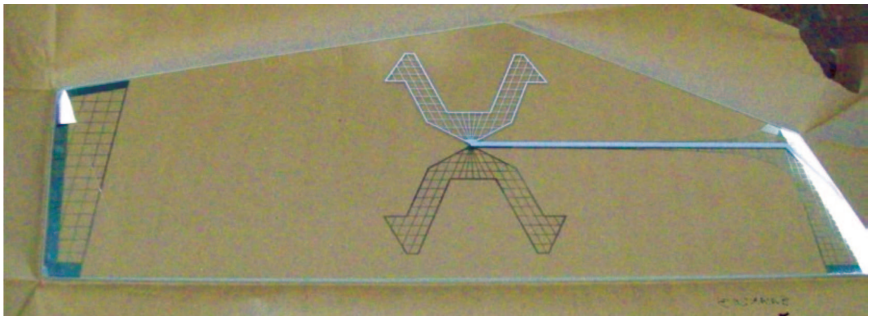

(a) Transparent antenna

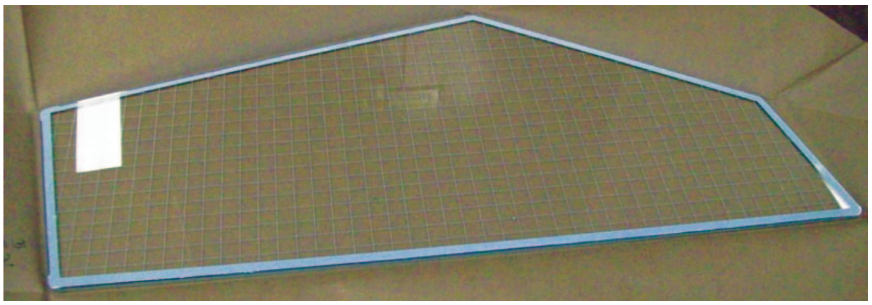

(b) Meshed ground plane

Figure 2.53: Fabricated antenna and ground plane layers for the side window of the MATV.

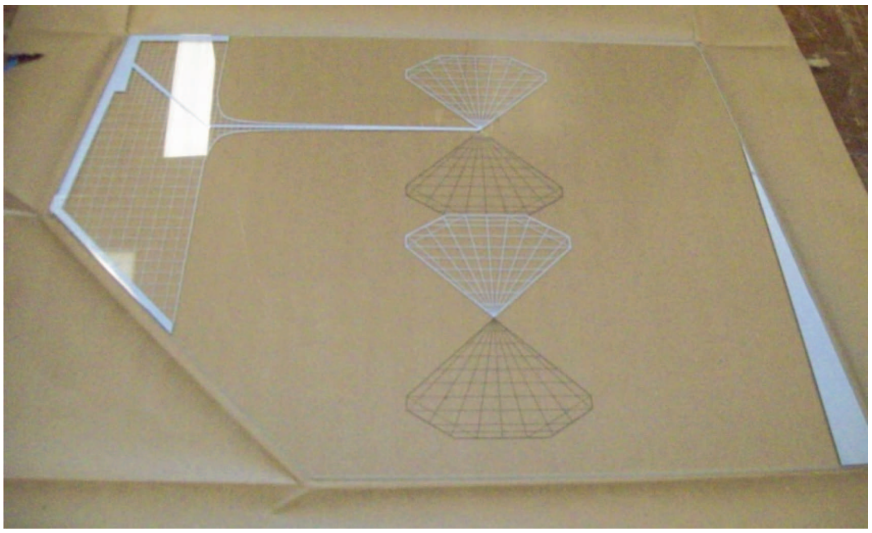

(a) Transparent antenna

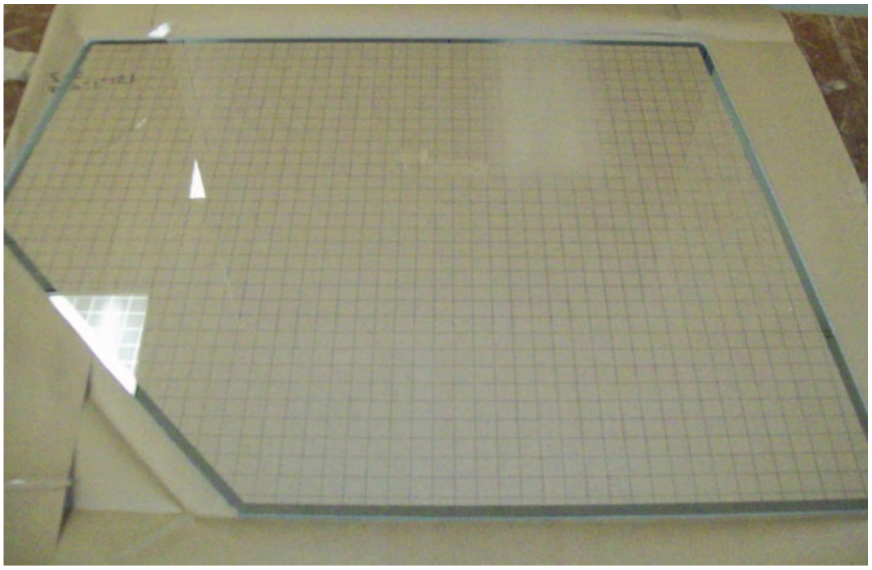

(b) Meshed ground plane

Figure 2.54: Fabricated antenna and ground plane layers for the windshield of the MATV.

2.7 Embedded Antenna Fabrication and Measurement

In order to test the performance of the designed transparent windows in a real scenario, a window similar to what is used in armored vehicle was fabricated. Most armors are made up of multi-layers of clear glass and polycarbonate material glued together with polyurethane under proprietary thermal and compression methods. Fig.2.55 shows the schematic of the transparent armor window fabricated to be tested with the monopole antenna. The lower layer is facing the interior of the vehicle and will contain the meshed ground plane. The other layer facing outside and will contain the transparent antenna.

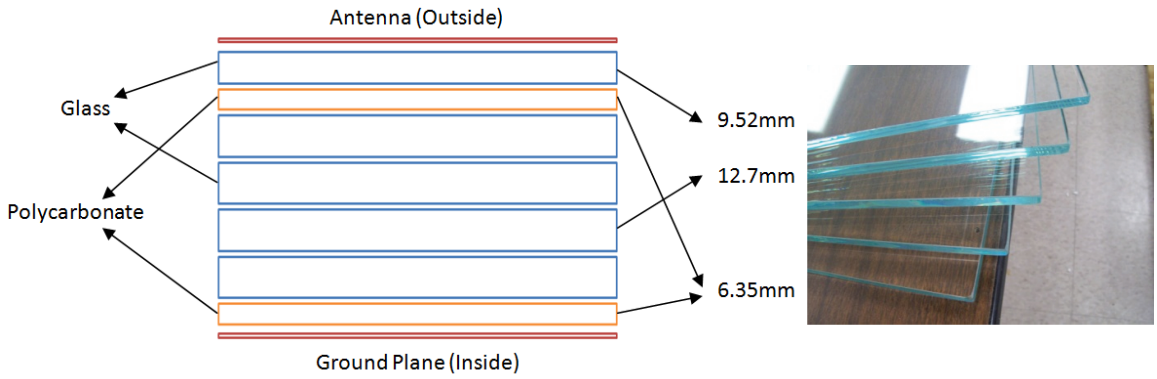

Figure 2.55: Armored windows are made up of several slabs of glass and polycarbonate that are attached to each other using a thin layer of polyurethane between consecutive slabs

Glass, polyurethane and polycarbonate layers can be bounded using polyurethane sheets at a certain pressure and temperature. There are general guidelines for the temperature and pressure required for the bonding but the conditions may vary based on the specific application. In addition to the final conditions, the profile that is used for increasing the pressure and temperature plays a role in determining the quality of the finished product. A series of tests were performed to find out the best conditions for bounding. Fig.2.56 shows one of the prepared samples in an autoclave. A layer of polyurethane is placed between each two adjacent layers in the stack before placing the sample in the autoclave. The entire sample is placed in a vacuum bag and is connected to a vacuum pomp during the process to make sure there are no air bubbles between the polyurethane layer and the glass layers. Without

the vacuum bag, air bubbles will form between the glass layers as shown in Fig.2.57.b. The initial test conditions were 125 psi pressure and the temperature of 225F. We observed that 125 psi of pressure causes the 2.1 mm glass layer to break as seen in Fig.2.57.a, This pressure would also cause the polycarbonate layers to deform and would therefore reduce the overall thickness of the stack (Fig.2.57.c.) Further trial and error revealed that a pressure of 75psi is sufficient to bond the glass layers without causing the thin glass layer to break even in the presence of metallic traces on the glass and wire connections to the metallic coating. Fig.2.57.d shows a 2.1mm glass layer bonded to a 6 mm glass sheet using 75 psi of pressure. In this test, we increased the pressure to an intermediate value of 25psi and reached the final value of 75psi after increasing the temperature to its final value. This procedure did not cause the polycarbonate layer to deform. However, we found some air bubbles in the stack containing polycarbonate layers. The reason for these bubbles are formed is that polycarbonate naturally absorbs some air and moisture as it is exposed to the air. The moisture is released at high temperatures and creates air bubbles in the stack-up. For this reason, the standard practice in the industry includes baking the polycarbonate sheets in a controlled temperature to release the trapped gasses before placing the polycarbonate sheets ı

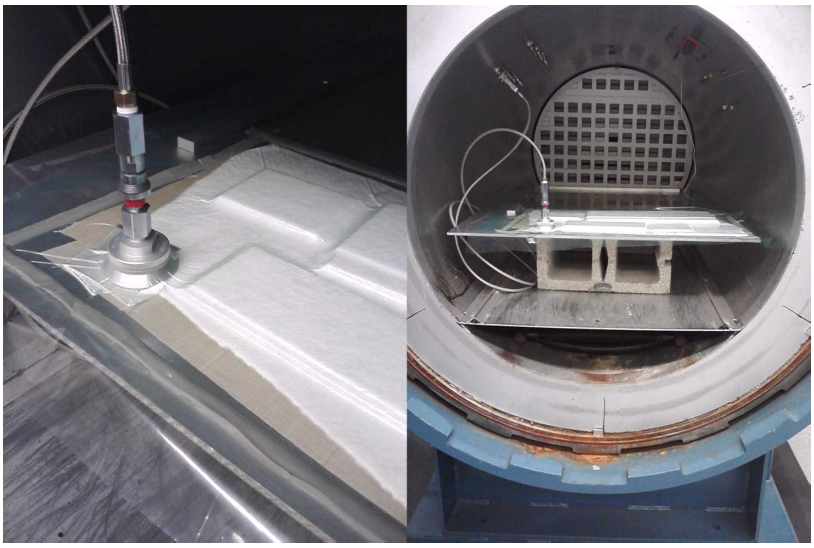

Figure 2.56: Samples of glass and polycarbonate layers in the autoclave. Several different pressure and temperature profiles are tried to find out the best configuration for autoclaving.

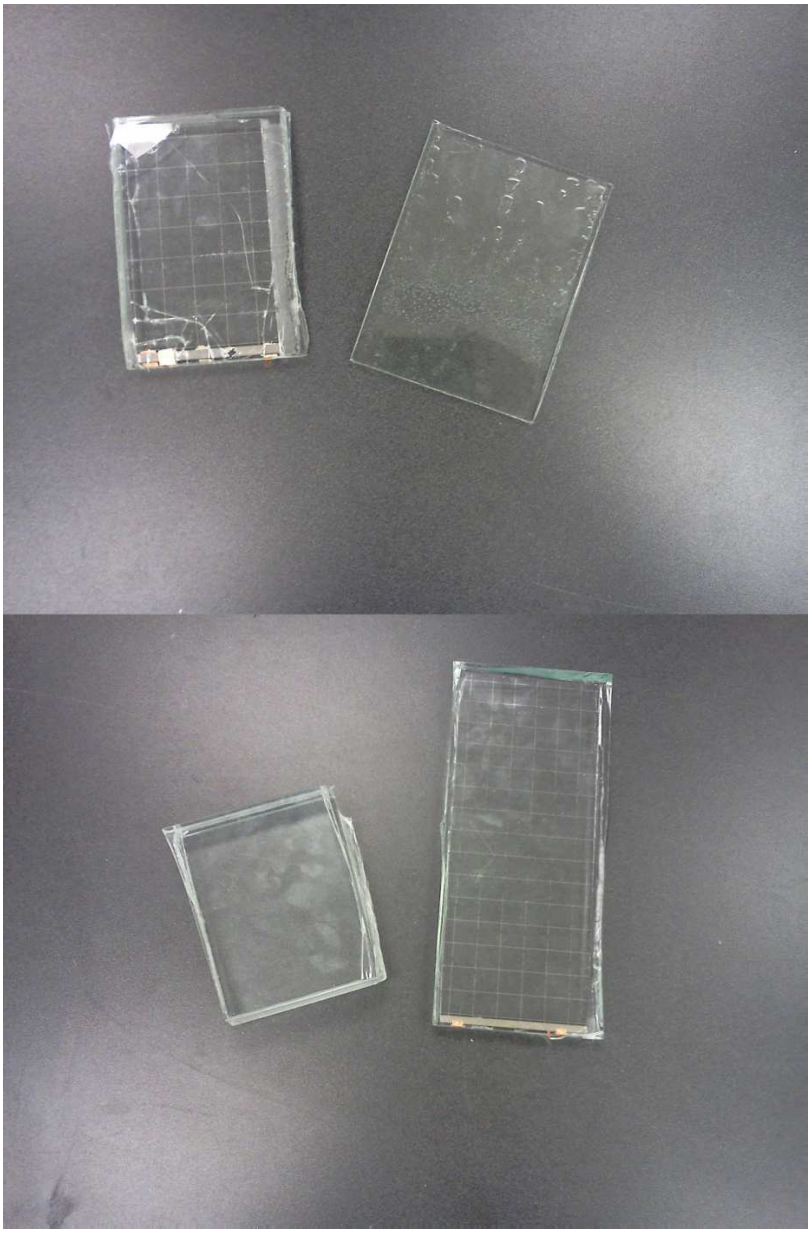

Figure 2.57: Several tests are performed to find out the best temperature and pressure profile. a) broken glass due to high pressure, b) air bubbles appear if a vacuum bag is not used, c) polycarbonate deforms at high pressure and tempreture, d) successful bound.

Without the vacuum bag, air bubbles will form between the glass layers as shown in Fig.3.b. The initial test conditions were 125 psi pressure and the temperature of 225F. We observed that 125 psi of pressure causes the 2.1 mm glass layer to break as seen in Fig.3.a, This pressure would also cause the polycarbonate layers to deform and would therefore reduce the overall thickness of the stack (Fig.3.c.) Further trial and error revealed that a

pressure of 75psi is sufficient to bond the glass layers without causing the thin glass layer to break even in the presence of metallic traces on the glass and wire connections to the metallic coating. Fig.3.d shows a 2.1mm glass layer bonded to a 6 mm glass sheet using 75 psi of pressure.

The fabricated window consists of layers of glass and polycarbonate as described before in addition to a metallic frame that holds all the layers including the antenna and ground plane layers together. The glass and polycarbonate layers have different thicknesses but they are all 30.5 mm wide and 61 mm long. The metallic frame dimensions are slightly larger than those of the glass and polycarbonate layers, allowing a 3 mm gap between the glass and the metallic frame on all sides of the glass. This gap is filled with rubber to provide protection for the glass. The fame itself was assembled from 6 different metallic parts: four aluminum U-shape channels for the sides and two aluminum rectangular frames for the top and back faces of the window.

The antenna was initially fabricated on a non-transparent substrate and the full-metal version of the antenna was used. This allows for corrections and adjustments to the design to be made before committing to the more expensive and time-consuming fabrication on a transparent substrate. The antenna is fabricated on a 1.6 mm thick FR-4 Substrate with dielectric constant of 4.4. The effect of the substrate on the performance of the antenna can be neglected because its thickness is very small compared to the wavelength. The substrate is used only to simplify the fabrication process. At the final stage of the project, this antenna will be replaced with an optically transparent antenna and the substrate will be eliminated.

The antenna feed system consists of a coaxial line whose inner conductor is directly connected to the feed point of the monopole antenna. The outer conductor of the coaxial cable is attached to the aluminum frame very close to the feed point. The other end of the coaxial cable is connected to an SMA connector that is mounted on the window frame and allows an external cable to be connected to the antenna. Fig.2.58.a and Fig.2.58.b

show the fabricated window with embedded antenna and ground plane. As shown in the figure, a full-metal ground plane is used with the antenna. The measurement setup is shown in Fig.2.58.c and Fig.2.58.d. The reflection coefficient at the input port of the antenna is plotted versus frequency in Fig.2.59. A return loss of 5.45dB or better is achieved over the full operational frequency range (250 MHz - 512MHz) which corresponds to voltage standing wave ratio (VSWR) of 3.3 or better.

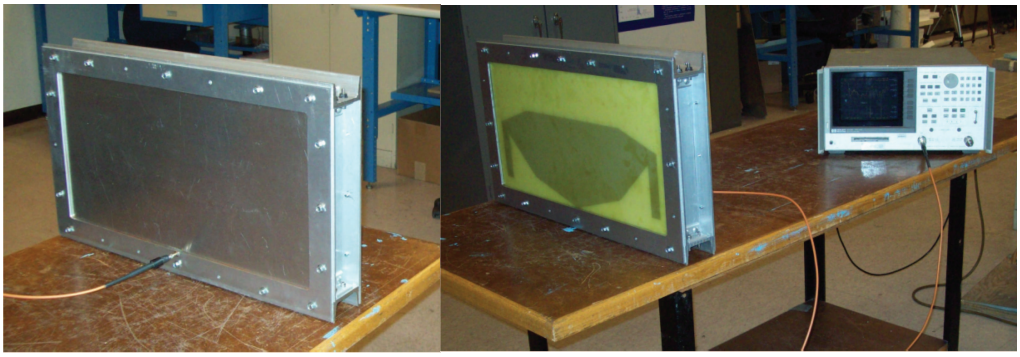

Figure 2.58: The monopole design is first fabricated on FR-4 ro verify the performance before committing to the more expensive and time consuming transparent antenna fabrication.

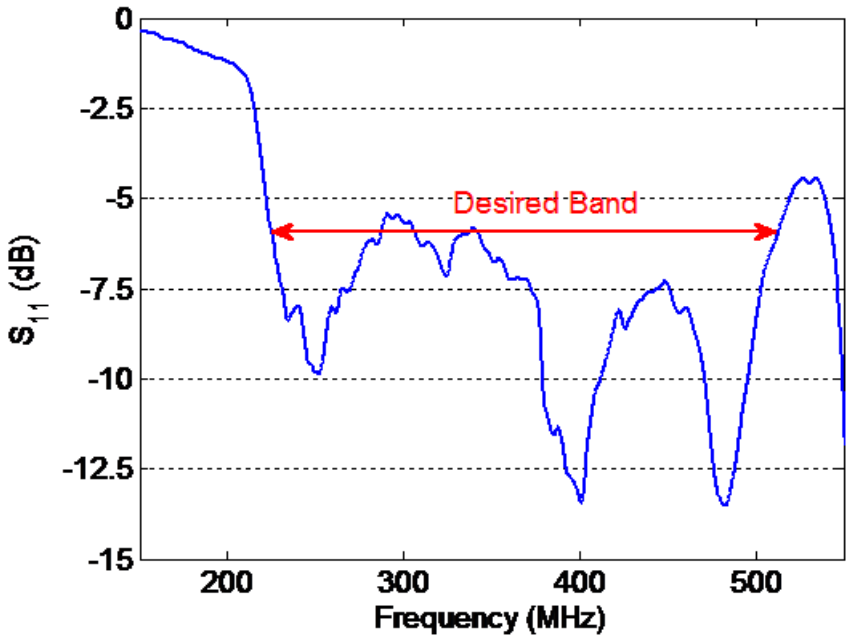

Figure 2.59: Measured input reflection coefficient of the fabricated monopole antenna.

After the initial test with the solid antenna, the transparent antenna and ground plane were fabricated and tested. The ground plane layer consists of a uniform wire mesh with the pitch of $25.4mm$ and the wire width of $0.25mm$. The antenna layer is identical to the modified mesh design discussed in the previous section. In the fabrication process, a uniform $16\mu m$ thick layer of aluminum is first deposited on a $3mm$ thick glass substrate using physical vapor deposition. In the next step, the aluminum layer is chemically etched to achieve the desired meshed antenna or ground plane pattern. Finally, the thin glass layers are integrated with the rest of the glass and polycarbonate stack-up to form a solid transparent slab identical in size to the original armored window glass. The stack up consists of two $12.7mm$ thick glass slabs with the dielectric constant of 7.25, four $11.5mm$ thick polycarbonate slabs with the dielectric constant of 2.8 and several $0.5mm$ layers of polyurethane with the dielectric constant of 3.2. The whole stack up is vacuum bagged and placed in an autoclave with the temperature of $300^{\circ}F$ and pressure of $70psi$ for 8 hours. The polyurethane layers melt at this temperature and bond the other layers together. The integrated glass slab is enclosed by an aluminum frame similar to the metallic frames used

in the military vehicles. The ground plane is electrically connected to the metallic frame on the edges. The antenna is fed using a coaxial cable whose outer conductor is connected to the aluminum frame and its inner conductor is connected to the antenna feed point. The window embedded antenna is placed in an anechoic chamber against a log periodic antenna and the transmission between the two antennas is measured. The window embedded antenna is then replaced by a log periodic antenna with a known gain to find the absolute gain of the antenna. The window embedded antenna is placed at a 15° tilt angle to emulate a tilted windshield. Fig.2.60 shows the measurement setup.

The measured input reflection coefficient and gain of the antenna in the horizontal direction are plotted in Fig.2.61 and Fig.2.62 respectively and show a good agreement with the simulation results. Fig.2.62 also shows the simulated efficiency of the antenna. Metallic and dielectric losses, as well as impedance mismatches, are accounted for in this simulation. An efficiency of 0.8 or better over the entire band is predicted by the simulation which is confirmed by the measurement since a significant gain drop is not observed between simulation and measurement results. Fig.2.63 shows the measured and simulated radiation patterns of the antenna in E-plane. Because of the symmetry of the antenna, the simulation results show no cross-pol in the E-plane. However, because of the fabrication and alignment tolerances in the measurement setup, a small cross-pol component is present. As expected a vertical shift in the radiation pattern of the antenna is observed at higher frequencies. Fig.2.64 shows the fabricated transparent antenna and ground plane embedded in a typical armored window. As seen in the picture, the armor embedded antenna is optically transparent and has a negligible effect on the optical functionality of the window.

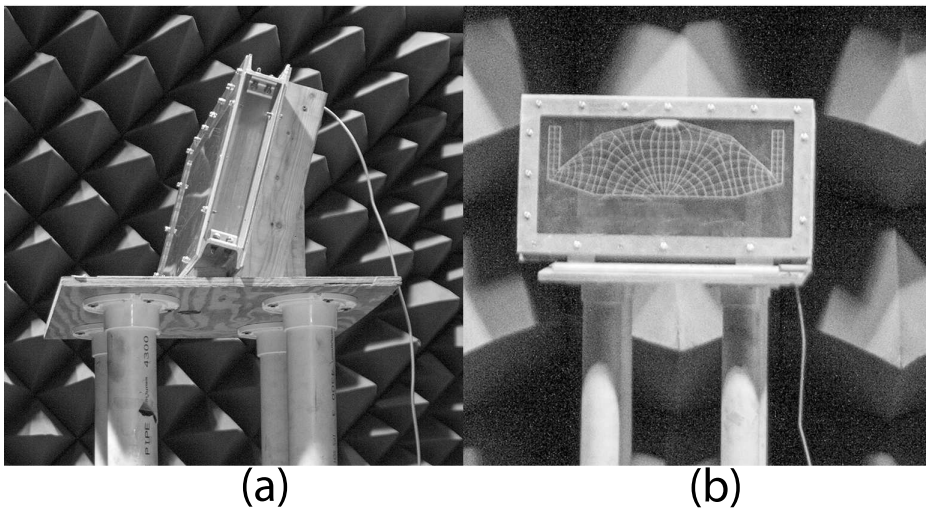

Figure 2.60: Measurement setup (a) Side view (b) Front view

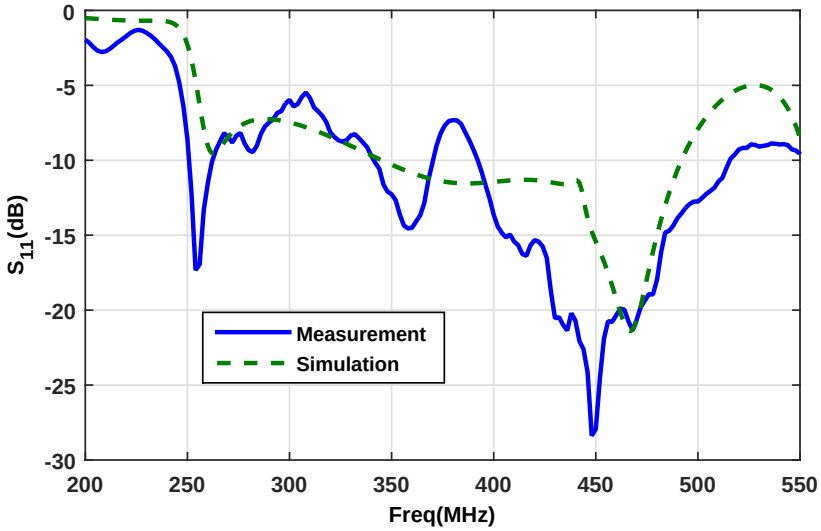

Figure 2.61: Simulated and measured input reflection coefficient of the antenna inside the radiation laboratory anechoic chamber

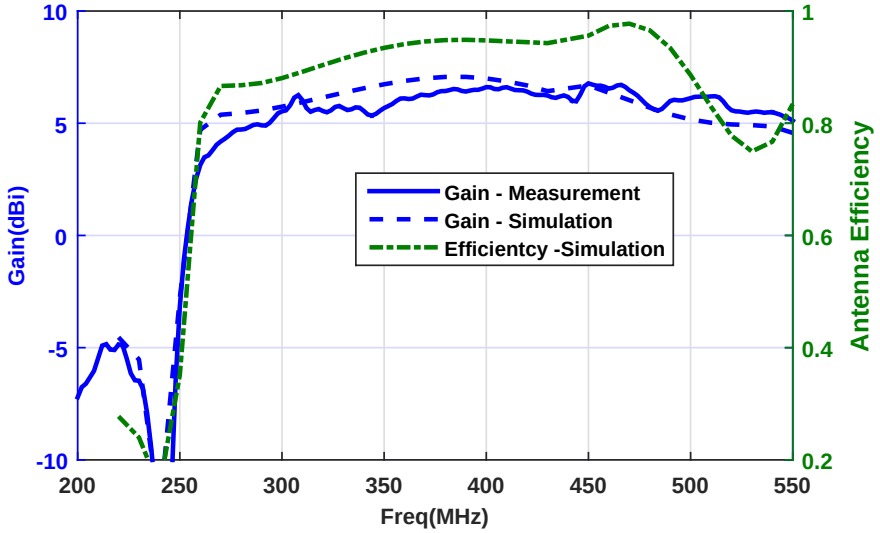

Figure 2.62: Simulated and measured antenna gain in horizontal direction as well as simulated antenna efficiency

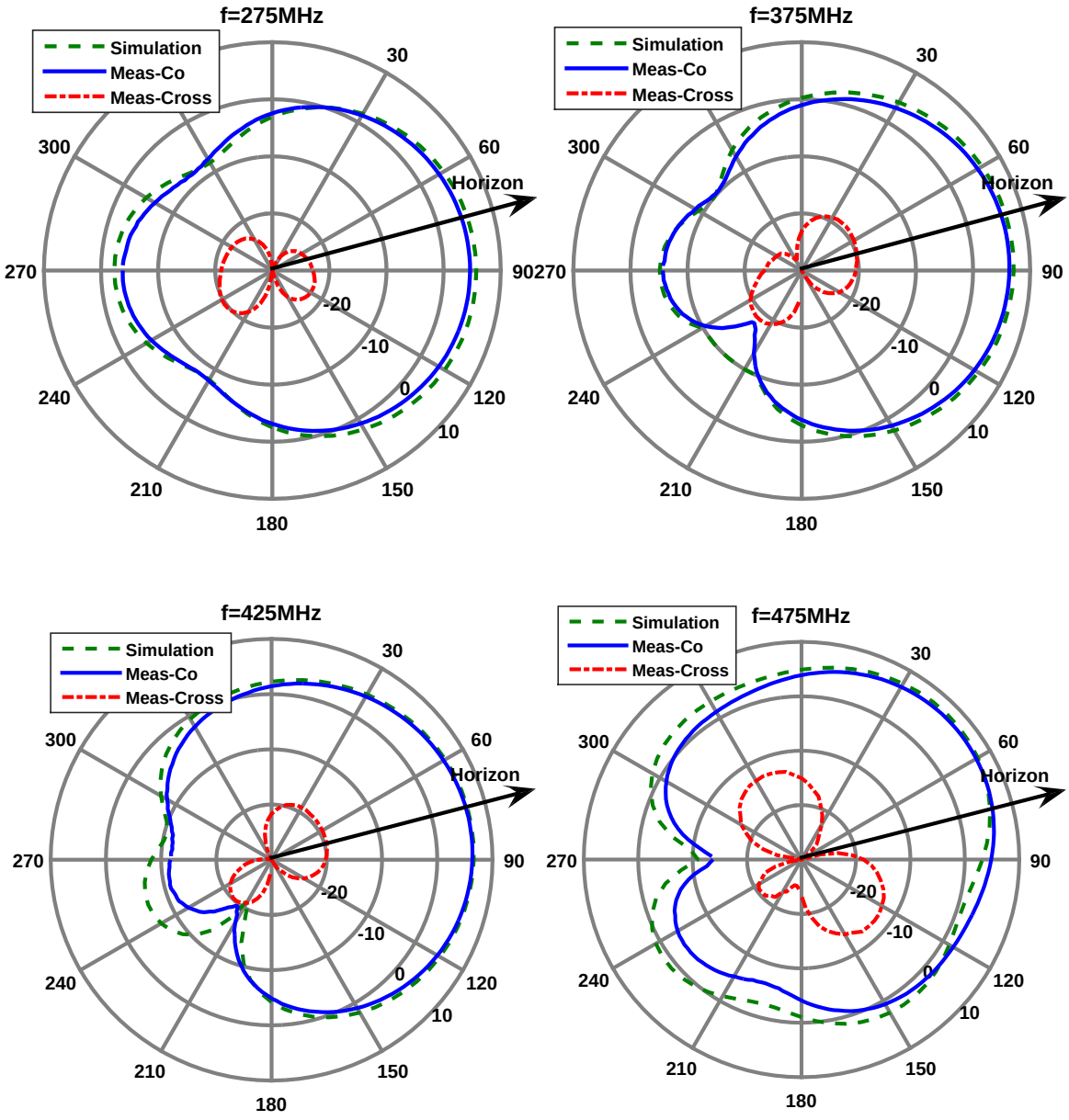

Figure 2.63: Simulated and measured co-pol and cross-pol components of the radiation patterns of the antenna in E-plane versus θ.

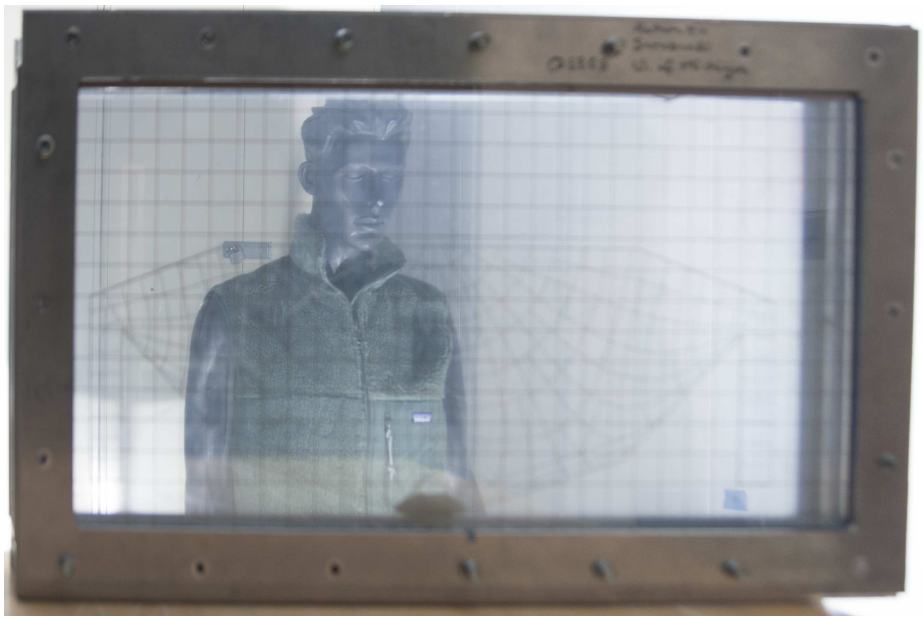

Figure 2.64: Fabricated transparent antenna embedded in a typical window

Two different transparent prototypes were fabricated for the dipole bow-tie design: one with a balun transformer and another one with a tapered mictrostrip balun. The fabricated windows are shown in Fig.2.65. The input reflection coefficient and radiation pattern of the antenna were measured using the same technique described above. However, these antennas are designed for maximum radiation along boresight and therefore the antenna is not tilted during the measurements.

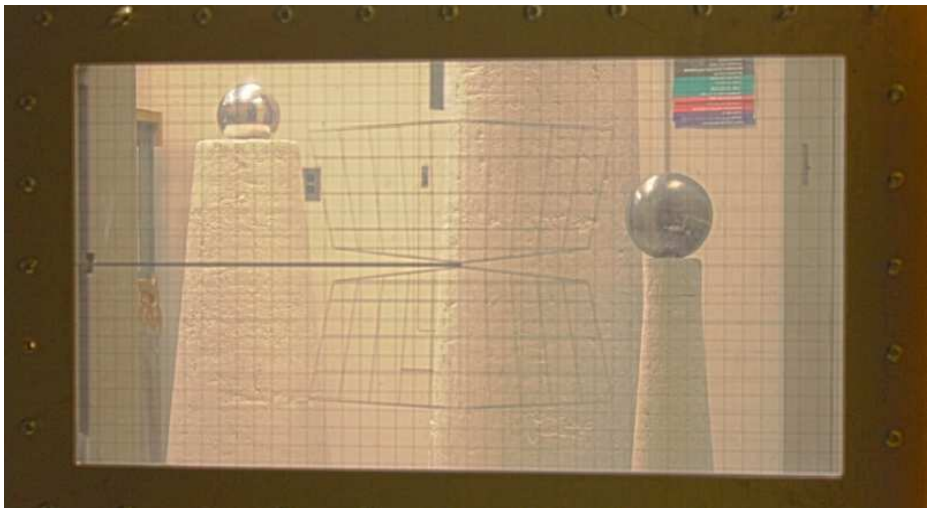

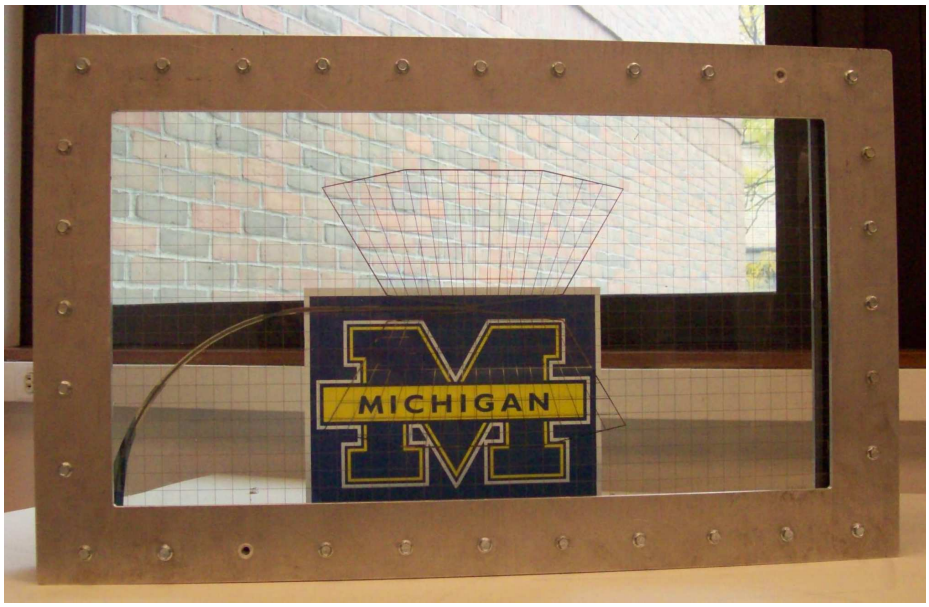

(b) Microstrip tapered balun based design

Figure 2.65: Fabricated transparent window embedded dipole bow-tie antennas to be used as the back window of MATV.

The gain of the transformer based antenna along its boresight is plotted in Fig.2.66. The graph also shows the insertion loss of the transformer that was used in the design. As seen in the graph, the measured gain shows a good agreement with the simulation results if the insertion loss of the transformer is taken into account. The ripples in the measured gain are because of multipath effects[]. These effects are present because the reflection from

the microwave absorbers in the chamber is not negligible at UHF and VHF frequencies. The measured radiation pattern of the antenna is plotted in Fig.2.67. The antenna was also tested using a solid metal ground plane on the backside of the window as opposed to a meshed ground plane. The radiation patterns of the antenna with solid ground plane are plotted in Fig.2.68 and are compared to the simulation results. The measurements show excellent agreement with simulation. In addition, a significant change is not observed in the front to back radio of the antennas when the meshed ground plane was swapped by a solid ground plane.

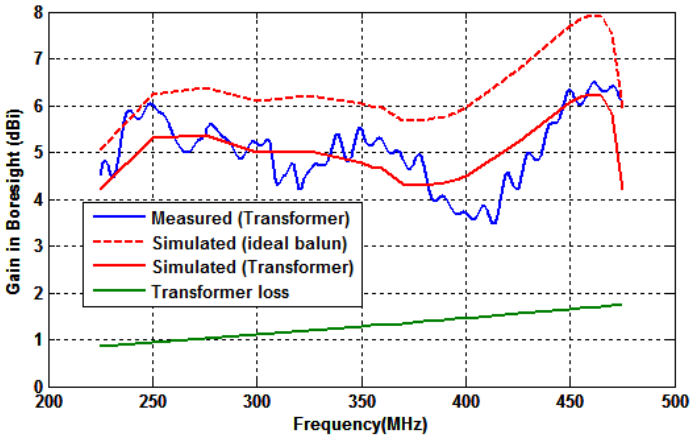

Figure 2.66: The measured gain of the dipole antenna (solid blue) compared to the simulation results with balun losses taken into account (solid red).

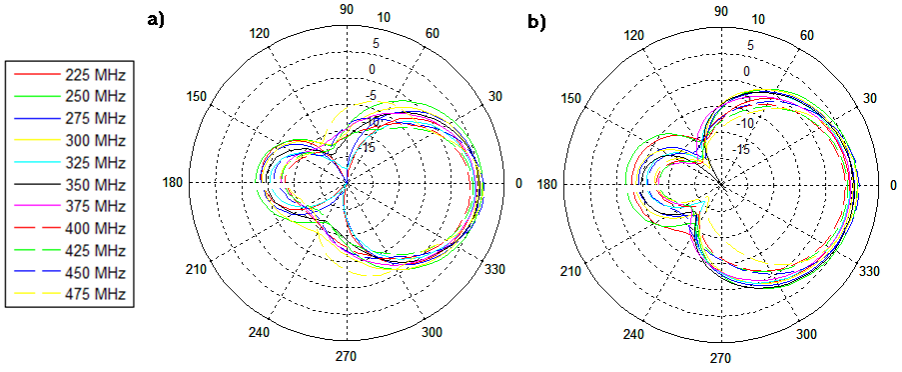

Figure 2.67: The measured radiation pattern of the transformer based dipole bow-tie in H-plane (a) and E-plane (b)

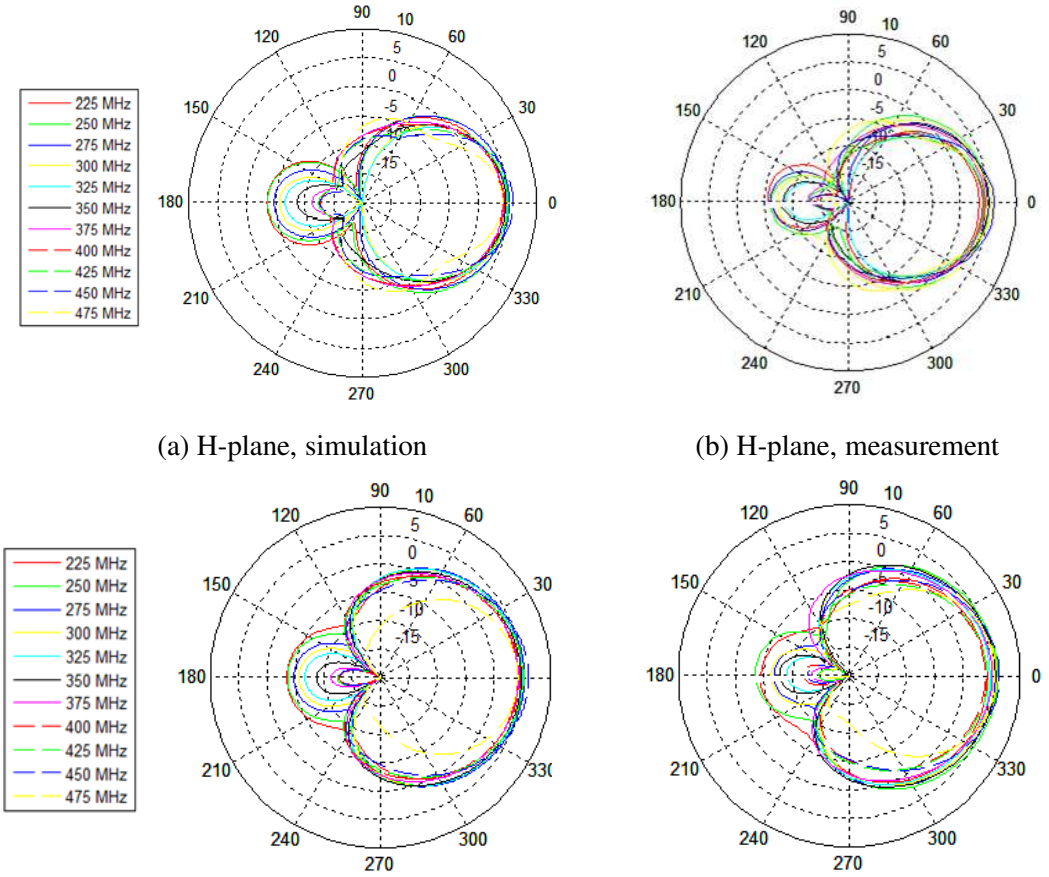

(a) H-plane, simulation

(b) H-plane, measurement

(c) E-plane, simulation

(d) E-plane, measurement

Figure 2.68: Simulated and measured radiation pattern of the fabricated dipole antenna with backed by a solid metal sheet instead of the meshed ground plane.

The gain of the microstrip balun based antenna along its boresight is plotted in Fig.2.69 and compared with the transformer based design. The mictrostrip taper provides a much lower insertion loss than the balun transformer. The radiation pattern of the antenna featuring a microstrip taper is plotted in Fig.2.70.

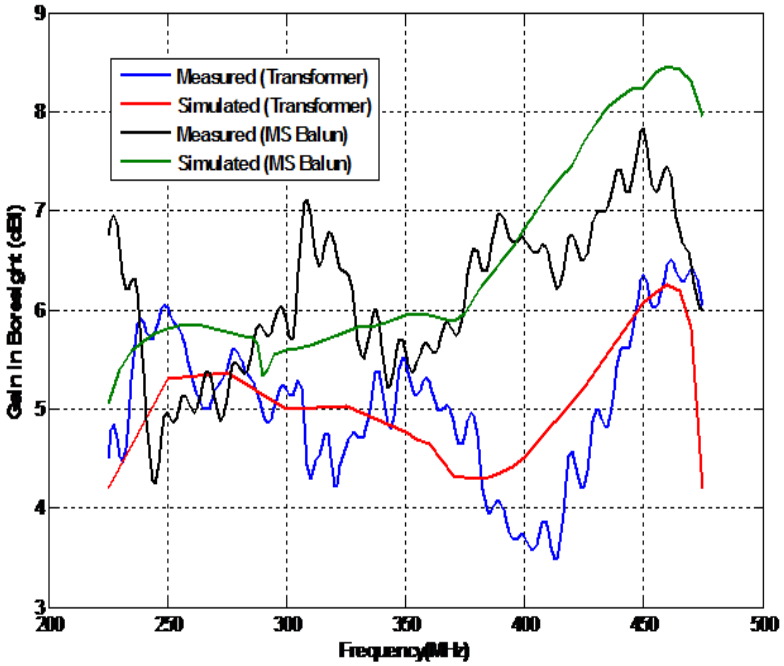

Figure 2.69: The gain of the mictrostrip taper based design along boresight compared to that of the transformer based design.

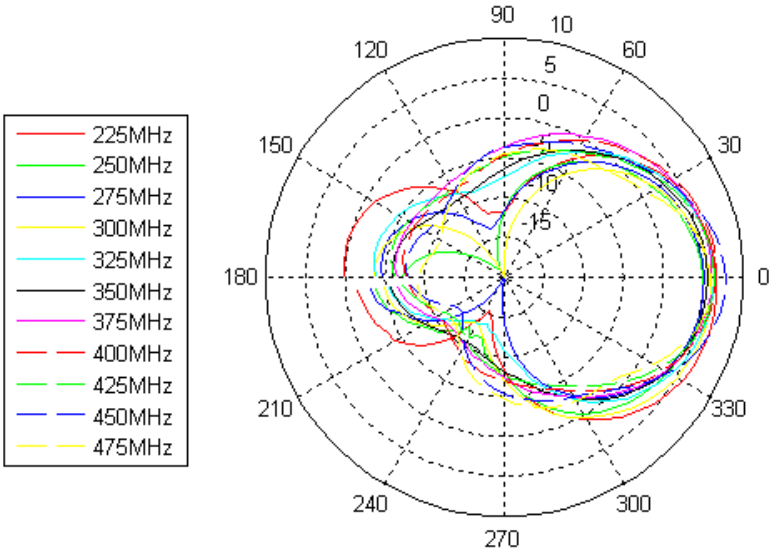

Figure 2.70: Radiation pattern of the mictrostrip taper based design in the H-plane.

Fig.2.71 shows a thin slab of glass on which the windshield antenna of MATV is fabricated. The antenna consists of an array of two bow-tie dipoles. It was determined that only

one of the antenna elements need to be fed while the second dipole antenna act as a parasitic element. The effect is a radiation beam tilted towards the horizon when the windshield window is tilted at 40 degrees from vertical. Note that the antennas are printed on both sides of the glass. The feed of the printed dipole is transitioned to 50 ohm impedance using a balun. In this configuration, the part of the feed printed on the top glass surface represents ground. In order to control the field inside the window cavity, metallic covers were introduced on the antenna glass sheet near the edges. To ensure that these covers are connected to the ground at the back of the window, additional grounding points were attached to the aluminum traces at the edges of the antenna sheet as shown in Fig.2.71. These grounding points will be connected to corresponding points on the inner side of the frame itself during the potting process after bonding the glass. The ground points consist of thin brass strips that were attached to the etched aluminum using silver epoxy and dried. Copper tape strips were added on top of the brass strips for reinforcement prior to autoclaving. The brass strips are not only thin and therefore do not interfere with the autoclaving process, but are also very flexible and resistant to tear.

Figure 2.71: grounding points attached to the edges of the antenna layer to ensure an electric connection between the metallic covers and the window frame.

Fig.2.72 shows the contact points on the inner side of the frame. The contact points were established using a special solder that bonds well to steel. Flexible brass strips are

soldered to these contact points which are then soldered to the antenna grounding points during the final assembly. Finger strips were attached to the frame as shown in Fig.2.72 and the transparent ground plane was placed on top of it, followed by the glass and polycarbonate sheets and topped with the antenna sheet. Fig.2.73 shows a simple diagram of the window placement inside the frame and the ground plane connection to the frame.

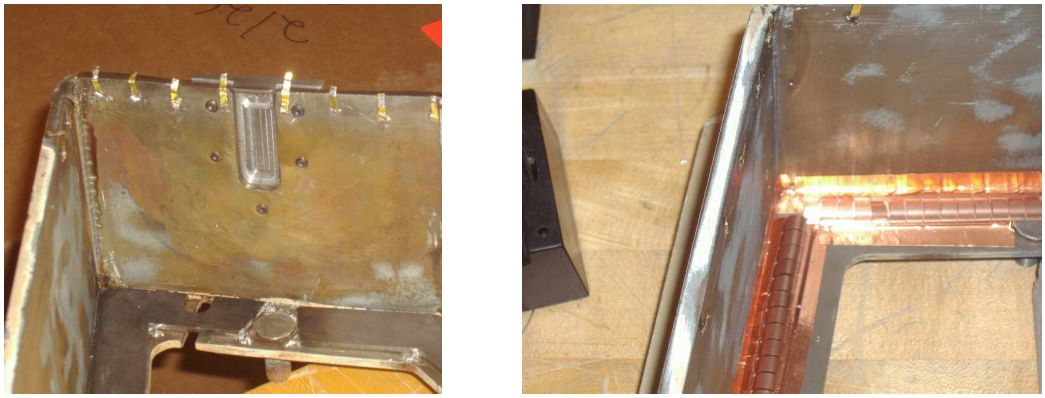

Figure 2.72: contact points fabricated on the window frame to be connected to the grounding points on the antenna. Fingers strips one attached to the bottom side of the frame to establish a good connection to the meshed ground plane layer.

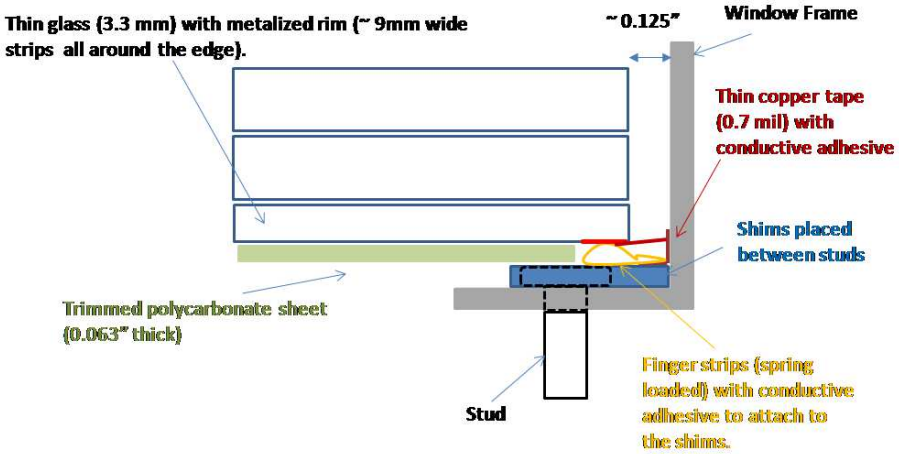

Figure 2.73: The schematic of the window placement inside the frame and the ground connections.

Similar steps were performed for the side windows, namely, having grounding points along the edges of the antenna, placing contact points on the inner side of the frame, and

using finger strips to establish electrical connection with the ground layer. The antennas were placed in a high pressure and temperature autoclave for 24 hours, after which the polyurethane sheets melt in the autoclave and bond all the layers together. The fabricated antennas are shown in Fig.2.74

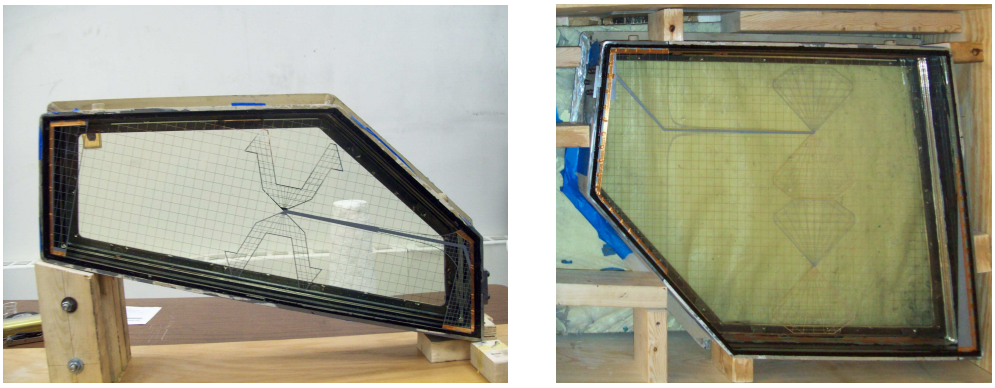

(a) Side window (b) Windshield

Figure 2.74: Fabricated windshield and side widows.

The radiation pattern of the antennas were measured by placing the antenna against a log periodic antenna with a known gain. The measurement results are plotted in Fig.2.75 through Fig.2.80.

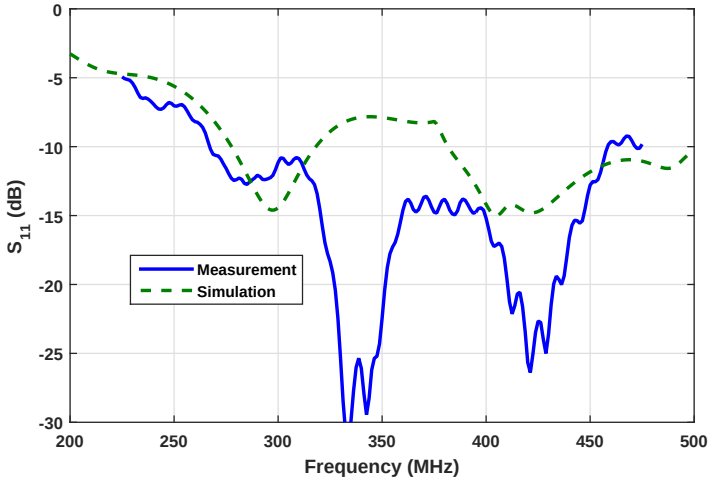

Figure 2.75: The measured input reflection coefficient of the windshield antenna compared to simulation.

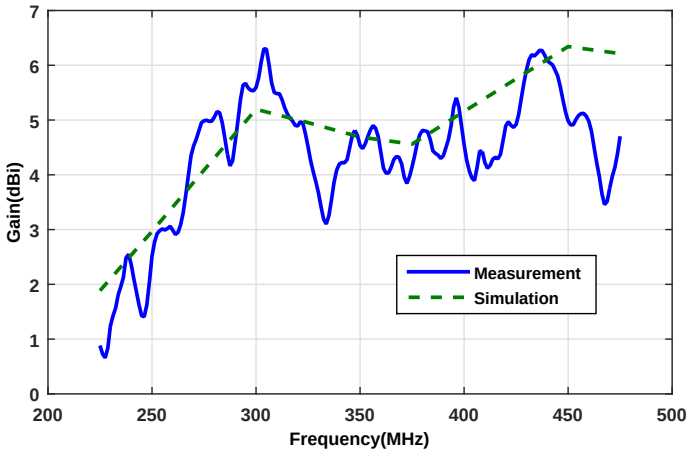

Figure 2.76: The measured gain of the windshield antenna at 40°from boresight compare to simulation.

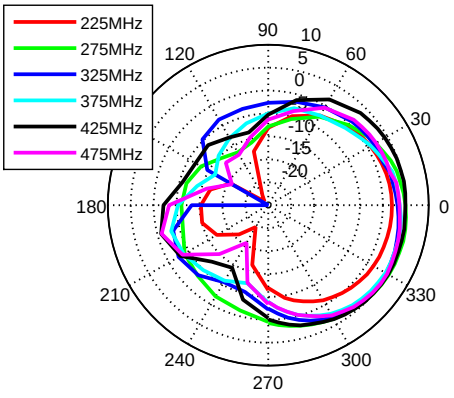

Figure 2.77: The measured radiation pattern of the windshield antenna at various frequencies.

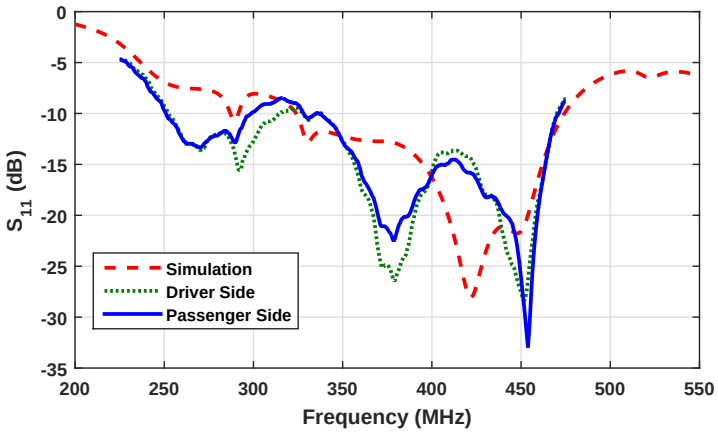

Figure 2.78: The measured reflection coefficient of the passenger side and driver side windows compared to simulation.

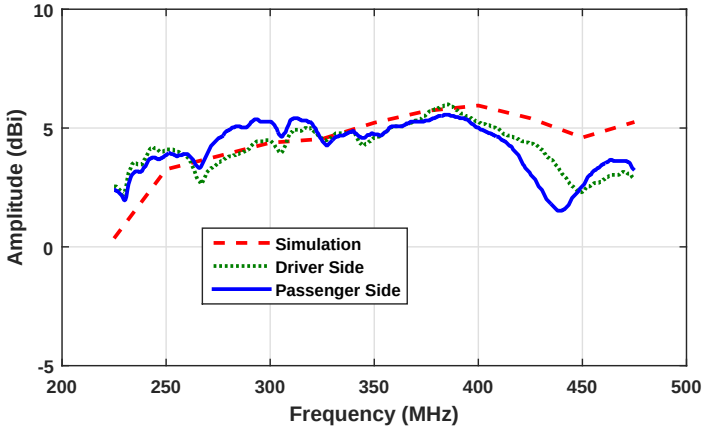

Figure 2.79: The measured gain of the passenger side and driver side windows along the boresight compared to simulation.

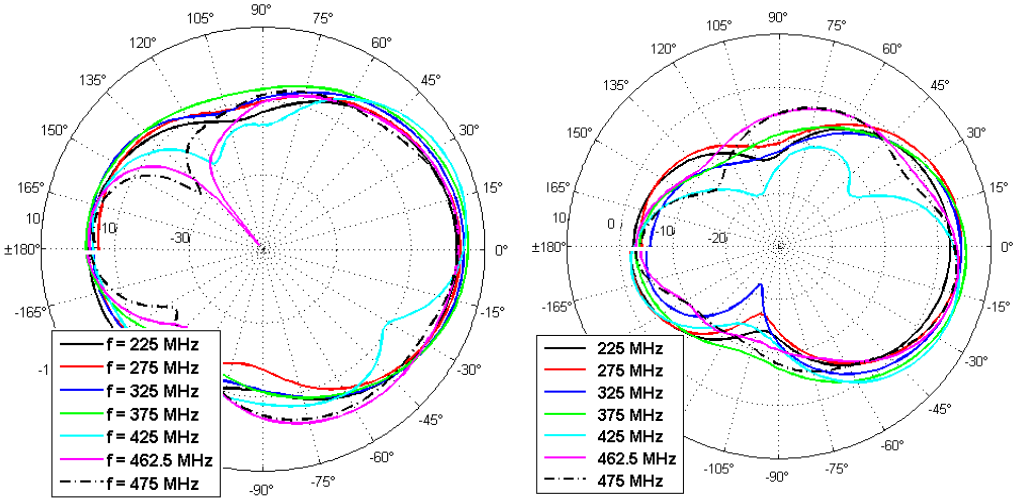

(a) Passenger side (b) Driver side

Figure 2.80: The measured radiation pattern of the drver side and passenger side windows in the H-plane.

2.8 Window Embedded Antennas Mounted on a Vehicle

The armored window embedded antennas discussed earlier are backed by a transparent ground plane. The presence of a ground plane is essential to protect the passengers from exposure to strong RF radiation from the antennas. Because of the presenc e of the ground plane and the body of the vehicle itself, the radiation patterns of the designed antennas are directional. In order to achieve an omnidirectional coverage multiple antennas must be placed on the same vehicle pointing at different directions as shown in fig.2.81. Having more than one antenna increases the flexibility of the design and its ability to perform in more challenging situations such as environments with strong multipath and fading effects. However, in order to benefit from these advantages, more advanced transmitting and receiving themes are required[]. These themes are not currently supported by the radios that are used in armored vehicles at UHF and VHF frequencies. Investigating advanced MIMO techniques that can take advantage of the diversity gained by using four antennas is beyond the scope of this dissertation. However, it is constructive to discuss the simplest way of taking advantage of this diversity in the receiver mode, namely selecting the antenna with the strongest signal at a given moment as the sole receiver.

The radiation pattern achievable using the theme described above can be approximated using simulated radiation patterns of individual antennas. The approximate pattern is plotted in Fig.2.82. Note that the effect of the metallic body of the vehicle is neglected.

More realistic results can be obtained by modeling the entire vehicle and four antennas simultaneously using full-wave simulation. However such analysis is impractical due to the large size of the problem. Alternatively, the four antenna scenario can be experimentally evaluated. To perform this test, four transparent window embedded antennas were fabricated to be mounted on an ordinary full sized VAN. All four antennas utilize the balun transformer based feeding mechanism.

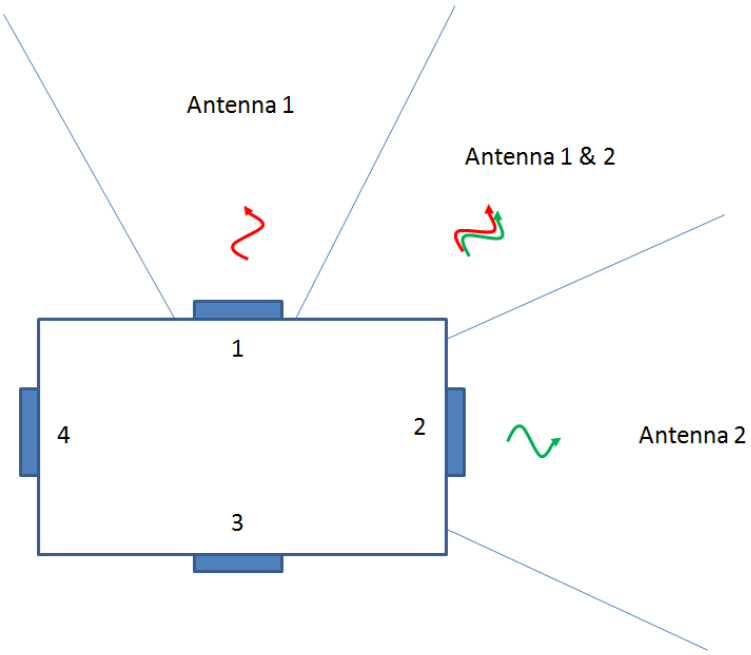

Figure 2.81: Multiple antennas are placed on the vehicle to achieve an omnidirectional coverage.

2.8.1 Experimental Setup:

The antenna measurements were performed in an outdoor facility managed by Willow Run Test Labs, LLC. The test facility has an in-ground turntable capable of holding a large vehicle. The transmit antenna is a large log-periodic antenna placed against the building wall and facing the turntable. The height of the transmit antenna is adjustable and is located 50 m from the center of the turntable. Fig.2.83 shows the transmit antenna and the turn table.

The large log-periodic antenna is dual-polarized and is capable of transmitting vertically and horizontally polarized signals spanning the frequency band between 50 MHz and 1000 MHz. The antenna height above ground can be adjusted so as to accommodate the physical location of the antennas on the test vehicle and to minimize multipath effects, when present. The antenna was placed 10 ft above ground and was used in transmit mode.

The signal received by the antenna(s) mounted on the test vehicle is routed through an RF cable (through a rotary joint at the center of the turntable) back to the building. A

low-noise amplifier was used along the receiver chain to improve signal-to-noise ratio.

Three of the 4 sides of the van had windows and the window-antennas were placed over these windows to the extent possible. The window-antennas placed on the driver side, the passenger side, and the back side where suspended from the metal frame on the vehicles roof using metallic wires while leaning against the vehicles walls, as shown in Fig.2.84. The window-antenna placed at the front side of the vehicle, was secured over the hood in front of the windshield on the passenger side. Adjustments were made to the different window-antennas using foam blocks to compensate for the curvature of the different parts of the vehicle where the antennas were placed and to ensure that the antennas boresight directions were within 5 degrees in elevation. Note that no solid contact between the antenna frames and the vehicles body was established during this test.

2.8.2 System Calibration:

The measurement system was first calibrated using a small broadband log-periodic antenna, of known gain, placed at the center of the turntable prior to placing the Van on the turntable. A broad-band dipole was then placed near the edge of the turntable, at the same height as the window-antenna would be when placed on the vehicle, and an antenna pattern measurement was collected in Azimuth. The purpose of this test is to validate the calibration technique and characterize the uniformity of the field illuminating the turntable. The dipole antenna covers the frequency range between 225 MHz and 400 MHz with a typical gain of 1 to 2 dBi. The measured and calibrated gain of the dipole antenna, for both V-polarized and H-polarized transmitted signals, are plotted as function of frequency in Fig.2.85. The radiation pattern of the broadband dipole is also plotted in two different frequencies. As seen in the graph, the radiation pattern is uniform in azimuth to within 1 to 2 db. The ripples and imperfections in the absolute gain and radiation pattern of the antenna are caused by multipath effects due to multiple reflections from the ground and surrounding objects. These errors cannot be avoided but their effect is not significant as can be verified by the

results.

2.8.3 Measurement Procedure:

Two different sets of measurements were conducted using the same test equipment and calibration data. The first set of measurements was aimed at characterizing the absolute antenna gain and pattern of each individual antenna, while being placed on the corresponding vehicle side. The antennas were connected one-at-a-time to the RF rotary joint which was in turn connected through an RF cable to one port of the VNA. It is important to note that each antenna was placed on the vehicle such that V-polarized signal is received. The turntable was rotated and the signals received by the test antennas due to V- and H-polarized transmitted signals were recorded using the VNA. Measurements were done at 1° increments in azimuth and over a frequency range spanning from 200 MHz to 500 MHz.

The second set of measurements involved combining the received signals from three of the four antennas using a signal-combining circuit. The circuit consists of an LNA, analog detector, and a microcomputer. The micro-controller compares between the 3 channels sampled by the analog detector, identifies the strongest channel and transmits TTL signals to an RF switch to select the strongest signal to pass through to the receiver. In performing the radiation pattern measurements, the VNA was set to a specific frequency. Then the antenna pattern was measured at that frequency while the turntable was rotating. Once the pattern is completed at one frequency, another frequency was selected and the measurement was repeated at the new frequency value. The data was then calibrated and plotted.

2.8.4 Absolute Gain of Individual Antennas:

Fig.2.86 through Fig.2.89 show the calibrated absolute gain patterns of all four antennas measured individually. In each figure, the gain along boresight for both co-polarized and cross-polarized components are plotted as a function of frequency. In addition, the azimuth patterns at a selected set of frequencies are plotted in both polarizaitons. Note that the

transparent window-antenna was designed to operate optimally between 225 MHz and 475 MHz. Hence, performance degradation is expected beyond this frequency range as apparent from the measured data.

2.8.5 Combined Gain Using Switch Box:

Using the signal-combining circuit, the received signals from three of the antennas were combined to ensure that maximum received signal is detected by the receiver. The signal-combining circuit was placed inside the Van. RF cables from all four antennas were routed through a side hole in the vehicles body to the switch box. The output of the box was connected via an RF cable to the rotary joint at the center of the turntable, positioned directly underneath the vehicle. The switch box was powered using an onboard AC power generator. For this set of measurements, the VNA was swept over a very small bandwidth of 10 KHz centered around the frequency of interest. In Fig. 4-66, the pattern of the combined signal from the three antennas was measured as a function of the azimuth angle for a given set of frequencies spanning the desired bandwidth. The added gain of the switch box amplifiers was calibrated out from the data. As seen in the plots, no significant signal is observed on the side of the vehicle that corresponds to the antenna that was not connected to the circuit. The resulting pattern demonstrate that a wide coverage can be obtained by combining the signals received from individual antennas.

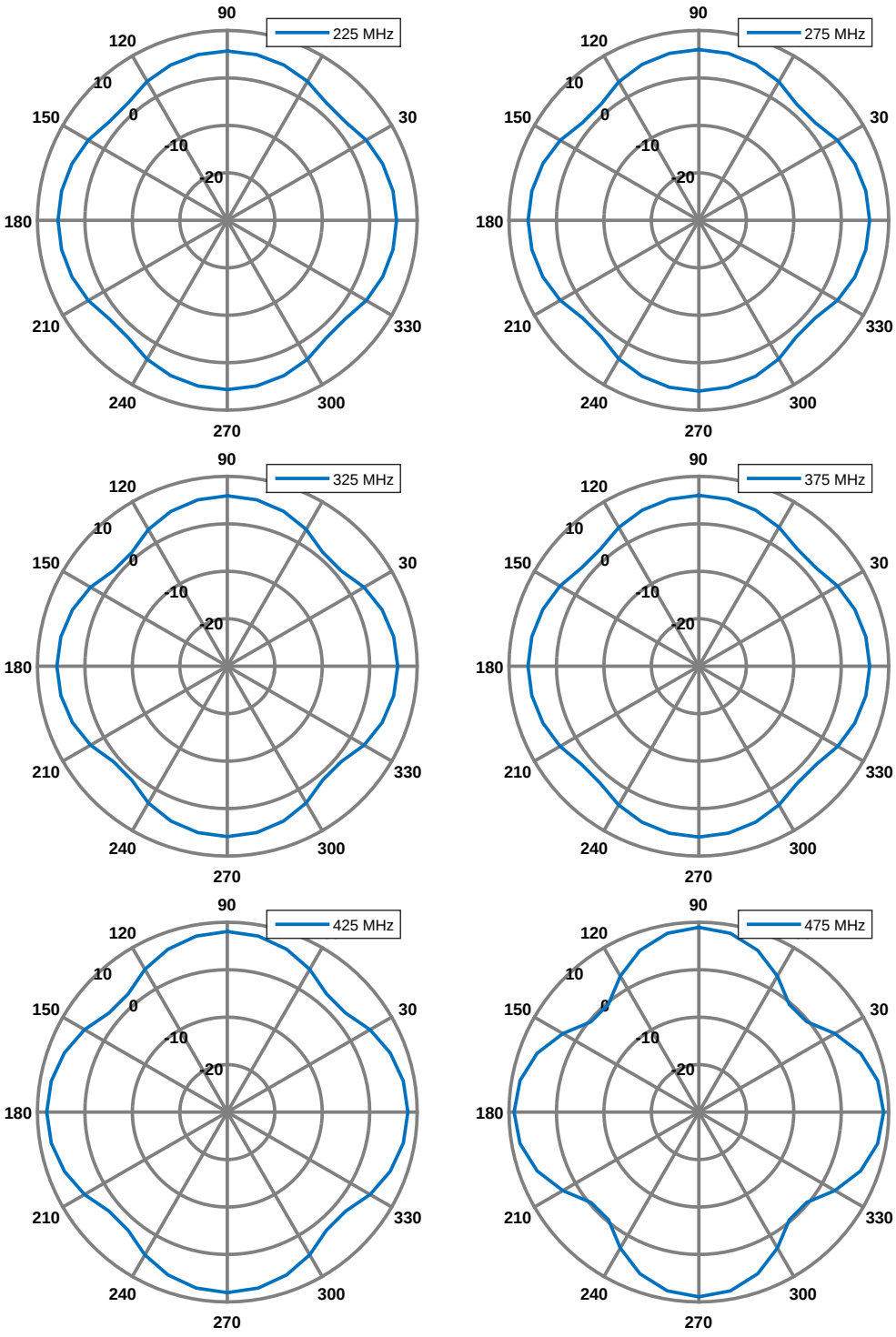

Figure 2.82: Theoretical coverage with four antennas placed on the vehicle in receiving mode. The antenna with the strongest received signal is selected as the sole receiver.

(b)

Figure 2.83: Outdoor test facilitys (a) turntable where the vehicle with window antennas will be placed and (b) dual-polarized log-periodic (wideband) antenna used as transmitter during testing. Note that the arch above the turntable in (a) is made out of fiberglass and will not interfere with the test.

(c) Passenger side

(d) Back window

Figure 2.84: Placement of four antennas around the vehicles four sides.

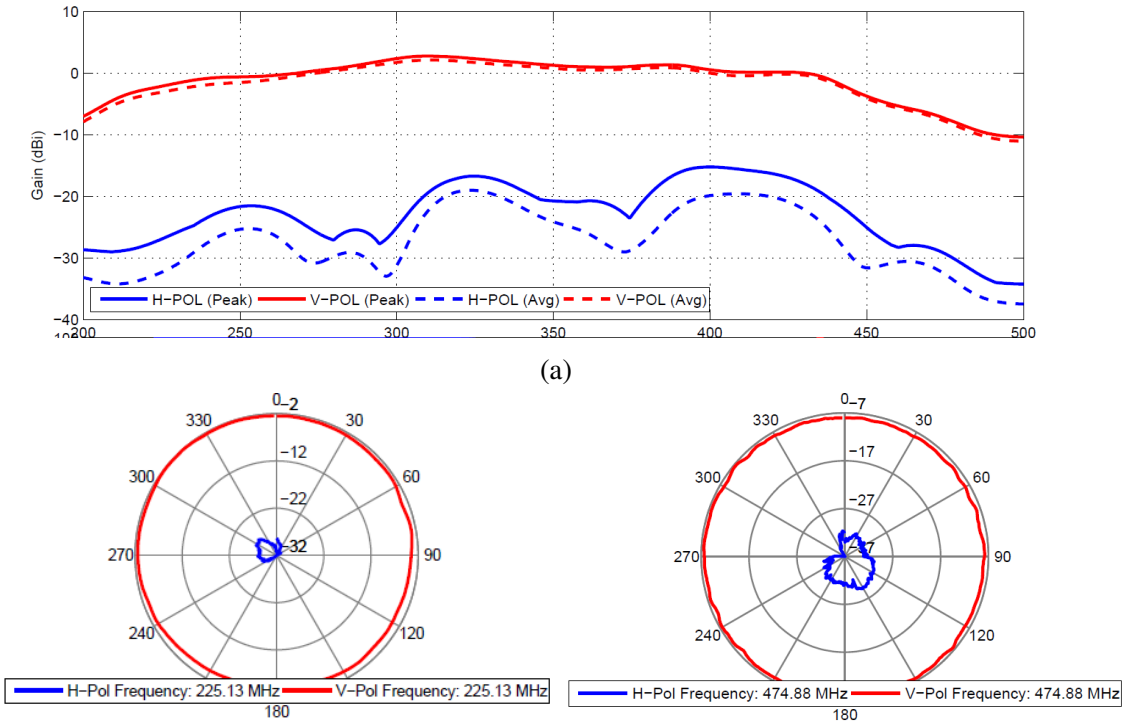

(a)

(b)

(c)

Figure 2.85: Measured radiation response of the broadband Wade antenna (a) absolute, calibrated gain in dBi across the frequency band of interest, (b) radiation pattern in azimuth at 225 MHz, and (c) radiation pattern in azimuth at 475 MHz

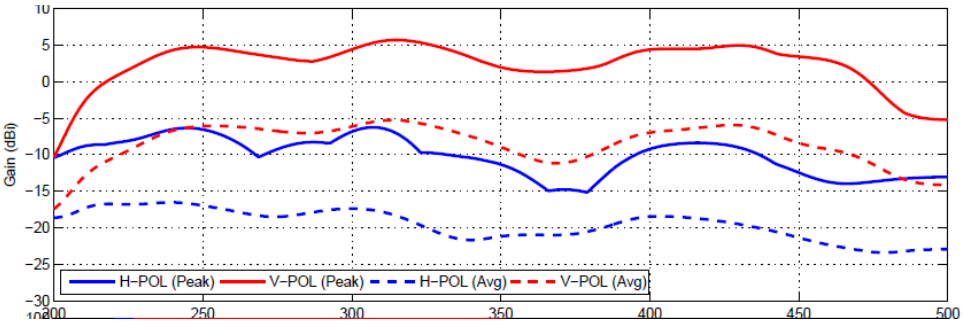

(a)

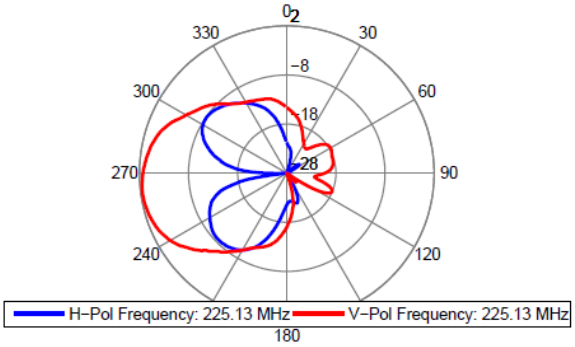

(b) 225 MHz

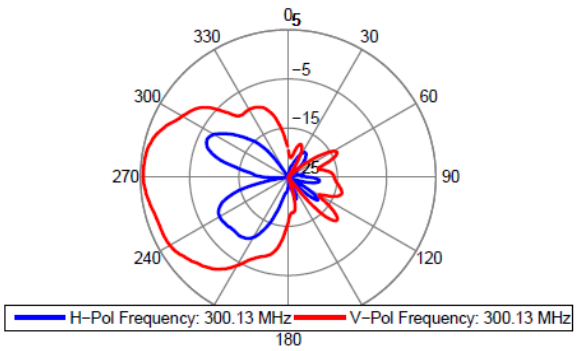

(c) 400 MHz

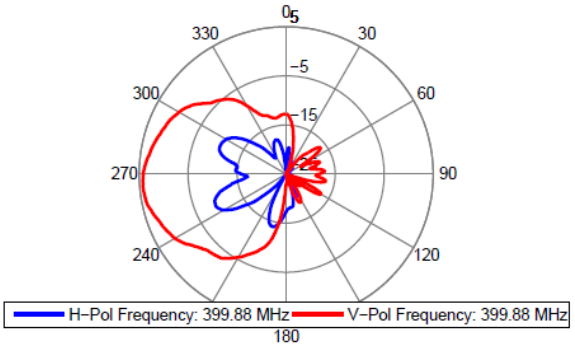

(d) 300 MHz

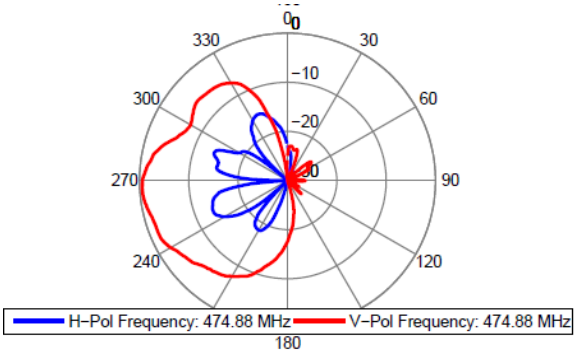

(e) 475 MHz

Figure 2.86: The measured absolute gain of transparent window-antenna placed on driver side (a) peak gain as function of frequency, (b-e) azimuth gain patterns at four different frequencies

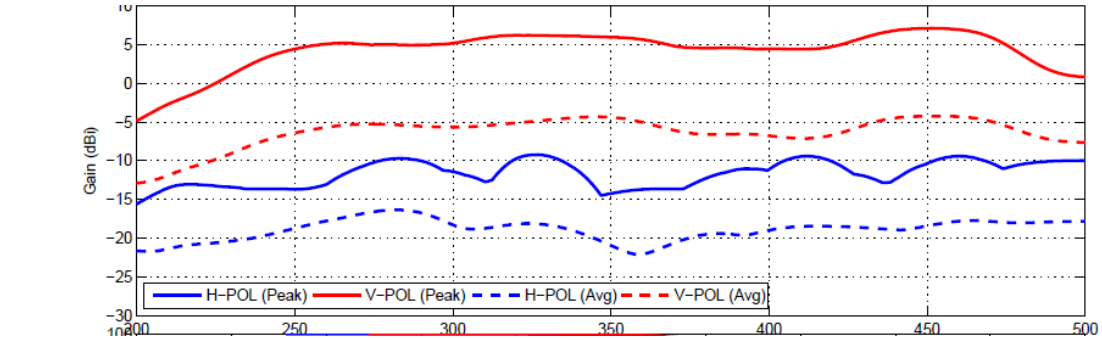

(a)

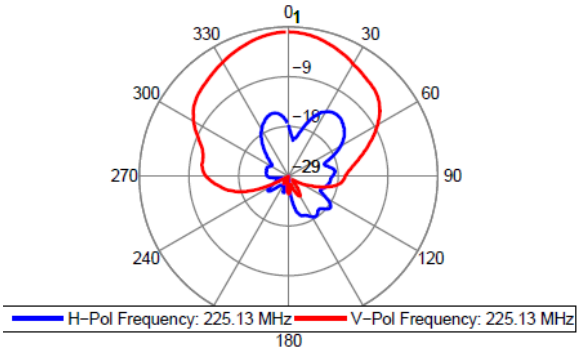

(b) 225 MHz

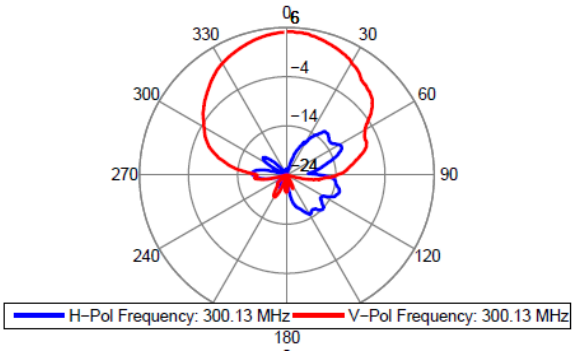

(c) 400 MHz

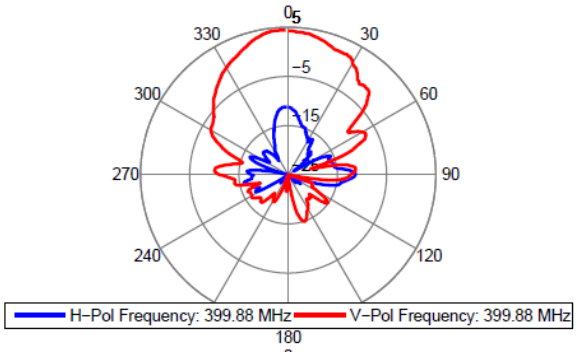

(d) 300 MHz

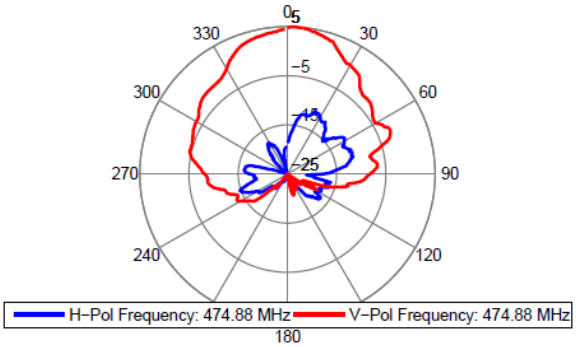

(e) 475 MHz

Figure 2.87: The measured absolute gain of transparent window-antenna placed on front side (a) peak gain as function of frequency, (b-e) azimuth gain patterns at four different frequencies.

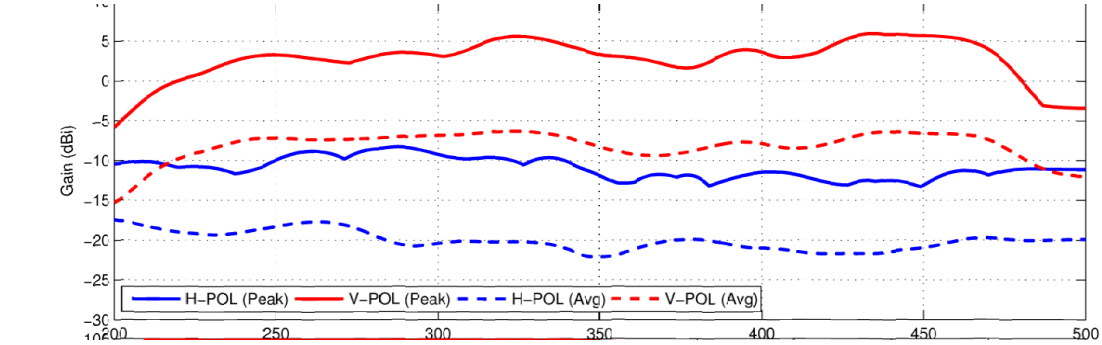

(a)

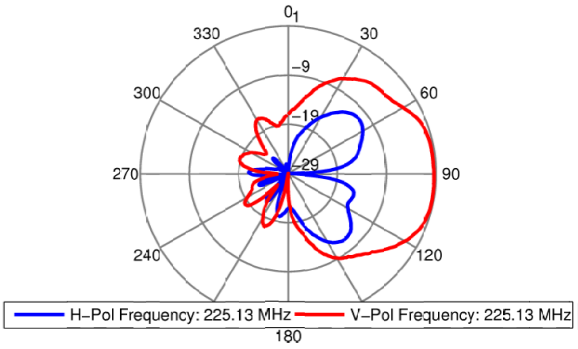

(b) 225 MHz

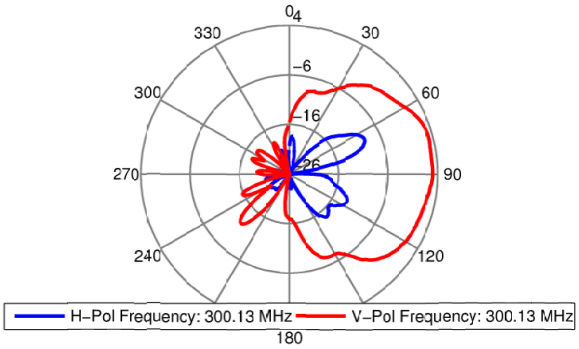

(c) 400 MHz

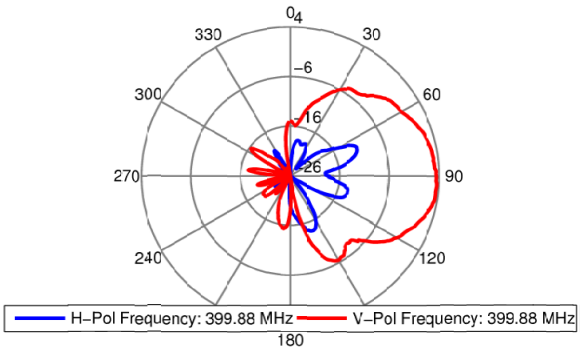

(d) 300 MHz

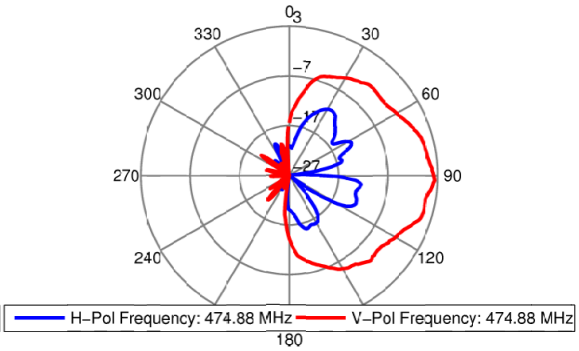

(e) 475 MHz

Figure 2.88: The measured absolute gain of transparent window-antenna placed on passenger side (a) peak gain as function of frequency, (b-e) azimuth gain patterns at four different frequencies.

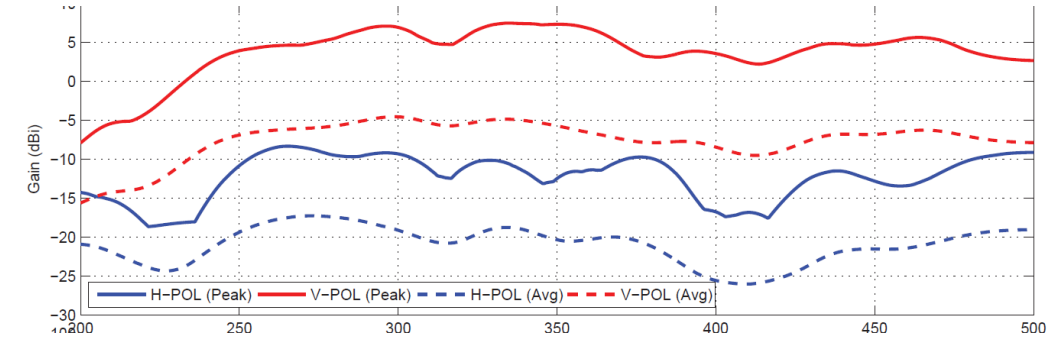

(a)

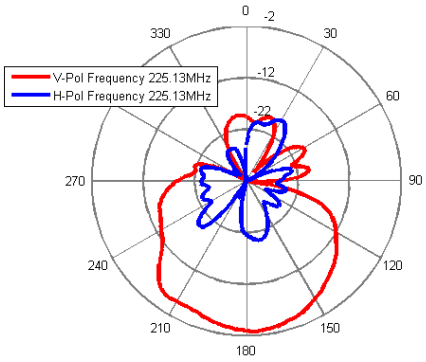

(b) 225 MHz

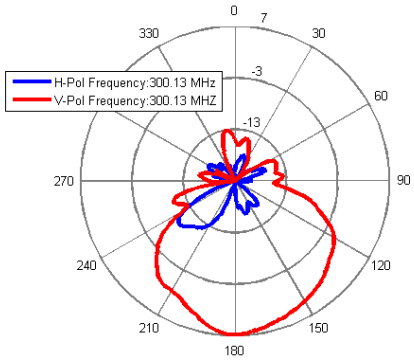

(c) 400 MHz

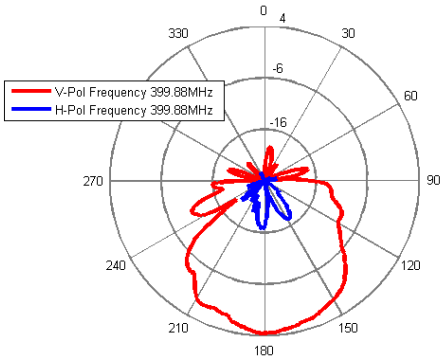

(d) 300 MHz

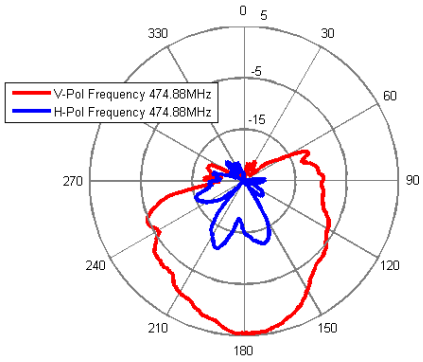

(e) 475 MHz

Figure 2.89: The measured absolute gain of transparent window-antenna placed on back side (a) peak gain as function of frequency, (b-e) azimuth gain patterns at 4 different frequencies.

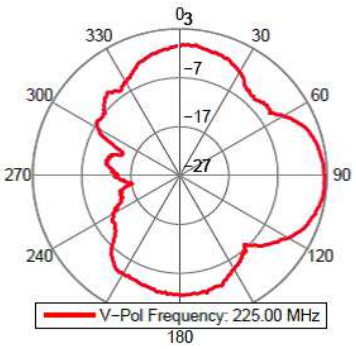

(a) 225 MHz

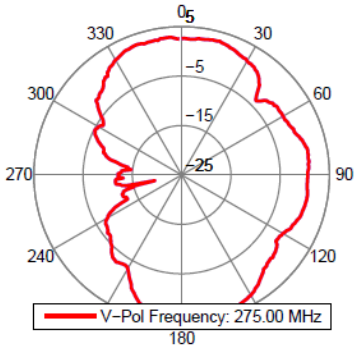

(b) 350 MHz

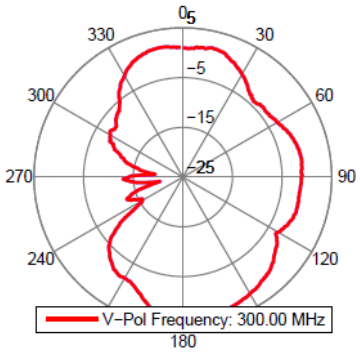

(c) 275 MHz

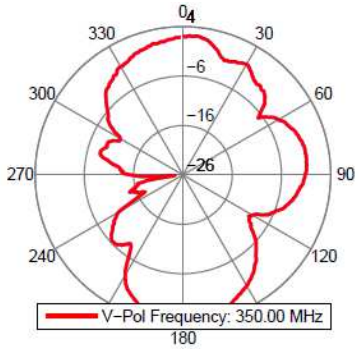

(d) 400 MHz

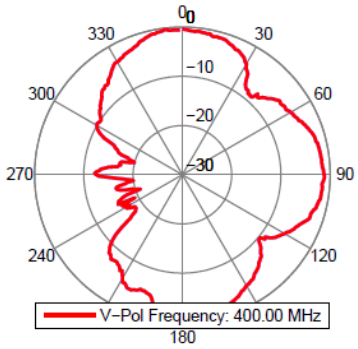

(e) 300 MHz

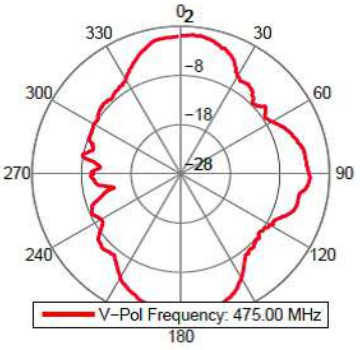

(f) 475 MHz

Figure 2.90: The measured maximum received signal using three antennas (front, passenger, and back side antennas) connected to the switch box.

Table 2.2: The fabricated antennas and their performance measures

Window	Tilt angle	Geometry	Bandwidth	Gain
Cougar front	15°	Monopole	250-550 MHz	5-7 dBi
MATV back	0°	Dipole	225-475 MHz	5-8 dBi
MATV front	40°	Dipole array	225-500 MHz	2-6 dBi
MATV side	0°	Dipole	225-475 MHz	3-5 dBi

2.9 Conclusion

In this chapter, the design and fabrication of a number of wideband optically transparent antennas embedded in armored windows for military ground vehicles were demonstrated. These designs are motivated by the need for reducing the vehicle signature, reducing air drag, increasing antenna protection and improving antenna gain. The antennas were designed to provide an octave bandwidth that covers the upper VHF and lower UHF bands simultaneously. It was demonstrated that a tilted beam could be achieved to allow for steering the main beam towards the horizontal direction for a tilted windshield. A unique meshing geometry was designed to reduce the optical opacity of the antennas and multiple prototypes were fabricated and it was shown that measured results were in good agreement with simulation. Table 2.2 lists the designed antennas, their topology, bandwidth and gain along the horizontal direction.

CHAPTER 3

Transparent Ground Planes for Automotive Applications

Optically transparent ground planes are considered to replace solid ground planes as shielding elements or antenna reflectors in applications where the ground plane is embedded in a platform with a desired optical functionality. Shielding elements or antennas that are embedded in vehicular or building windows or photovoltaic cells are among such applications [95–97]. Transparent conductors are readily available at frequencies above 2GHz. However, these conductors are not effective at UHF and VHF frequencies because of their extremely small thickness which is essential to their optical performance. A wire grid has high pass characteristics and therefore can replace a ground plane below its cutoff frequency. However, antennas have a specic band of operation and a reecting screen needs to act as a perfect ground plane only over the bandwidth of the antenna. Moreover, certain applications may require a bandpass behavior outside the operational band of the antenna to allow wave transmission at other frequencies. Hence a band-selective ground plane is more appropriate for antenna applications.

Miniaturized element frequency selective surfaces (MEFSS) can provide bandpass and bandstop responses with several advantages over the traditional frequency selective surfaces. These advantages include the ability to shrink the size of the screen to achieve a more uniform phase front, localized frequency selective behavior due to small element size, lower loss due to the fact that individual elements are not resonant at the operational

frequency, reduced dependency to the angle of incidence, and easer design and analysis since they can be treated as lumped elements. The bandpass properties of the MEFSS structures have been studied rigorously in recent years [98–100]. However, the bandstop properties of these structures are not properly studied and exploited. Furthermore, because the bandstop MEFSS is intended to be used as transparent ground planes, additional optimization steps are required to minimize the metallized area of the structure and therefore reduce their opacity.

In this chapter, the bandstop properties and optical transparency of an existing design commonly used as a bandpass MEFSS is studied. A simpler design with a bandstop behavior and superior optical performance is introduced and several techniques for increasing the bandwidth and improving the transparency of the structure are proposed. Several prototypes have been fabricated and their performance is evaluated.

3.1 Loop-grid MEFSS as a Ground Plane

Fig.3.1 shows the top view of two adjacent unit cells MEFSS similar to what was reported in [98]. The structure consists of a wire grid on one side and an array of square loops on the other side of a thin transparent dielectric slab. It is possible to place the wire grid with a lateral shift such that the horizontal and vertical wires meet at the center of the loop. The lateral shift changes the coupling coefficient between the two layers which slightly affects the performance of the structure. In order ro increase the transparency of the design, the loops and wires are placed with no lateral shift so that the metallized areas overlap for small values of g.

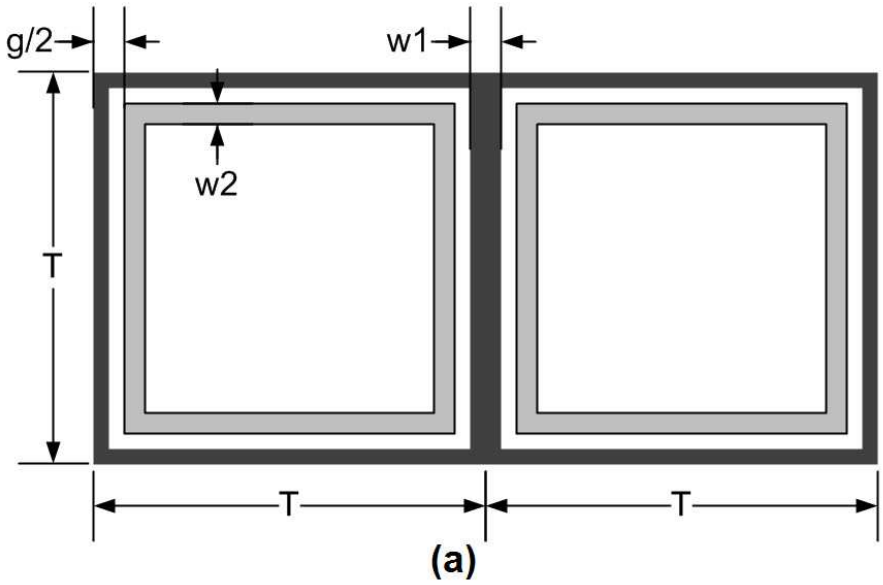

Figure 3.1: Two adjacent unit cells of the loop-grid MEFSS. The structure consists of an array of square loops on one side and a wire grid on the opposite side of a very thin transparent substrate.

The unit cell size of the structure is electrically small. Therefore the behavior of the structure can be accurately using a circuit model consisting of lumped elements. The equivalent circuit model of the structure is shown in Fig.3.2. The circuit model is best understood assuming a TEM wave excitation as shown in the picture. The incident magnetic field induces currents on the sides of the wire grid that are perpendicular to the incoming magnetic field. These sides are modeled as a shunt inductor (L_2 and L_3). Similarly the sides of the square loops that are perpendicular to the incoming magnetic field are modeled as a shunt inductor (L_1). The two sides of the adjacent loops that are perpendicular to the incoming electric field form a capacitor(C_g). The loop array and the wire grid also have a weak coupling due to the capacitance formed between the metallic traces as well as the mutual coupling between the inductors on the two sides of the substrate. The wave propagation in free space is modeled using a transmission line with the characteristic impedance of $Z_0 = \sqrt{\mu/\epsilon}$ and the wave propagation through the thin substrate is modeled using a transmission line with the characteristic impedance of $Z_1 = \sqrt{\mu/\epsilon\epsilon_r}$ where ϵ_r is the dielectric constant of the substrate.

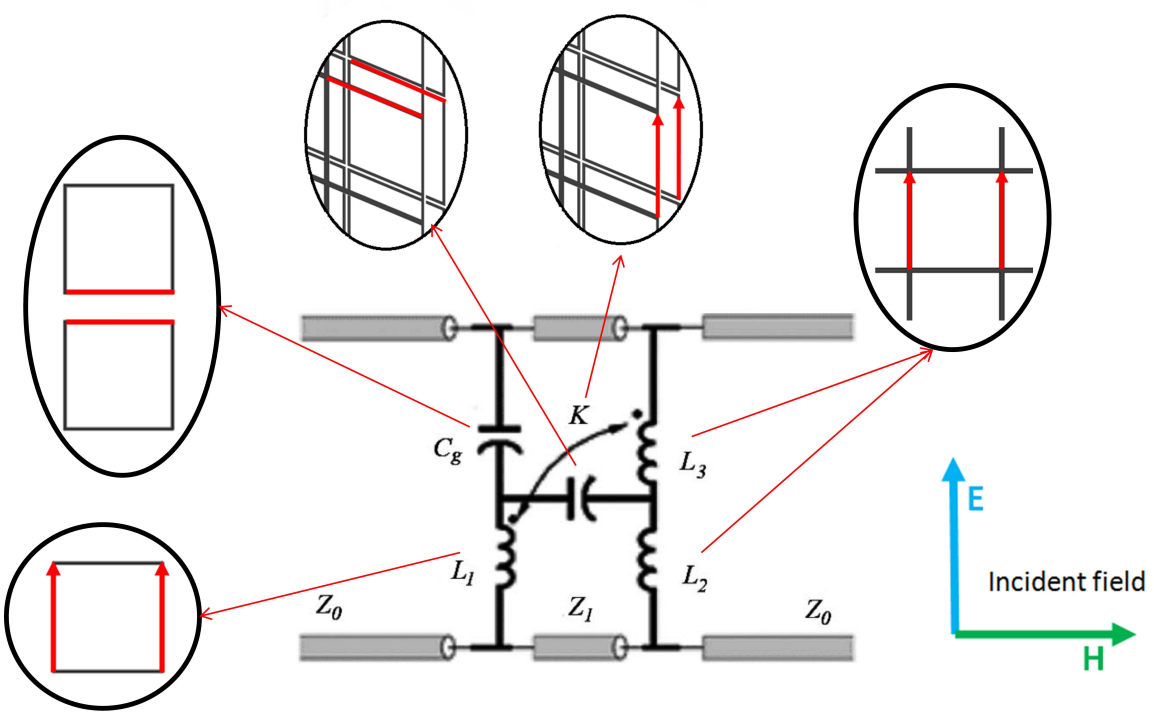

Figure 3.2: The circuit model of the loop-grid MEFSS.

Decreasing the unit cell size of the FSS (T) reduces the equivalent inductances and therefore increases the bandwidth. However, decreasing the unit cell size without changing the wire thicknesses increases the opacity. In order to keep the same opacity, the wire thicknesses should be reduced, which in turn increases the inductances. Nevertheless, the equivalent inductances are less sensitive to the wire thicknesses ($w1$ and $w2$) than the unit cell size. Therefore the bandwidth of the FSS can be increased by reducing the unit cell size and the wire thicknesses simultaneously and maintaining the opacity. Fig.3.3 shows the full-wave simulation results of two different designs. For the second design, T and $w2$ are half the values of the first design. The gap size is also reduced to adjust for the shift in the reject band due to unit cell size reduction. $w1$ is set to be $g + 2w2$ for both designs to maximize the width of the wire grid without increasing the overall opacity of the design. The substrate thickness $h = 6mm$ and dielectric constant $\epsilon_r = 2.2$ are the same for both designs. The results show that the 20dB insertion loss bandwidth of the FSS is tripled even

though the opacity (defined as the ratio of the area covered with copper to the entire surface area of the FSS) is reduced from 8% to 4.8%. However, the gap size has been reduced from 1 mm to .2 mm to lower the resonant frequency which would otherwise be much higher due to the reduction in the inductances. The maximum bandwidth that can be achieved using this design is limited by the minimum gap size permitted by the fabrication method used.

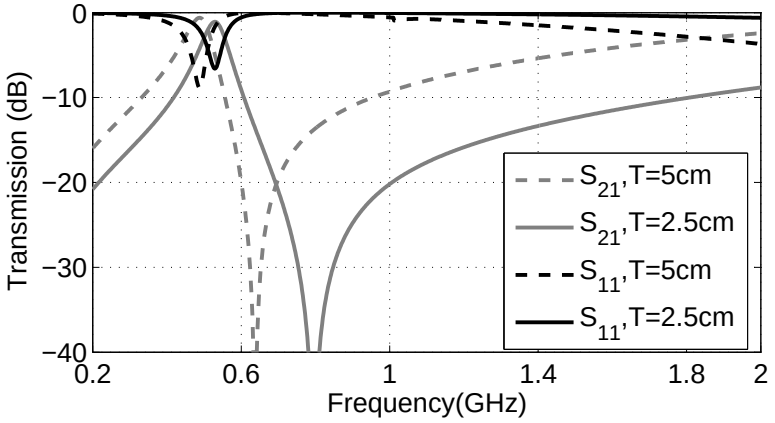

Figure 3.3: The frequency response of the MEFSS. Dashed line: T=5cm, g=1mm, $w1$=2mm, $w2$=0.5mm. Solid line: T=2.5cm, g=0.2mm, $w1$=0.6mm, $w2$=0.2mm

3.2 Square Loop Ground Plane

The wire grid is necessary if the bandstop properties are required at very low frequencies. However, for most microwave applications a ground plane over a certain frequency band is sufficient. The bandstop properties can be achieved using only an array of square loops. Fig.3.4 shows a unit cell of the single layer design and its design parameters. The structure is consisted of a two dimensional array of square metallic loops that are fabricated on a thin dielectric substrate. The circuit model of the structure is shown in Fig.3.4. In this model the inductance represents the thin vertical metallic strips of the loop and the series capacitance is placed for the small gap between the horizontal strips for a vertically polarized incident wave. It is evident that the circuit model represents a one stage band-stop filter with shunt components. The transmission lines are circuit representation of free space and

the dielectric substrate media supporting a TEM wave. The frequency response of the FSS is simulated using HFSS full-wave simulator with periodic boundary conditions. Fig.3.5 shows the simulation setup. An x-polarized plane wave is used for excitation but the results are valid for any polarization because of the symmetry of the problem. The frequency response of the structure is plotted in Fig.3.6 with w=0.25mm, T=40.6mm ($\lambda/7.5$ in free space), g=1.52mm, d=2.36mm ($\lambda/60$ in the substrate), $\epsilon_r = 4.4$ and dielectric loss tangent of 0.02. The reflection coefficient at 1GHz is -0.11dB which confirms that the effect of dielectric losses on the performance of the designed ground plane is negligible. This is despite the fact that a loss tangent of 0.02 is assumed in this simulation which is more than five times that of sodalime glass, 0.0037 at 1GHz. The response of the MEFSS is also compared with that of a square wire mesh with the unit cell length of 12.8mm and wire width of 0.25mm. As seen in the graph, if a 10dB insertion loss bandwidth of 40% around the center frequency of 1GHz is sufficient for a certain application, the one layer MEFSS outperforms the traditional wire mesh. Unlike the wire-grid, the insertion loss of the MEFSS based design peaks at the desired frequency, creating a very strong rejection. Furthermore, the opacity of the MEFSS in this design is about 2.5% which is less than that of the wire mesh design (4%). Fig.3.7 shows the opacity of the two designs versus bandwidth at the center frequency of 1GHz. In obtaining this data it is assumed that the minimum realizable line width for both designs is 10mils. As seen in the graph, if a bandwidth of 55% or less is needed, the MEFSS design results in less opacity and better rejection in the stop-band. In addition, the wire grid reflects the waves at all the frequencies that are lower than the desired frequency. Therefore the wire grid cannot be used for applications where a pass band is needed below the center frequency of the antenna.

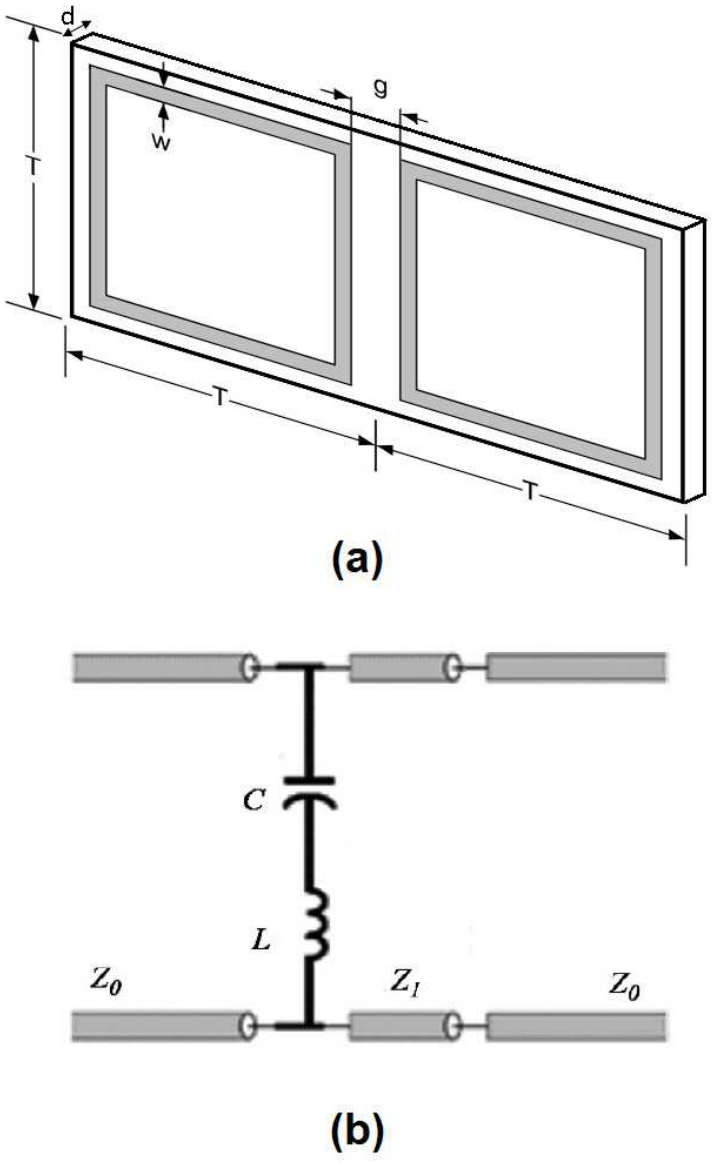

Figure 3.4: a) Two unit cells of the one layer MEFSS and its design parameters b) The circuit model of the one layer MEFSS.

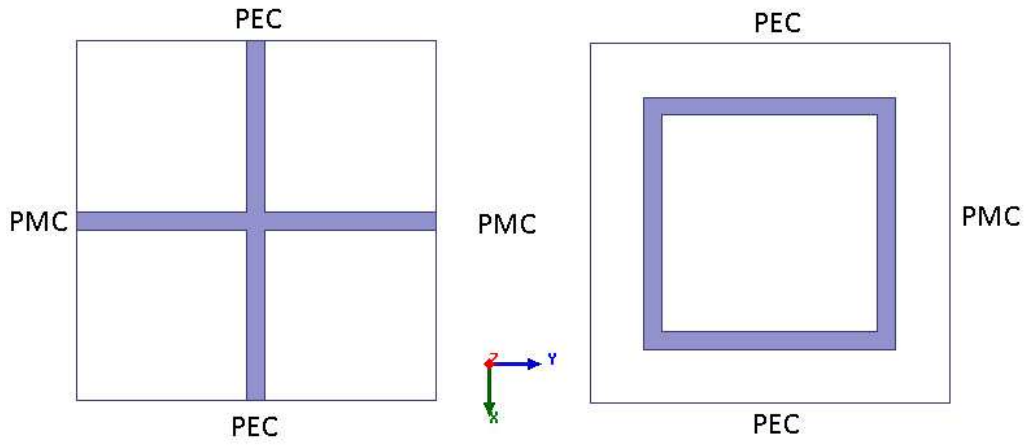

Figure 3.5: HFSS simulation setups of the wire mesh and square loop designs. In both cases an x-polarized plane wave is illuminated in normal direction to the surface and the reflection and transmission coefficients are calculated.

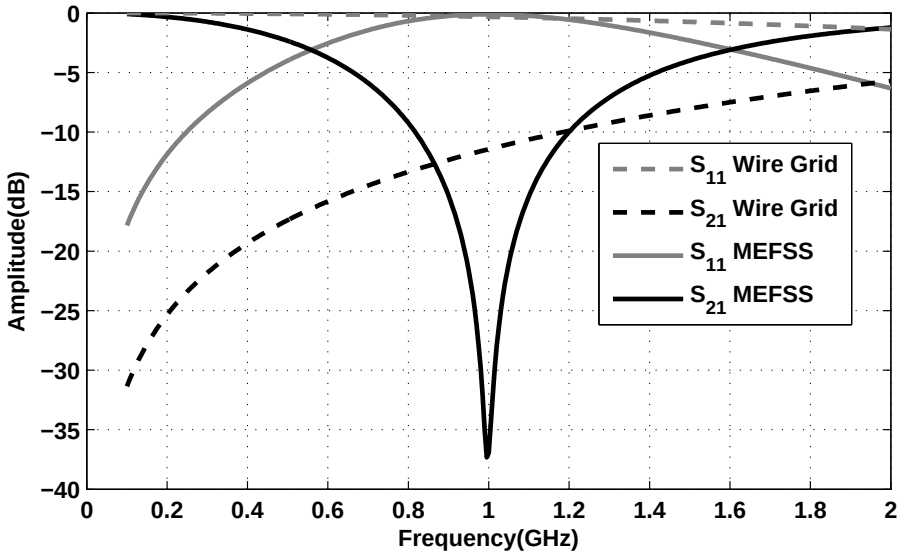

Figure 3.6: Comparison between the HFSS simulation results of the one layer MEFSS (opacity of 2.5%) and the square mesh (opacity of 4%)

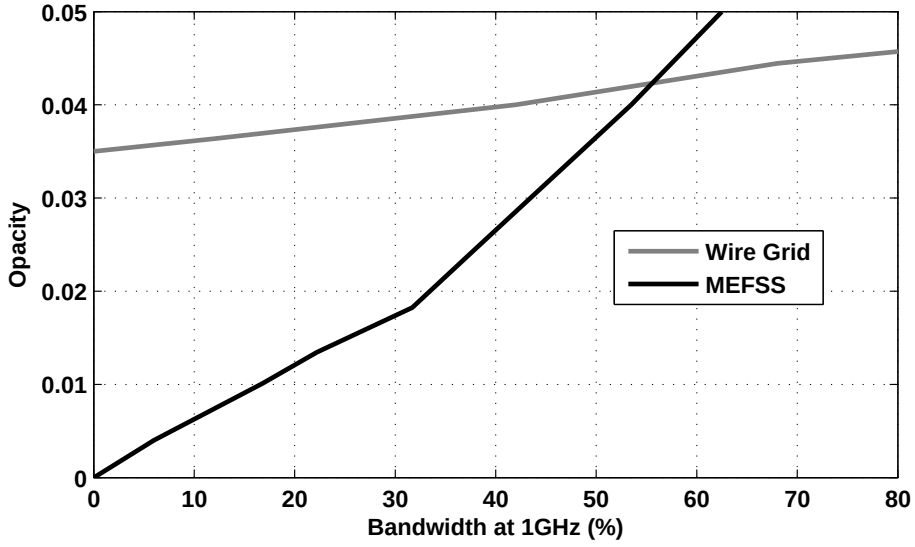

Figure 3.7: Opacity of mesh and loop design changes with bandwidth. For bandwidths of less than 55%, the one layer MEFSS is less opaque.

3.3 Practical Design Considerations at UHF Frequencies

As mentioned earlier, transparent conductors are readily available at frequencies above 2GHz. A MEFSS-based design must be used at lower frequencies or in situations where a sharp filtering behavior consisting of at least one pass-band and one stop-band is required. The latter will be addressed later in this chapter. Figure 3.8 shows the simulated response of the MEFSS at normal incident for two different designs at UHF frequencies. In practice, the ground plane will be used as a reflector for an antenna that will be embedded inside the window glass. For this reason, in this simulation the MEFSS is placed on the boundary of a hypothetical half space made of glass with dielectric constant of 7.25. The design parameters of the wide-band design are w=1mm, a=50mm and S=250μm with opacity of Op=8% and 20dB insertion loss bandwidth of BW=12%. For the narrow band design, w=1, a=70mm and S=2500μm with Op=6% and BW=9%. As shown by the simulation results, it is possible to increase the bandwidth of the ground plane by reducing the unit

cell size and therefore reducing the inductance in the circuit model. The extra bandwidth is achieved at the cost of increasing the opacity and reducing the gap between the adjacent loops. For example the 20dB insertion loss bandwidth can be increased even further to 19% by reducing the loop size to a=41mm. However, the opacity increases to 10% and the gap size between the adjacent loops reduces to 25μm. The increase in the opacity can be avoided relatively easily as will be shown here. The main constraint in increasing the bandwidth of the MEFSS is therefore the gap size between the loops. The metallic traces are commonly fabricated using chemical etching of a thin layer of metal deposited on glass. Unlike transparent conductors, the thickness of the metallic layer can be in the order of tens of micron since the metallic traces themselves are not transparent. Optical transparency in this case is a result of the fact that metalic traces on the glass cover a relatively low percentage of the surface area of the glass. The typical tolerances of this method of fabrication does not allow for traces that are less than 100μm apart. Therefore the capacitor value must be increased by means other than decreasing the gap size between the adjacent loops.

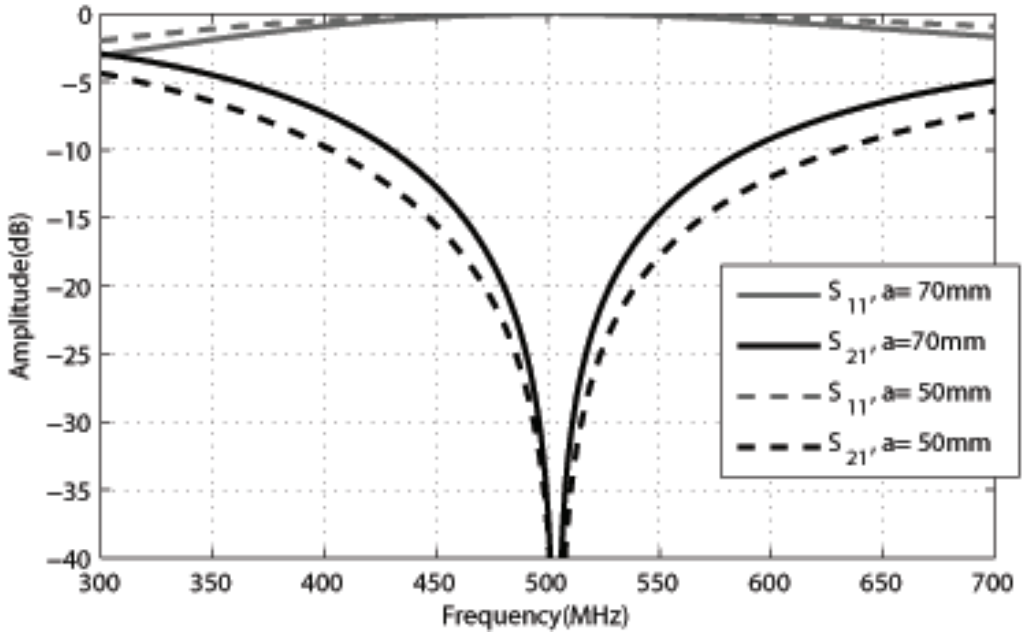

Figure 3.8: The frequency response of the square loop MEFSS.

In order to increase the bandwidth, the equivalent inductance of the MEFSS must be decreased while increasing the its equivalent capacitance. It can be shown that connecting the two opposite sides of the square loops using multiple thinner wires results in lower inductance values than the traditional square loop of the same opacity. Figure 3.9 shows three different unit cell designs of the same opacity but drastically different inductance values. For all three designs w=1mm, a=50mm and opacity is 8%. The simulation results suggest that to achieve the lowest value of inductance for a given opacity and unit cell size, the wires must be as thin as possible and distributed evenly over the surface of the loop. The width of the wires are limited by metallic losses and fabrication limitations. Using chemical etching, the minimum width of the traces is limited to 100μm. The metallic losses at UHF frequencies (200MHz to 1GHz) are negligible for 100μm wide traces that are etched on an aluminum or copper coated glass with metal thickness of higher than 17μm (0.5 oz copper).

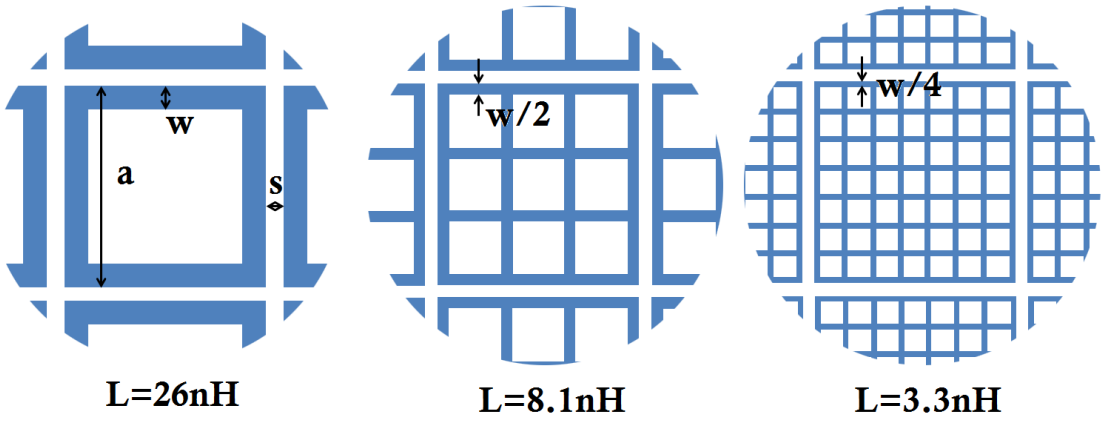

Figure 3.9: Lower inductances can be achieved without compromising transparency if a meshed square loop is used instead of the traditional square loop.

In addition to lowering the inductance, the capacitance between the adjacent loops must be increased to maintain the center frequency of the MEFSS. The capacitance value can be increased by using interdigital capacitors as shown in Figure 3.10. Using interdigital capacitors on the edges of the adjacent loops increases the capacitance between the loops without the need to reduce the gap size between traces. However, this is achieved at the

cost of increasing the opacity of the MEFSS since realizing interdigital capacitors requires more metal surface.

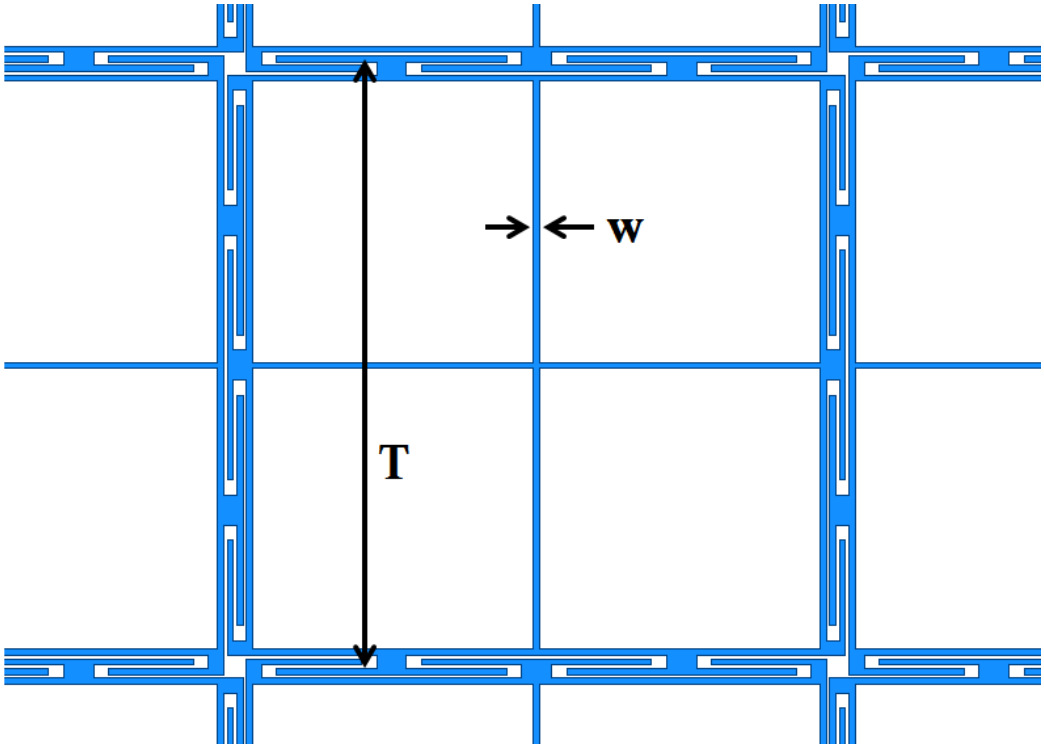

Figure 3.10: MEFSS with interdigital capacitors.

Figure 3.11 shows the frequency response of the MEFSS with interdigital capacitors for W=0.25mm, T=50mm and S=150μm and Op=8%. This design has a 20dB insertion loss bandwidth of BW=24%. The inductance is reduced compared to the original square loop design by using a middle conducting wire on the loop. The Capacitance is increased by using the interdigital capacitors. The unit cell size and opacity of both designs are the same. However, the design with interdigital capacitors has twice the bandwidth of the original design.

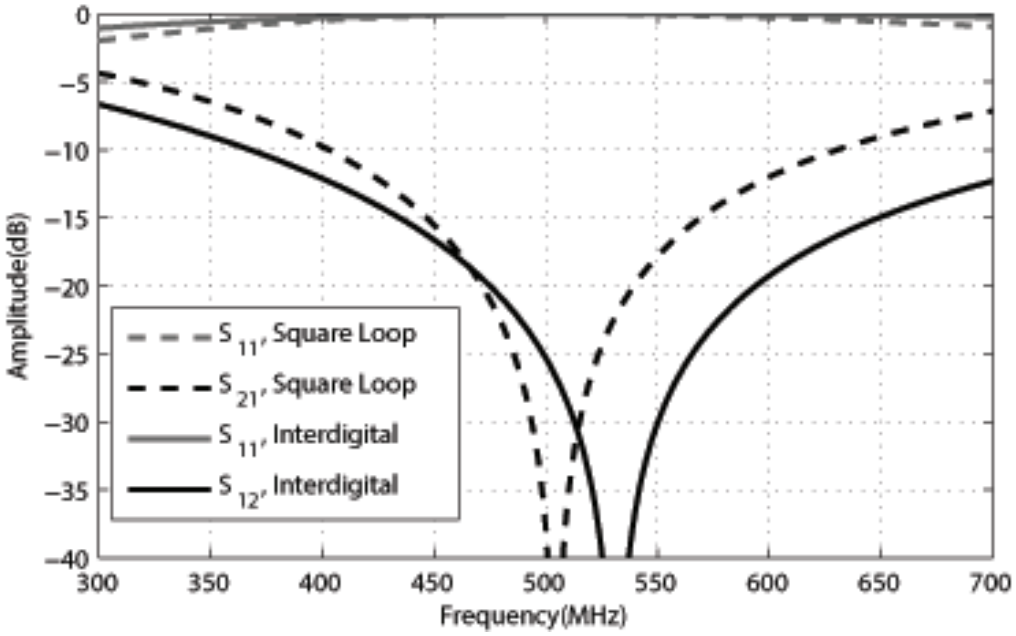

Figure 3.11: The frequency response of the MEFSS with interdigital capacitors compared to that of the square loop.

In order to realize wider band ground planes, more rows of the interdigital capacitors are needed. Adding more rows to the capacitors severely affects the optical transparency of the ground plane. To overcome the aforementioned difficulties in designing a transparent ground plane, a novel MEFSS is proposed that outperforms the square Loop MEFSS with interdigital capacitors and eliminates the mentioned challenges.

The proposed MEFSS is a periodic structure consisting of metallic loops on opposite sides of a very thin dielectric substrate. Figure 3.12 shows the relative placement of the loops on the front and back layers. The loops on the back layer are drawn with wider traces to demonstrate the relative placement of the loops. In practice the trace widths are chosen to be the same for optimum optical performance. This structure works based on the same principle as the square loop MEFSS. The sides of the loops that are perpendicular to the incoming magnetic field act like inductors and the sides that are perpendicular to the incoming electric field form capacitors between the loops on the front and back sides of the substrate. The most important difference between the two designs is that in the two

layer structure, the capacitor between the overlapped loops is confined within the dielectric substrate on which the loops are fabricated.

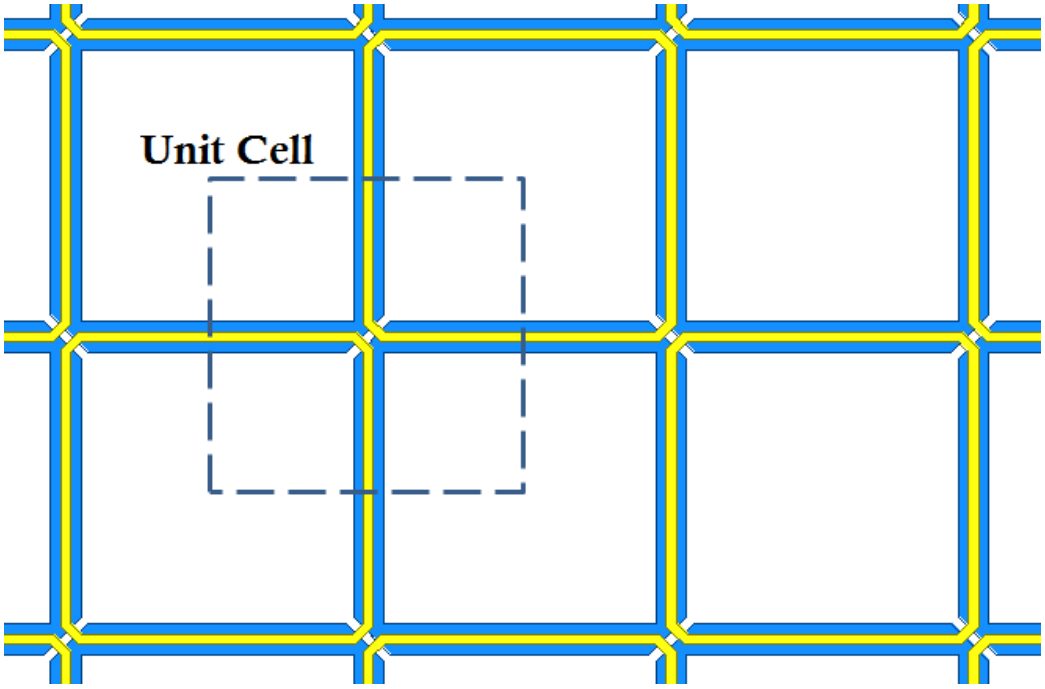

Figure 3.12: The proposed two layer MEFSS geometry.

Fig.3.13 the electric field distribution of the two types of capacitors. The capacitance is much greater for the overlapping case because the whole widths of the two traces are placed in proximity of one another. Moreover, the electric field between the two traces is confined within the substrate which has a higher dielectric constant than air. The other advantage of the overlapping structure is that the capacitance value is far less restricted since the substrate thickness can be reduced to a few hundred nano-meters by coating the first layer by silicon dioxide, parylene or other vapor-depositable materials and building the second layer on top of the first one. In addition, the loops on the front and back sides of the two layer design overlap and reduce the opacity by a factor of two.

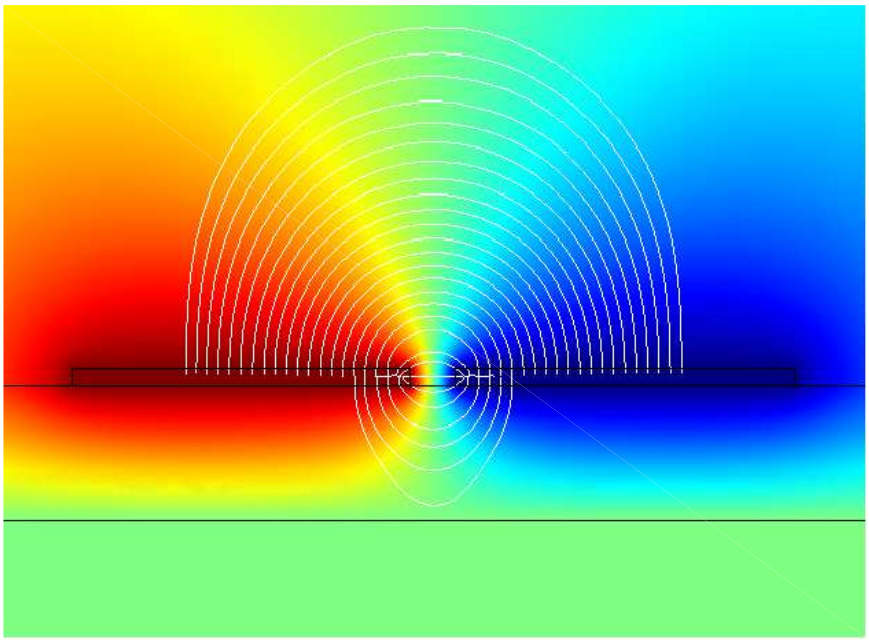

(a) Single layer capacitor

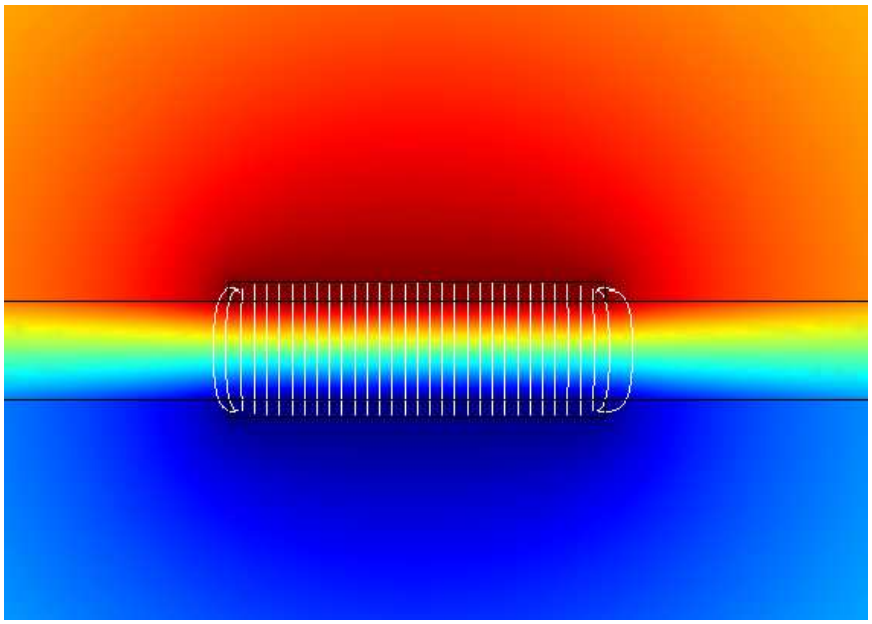

(b) Overlapping capacitor

Figure 3.13: The filed distribution between the traces of adjacent loops in the single layer and overlapping designs. The overlapping design results in a much greater capacitance.

Figure 3.14 shows the frequency response of a two layer MEFSS designed on a 25μm thick polyamide substrate with dielectric constant of 3.5. The ground layer is placed at the boundary of a glass half-space and its performance is compared with the square loop with

interdigital capacitors. The design parameters for the two layer MEFSS are a=18mm and w=15mm. The opacity of this design is only 4% which is half of that of the interdigital MEFSS and its 20dB insertion loss bandwidth is 32%.

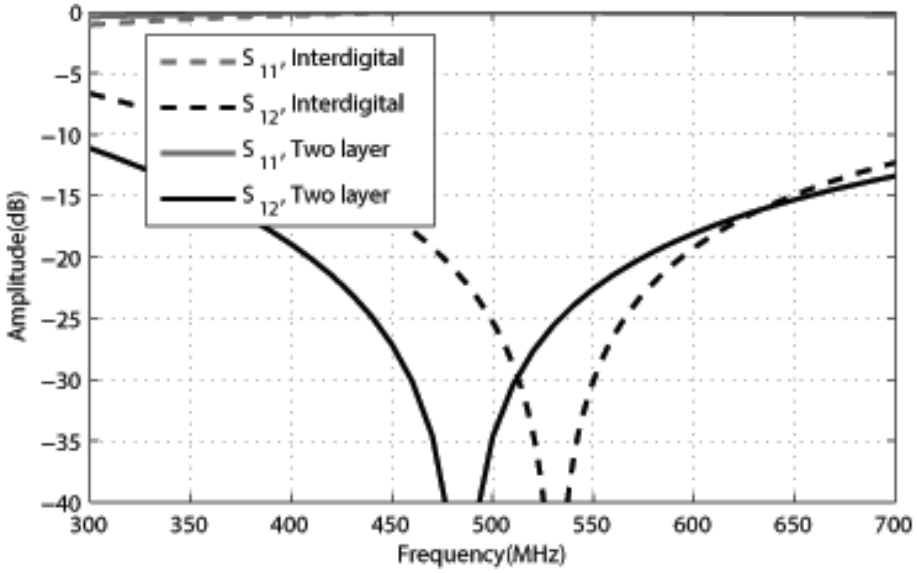

Figure 3.14: Frequency response of the two layer MEFSS compared with that of the square loop with interdigital capacitors.

The proposed design also allows for a very easy way to increase the bandwidth without increasing the opacity dramatically. The number of layers can be increased arbitrarily by alternating between the front and back side patterns on consecutive layers. The equivalent circuit of the combined multilayered design is still the same with the equivalent capacitance of all the layers placed in parallel. Because of the coupling between the inductances of different layers the equivalent inductance is more than the inductance of all layers placed in parallel. However, the inductance can be further refocused by connecting the opposite sides of the square loops together using wires as mentioned above.

3.4 Band-selective Ground Plane

According to standard filter theory, the order of a filter can be increased by adding series and shunt stages alternatively. Fabrication of series components between two layers of MEFSS is difficult and very costly. A common alternative approach for realizing series components is to use a $\lambda/4$ long segment of transmission line as an impedance invertor between the two shunt resonators. The transmission line will effectively transfer the shunt elements into series elements as far as the input impedance of the filter is concerned [94]. However, this approximation is only accurate for narrow band filters (10% or lower) since the electrical length of the transmission line varies with frequency. Furthermore, the number of transmission line sections needed increases linearly as the order of the filter increases. As alluded previously transmission line sections are realized using spacers between the MEFSS layers. Increasing the number of spacers increases the angle dependency of the frequency response of the MEFSS, not to mention increasing the cost and weight of the overall design.

Fig.3.15 shows the response of a third order standard Chebychev filter and its equivalent realization using only shunt elements. The filter is designed to have more than 10dB insertion loss in its stop-band (0.88GHz-1.14GHz) and more than 10dB return loss below 0.828GHz and above 1.2GHz. As shown in the graph, the intended out of band properties is not achieved when the filter is realized using shunt elements and transmission lines. This is expected due to the fact that transmission line sections can be modeled as impedance invertors only over a small bandwidth. One way to obtain the desired out of band response is to design the original filter to have much better out of band properties than required so that the shunt realization still meets the required criteria. The tradeoff is that the bandwidth of the stop-band will be reduced as shown in Fig.3.15.

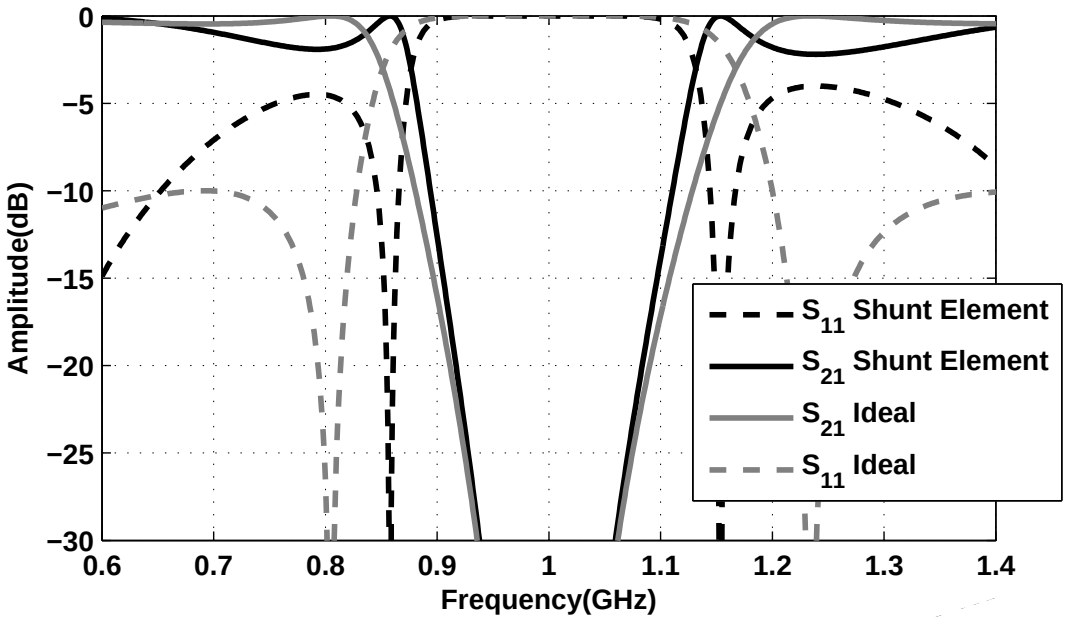

Figure 3.15: comparison of the ideal chebyshev filter and its shunt element realization using $\lambda/4$ long transmission lines as impedance invertors

In standard filter design, the common approach is choosing all resonators to have the same resonant frequency. As will be discussed below, relaxing this constraint can improve the response of the filter especially when FSS realization of the filter is intended and placement of shunt elements are the only option. Each FSS layer can be modeled with a shunt admittance Y_n. If the layers are stacked very close together, the entire N-layer structure can be modeled with a single shunt admittance $Y = \Sigma_{n=1}^{N} Y_n$. The normalized shunt admittance can be written in the form of the ratio of two polynomials of ω^2:

$$\bar{Y} = \frac{Y}{Y_0} = \frac{j\omega P(\omega^2)}{Q(\omega^2)} \tag{3.1}$$

The reflection coefficient of the FSS in term of the this admitance takes the following form:

$$\Gamma = \frac{1 - (1 + \bar{Y})}{1 + (1 + \bar{Y})} = \frac{-j\omega P(\omega^2)}{2Q(\omega^2) + j\omega P(\omega^2)} \tag{3.2}$$

The normalized admittance of each layer composed of a series LC circuit has the form,

$$\bar{Y_n} = \frac{j\omega P_n(\omega^2)}{Q_n(\omega^2)} = \frac{k_n j\omega}{\omega_n^2 - \omega^2} \tag{3.3}$$

where $k_n = Z_0/L_n$ and $\omega_n^2 = 1/L_nC_n$. Therefore,

$$\begin{aligned} Q(\omega^2) &= \prod_{n=1}^{N}(\omega_n^2 - \omega^2) \\ P(\omega^2) &= \sum_{m=1}^{N} k_m \prod_{n\neq m}(\omega_n^2 - \omega^2) \end{aligned} \tag{3.4}$$

Using (3.2), the magnitude of the reflection coefficient can be computed from:

$$|\Gamma|^2 = \frac{\omega^2|P(\omega^2)|^2}{4|Q(\omega^2)|^2 + \omega^2|P(\omega^2)|^2} \tag{3.5}$$

It is evident that $|\Gamma| = 1$ when $Q(\omega^2) = 0$ and $|\Gamma| = 0$ when $P(\omega^2) = 0$. $Q(\omega^2)$ has exactly N zeros at $\omega^2 = \omega_n^2$. $P(\omega_n^2)$ can be expressed as

$$P(\omega_n^2) = k_n \prod_{m=1}^{n-1}(\omega_m^2 - \omega_n^2) \prod_{m=n+1}^{N}(\omega_m^2 - \omega_n^2) \tag{3.6}$$

Assuming ω_n^2 are indexed in ascending order, all the terms in the first product in (3.6) are negative and all the terms in the second product are positive which yields:

$$\begin{aligned} P(\omega_n^2) > 0 \quad &\text{for even n} \\ P(\omega_n^2) < 0 \quad &\text{for odd n} \end{aligned} \tag{3.7}$$

Therefore the sign of $P(\omega^2)$ changes between any two consecutive zeros of $Q(\omega^2)$. Hence $P(\omega^2)$ has at least one zero between ω_n^2 and ω_{n+1}^2. Moreover, since $P(\omega^2)$ is of order $N-1$, it must have exactly one zero between ω_n^2 and ω_{n+1}^2. Therefore the response of the filter consists of N stop-bands and N-1 pass-bands. There are $2N$ unknowns, C_n and L_n, that

have to be determined to complete the filter design. Poles, ω_n^2, and zeros, ν_m^2, of the entire filter can be selected independently except that there should be one zero between each two consecutive poles. The values of k_n, ω_n^2 and ν_m^2 have the following relationship:

$$\mathbf{A}k = b \tag{3.8}$$

where

$$\begin{aligned}
[k]_m &= k_m \\
[b]_m &= -k_N \prod_{n=1}^{N-1} (\omega_n^2 - \nu_m^2) && m = 1, 2, ..., N-1 \\
[\mathbf{A}]_{n,m} &= \prod_{i \neq n}^{N} (\omega_i^2 - \nu_m^2) && n = 1, 2, ..., N-1
\end{aligned}$$

Once ω_n^2 and ν_m^2 are selected, k_1 to k_{N-1} can be found as a factor of the free parameter k_N using equation (3.8). The existence of $N-1$ pass bands in the response is clearly unwanted. The pass bands can be suppressed by separating the layers by dielectric spacers. As will be shown next, only one such spacer is sufficient to eliminate all the pass bands provided that a certain arrangement of the resonators is used. Let us divide the resonators into two groups each having a combined admittance of $Y_1 = \frac{j\omega R(\omega^2)}{S(\omega^2)}$ and $Y_2 = \frac{j\omega T(\omega^2)}{U(\omega^2)}$ respectively. The groups are selected such that zeros of S, s_i^2 and zeros of U, u_i^2 are equal to ω_{2i-1}^2 and ω_{2i}^2 respectively where ω_j^2 are the zeros of $Q(\omega^2)$ in ascending order. Based on the above discussion, zeros of R, r_i^2 can be selected arbitrarily as long as the following inequality holds: $s_i^2 < r_i^2 < s_{i+1}^2$. Since U has a zero between each two consecutive zeros of S, it is possible to select k_{2i-1} such that zeros of R are also zeros of U. Similarly, k_{2i} can be selected such that zeros of T are also zeros of S. If Γ_2 represents the reflection coefficient of the second group (Y_2) only, then the response of the entire filter, in terms of Γ_2 can be

written as

$$|\Gamma|^2 = \left| \frac{2\Gamma_2 S - j\omega(1+\Gamma_2)R}{2S + j\omega(1+\Gamma_2)R} \right|^2 = \frac{\omega^2 |RU - ST|^2}{|2SU|^2 + \omega^2 |RU + ST|^2} \tag{3.9}$$

This result has to be consistent with the equation (3.5). Therefore zeros of $(RU - ST)$ must be equal to ν_n. If the two subsets of layers are separated using a spacer such that the reflection coefficient due to the second subset can be written as $\Gamma_2' = \Gamma_2 exp(-j2\theta)$, the transmission in pass-bands will be suppressed. Assuming a constant θ of $\pi/2$, the magnetite of reflection coefficient in this case can be computed from

$$|\Gamma|^2 = \frac{\omega^2 |RU - ST|^2 + \omega^4 |RT|^2}{|2SU + \omega^2 RT|^2 + \omega^2 |RU + ST|^2} \tag{3.10}$$

The reflection coefficient vanishes at a certain frequency only if both $(RU - ST)$ and (RT) are zero at that frequency. This is not possible since zeros of $(RU - ST)$ are ν_n^2 and zeros of (RT) are selected to be ω_n^2.

In practice, the phase shift between the two layers depends on frequency. However, as will be shown here, a $\lambda/4$ segment of transmission line at the center frequency of the filter can provide enough phase shift over a relatively wide frequency band to prevent unwanted pass-bands. Fig.3.16 shows the circuit model of one such design with 5 LC layers and a quarterwave spacer. This circuit shows a 5-pole band-stop response with no unwanted pass bands as plotted in Fig.3.17. As mentioned before the position of all poles can be selected independently. In this example the poles are distributed with uniform distance over the bandwidth. As seen in the graph, a $-20dB$ bandwidth of better than 5 to 1 is achieved.

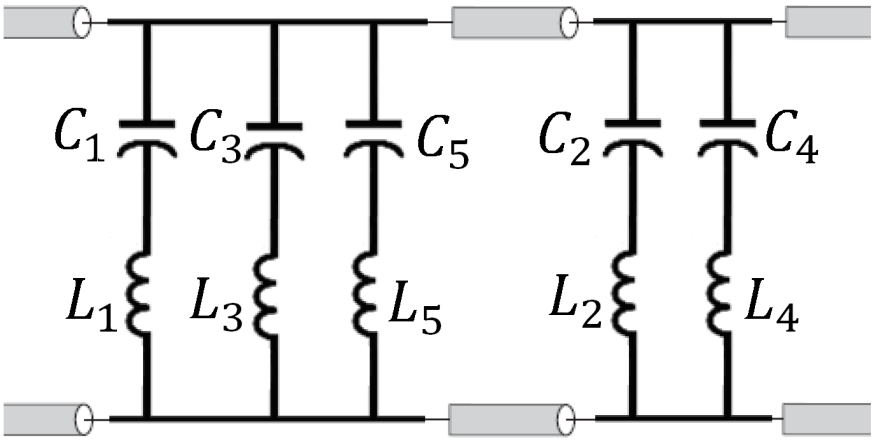

Figure 3.16: The circuit model of the cascaded 5 MEFSS layers separated with only one quarter wavelength spacer

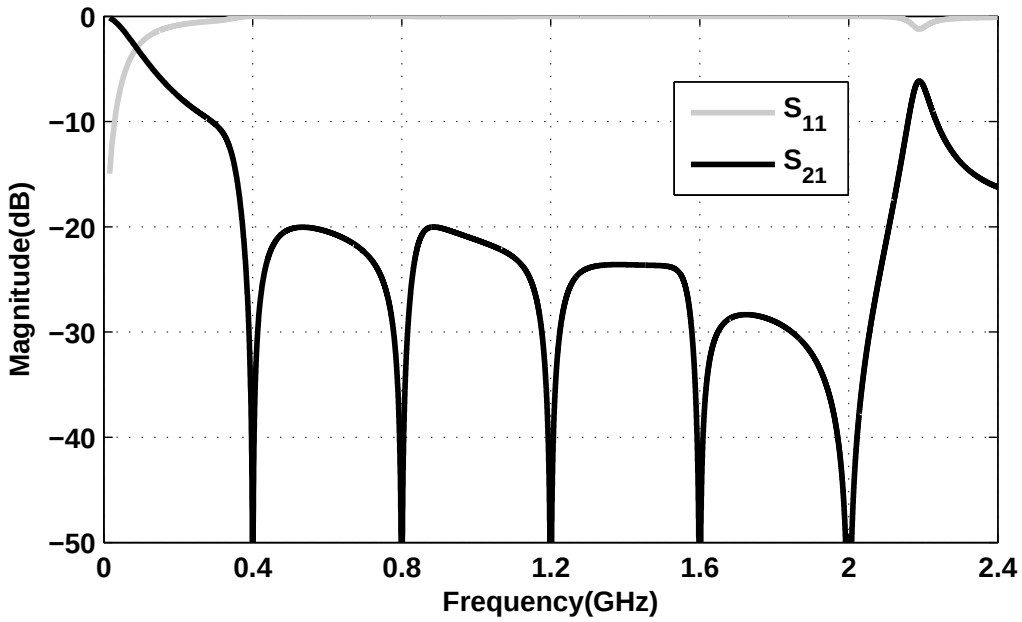

Figure 3.17: The frequency response of the cascaded MEFSS with 5 layers based on the circuit model shown in Fig.6. The circuit elements are calculated using equation (3.8) for uniformly distributed poles between 0.4GHz and 2GHz

As shown in Fig.3.17, the out of band rejection of the designed five pole filter is very poor. This is a common characteristic of wide band filters that are realized using $\lambda/4$ transmission line sections. This configuration is particularly useful for applications where out of

band properties of the FSS are not important. The transparent antenna system that was discussed earlier is an example. However if a relatively narrow bandwidth ($\sim 25\%$) is desired, the out of band properties of the filter improves dramatically. This is a common property of shunt element filters as was discussed before. Fig.3.18 shows the frequency response of a 3 layer filter that was designed with the proposed method. A genetic algorithm was used to determine the position of the poles and the free unknowns (K_i) to achieve more than 10dB insertion loss inside the stop band (0.88GHz-1.14GHz) and more than 10dB return loss in the pass band (below 0.828GHz and above 1.2GHz). As seen in the graph, the proposed cascaded filter has a wider stop-band than the standard Inverse-Chebyshev filter of the same order while having the same pass band. Although the Inverse-Chebyshev filter shows lower insertion loss outside the stop band, it requires realization of series elements with MEFSS structures which is extremely difficult. Therefore, the shunt element realization of the filter must be used. Fig.3.19 and Fig.3.20 show the response of the shunt element realization of the Chebyshev filters of type I and II and the Elliptical filter. All filters were designed to have at least 10dB insertion loss in the stop band of the proposed cascaded filter and more than 10dB return loss in its pass band. As seen in the graphs, all standard filters except for the Inverse-Chebyshev filter fail to maintain the desired characteristics when realized using only shunt elements. This is due to the fact that the transmission line sections act close enough to ideal impedance invertors only at a very small bandwidth ($\sim 10\%$) around the center frequency. Fig.3.21 shows the circuit models of the filters that were used for comparison. Note that the Inverse-Chebyshev filter uses more transmission line sections and its inner layer is much more complicated than the proposed cascaded filter. Therefore the proposed cascaded filter clearly outperforms all traditional filters when the MEFSS realization of the filter is intended. The values of L_1 to L_3 for the cascade filter are $66.61nH$, $17.35nH$ and $52.91nH$ with C_1 to C_3 of $0.474pF$, $1.457pF$ and $0.382pF$ respectively. All stages of the standard filters used have resonant frequencies of 1GHz therefore we only report the inductances. For the standard Chebyshev filter, $L_1 = L_3 = 13.69nH$ and $L_2 = 19.35nH$.

For the Inverse-Chebyshev, $L_1 = L_3 = 48.9nH$, $L_2 = 24.63nH$ and $L_2' = 1.170nH$, and for the elliptic filter, $L_1 = L_3 = 22.66nH$, $L_2 = 48.11nH$ and $L_2' = 4.50nH$.

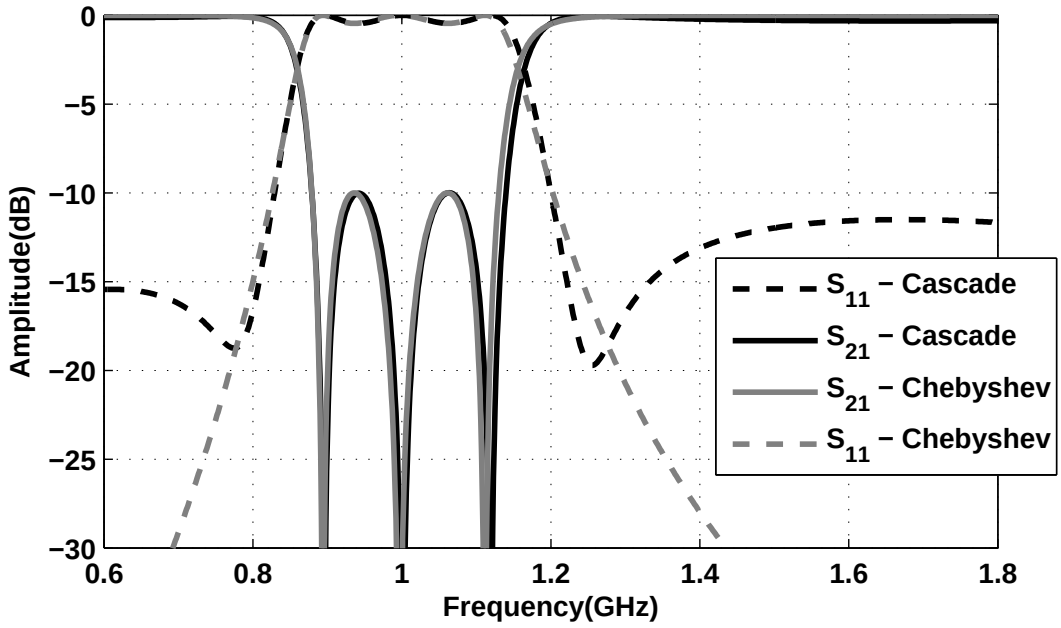

Figure 3.18: Comparison of the proposed cascaded 3-pole filter with the ideal Inverse-Chebyshev filter

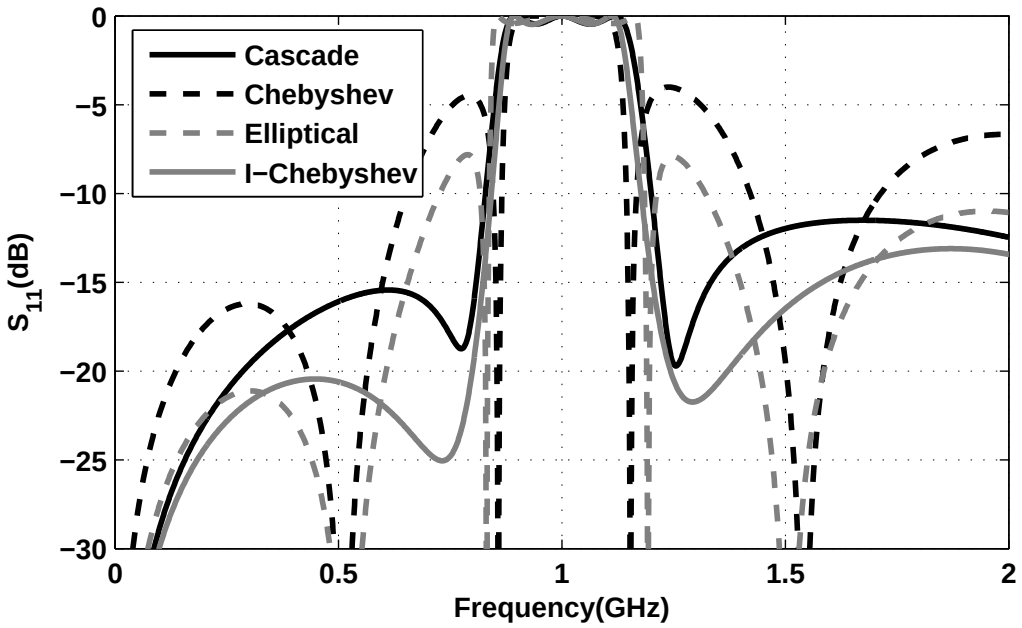

Figure 3.19: S_{11} of the Cascade 3-pole filter (Fig.3.21.a) and the shunt element realization of the Chebyshev filter (Fig.3.21.b,) the Inverse-Chebyshev filter (Fig.3.21.c) and the Elliptical filter (Fig.3.21.c)

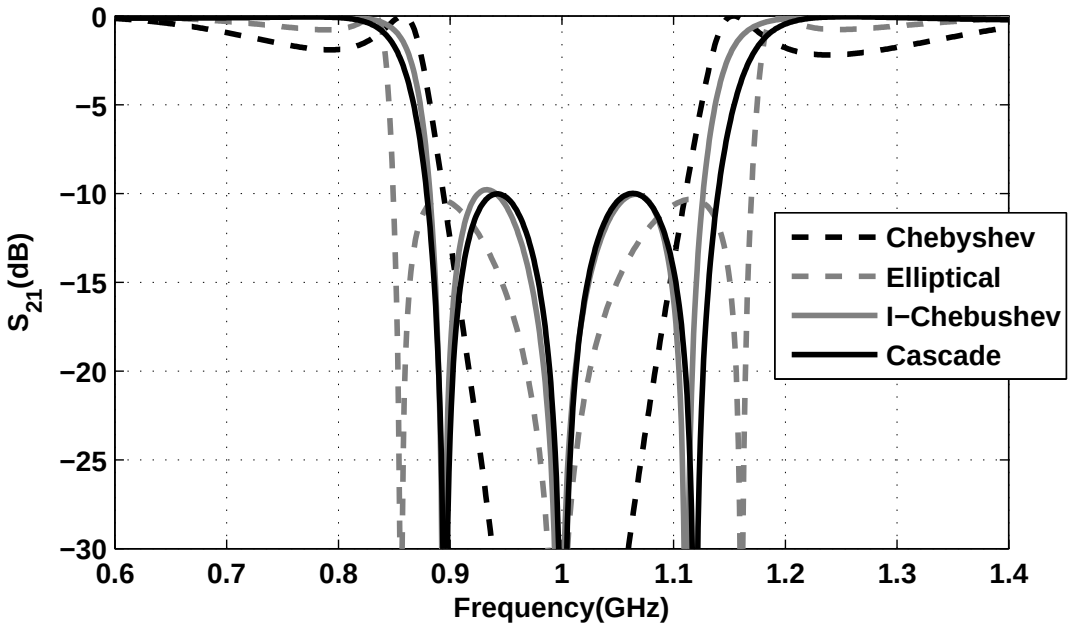

Figure 3.20: S_{21} of the Cascade 3-pole filter (Fig.3.21.a) and the shunt element realization of the Chebyshev filter (Fig.3.21.b,) the Inverse-Chebyshev filter (Fig.3.21.c) and the Elliptical filter (Fig.3.21.c)

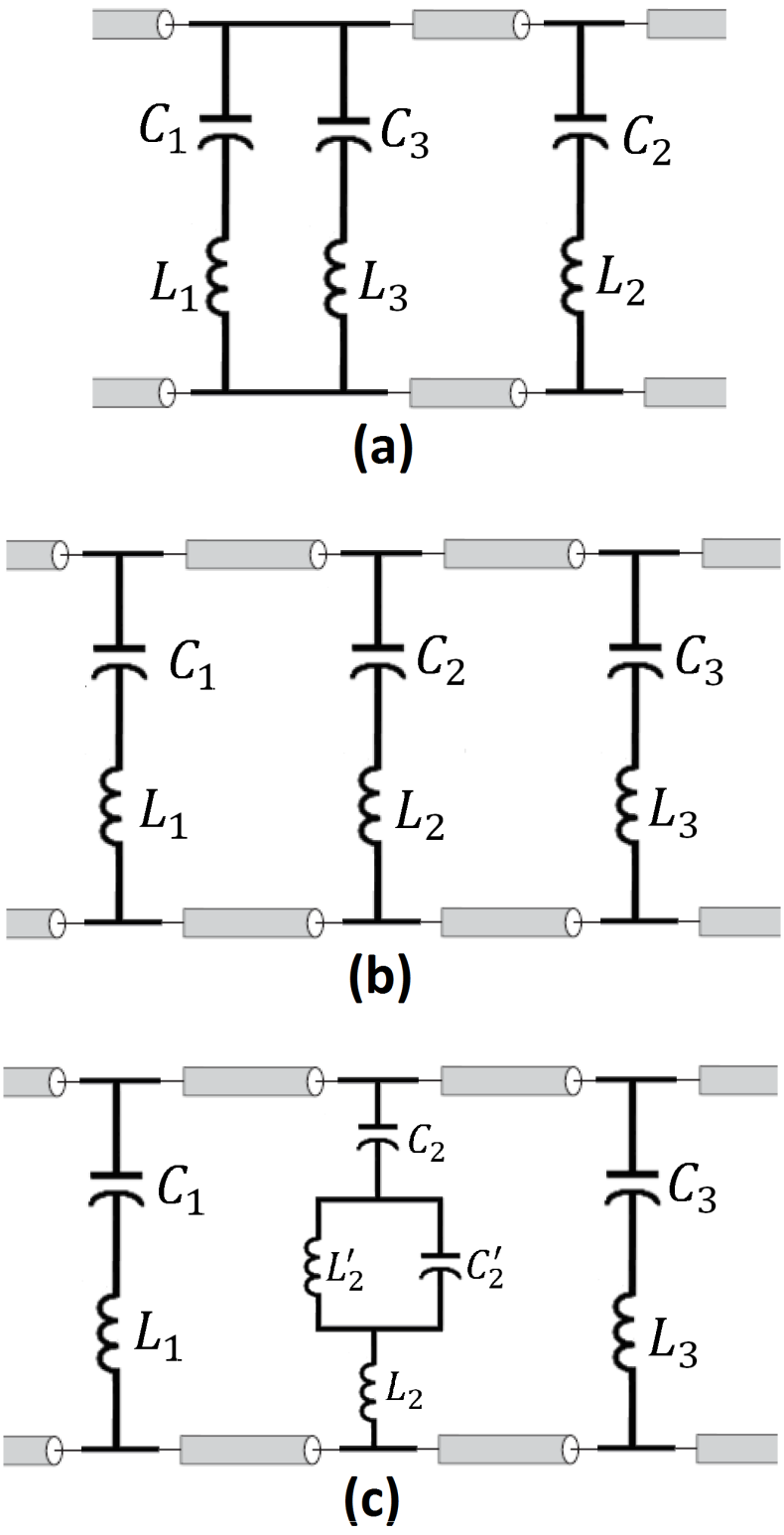

Figure 3.21: The circuit models of a) the cascade filter, b) the Chebyshev filter and c) the Elliptic and Inverse-Chebyshev filters.

3.5 Design and Optimizatin of Transparent BSGP

Design of transparent ground plane is accomplished by designing MEFSS layers on transparent substrates (glass, polycarbonate, polyester, etc.). The number of layers is determined by the required bandwidth of the equivalent ground plane and the level of reflectivity (within the stop-band) and transmissivity (outside the stop-band) in addition to the requirement on the layer opacity. The filter characteristics are the poles and zeros as discussed before which are in turn determined from the characteristics of individual layers. Once the circuit model of the desired MEFSS is determined, the design parameters of each layer (i.e. periodicity, gap size, etc) can be identified. However, extracting the design parameters from the capacitor and inductor values of the circuit model is not straightforward. The equivalent circuit of a one layer MEFSS can be found numerically by matching the response of the circuit model and full-wave analysis of the MEFSS. The inverse problem can be solved using iterative methods to the desired accuracy and therefore the design parameters of all layers can be found. However, because of parasitic capacitances and mutual inductances between the adjacent layers, the design parameters found using this method will not be the optimal values. Nevertheless, the MEFSS designed using this method is expected to be very close to the optimal one since the coupling between the layers can be kept small by introducing a lateral shift between the two consecutive layers of the FSS. Also the initial design can be used as a start point for further optimization of the entire structure using full-wave simulations.

For antenna applications, the out of band characteristic of the equivalent ground plane (reflector)is not of significant importance. Relaxing the out of band behavior of the transparent ground plane (multi-layer MEFSS,) the accurate placement of the poles of the filter is not necessary so long as a minimum insertion loss in the band-stop is obtained. Hence, the poles should be placed as far away from each other as possible to result in the widest band. The maximum separation of the poles is limited by the realizable values of capacitors and inductors.

3.6 Fabrication and Measurement

shows a simple one-layer Loop-Loop ground plane that is fabricated on a 2.33mm thick FR-4 substrate using conventional printed circuit board technologies. Fabrication on a transparent substrate is significantly more expensive. For this reason the initial verification is done using an opaque substrate. The spacing between the loops and the unit-cell size is designed such that the structure acts like a ground plane with a center frequency of 350MHz frequency if placed inside a glass window.

In order to achieve accurate results, the size of the ground plane must be large compared to the wavelength to reduce the effect of diffractions from the sides of the ground plane. The ground plane that is fabricated is intended to be used in the fabricated armored window with dimensions of 30.5 cm by 61 cm, or $.3\lambda$ by $.6\lambda$ at 300MHz. If this ground plane is placed between two antennas for characterization, the frequency response of the ground plane is significantly influence by the diffraction from the edges of the ground plane. A larger ground plane is required to obtain accurate results. In order to increase the dimensions of the ground plane, a 121 cm by 91 cm ground plane made of aluminum foil was fabricated. A 61 cm by 61 cm square was cut out of the aluminum ground plane and was replaced with two adjacent transparent ground planes over FR4 substrate as shown in Fig.4-3.

The window glass that is placed on the ground plane has a notable impact on the capacitance between the adjacent sides of the loops and therefore shifts the stop-band of the ground plane to lower frequencies. This effect is considered in the fabricated design. However, the glass and polycarbonate layers are extremely heavy which makes it difficult to include the window layers when measuring the response of the ground plane. Fortunately, the ground plane shows the same behavior, even in the absence of the window layers, at a higher frequency.

Fig.4-2. shows the schematic of the measurement setup that was used to measure the frequency response of the ground plane. The setup consists of two log periodic antennas as transmitter and receiver antennas and the fabricated ground plane which is placed in the

line of sight of the antennas. Fig.4-4. shows the transmission coefficient between the two log periodic antennas in the presence of the ground plane, calibrated by the transmission coefficient between the antennas in the absence of the ground plane. This value can be used as an estimate for the transmission coefficient of the ground plane. The approximation is due to the fact that the ground plane is not infinite and the incident wave is not a plane wave. The simulated transmission coefficient for an infinite ground plane with the same unit cell size and spacing as the fabricated ground plane is also shown in Fig.4-4 for comparison. It is seen that the results have a very good agreement at higher frequencies but there is a notable difference between measurement and simulation at lower frequencies. The reason is at lower frequencies, the size of the ground plane becomes comparable to the wavelength. Therefore the effect of diffraction from the edges becomes more significant. There is a 20MHz difference between the measured and simulated center frequency results which is due to uncertainties in the dielectric constant of the substrate and the trapezoidal shape of the cross-section of the metallic traces which is an artifact of the chemical etching process. Both of these errors are systematic for the most part and can be accounted for in the design stage.

The proposed multilayered technique was also used to design a three layer wideband transparent ground plane with the center frequency of 550MHz. Each layer consists of an array of square loops. All three layers have the same line width of $w = 0.2mm$, and periodicity of $T = 46mm$. The opacity of the three layer design is 2.6%. The gap sizes of the three layers are $g_1 = 1.47mm$, $g_2 = 0.3mm$ and $g_3 = 0.91mm$. The spacing between the first and second layer is filled with a polyester sheet with the thickness of $d_1 = 0.5mm$ and dielectric constant of $\epsilon_{r1} = 3.2$. A slab of glass with the thickness of $d_2 = 50.8mm$, the dielectric constant of $\epsilon_{r2} = 7.75$, and the loss tangent of 0.0037 (soda-lime glass) is used between the second and third layers. Fig.3.23 shows the simulated reflection and transmission coefficient of the designed BSGP. As shown in the graph, an insertion loss of more than 20dB is achieved at 290MHz to 810MHz and a return loss of less than 0.1dB is

achieved at 320MHz to 770MHz.

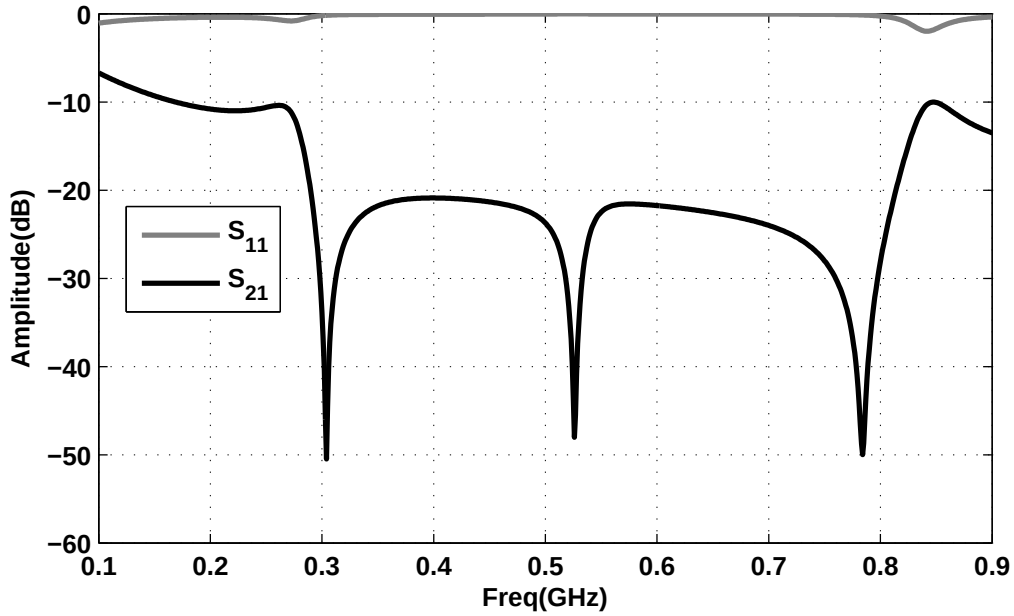

Figure 3.22: Simulated frequency response of the designed BSGP

The total thickness of the designed ground plane is about 5cm which makes it suitable for placement in typical armored windows with glass thicknesses ranging from 10cm to 12cm. However, experimental validation of the designed BSGP is difficult because of its size and weight. To reduce the cost and size of the measurement setup, a smaller ground plane with the center frequency of 5.75GHz is designed and fabricated. The geometry of this design is the same as the ground plane described above with the design parameters of $w = 0.2mm$, $T = 8mm$, $g_1 = 1mm$, $g_2 = 0.25mm$ and $g_3 = 0.54mm$, $d_1 = 0.25mm$, $d_2 = 5mm$. The polyester layer can be bounded to the glass sheet using a frame that is holding both sheets. The size of the fabricated ground plane is $30cm$ by $30cm$ with 37 unit cells on each side. The insertion loss through the BSGP was measured by placing the ground plane between two horn antennas and measuring the spectral response of the transmission coefficient between the two antennas in the presence and absence of the ground plane. Fig.2.60 shows the receiving horn antenna and the fabricated BSGP placed close to it. The transmitting horn antenna is at a far enough distance so that the incoming radiation

can be approximated by a plane wave. Fig.3.24 shows the measured and simulated transmission coefficient of the surface. As shown in the graph, a 10dB insertion loss is acherived at 3.2GHz to 8GHz. The slight difference between the measurement and simulation results is due to the near field interaction of the finite sized BSGP with the adjacent antenna which creates the observed fluctuations in the measured frequency response.

Fig.3.25 shows the logo of the University of Michigan as seen from behind the fabricated ground plane. The metallic traces are fabricated using silk printing on polyester and glass using a silver based conductive ink. The minimum trace width that can be achieved using this method of fabrication is $0.2mm$ which is the main limiting factor in reducing the opacity of the final design (30%). As seen before, tt lower frequencies, the unit cell size of the structure will be much larger while keeping the line width the same ($0.2mm$). Therefore the opacity will be reduced to only a few percents. In addition, the minimum line width limit can be reduced to $5\mu m$ by employing more precise methods of fabrication such as depositing metal on a transparent substrate using a combination of sputtering, electroplating and chemical etching. Hence opacity values as low as a few percents is achievable up to W-band.

Figure 3.23: Measurement Setup. The transmitting antenna is placed far enough for the plane wave approximation to be fairly accurate.

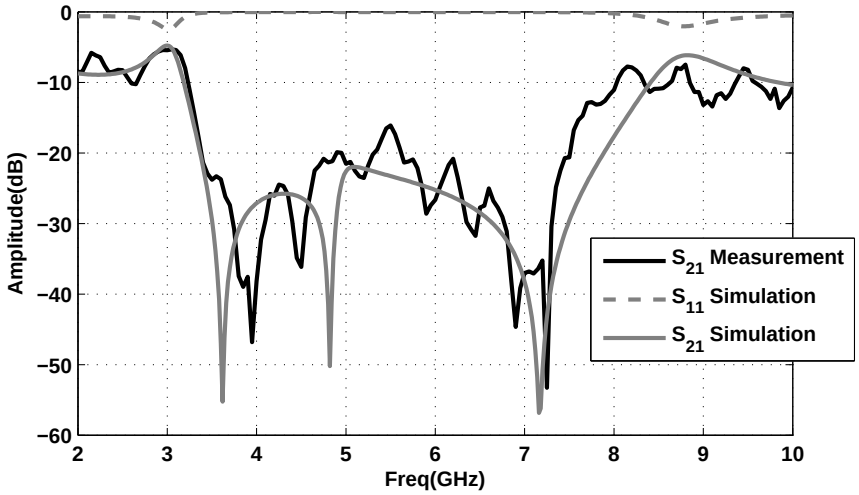

Figure 3.24: Comparison of the measured S_{21} of the fabricated 3 layer ground plane with the HFSS results

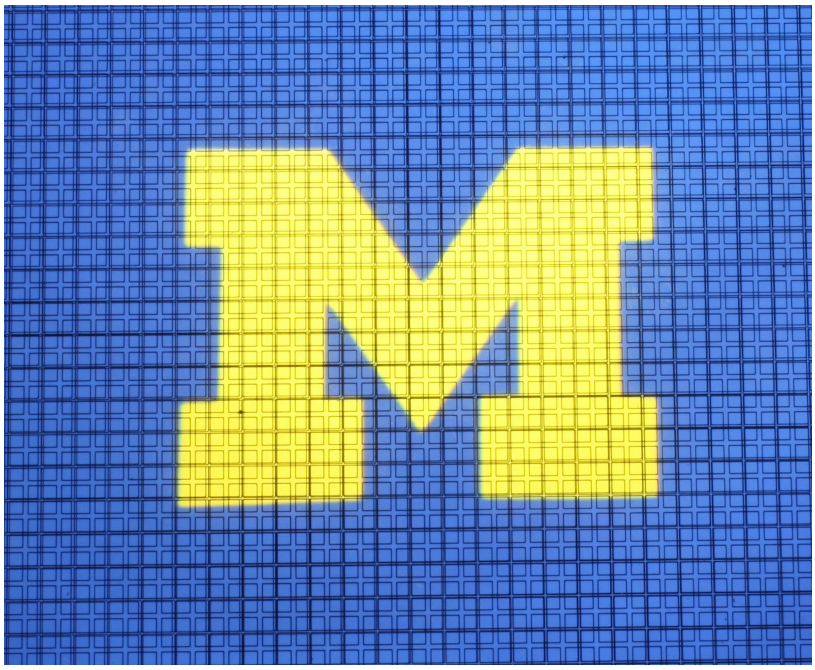

Figure 3.25: To show the optical transparency of the proposed design, the logo of the University of Michigan is placed behind the fabricated ground plane. The opacity is almost 30%.

3.7 Conclusion

In this chapter, the band-stop performance of existing miniaturized element frequency selective surfaces was investigated. A simple MEFSS based on square loop unit cells was introduced and the challenges associated with using this design as a reflector for antennas at UHF anf VHF bands were presented. It was shown that the bandwidth of the structure is limited at the target frequency bands because of difficulties in fabricating extremely small gaps between metallic traces to create large enough capacitors.

Following the basic studies, a novel design with overlapping capacitors was introduced that requires fabrication of square loops on the opposite sides of a very thin transparent substrate. It was shown that the novel design can be used to drastically increase the capacitors between the adjacent loops and hence the bandwidth of structure.

In addition to the single-pole design, a multi-pole stop-band miniaturized MEFSS was introduced that consists of multiple layers of single pole MEFSS. It was shown that the proposed method allows achieving a wide-band multi-pole response while maintaining a relatively small thickness which renders the design to be light and independent of the angle of incidence. A three pole transparent BSGP was designed using the proposed method and a 10dB insertion loss bandwidth of 2.5 to 1 was demonstrated.

CHAPTER 4

A Full-duplex Repeater for the 2400 MHz ISM Band

4.1 Introduction

Radio repeaters are used in complex environments to mitigate the adverse effects of the communication channel such as non-line-of-sight and multipath fading. In addition, they can be used in environments closely resembling free space to simply extend the range of communication without requiring high power transmission [101].

For simplicity, let us assume the case of free space with all repeaters having transmit and receive antenna gains of G_t^{ant} and G_r^{ant}, respectively, and an active gain of G^{amp}. The signal that is received by the ith repeater along the path is therefore given by:

$$\begin{aligned} P_f^i &= P_f^{i-1} + 20log(\frac{\lambda}{4\pi}) + G_t^{ant} + G_r^{ant} + G^{amp} - 20log(R_i) \\ &= P_f^{i-1} + \mathcal{G}^i \end{aligned} \tag{4.1}$$

where $\mathcal{G}^i$ is the total power gain from repeater $i-1$ to repeater i and R_i is the distance between the repeater i and $i-1$. In addition to the forward transmission, there is an unwanted backward propagation due to the backlobe of the antennas. This back-propagation is not to be confused with the desired backward communication when a two-way link is required. Since the repeaters are directional, supporting a two-way link requires two separate sets

of repeaters for forward and backward communication. This case will be addressed separately. Assuming front-to-back ratios of F_t and F_r for the transmit and receive antennas of all repeaters, the amount of back propagation signal received by the repeater i is given by

$$P_b^i = P_f^{i+1} + \mathcal{G}^{i+1} - F_t - F_r \tag{4.2}$$

The back-propagation signal creates feedback and can cause the repeater pair to go to oscillation. To avoid oscillation, P_b^i must be smaller than P_f^i which ensures a loop gain of less than $0dB$ for the feedback loop. Moreover, since the repeaters are usually placed several wavelengthes apart from each other, the back-propagating signal and the main signal have no correlation and therefore the back-propagating signal is essentially noise and must be significantly lower than the front propagating signal. For a signal to noise ratio of $20dB$, that is $2\mathcal{G}^i - F_t - F_r < -20dB$. Ideally $\mathcal{G}^i$ is kept at $0dB$ to ensure all the repeaters receive the same power and the signal level does not decay along the path. To satisfy this condition, a front-to-back ratio of better than $10dB$ for the antennas is required.

If unidirectional repeaters are used, the front-to-back ratios are negligible. Therefore $\mathcal{G}^i$ must be kept below $-10dB$. This constraint renders the entire repeater network useless in close to free space conditions since the power received at the repeater i from the repeater $i-1$ is $P_f^i - 10dB$ but the power received from repeater $i-2$ is $P_f^i - 6dB$ assuming equal distances between all repeaters. Therefore adding the repeater $i-1$ does not improve the signal received by the repeater i and so on. Unidirectional repeaters are still useful in complex environments where a direct line of sight between repeaters $i-2$ and i does not exist or the path loss is significantly more than that of free space due to multipath fading or other undesired effects. However, because of the above constraint on $\mathcal{G}^i$, which is still valid in complex environments, the signal-to-noise ratio will be reduced by $10dB$ every time the signal is passed through a repeater. This fact severely limits the performance of the repeater network in practical scenarios.

In view of the mentioned performance deficiencies of the omni-directional repeaters, a directional repeater configuration is considered. However, in this case a separate set of repeaters is needed to establish a two-way link between different communication devices in the system. There are many ways to accomplish this without causing the entire system to go to oscillation. Considering the simple one-dimensional case mentioned above, each backward link repeater can be placed in between two forward link repeaters and with equal distance from both repeaters. A similar analysis to what was presented above shows that the cross talk between the two links will not cause oscillations in the system if $F_t + F_r > 6dB$.

In this chapter, a directional repeater system operating at the 2.4 GHz ISM band is discussed. A number of designs with different levels of isolation between the transmit and receive antennas are reported. The massive improvement in isolation is achieved by separating the antennas by a ground plane in between and also creating a polarization mismatch between the two antennas. This technique exploits the fact that most mobile platforms that use the ISM band to communicate are designed to be able to transmit and receive in both vertical and horizontal polarizations. In addition, a two element receiver array is proposed that further decreases the coupling using near-field cancellation.

4.2 Repeater Design

The main challenge in designing a high gain radio repeater, simply composed of Tx and Rx antennas and an amplifier, is establishing a good isolation between the transmitter and receiver antennas. In order to achieve high levels of isolation between the two antennas a number of steps are proposed. Back-to-back patch element antennas separated by a common ground plane is chosen. This allows for the design of a directional repeater with inherent isolation provided by the ground plane. In fact infinite isolation can be achieved if the ground plane is infinite in extent. In practice it is desired to minimize the size of the repeater and as such the ground planes are finite and designed to be as small as possible.

Depending on the size of the ground plane, there exists a magnetic field circling around the ground plane which is the main source of coupling to a patch element placed on the opposite side. The magnetic field distribution around a patch antenna with a finite ground plane is shown in Fig.4.1. As seen in the graph, the magnetic field does not vanish in the shadowed area behind the patch antenna and a second antenna placed in the shadowed region will have a finite coupling with the original antenna.

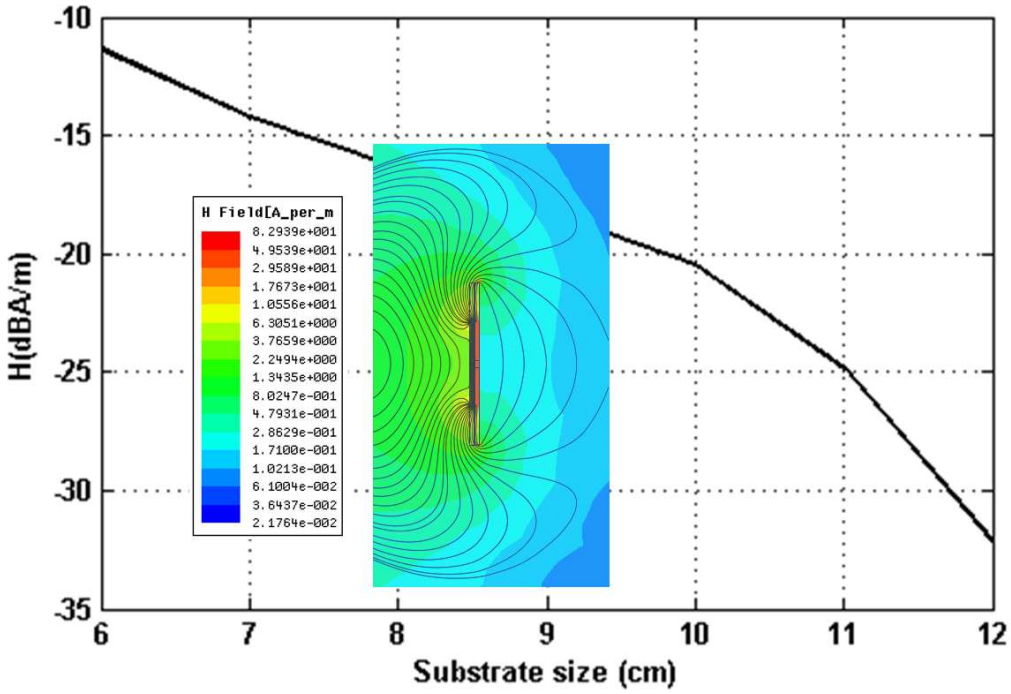

Figure 4.1: Magnetic field of a double stacked pin-fed patch antenna with a finite ground plane measured at the center point at the back of the ground plane plotted as a function of the ground plane size. The magnetic field does not vanish in the shadowed region behind the ground plane due to circulating magnetic field. If the receiver antenna is placed in this region parallel to the transmit antenna, the two antennas will have a finite amount of mutual coupling

Fig.4.2a shows the geometry of a unidirectional repeater utilizing vertically polarized patch antennas as both transmitter and receiver. The patch antennas are printed on a 1.6 mm thick substrate with dielectric constant of 2.2 and are backed by an 8cm by 8cm ground plane, keeping the size of the repeater relatively small. As a result of maintaining small dimensions for the ground planes, the coupling between the two antennas is as high as -30

dB as seen in Fig.4.2a. This only allows for a 30 dB active gain before the amplifier starts to oscillate.

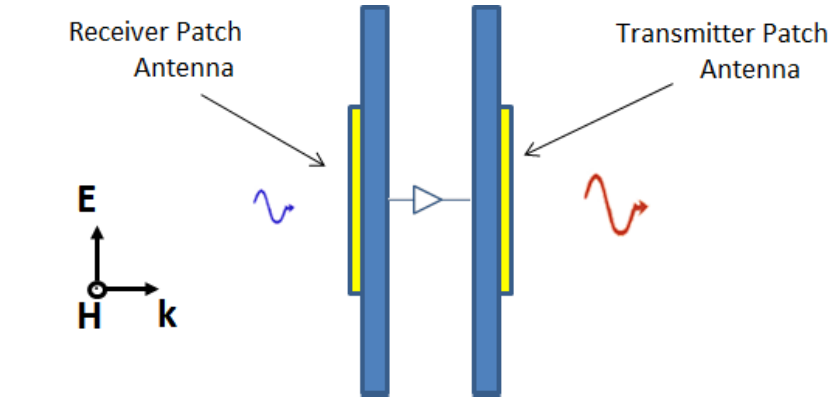

(a) Geometry

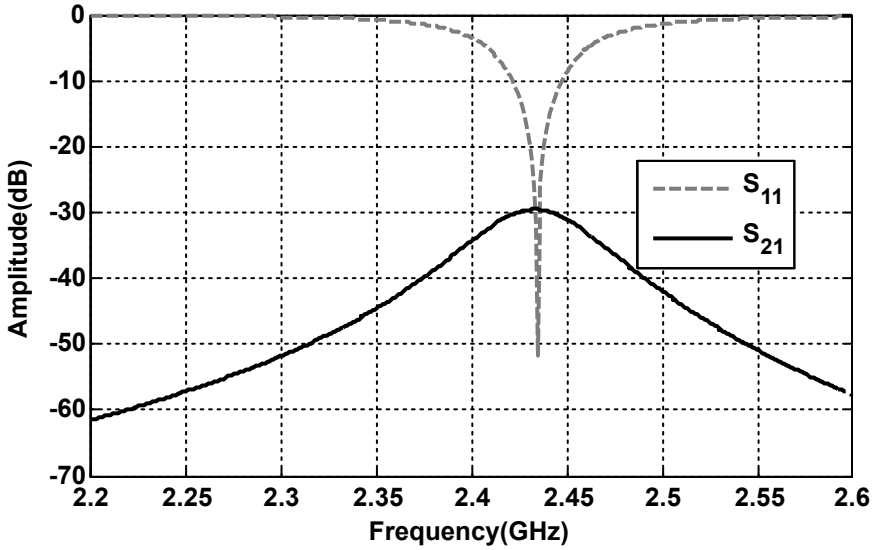

(b) Simulation results

Figure 4.2: Two patch antennas placed on opposite sides of a common ground plane. The isolation between the two antennas is only 30dB close to the resonant frequency of the antennas.

The coupling between the transmitter and receiver antennas will be reduced significantly if they are placed perpendicular to each other, one having a vertical polarization and the other one having a horizontal polarization. However, horizontal transmission in near ground applications suffers from a significantly higher path loss than vertical polarization. Therefore the mentioned arrangement is not practical. Nevertheless, by rearranging the antennas as shown in Fig.4.3a, the coupling can be reduced without significantly increasing

the path loss. In this configuration both transmitter and receiver patches are tilted 45°in the plane of the patch so that they make a 90°angle with each other and a 45°angle with the normal direction to the earth. Both vertical and horizontal polarizations are excited equally by both patches.

Sufficient care must be taken while using this configuration in a practical scenario since the signal polarization undergoes a 90°change when going through each repeater along the repeater chain. Most commonly used platforms (cellphones, mobile robots, surveillance cameras, etc.) that would communicate through the repeater network do not operate in pure horizontal or vertical polarization and therefore are able to communicate with the repeater in either polarization. For this reason, the change in polarization does not impact the network connectivity. However, in cases where the repeaters are placed in proximity of the ground at a lower height than two times the wavelength, communication in horizontal polarization is immensely compromised due to interference with ground reflections. In such cases, the repeater must be tilted 45°with respect to the ground in plane of the patch so that both receiver and transmitter antennas operate in both vertical and horizontal polarizations. In the worst case scenario, since the repeater is close to the ground, the horizontal polarization does not reach the next repeater in line and the received signal is purely vertical. Hence the path loss is 3dB more than the case where pure vertical polarization is transmitted. In addition, the receiver antenna makes a 45°angle with respect to the vertical direction which creates an additional 3dB loss due to polarization mismatch. As a result, the overall improvement is 6 dB less than the case where the repeater is placed well above the ground.

As shown in Fig.4.3b the coupling between the two antennas is reduced to -67 dB, allowing for a maximum of 67 dB active gain in the repeater. Moreover, since the patch antennas are unidirectional, they each have a passive gain of 3.6 dBi with the polarization mismatch taken into account. This brings the maximum gain of the repeater to 74 dB. There is a valley in the value of coupling between the two antennas at the resonant frequency of the antennas. The reason for this decrease in the coupling is that the polarization purity of

the patch increases at the resonant frequency which in turn reduces the coupling between the receiver and transmitter patch antennas.

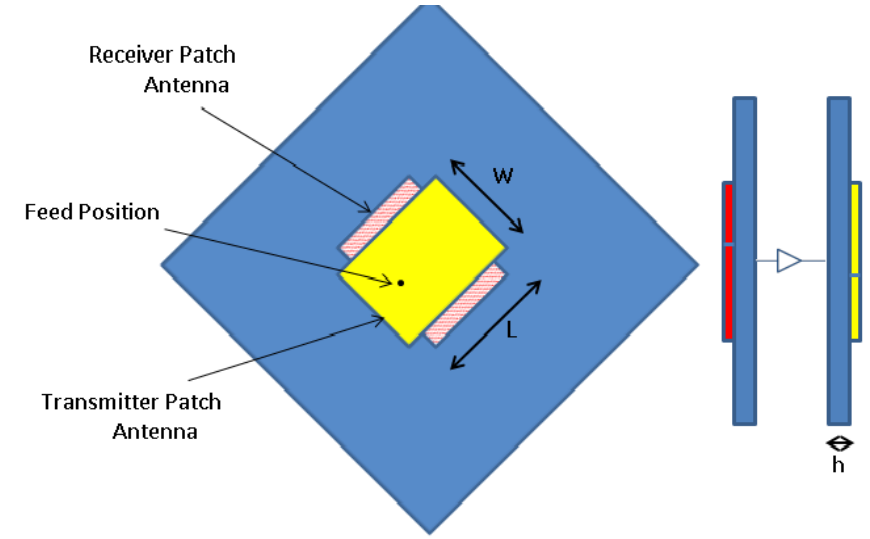

(a) Geometry

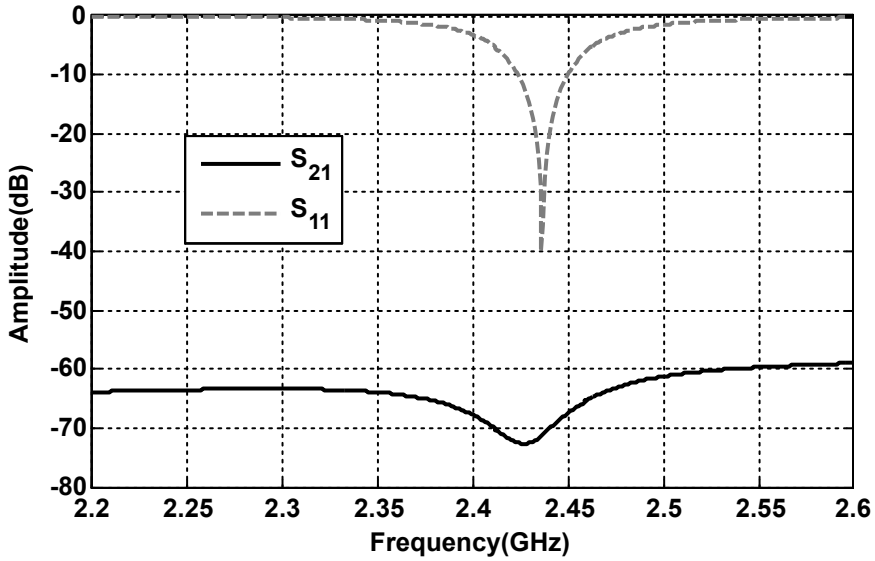

(b) Simulation results

Figure 4.3: Two patch antennas placed on opposite sides of a common ground plane. The patches are rotated such that they make a 90°angle with each other. The isolation between the two antennas is drastically increased as a result of the polarization mismatch between the antennas.

Fig.4.3b shows the input impedance matching of both patches as well as the coupling between them. In this design, an 8cm by 8cm substrate with the thickness of h = 1.6 mm and dielectric constant of 2.2 is used. The patch dimensions are W = 30 mm and

L=40mm and the feed position is selected to match the input impedance of the antenna to 50Ω. As seen in the graph, a 10 dB return loss bandwidth of 22 MHz is achieved. The bandwidth can be increased by increasing the substrate thickness or increasing the Width (W) of the patch. Both of these modifications increase the bandwidth at the cost of also increasing the coupling between the antennas as seen in Fig.4.4. Increasing the thickness of the substrate increases the excitement of surface modes in the substrate that are responsible for the coupling between the two antennas and therefore increases the coupling. Similarly, increasing the width of the patch increases the bandwidth but reduces the polarization purity of the patch as well as the relative size of the ground plane with respect to the patch and therefore increases the coupling between the two antennas.

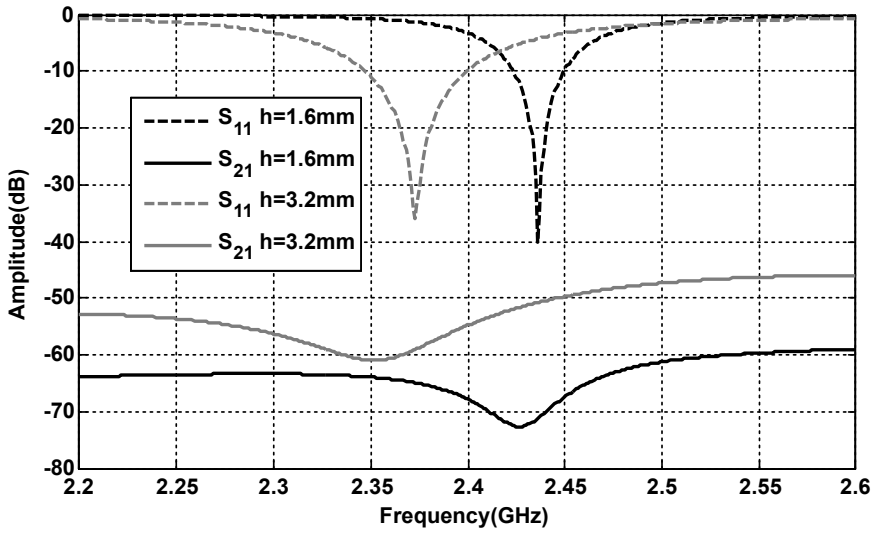

(a) Substrate thickness

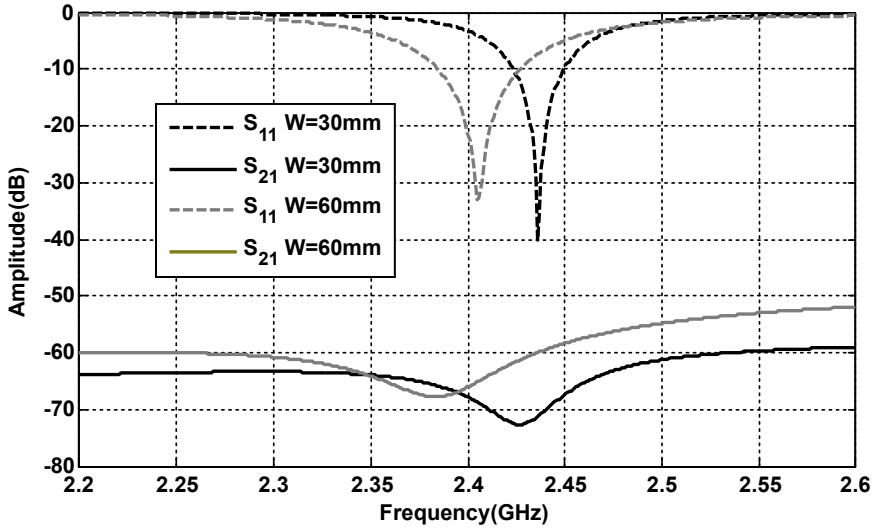

(b) Antenna width

Figure 4.4: The effect of substrate thickness and antenna width on the bandwidth and coupling between the patches. Increasing the substrate thickness or widening the antenna can help increase the bandwidth at the cost of reducing the isolation between the antennas.

The bandwidth of the patch antennas can also be increased by using a microstrip feed instead of a pin feed and inserting an interdigital capacitor section in the path of the feed. The capacitor section offsets the inductive impedance of the patch antenna at a frequency slightly above its resonant frequency and creates a secondary resonance. The design parameters can be optimized to place these to resonant frequencies close to each other to create a wideband response. This geometry and its frequency response are shown in Fig.4.5. Here

a 1.6 mm substrate with dielectric constant of 2.2 is used and the antenna parameters are optimized to maximize the bandwidth. The optimized values are W = 47 mm and L = 37 mm. As seen in the graph, the 10 dB return loss bandwidth is increased to over 100 MHz. However, the coupling between the two antennas is also increased to about -52 dB which is not ideal.

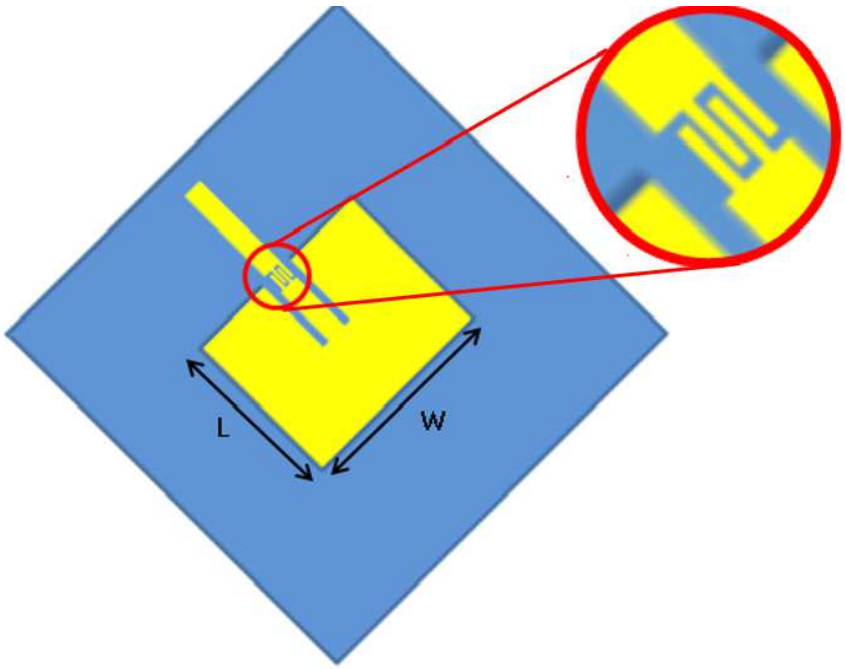

(a) Geometry

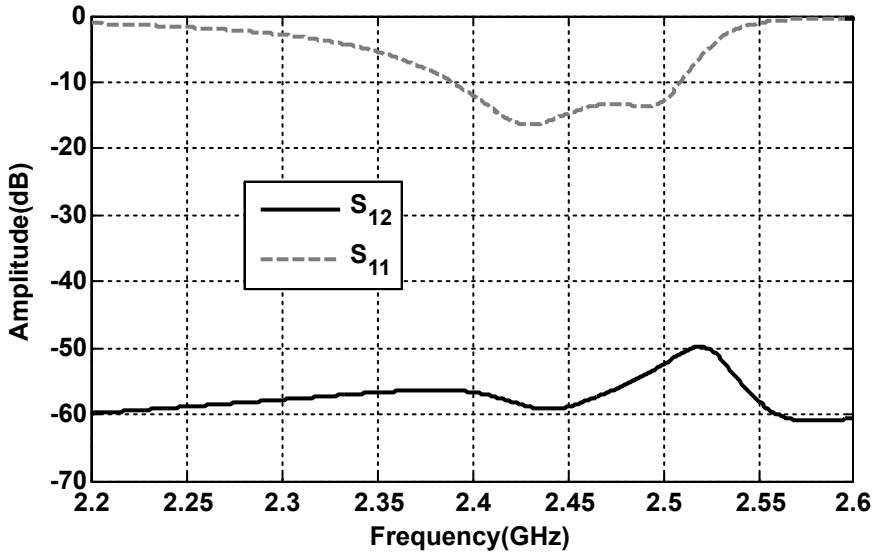

(b) Simulation results

Figure 4.5: The bandwidth of the patch antenna can be increased using a microstrip feed with an interdigital capacitor inserted in the path of the feed. Because of the asymmetry introduced in the design by the mictrostip feed, the coupling between the two antennas increases.

Another technique that can be used to increase the bandwidth of patch antennas is placing a parasitic patch on top of the radiating patch antenna. This geometry is shown

in Fig.4.6. The fabrication of this antenna is more complicated than a single layer patch antenna since the parasitic element and the main patch are fabricated on separate layers. However a wide bandwidth as well as extremely low coupling can be achieved using this technique. Fig.4.7 shows the isolation between the two antennas with and without the polarization mismatch. As seen in the graph, a 40 dB or better improvement in the isolation over the operating band (2.4GHz to 2.5GHz) is achieved by introducing a polarization mismatch between the two antennas. As seen in the graph, a bandwidth of more than 100MHz and coupling of -72dB is achieved using this method which allows for a total gain of 80dB for the repeater assuming a passive gain of 4.0 dBi for each antenna.

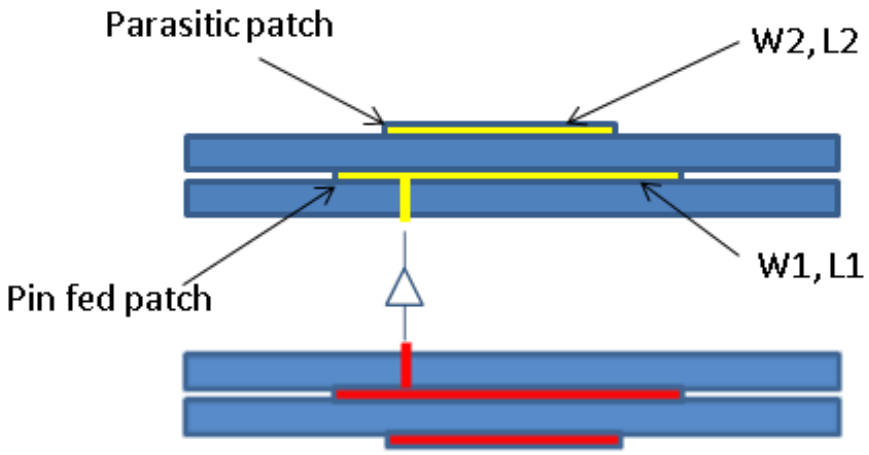

Figure 4.6: Orthogonal arrangement of the Tx and Rx double stacked patch antennas to reduces the front-to-back coupling by creating a polarization mismatch between the antennas. The coupling is unwanted and can cause the system to go to oscillation

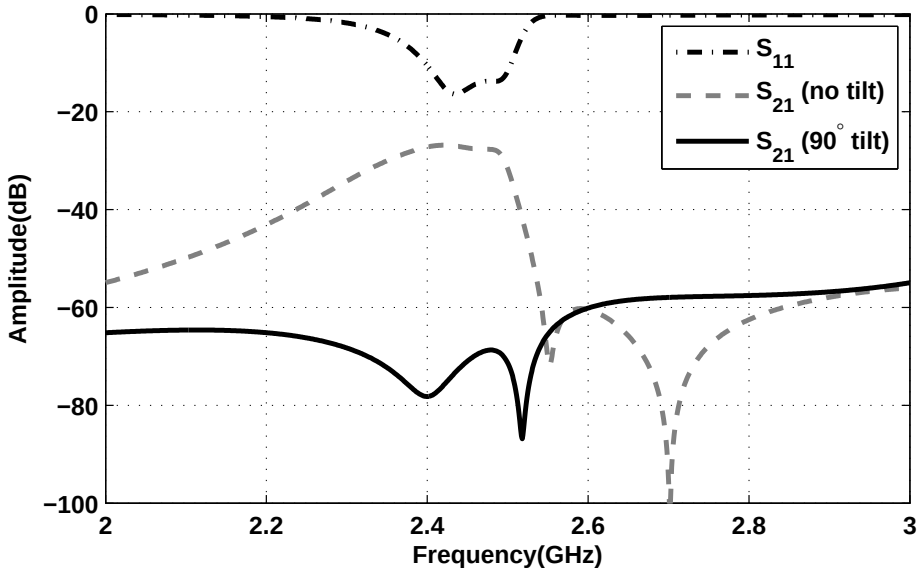

Figure 4.7: Isolation between the two patch antennas with parallel and orthogonal arrangements. Because of the ground plane, there is a 30dB isolation between the two antennas. The orthogonal arrangement of the antennas helps increase the isolation by more than 40dB.

Placing circuit components in between the transmitter and receiver antennas disturbs the near filed of the antennas and can result in less isolation than predicted above. To circumvent these unknown effects, the entire circuitry is placed inside a metallic box in between the two antennas as shown in Fig.4.8. The coupling between the two antennas is slightly affected by placing the metallic box between the two substrates compared to the case where the area between the two substrates is filled with air. The metallic box cannot be avoided since the circuit elements that would otherwise be placed between the two substrates create cross-pol and therefore significantly increase the coupling between the two antennas. However, the coupling is a weak function of the dimensions of the box (a) and the separation between the two antennas (S). These values can be tuned to achieve an isolation level very close to what was achieved in absence of the box. The optimized values are $S = 8mm$ and $a = 8cm$.

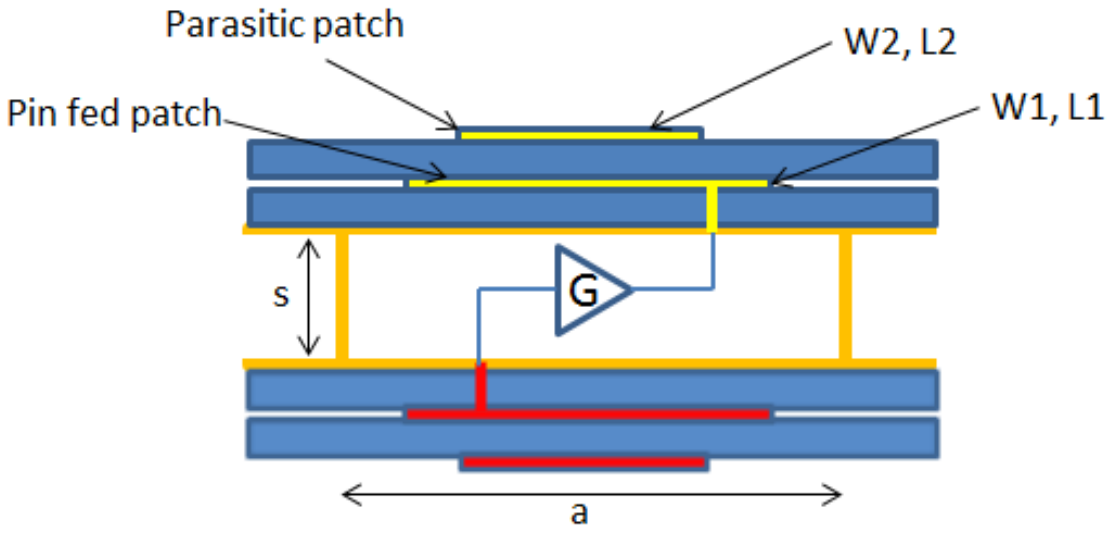

Figure 4.8: Placement of Tx and Rx double stacked patch antennas with a metallic box inserted between the two substrates. The metallic box isolates the internal circuitry of the repeater from the antennas. The box dimensions are tuned to maximize the isolation between the antennas.

The main source of coupling between the two perpendicular patches is the cross-polarized component of the near field of the antennas. Fig.4.9 shows the phase of the normal component of the electric filed when the horizontally polarized patch is excited. As seen in the graph, the phase of this component undergoes a rapid 180°change when crossing the plane of symmetry of the structure. This fact can be used to further reduce the coupling between the two antennas. By using a two-element patch array as the receiver antenna as opposed to a single patch, the array elements can be placed such that they receive out of phase coupling from the transmitter antenna. As a result the coupling between the array antenna and the transmitter antenna can be further reduced. The spacing between the two array elements must be optimized to achieve a 180°phase difference in the received coupling signal by the two antennas. Fig.4.10 shows the proposed geometry where the receiver antenna is replaced with a two-element array. As shown in Fig.4.11, the coupling between the transmitter antenna and each element of the receiver array is more than the case where a single element antenna is used as the receiver. This is due to the fact that array elements are not centered with respect to the plane of symmetry of the transmitter patch. However, the

coupling reduces significantly when the two elements are combined in-phase to form a two-element array. The spacing between the array elements was optimized to achieve the highest isolation within the operating frequency band of 2400MHz to 2500MHz. The coupling between transmit and receive antennas for different values of spacing between the two array elements is plotted in Fig.4.12. The transmitter antenna is kept as before but the array elements are redesigned to have an input impedance of 100Ω and array bandwidth of 100MHz. The design parameters are $W_1 = 21mm, W_2 = 20mm, L_1 = 38.6mm, L_2 = 38.8mm$ and $Y_0 = 9mm$ and the separation between the two back to back substrates is $S = 10mm$.

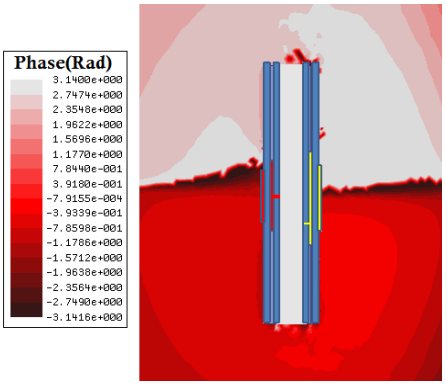

Figure 4.9: Phase of the normal to the plane of the plot (co-pol) component of the electric field when the transmitter patch (right) is excited. There is an abrupt 180°phase shift between the top and bottom halves of the plot that can be exploited to reduce the coupling if a two element array is used as the receiver antenna.

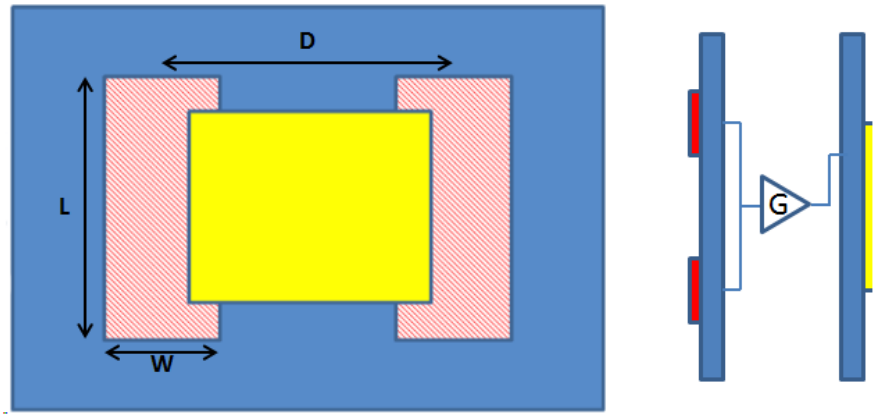

Figure 4.10: The receiver array is placed symmetrically and the elements are fed in phase. In this configuration the coupling between the receiver antenna and the two Rx elements are out of phase and cancel each other.

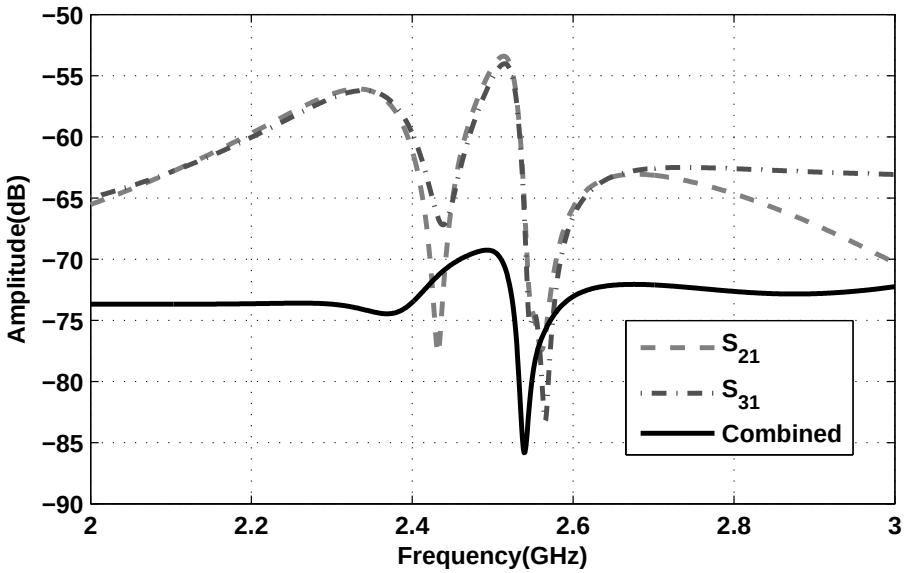

Figure 4.11: Coupling between the transmitter patch and each antenna on the receiver array (dashed lines) and coupling between the transmitter patch and the combined array (solid line). Although each element has more coupling than the original single patch receiver antenna, the combined array coupling is significantly smaller.

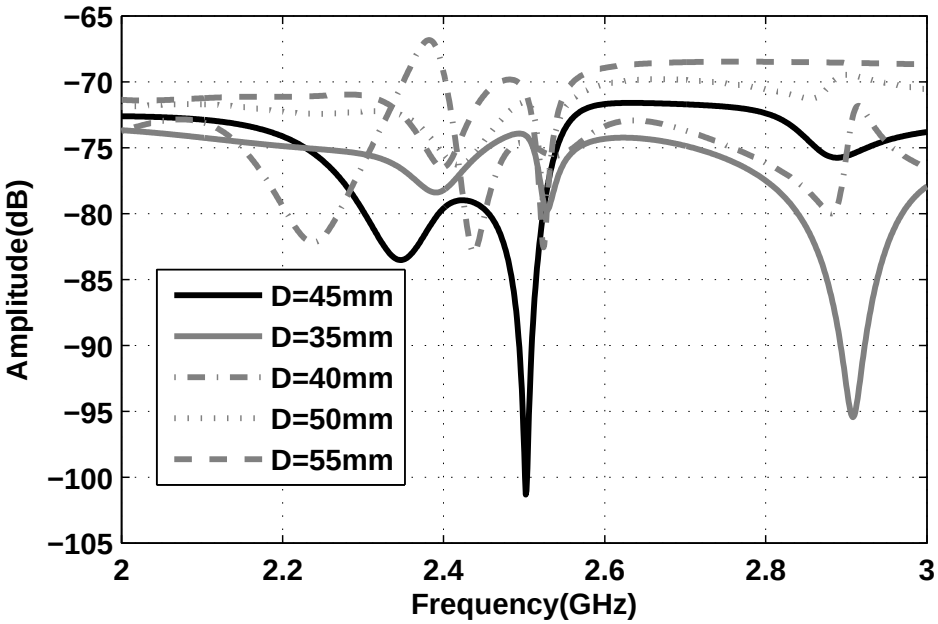

Figure 4.12: Coupling between the transmitter antenna and the receiver array for different values of array separation (D). The separation between the two elements has a significant impact on the coupling and can be optimized ($D = 45mm$) to achieve the lowest coupling within the desired band. A filter is then used to reduce the coupling outside the operation band.

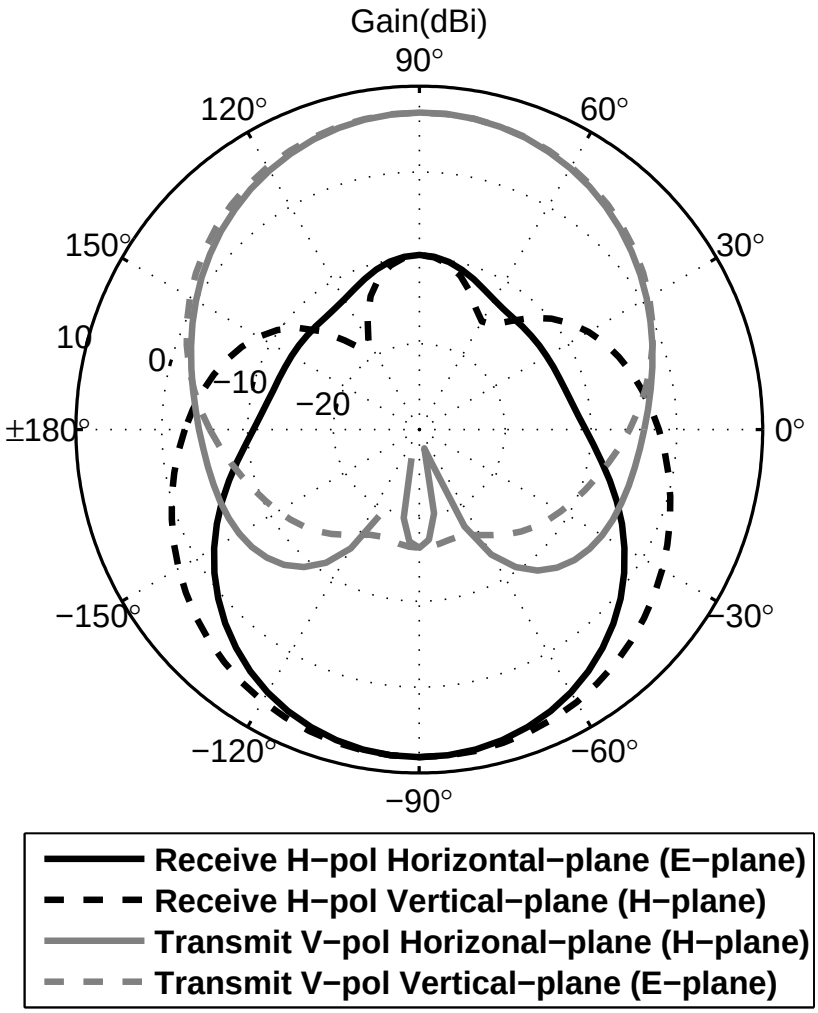

Figure 4.13: Transmit and receive radiation patterns in both vertical and horizontal planes.

4.3 Fabrication

The receiver and transmitter patch antennas are fabricated on separate substrates and are placed back to back as shown in Fig.4.14. The receiver antenna consists of two pin-fed patch antennas that are connected to the ends of two identical 100Ω microstrip lines which are in turn connected to a T-junction power divider that matches the total input impedance

of the array to 50Ω . The T-junction and microstrip lines are shielded form the rest of the circuit to reduce the coupling between different segments of the circuit. The received signal from the array is initially amplified on the receiver board using a two stage amplifier with a total gain of 32dB. The amplified signal is then transferred to the transmitter board using a pair of MCX RF connectors that are attached directly to the boards and clip onto each other as the two boards are placed back to back. The signal undergoes an additional stage of amplification and filtering on the transmitter board before it reaches the transmitter antenna. The amplifier chain on the transmitter board consists of a 16dB amplifier and a voltage controlled variable gain amplifier (-15dB to 25dB). The transmit and receive antennas are designed to have the maximum isolation within the desired operation band. However, the isolation drops outside the operation band and can cause the system to oscillate if proper filtering is not used. A coupled microstrip line bandpass filter with a three pole response and passband of 2.4GHz to 2.5GHz is inserted before the second amplifier chain. The total active gain of the system can be varied between 33dB and 73dB using a potentiometer that is accessible via an opening on one of the sides of the metallic box. The system is powered using a 3.7V battery with 1500mAh capacity and this voltage is down converted to 1.8V using a linear regulator. The entire amplifier chain draws less than 50mA at 1.8V for output powers below 0dBm. The current consumption increases to 150mA when the last stage amplifier goes to saturation with output power of 21dBm.

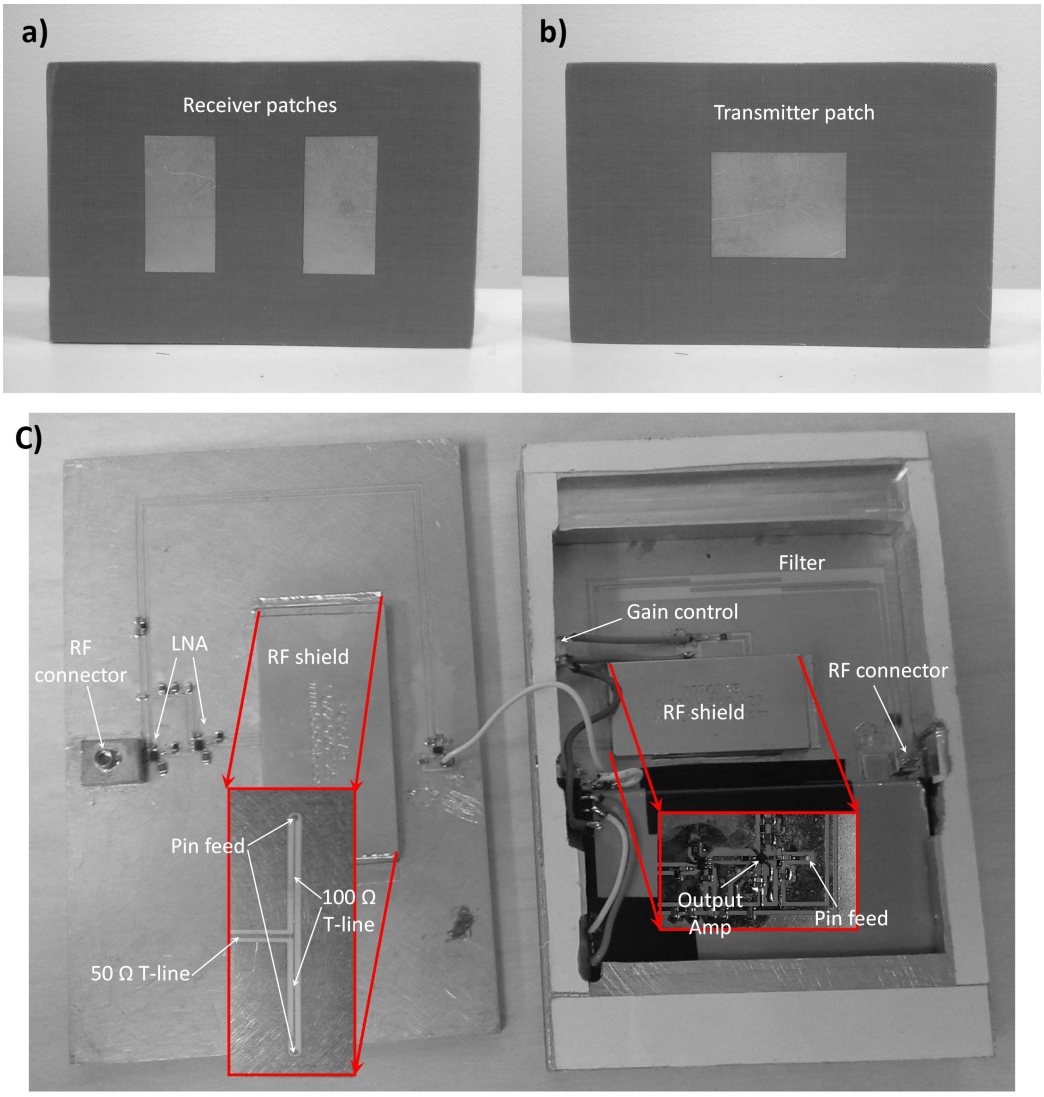

Figure 4.14: The fabricated repeater a) Rx side b) Tx side c) Inner circuitry. The circuit consists of a power divider, a four-stage voltage-variable gain amplifier, and a microchip filter as well as a battery which is capable of powering the system for 30 hours.

4.4 Performance Evaluation

To evaluate the performance of the repeater when direct line-of-sight exists between two communication devices, the repeater was placed between two horn antennas and the enhancement in the transmitted signal level between the two horn antennas was measured. The horn antennas were placed inside an anechoic chamber and had a distance of 14 me-

ters. The proposed directional repeater was oriented at a 45°tilt to be able to communicate with both horn antennas in vertical polarization. Based on the discussion in the previous section this method reduces the performance of the repeater by 6dB because of 3dB polarization mismatch in both transmitter and receiver patch antennas. The transmission between the two horn antennas is measured in the presence and absence of the repeater. The ratio between the two measurement (transmission improvement) is plotted in Fig.4.15. This value is measured for both the single-patch repeater and the two-element patch array repeater. The results show a 25dB to 35dB improvement in transmission between the two horn antennas in the presence of the patch array repeater. The total active gain for the repeater utilizing the patch array is 62dB and that of the single patch design is 50dB.

As seen in Fig.4.15, there are several ripples in the overall gain of the repeater even though the amplifier and antenna gains are smooth functions of frequency. The reason for this ripple is the leakage between the two antennas. The leakage between the transmitter and receiver patch antennas creates a feedback loop and affects the overall gain of the system. The total gain of a feedback loop can be expressed as $G/(1-GF)$ with G and F being the forward gain and feedback respectively. The GF term is a function of frequency and its phase in particular varies rapidly with frequency. Depending on the phase of GF, the total system gain can be lower or higher than the forward gain G. As a result of the phase variation of GF, the overall gain of the system varies rapidly with frequency as is observed in our measurement results.

Once the repeater is assembled, the exact coupling between the transmitter and receiver antennas as a function of frequency cannot be easily measured. Any attempt to connect an outside source such as a vector network analyser to the antennas will change the coupling between the two antennas. However, an estimate of the coupling between the antennas can be obtained using Fig.4.15. Considering the worst case, the difference between the two consecutive peaks and nulls in the overall gain of the system is about 11dB. Assuming the magnitude of coupling between the two antennas does not change significantly between a

null and the next peak, the difference in overall gain can be attributed to a 180°change in phase of GF and therefore the peak to peak ripple value can be estimated as $\frac{1+|GF|}{1-|GF|}$. Using this estimation the value of $|GF|$ is found to be -5dB which results in an estimated coupling value of $|F| = -67dB$. The isolation between the two antennas were theoretically predicted to be better than $80dB$ which is $13dB$ more than our estimate. This difference between measurement and simulation is caused by imperfections in fabrication. Fig. 4.15 also shows the same measurement results for our single patch repeater design. In this case a coupling of less than $-70dB$ between the two antennas in the operation band of 2.4GHz to 2.5HGz is predicted theoretically. However the estimated coupling from the measurement results is slightly less than $-54dB$ which shows a $16dB$ difference with the theoretical value. In this case the active gain of the amplifiers used is $50dB$. Note that additional reflections from the measurement setup or surrounding objects are not likely sources of the large coupling observed in measurements. Since the measurement setup for both repeaters was the same, the coupling due to surrounding objects would be very close in magnitude in both cases. However the coupling values observed in these cases are greatly different. The main contribution to the mentioned fabrication errors is from our inability to accurately solder the MCX connectors to the transmit and receive boards. These inaccuracies amount to a 1-degree misalignment between the two boards. Full-wave simulations show that such misalignment can significantly increase the isolation between the two antennas (up to 15dB). The misalignment can be avoided using automated fabrication techniques.

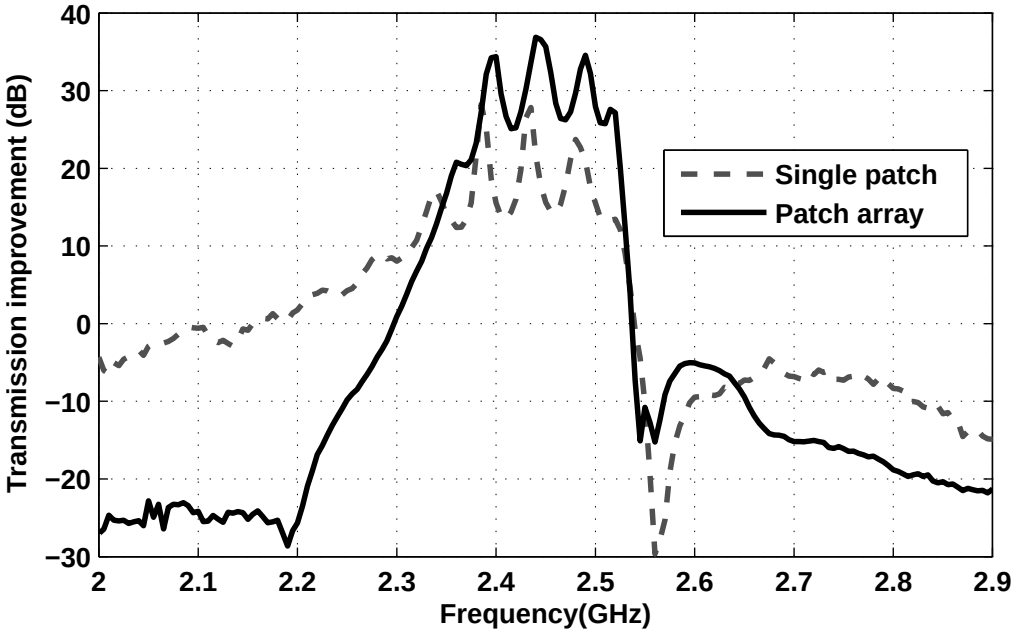

Figure 4.15: Improvement in transmission when the line-of-sight is not blocked. The repeater is placed between two horn antennas in an anechoic chamber and the transmission ratio between the two antennas with and without the repeater is plotted. Two different repeaters are used.

The repeater performance is also evaluated in a scenario where a direct line of sight cannot be established between the source and the receiver. To characterize the channel without the repeater, a short dipole was placed inside EECS building of the Univeristy of Michigan and the field distribution across the hallways was measured. An identical short dipole was used as the receiver. To mimic the polarization impurity of most common platforms, the receiver dipole was deployed at a 45 degree angle with respect to the ground whereas the transmitter antenna was placed vertically. The received signal by the receiver dipole was amplified and measured using a spectrum analyzer. The noise floor of the combined amplifier chain and spectrum analyzer was around -130dBm. The measurements were repeated in the presence of a repeater at an intersection between two perpendicular hallways and oriented 45 degree with respect to hallway directions in order to be able to send/recieve signal through both hallways. Fig.4.16 shows the measurement setup. A single frequency signal with $0dBm$ power at $2.45GHz$ was used as the transmit signal.

The receiver antenna and spectrum analyzer were moved at a constant speed along the hallways and the measured signal was recorded four times every second. The measurement results are shown in Figures 4.17 to 4.19. In the absence of the repeater, there is a good coverage through the three hallways that are in direct line-of-sight of the source. However, the signal level drops abruptly (roughly by 20dB) for each corner in the path such that the four remaining hallways are not efficiently illuminated by the source. Fig.4.18 confirms a significant improvement in the signal level in the shadowed hallways in the presence of the repeater. The signal levels along three hallways are plotted in the presence and absence of the repeater in Fig.4.19. The sharp ripples in the signal levels along pathes are due to multipath effects in the communication channel. As expected, the signal level is improved by 20-40dB along path1 which is in direct line-of-sight of the repeater. In addition, on average a 20dB improvement is observed for path2 due to the backlobe radiation of the repeater as well as reflections from the corners, walls and ceiling. There is no improvement towards the beginning of path3. This area of the building is not in the line-of-sight of the repeater and is primarily illuminated by the source signal reflected from the top left corner. However, there is a 10-20dB improvement in the measured field intensity towards the end of path3 which was otherwise the darkest region in the building. This area is illuminated by the repeater signal reflected from the bottom left corner.

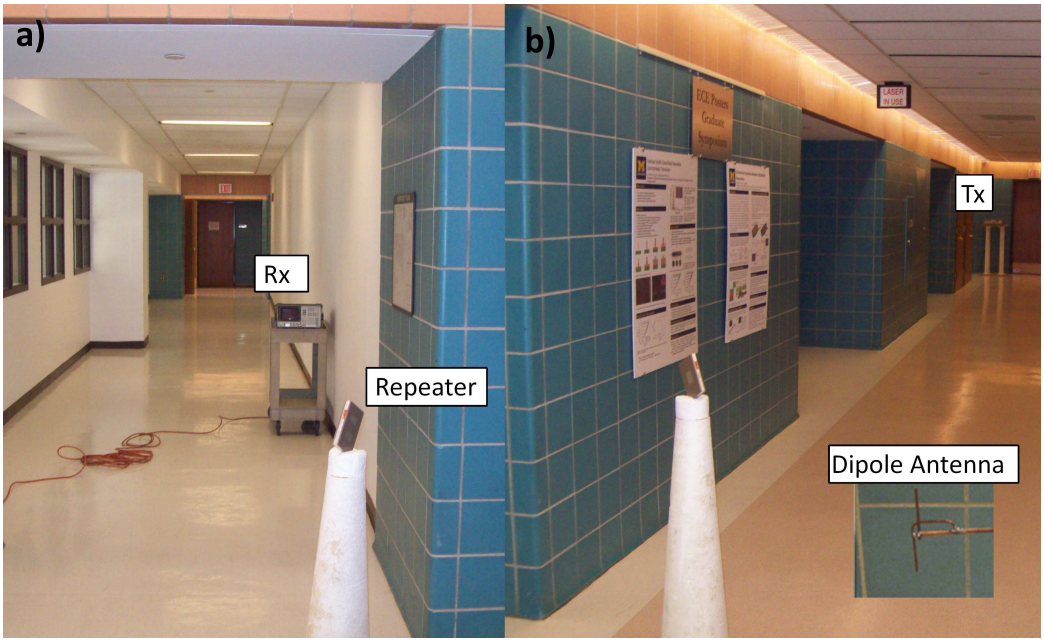

Figure 4.16: The measurement setup used to evaluate the performance of the repeater in a realistic scenario. The source and field probe are dipole antennas. Field intensity throughout the hallways in the presence and absence of the repeater is measured and compared.

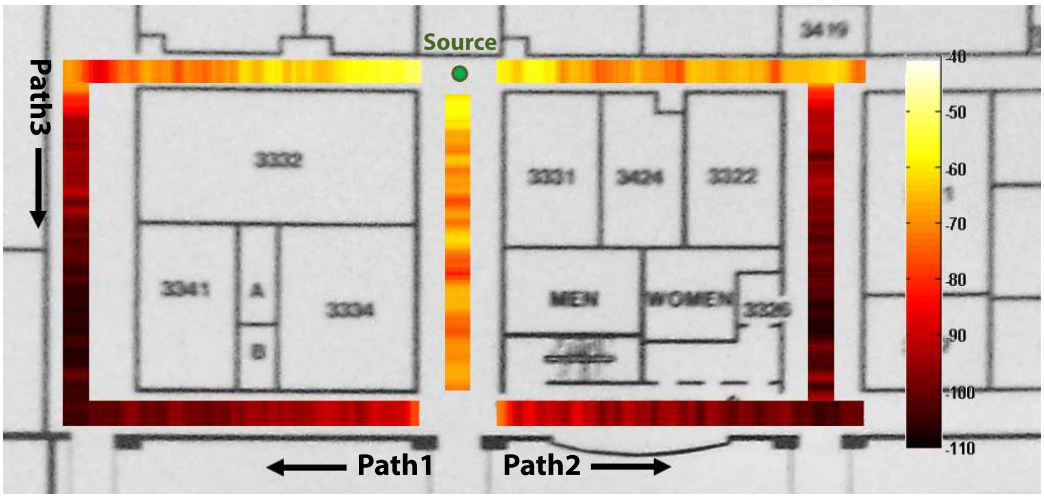

Figure 4.17: Field distribution of a short dipole source in the EECS hallways with the repeater turned off. There is a good coverage along the hallways where a direct line of sight exists between the source and receiver.

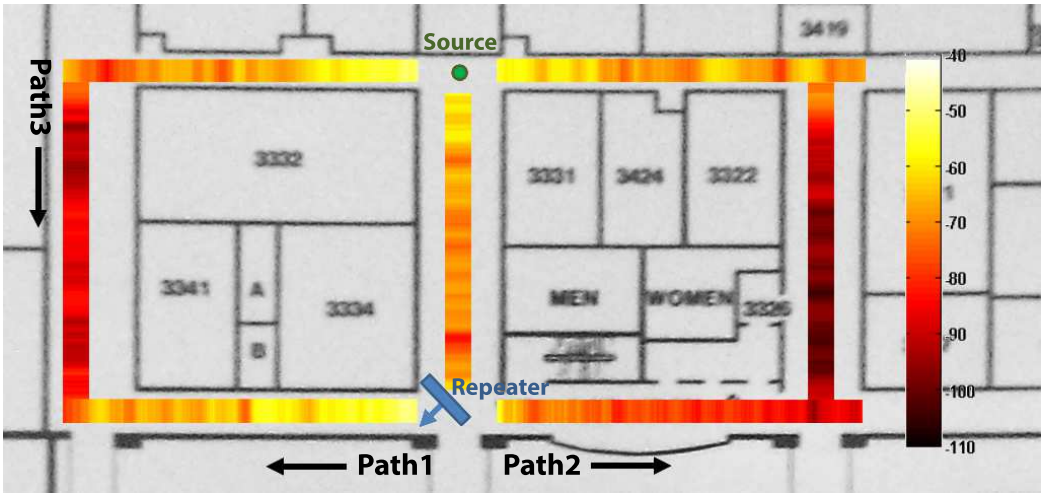

Figure 4.18: Improvement in coverage in the hallways in presence of the repeater. The repeater is placed such that a line of sight exists between the repeater and the source. The repeater creates line of sight along path1 while path2 benefits from the backlobe radiation of the repeater. There is even some improvement observed in path3 where direct line of sight with the repeater does not exist.

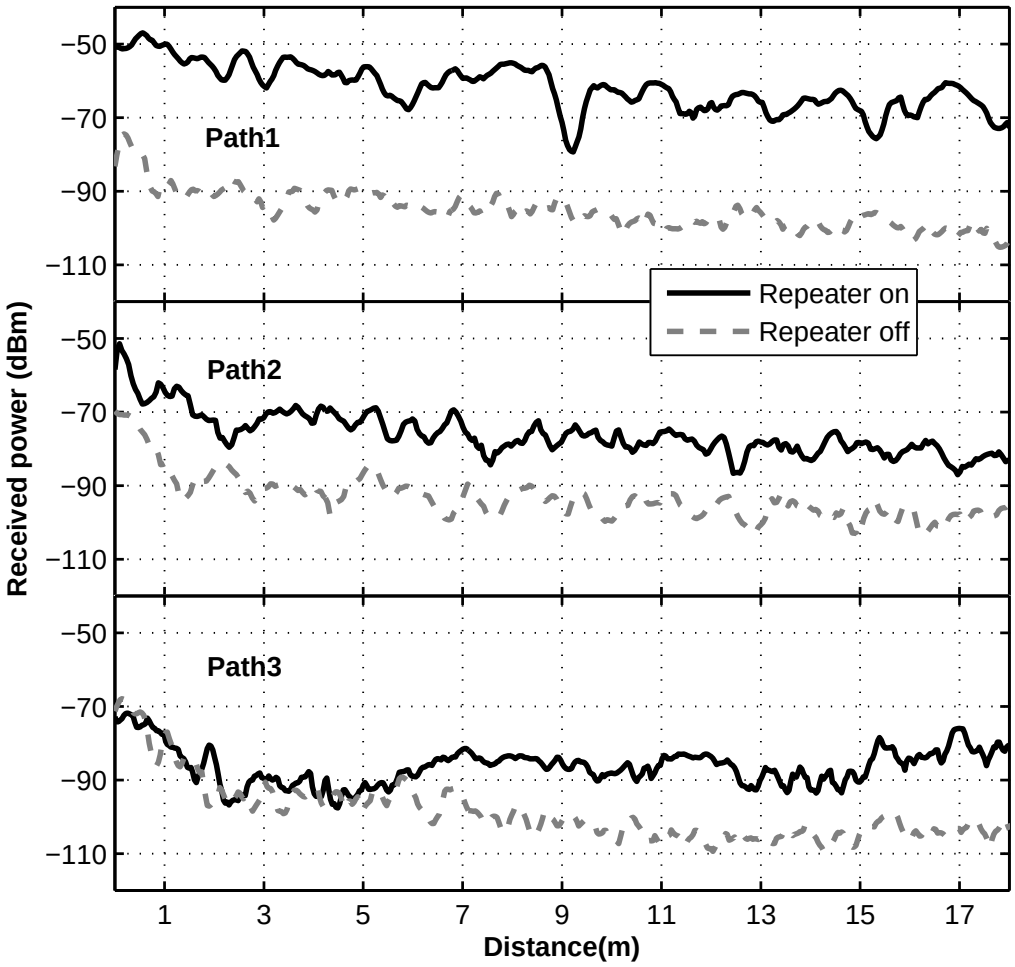

Figure 4.19: Improvement in transmission between the antennas in presence of the repeater. There is an average of more than 30dB improvement in path1 where direct line-of-sight with the repeater exists. A 20dB improvement is observed in path2 due to the backlobe radiaiton of the repeater. Some improvement is observed in path3 due to reflections from the corner between path2 and path3.

4.5 Conclusion

In this chapter a directional repeater system with a simple architecture composed of a transmit antenna, a receive antenna and an amplifier and filter was presented. Because of this simplicity, the repeater is energy efficient and does not require down-conversion and up-

conversion with frequency translation and complicated operational protocols to manage users. In fact, different protocols and channels can be simultaneously supported. Close to 70dB of isolation is achieved between the Tx and Rx antennas that allows significant amplification of the received signal to be retransmitted in desired directions. The isolation improvement between the Tx and Rx antennas is achieved by separating the antennas by a ground plane in between and also creating a polarization mismatch between the two antennas. Additional isolation between the Tx and Rx antennas is achieved using a novel two-element Rx antenna whose elements are appropriately located with respect to the Tx antenna to cancel the signal leakage from the Tx antenna to the Rx antennas. The repeater is fabricated and tested in different environments and significant signal coverage enhancement is demonstrated in all cases.

CHAPTER 5

A High-gain Transponder at L-band for Radar Calibration of SMAP

5.1 Introduction

In this chapter, the design and fabrication of a polarimetric active radar calibrator (PARC) consisting of a square shaped horn antenna and an ortho-mode transducer (OMT), following the same principles as what was reported in [73] is introduced. In the earlier design, a high cross-polarization isolation is achieved over a wide bandwidth using a square horn antenna with a waveguide orthomode transducer (OMT). The OMT isolation was measured to be better than 35 dB with the common port short-circuited. The isolation improves to about 55 dB when the common port is connected to the antenna, provided that the antenna has more than 20 dB return loss. Several other OMT configurations have been introduced with the isolation between the two ports ranging from 35 dB to 50 dB [74–78]. However, as mentioned in the first chapter, to achieve a stable RCS of 65-75 dBSm a much higher isolation between the two antennas (75 dB) is desired.

To improve the performance, the structural parameters such as the taper lengths and angles of the horn and OMT ports are optimized using full-wave simulation. As a result, the length of the OMT and antenna bundle is reduced by a factor of two compared to the earlier design. In addition, the position of polarizing wires that are essential to the performance of the OMT are optimized to reduce the mutual coupling between the two

ports of the antenna. There are a number of other improvements using perturbation and leakage cancellation techniques to increase the isolation between the two ports to about 75 dB over the desired band of 1.22 GHz to 1.32 GHz. Finally, a stable gain amplifier system with the ability to compensate for temperature and aging drifts in the system is included. The RCS of the fabricated PARC is measured in the field and reported as well as the radar image of the area created by the SMAP (Soil Moisture Active Passive) radar.

5.2 The OMT and Antenna Design

The proposed OMT structure is shown in Fig. 5.1a. The structure consists of a square waveguide channel that is connected to a rectangular waveguide section via a linear taper at one end, and to a square horn antenna at the other end. This rectangular waveguide section supports a vertically polarized electric field. Another rectangular waveguide section is attached perpendicularly to the square waveguide section using a linear taper and supports a horizontally polarized electric field. Because of their polarization mismatch, the two rectangular waveguide sections are isolated from each other. However, there are significant reflections from the three-way junction for both polarizations. The matching can be improved by placing a number of polarizing wires in appropriate places as seen in Fig. 5.1a The polarizing wires inserted in the waveguide channels reflect the component of the electric field that is parallel to the wires and only pass the perpendicular component.

Assuming only the vertically polarized rectangular waveguide section (port 1) is excited, the electric field in the square section is purely vertical and therefore the signal is not reflected by the wires placed in the square section. The primary source of reflections, in this case, is the impedance mismatch caused by the three-way waveguide junction. A perfect impedance match can be achieved if the vertical section (connected to port 2) acts like an open circuit for the vertical mode. This condition can be achieved for a relatively wide band if L_2 is selected to be about a quarter of the wavelength in the vertical tapered section. The

wires that are placed inside the vertical tapered section act like a short circuit which is, in turn, transformed to an open circuit by the quarter wavelength tapered waveguide section.

Alternatively, if only the horizontally polarized rectangular waveguide (port 2) is excited, the wires placed in the square waveguide section act like a reflector and form an indented waveguide bend. The indentation size, L_3 can be optimized to minimize the reflections from the waveguide bend over the desired band. Additional wires are placed in the horizontal tapered section (connected to port 1) at a distance L_1 to reflect the small fraction of the electric field that passes through the first set of polarizing wires. The distance between the wires must be kept small compared to the wavelength to ensure adequate reflection from the wires. The taper length, WT, and other design parameters L_1, L_2 and L_3 are optimized to maximize the impedance matching and isolation between the ports simultaneously. Fig. 5.1b-c depict the electric field intensity in the OMT and Antenna structure when the horizontal or vertical ports are excited. The graphs confirm the proper operation of the OMT. The optimized values are $L_1 = 10.2$ cm, $L_2 = 14.0$ cm, $L_3 = 11.8$ cm, $WT = 17.0$ cm, the waveguide dimensions are $W_x = 16.5$ cm, $W_y = 8.3$ cm, and the optimized S-parameters of the system are plotted in Fig. 5.2. As seen in the graph, better than 20 dB return loss for both ports and close to 80 dB isolation between the ports are achieved over the desired band of 1.2175 GHz to 1.3175 GHz. In addition, the OMT dimensions are significantly smaller than those of [13] (the biggest dimension is reduced by a factor of 2) and the antenna has only one tapered section which makes it much more suitable for accurate fabrication.

5.3 Fabrication and Integration

The proposed OMT and horn antenna were fabricated using aluminum sheets that were cut using a laser cutter and welded together. The polarizing wires were installed by drilling holes in opposite walls of the waveguides and passing steel wires through them. Two $50\,\Omega$

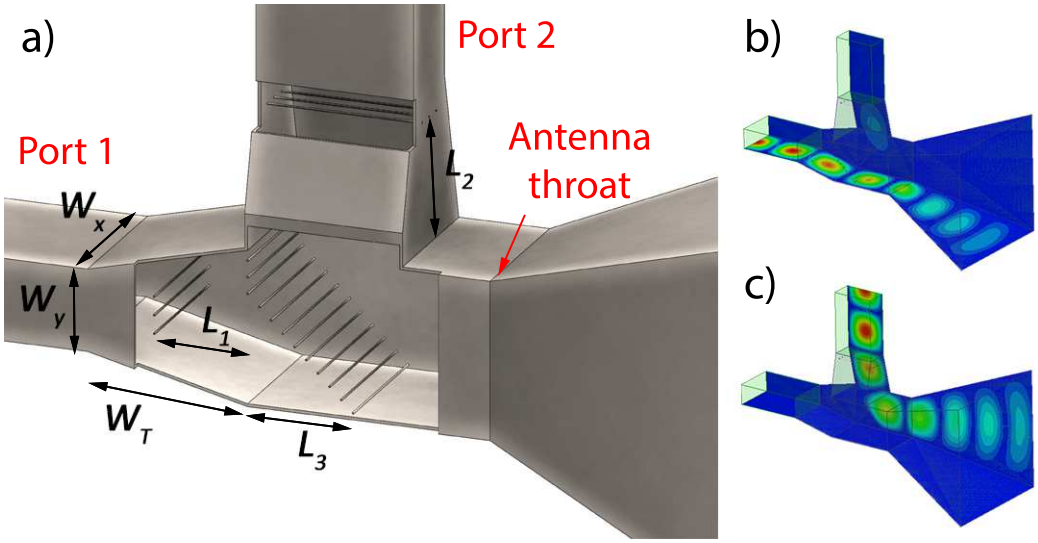

Figure 5.1: The OMT geometry and design parameters. The OMT consists of a T junction connecting the horizontal and vertical ports to the antenna. The polarizing wires allow for both ports to be matched simultaneously over the desired frequency band.

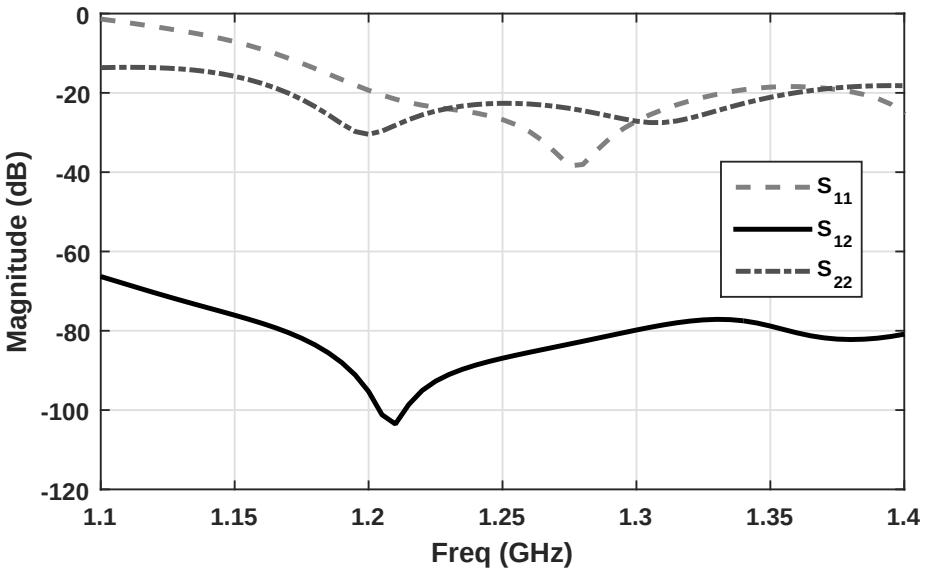

Figure 5.2: The simualted two-port S-parameters of the OMT and the horn antenna. Better than 80 dB isolation is achievable over the desired frequency band.

waveguide-to-coaxial adapters were used as the input ports for the OMT. The antenna was integrated into a full metallic frame, along with RF and control circuits. The isolation between the two ports was measured using a network analyzer with the OMT/Antenna system placed in an anechoic chamber and was found to be just over 60 dB for the desired frequency band. Fig. 5.3a shows the fabricated antenna and the measurement setup. There are a few unavoidable fabrication inaccuracies that can contribute to a lower isolation between the two ports than what was predicted by simulation. In particular, errors in the angles between the waveguide walls, alignment of the polarizing wires, alignment of the ports with respect to the waveguide, and reflections from numerous junctions and discontinuities in the structure are the dominant sources of leakage between the two ports.

To compensate for the increase in coupling between the two ports due to fabrication inaccuracies a leakage cancellation circuit is added to the antenna. Fig. 5.3 shows the fabricated antenna and the leakage cancellation circuit. The circuit is passive and reciprocal and consists of two directional couplers, a variable attenuator, a phase shifter and a delay line. The circuit samples the signal transmitted through one port, adjusts its phase and amplitude through phase shifters and attenuators, and combines this signal with the received signal from the other port. The attenuators and phase shifters can be tuned such that the additional coupling created by the leakage cancellation circuit is close in magnitude and out of phase with the internal leakage of the OMT/antenna system. The performance of the OMT/antenna system in the presence and the absence of the leakage cancellation system is evaluated and presented in the measurements section.

The antenna was integrated into a water-resistant metallic frame to protect it against all weather conditions in the field. The horn antenna opening is protected by a foam-based radome covered with a thin layer of polycarbonate and secured to the metallic structure using a fiberglass frame. Also enclosed in the metallic frame is the RF circuit as well as a control box with a small computer to process and record the received satellite data. The system is also capable of transmitting the processed data over a 4G network to the

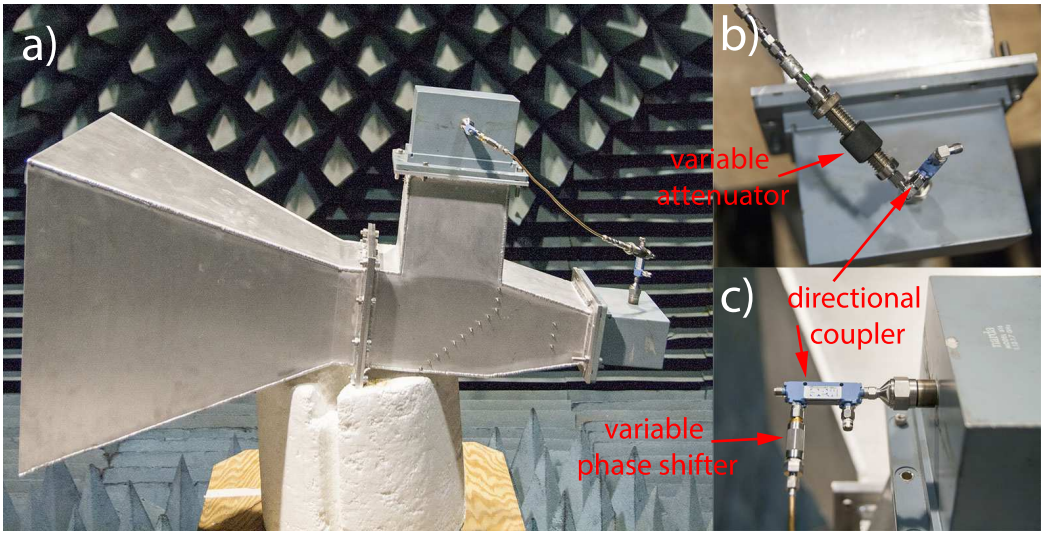

Figure 5.3: a) The fabricated OMT and antenna. A leakage cancellation circuit consisting of two directional couplers, a delay line, a phase shifter, and an attenuator is used to sample the transmitted signal and insert back at the receiver port to reduce the mutual coupling between the two ports b) variable attenuator c) variable phase shifter

developers. The data is used to monitor the performance of the SAR, find the exact position of the SAR with respect to the earth coordinates, and find preliminary information about the SAR such as its footprint and radiation pattern.

In order to assure the quality of the data products of SMAP, it needs to be frequently calibrated throughout the year. Calibrating the PARC itself after each SAR calibration requires significant effort and is not practical if multiple PARCs are deployed in different locations. Therefore it is imperative for the PARC to have a fixed performance over time and in different ambient temperatures. To achieve this, a stable gain amplifier system with a gain stability of better than 0.1 dB is designed and used with the PARC. A slightly out-of-band signal at 1060 MHz is used as a reference to stabilize the gain of the system. The reference signal is generated using a VCXO (voltage controlled crystal oscillator) with a low thermal drift factor and enclosed in a temperature-controlled box. To increase the thermal stability of the reference signal even further, the VCXO is enclosed in a heat-controlled box and its temperature is stabilized to less than one 1°C. In addition, all the bias currents required for the VCXO and amplifiers are provided by a temperature stabled

DC supply with less than 1 mV voltage drift over the temperature range of $-25°$C to $40°$C.

Fig.5.4 shows the circuit diagram of an amplifier system that can provide a high and stable active gain. The received signal from the antenna is first filtered and combined with the reference signal. The combined signal is then passed through a low-noise amplifier and an automatic gain controller(AGC). After amplification, the combined signal is sampled by a directional coupler and fed through a diplexer that separates the reference signal from the main signal. The amplitude of the main signal is detected using a logarithmic diode detector with a 55 dB linear dynamic range and 12 ns pulse response time. The output of the detector is digitized using a sampling rate of 2 mega sampled per second (MSps) and is stored for postprocessing by the PARC's built in microprocessor. The reference signal is returned back to the feedback port of the AGC. The AGC automatically adjusts its gain to keep the level of the feedback signal at a preset value. Since the amplitude of the reference signal before the amplifier is kept stable as described before, the overall gain of the amplifier system remains stable over a wide temperature range. The amplified signal goes through an isolator and a final filter to eliminate the reference signal before feeding the transmit antenna.

5.4 Measurements

The fabricated PARC is placed inside the anechoic chamber of the University of Michigan as shown in Fig. 5.5 and the coupling between the transmit and receive ports of the OMT/antenna system is measured using a vector network analyzer. Fig. 5.6 shows the transmission coefficient, S_{12}, between the two ports in the time domain. There are several peaks in the time domain signal that correspond to leaks from different points in the OMT and antenna system as well as the anechoic chamber. Time-of-arrival analysis suggests that the main leakage contribution is from the polarizing wires and the throat (flare interface) of the horn antenna.

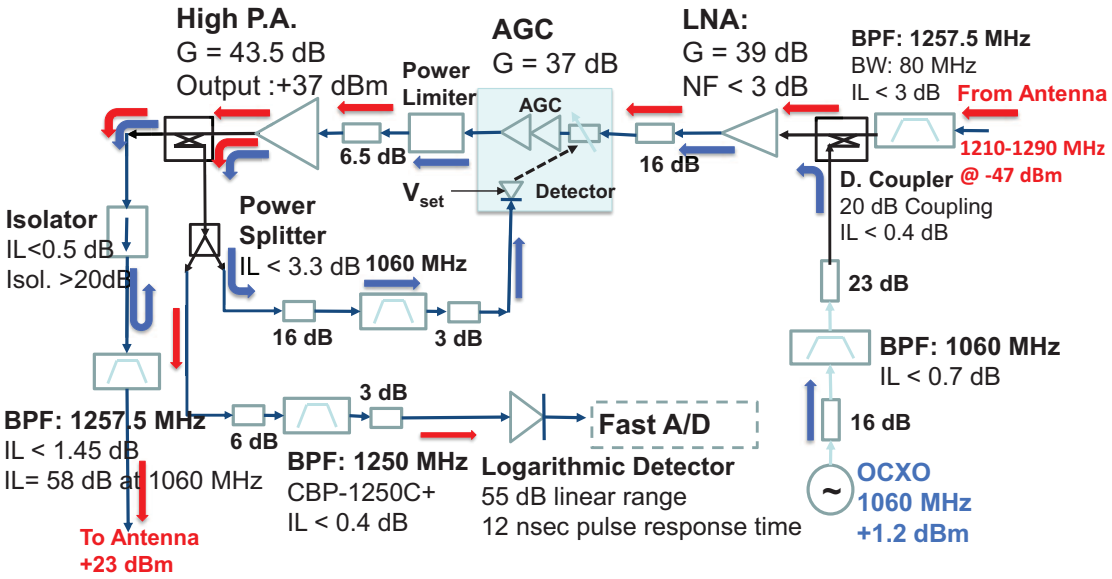

Figure 5.4: The stable-gain amplifier schematic. A reference signal at a frequency slightly out of the operation band is combined with the received signal before amplification. The reference signal is then filtered out and monitored to keep the amplifier gain constant. All voltage supplies are temperature compensated, and the local oscillator is placed in a temperature controlled box.

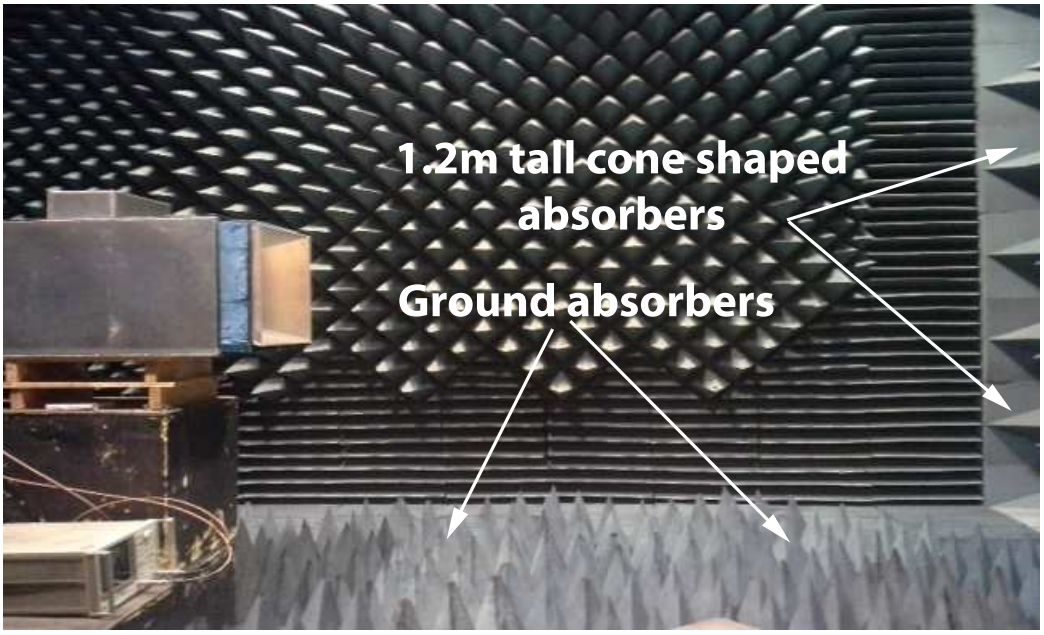

Figure 5.5: Isolation measurement setup. The PARC is placed in an anechoic chamber and OMT ports are connected to a VNA to characterize the mutual coupling between the ports.

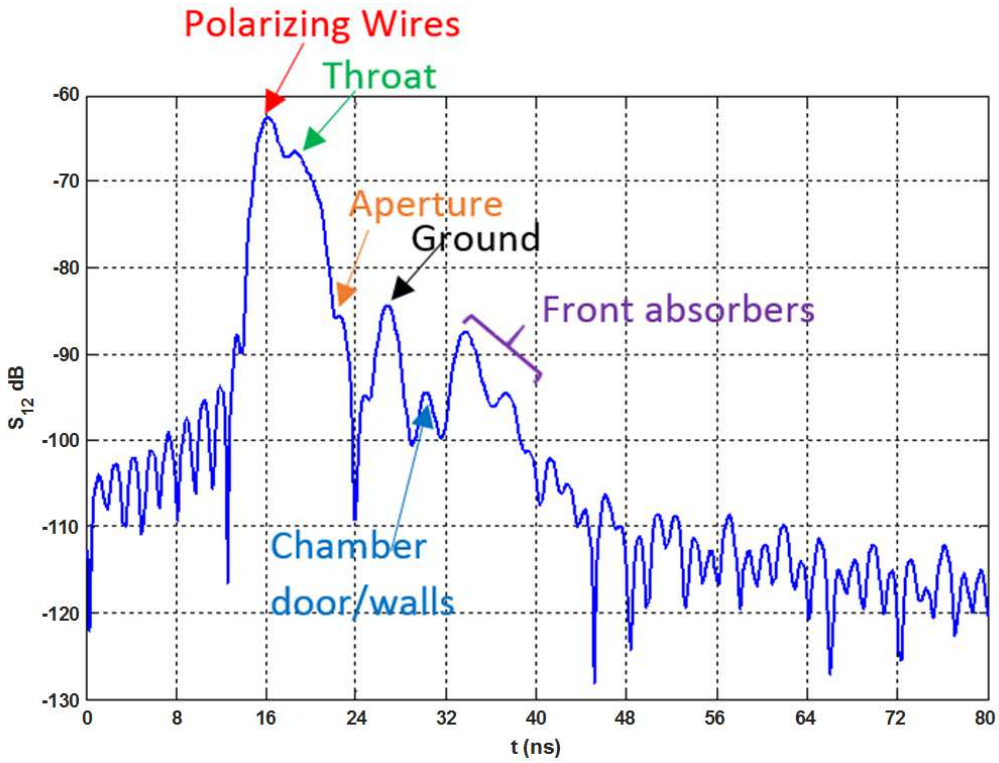

Figure 5.6: The mutual coupling between the two OMT ports represented in time domain. The strongest contribution is due to leakage from the T-junction. The rest of the peaks are due to different reflections including reflections from the chamber absorbers

Since the leakage is a result of scattering from the polarizing wires and discontinuities in the system, it might be possible to manually create an artificial scattering from within the OMT structure or the horn antenna in such a way as to cancel the effect of the inherent leakage in the system. The corrective scattering must be close in magnitude and out of phase with the inherent leakage. Therefore any reflective perturbation needs to create an additional -60 dB leakage between the two ports. A very short piece of wire that makes a 45 degree angle with the waveguide walls creates a small cross-pol scattering and can be placed at the throat of the OMT to create the desired corrective reflection. The magnitude of the reflection can be adjusted by changing the length of the wire and the phase by moving the wire along the length of the waveguide. This technique is used in combination with the external leakage cancellation circuit that was described in the fabrication section to minimize the leakage between the transmit and receive ports.

Because the coupling between the two ports is extremely small, the environmental effects, such as reflections from the chamber doors, walls and floor, have considerable contributions to the measured coupling between the two ports. To achieve the most accurate leakage cancellation over the entire bandwidth the environmental effects must be eliminated using time-domain gating during the optimization. Fig. 5.7 shows the gated and ungated transmission coefficients in the presence of both leakage cancellation apparatuses in the frequency domain. As seen in the graph, the leakage cancellation methods improve the isolation between the two ports by better than 12 dB over the entire band. The response without leakage cancellation is also plotted for comparison.

Once the coupling between the two ports is reduced through the aforementioned techniques, the RCS of the PARC can be measured. Accurate measurement of the RCS of the PARC requires significant diligence due to the environment effects on the coupling between the horizontal and vertical ports. The RCS can be expressed in terms of the transmit and receive antenna gains, G_t, G_r, coupling between the ports, F, and the amplifier gain, G_{amp}

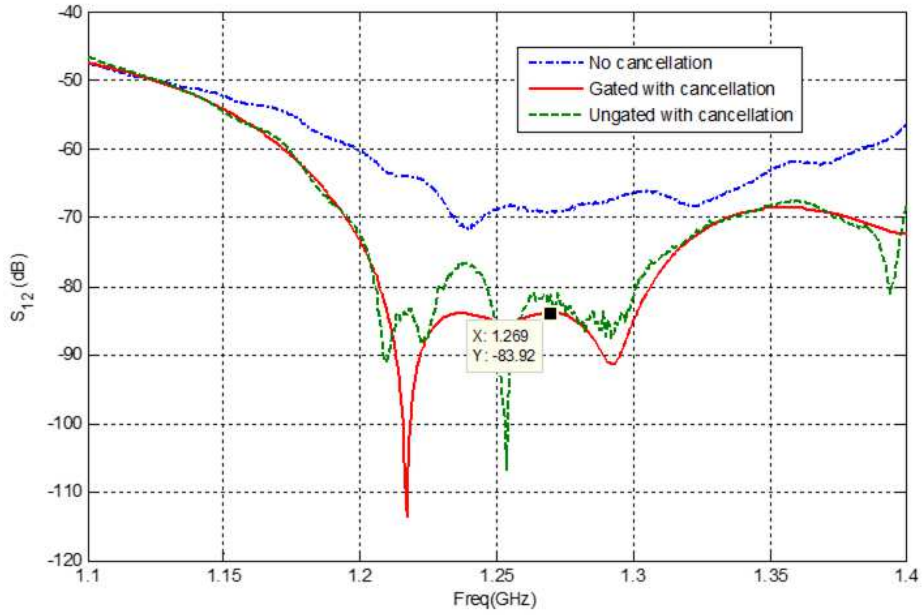

Figure 5.7: The mutual coupling between the two ports in the presence and absence of leakage cancellation mechanism. The signal needs to be gated to eliminate chamber effects for accurate leakage cancellation. Better than 12 dB isolation improvement is achieved using leakage cancellation.

as follows:

$$\sigma^{PARC} = \frac{\lambda^2}{4\pi} \frac{G_{amp} G_{ant}}{1 - F G_{amp}} \tag{5.1}$$

If the amplifier gain is selected such that FG_{amp} is very small, the RCS of the PARC is not a function of the coupling level between the two ports. However, this constraint severely limits the gain of the amplifier and therefore the RCS of the PARC. It is desirable to have the amplifier gain only a few dB less than the isolation between the two ports to achieve the highest RCS possible. Therefore the loop gain is a function of the coupling between the two antennas which is greatly affected by the reflections (scattering) from the objects surrounding the PARC. Placing the PARC in an anechoic chamber can suppress these reflections to a certain degree. However, if the PARC is used with its nominal amplifier gain of 72 dB, the reflection from the walls of a less-than-perfect anechoic chamber is enough to cause the PARC to go to oscillation or dramatically change its RCS. For this reason the RCS measurements cannot be performed in the chamber. Instead, an outdoor test at the location where the PARC is to be mounted is required. Moreover, the permanent position of the PARC should be selected such that there are no large reflectors in the proximity of the PARC especially close to its boresight. The same conditions must hold during the RCS measurements of the PARC. Consequently, the polarimetric radar that is used to measure the RCS of the PARC must be placed very far away from the PARC on an elevated platform so that the radar is along the PARC's antenna boresight. Arranging for such an experiment is rather complicated.

Considering the aforementioned difficulties, a multi-step RCS measurement technique is proposed that uses measurements along boresight only when the gain of the PARC is significantly lower than its nominal gain. Three sets of measurements are performed to determine the RCS of the PARC:

1) Initially, the RCS of the PARC is measured in an anechoic chamber for different incident angles and in the two principal planes of incidence. For this measurement, a well characterized 30 dB attenuator was placed at the output of the amplifier box resulting in an

effective gain of 42 dB. We will denote this value by $\sigma^{Chamber}$.

2) The RCS of the PARC is measured through a sidelobe of the PARC antenna in the field where the PARC is to be permanently mounted. For this measurement, the 30dB attenuator is kept in place, resulting in an effective amplifier gain of 42dB . This value is denoted by σ^{LG}.

3) The gain of the PARC is increased to 72 dB by removing the attenuator without changing the position of the PARC or the polarimetric radar used for the second measurement. The gain adjustment is performed through a window that is contrived in the body of the PARC and provides access to cables that are connecting the RF box to the OMT. The measured RCS value in this step is denoted by σ^{HG}.

The RCS of PARC can then be found in terms of the measured values as follows:

$$\sigma^{PARC} = \frac{\sigma^{HG}}{\sigma^{LG}}\sigma^{Chamber} \tag{5.2}$$

Initial RCS and pattern measurements were carried out in the chamber while the gain of the PARC was lowered to 42 dB. The polarimetric radar used for this measurement was calibrated using the STCT method [63] with a metallic sphere as the known target. The second and third sets of measurements were performed in the field while the PARC was mounted at the initial test location as shown in Fig. 5.8. The PARC is considerably elevated to reduce the effect of reflections from the ground through the PARC's antenna sidelobe. Fig. 5.9 shows the vv-polarized component of the received signal by the polarimetric radar in the field in the time domain. The same measurement was carried out while the PARC was turned off to measure the background and subtract from the measured response. Both responses are plotted for comparison. The first peak in the response is due to the internal mismatch of the radar antenna. The second peak is due to passive scattering from the metallic parts of the PARC including the horn antenna and the metallic cover. The active response appears about 30 ns after the passive response because of the time delay in the

internal cables, amplifiers, and filters of the PARC. The frequency response of the PARC is plotted in Fig. 5.10. As seen in the graph, an RCS of 75 dBsm or better is achieved over the entire band. There is a 5 dB ripple in the RCS as a function of frequency. The ripples can be explained by examining the term $(1 - FG_{amp})$ in (5.1). Because of the group delay of the filters, cables and amplifiers in the system, the phase of FG_{amp} changes rapidly as a function of frequency. Every time the phase of FG_{amp} wraps around, the amplitude of σ^{PARC} goes through a minimum and a maximum. A larger group delay results in an increase in the number of ripples and a larger amplitude of FG_{amp} results in larger ripples. Most of the group delay is due to the presence of bandpass filters in our design. The filters are essential for reducing RFI and reducing the coupling between the two ports of the OMT outside the optimized band, thus preventing the system from going to oscillation. The gain of the amplifiers is kept 10 dB below the isolation level to keep the amplitude of ripples below 5 dB. Despite the ripples, the RCS is a relatively smooth function of frequency over any given 1 MHz wide channel. Therefore the presence of ripples does not severely impact the accuracy of calibration for SMAP. The frequency dependence of the RCS of the PARC is documented accurately for each channel and used for calibration of SMAP.

5.5 Analysis

After the launch of the SMAP satellite, the fabricated PARC was deployed at a test location and the area was imaged by the SMAP radar. The PARC was carefully positioned to face the expected location of the satellite. The antenna was rotated 45°in the plane perpendicular to the direction of incidence so that the scattering matrix of the PARC with respect to SMAP polarization coordinates has equal entries that enable radiometric calibration of all four channels simultaneously. The scattering matrix of the rotated PARC, $\mathbb{S}^r$ can be related to the scattering matrix of the vertically polarized PARC using a rotation matrix, $\mathbb{R}$ as follows:

Figure 5.8: Measurement setup in the initial test location. The PARC is elevated to prevent ground reflections through the PARC's antenna sidelobe from increasing the coupling between the OMT ports. The PARC is controlled manually during the initial test period using an external monitor and keyboard. This procedure is performed autonomously after the final deployment of the PARC.

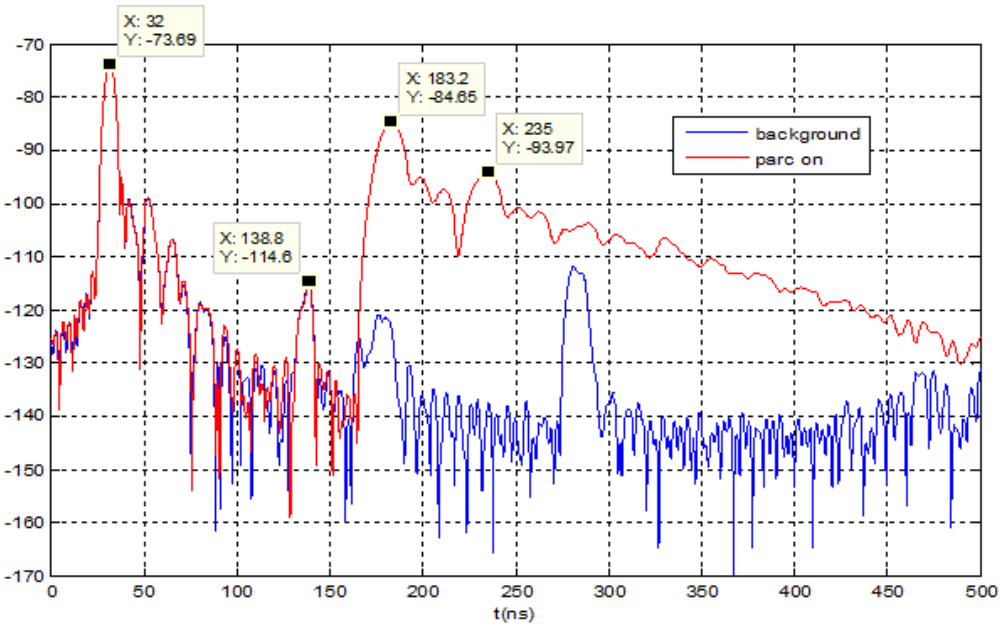

Figure 5.9: The time domain backscattered response of the PARC through a sidelobe (the boresight of the PARC's antenna is pointed away from the boresight of the polarimetric radar). The first peak is due to the internal mismatch of the polarimetric radar and the second peak is the passive reflection from the PARC's antenna and metallic body. The third peak is the active response of the PARC.

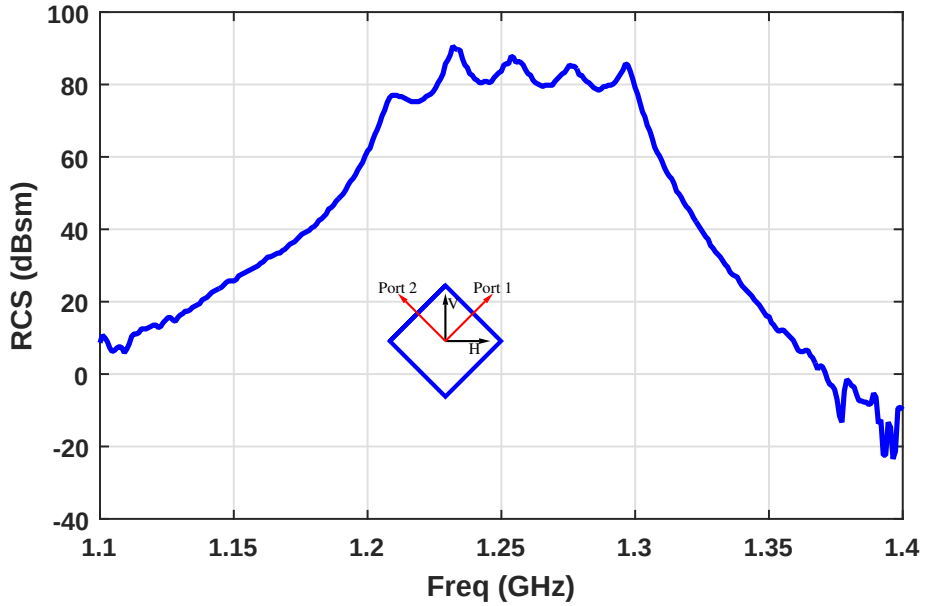

Figure 5.10: The RCS of the PARC at boresight when the PARC is rotated 45°around its axis. The RCS is measured using a three step measurement technique that allows for accurate characterization of the PARC in the field and minimizes the load of the measurement system on the PARC.

Table 5.1: performance summary

Paremeter	Description
Center Frequency	1257 MHz
Bandwidth	80 MHz
RCS (45°orientation)	σ^{VV} = σ^{HH} = σ^{HV} = 78-85 dBsm
Repeatability	$\pm$0.1 dBsm
Relative Phase (45°orientation)	$\angle$HH - $\angle$VV = 0°
Relative Phase (45°orientation)	$\angle$HV - $\angle$VV = 180°
Cross talk (vertical orientation)	$<$-40 dB
Time delay	45 ns

$$\mathbb{S}^r = \mathbb{R}\mathbb{S}^o\mathbb{R}^T = \frac{1}{2}\sigma^{PARC}\begin{bmatrix} 1 & -1 \\ -1 & 1 \end{bmatrix} \tag{5.3}$$

$where,$

$$\mathbb{S}^o = \sigma^{PARC}\begin{bmatrix} 1 & 0 \\ 0 & 0 \end{bmatrix} \; and\, \mathbb{R} = \frac{1}{\sqrt{2}}\begin{bmatrix} 1 & -1 \\ 1 & 1 \end{bmatrix}$$

In practice, because of the cross talk between the channels, VH and HH components of $\mathbb{S}^o$ are not zero. These components were measured to be more than 40 dB lower than the VV component over the entire band. Therefore the effect of these components does not appear in the rotated scattering matrix. The performance parameters of the PARC are summarized in Table.1.

The SMAP satellite records its exact location and pointing direction with respect to a well-defined coordinate system referenced to the Earth as it flies. This information can be used to account for any possible misalignment between SMAP and the PARC and achieve an accurate calibration. The exact details of this procedure are beyond the scope of this paper. Fig. 5.11 shows the vv- and vh-polarized images of the area around the PARC

as recorded by SMAP while the PARC was in service. The PARC is positioned in an urban setting which means it is surrounded by pixels with rather large backscattering due to buildings and other larger scatterers. Fig. 5.12 shows the SMAP image overlayed on the map of the area where the PARC was deployed. As seen in the graph, the pixel containing the PARC is seen much brighter in the image. The permanent position of the PARC must be chosen such that the surrounding pixels have below average backscattering to increase the signal to clutter as much as possible.

The SMAP radar transmits a $15\,\mu$s wide linear chirp pulse with a 1 MHz bandwidth in vertical polarization followed by a $9\,\mu$s gap and a similar pulse in horizontal polarization. The whole cycle is repeated with an approximate period of $360\,\mu$s. The amplitude of the received signal is measured in real time using a directional coupler and a fast logarithmic power detector with appropriate filtering, before being transmitted back to the SMAP Radar. The output of the power detector is sampled using a digitizing oscilloscope with the sampling frequency of 2 MHz corresponding to a $0.5\,\mu$s time scale resolution. The recorded signal is then post-processed by the PARC's built-in microprocessor to isolate the time intervals where a satellite signal is received by the PARC. The post-processed data is transmitted to the developers after each satellite pass using a 4G LTE modem and antenna.

The magnitude of the received pulses corresponding to SMAP's v and h polarizations are plotted in Fig. 5.13. The duration and separation between the measured pulses matches with the SMAP radar's specifications. The SMAP radar is capable of transmitting a maximum of 550W of power. The SMAP antenna gain is 36 dB and the target was at a distance of 866 Km. Therefore the upper limit for the received power is $0.23\,\mu\text{W/m}^2$. The plot shows a peak received power density of $0.16\,\mu\text{W/m}^2$ which is consistent with the expected power. In addition to the peak value, the roll-off of the signal as the SMAP satellite flies by the PARC can be characterized from the plot. This information can be used to estimate the radiation pattern of the radar's antenna and verify its integrity. Note that the peak signal level is close to 40 dB above the noise floor of the signal recording system of the

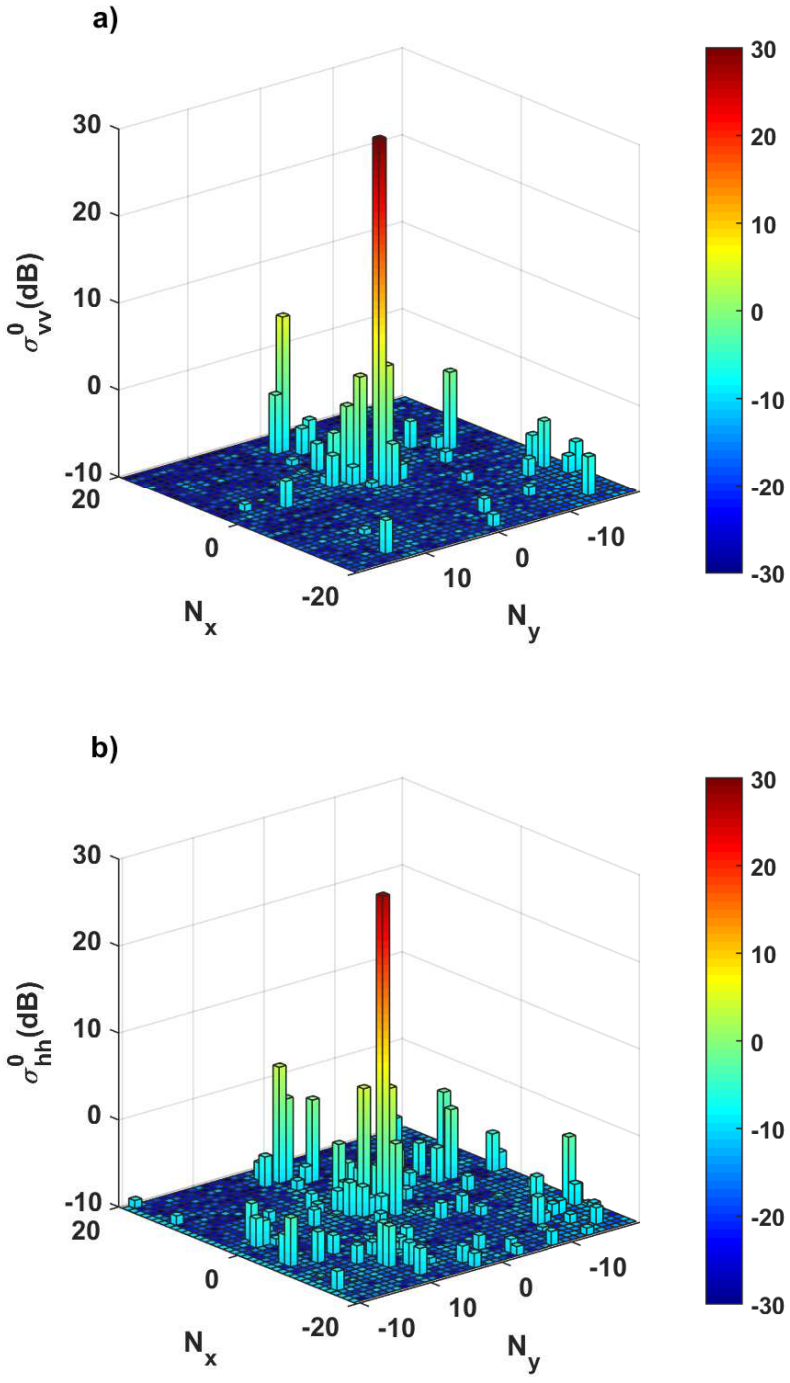

Figure 5.11: The image of the PARC as seen by the SMAP satellite plotted over a 20 pixel by 20 pixel area. N_x and N_y denote the pixel As expected the PARC's reflection is over 25 dB above the surrounding pixels.

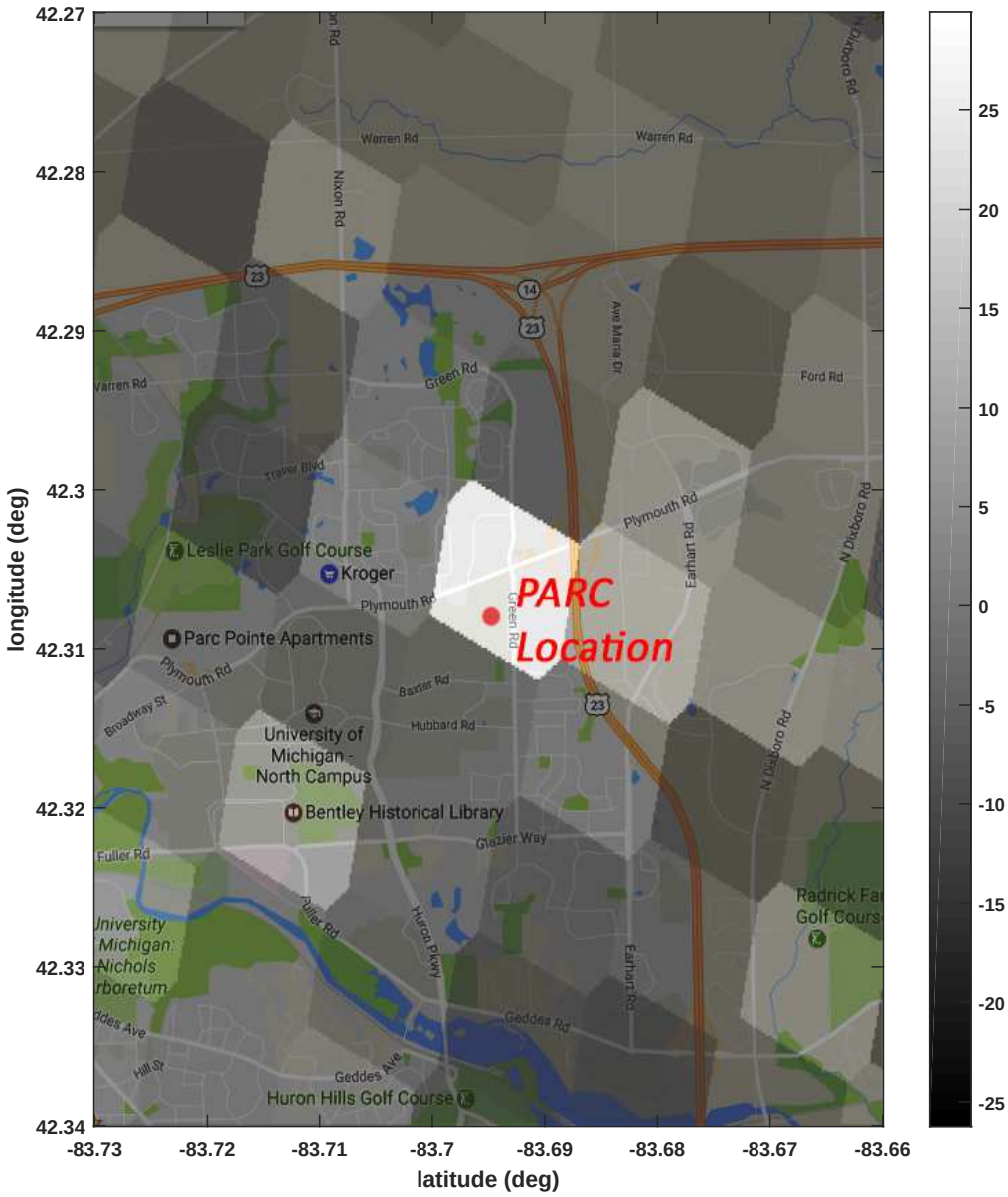

Figure 5.12: The image of the PARC and its surrounding pixels as seen by the SMAP satellite overlayed on the map of the area. The gray scale rectangles show the approximate coverage area of each pixel and their brightness is proportional to the intensity of the backscattering in dB scale

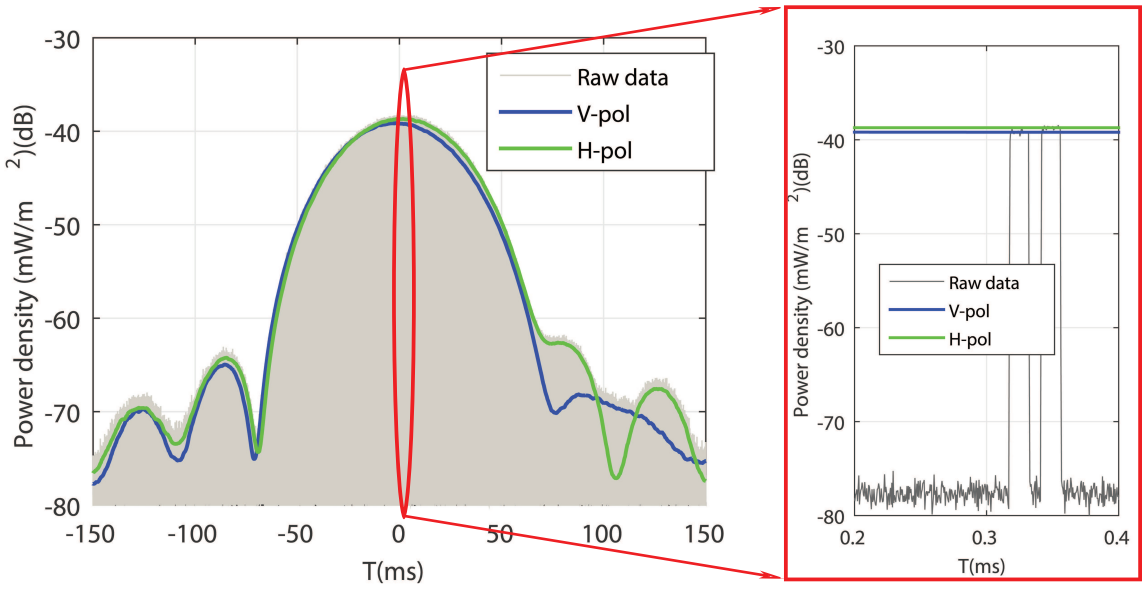

Figure 5.13: The SMAP signal as received by the PARC. This information can be used to characterize the radiation pattern of the SMAP radar. It can also be used to monitor the performance of SMAP for possible malfunctions.

PARC which corresponds to a 40 dB dynamic range for radiation pattern characterization of the SMAP radar. The difference between the received power in v and h channels is due to misalignments between the satellite and the PARC and Faraday's rotation through the atmosphere.

5.6 Conclusions

A single-antenna polarimetric active radar calibrator to be used with NASA's SMAP radar is introduced. It is shown that due to the large footprint of the SMAP radar, a point calibration target with an RCS of 75 dBsm or more is needed to achieve a 20 dB or better signal-to-clutter ratio for calibration. An orthomode transducer was used to isolate the transmit and receive isolation and better than 60 dB of isolation was initially achieved over the desired bandwidth. The isolation was improved further using a number of techniques including an external leakage cancellation circuit and a perturbation method. A stable-gain amplifier system with thermal stability of better 0.1 dB over the temperature range

of -25°C to 40°C was fabricated and integrated with the antenna. The very large RCS of the PARC was measured using a three-stage non-intrusive measurement technique and the results were presented. The PARC was deployed during the operation period of SMAP and satisfactory performance of the PARC was verified using the data collected by the SMAP radar.

CHAPTER 6

An Accurate Circuit Model For the Two-port Loop Antenna

6.1 Introduction

The HF band (1 MHz to 30 MHz) is commonly used for long range applications because of the extremely large wavelength at these frequencies. The large wavelength allows for better penetration through common obstacles and is less prone to multipath and fading effects. In addition, under the right conditions especially towards the lower end of the band, HF radio waves are reflected by the ionosphere allow for cross-contitential communication or over the horizon radar applications.

Traditional methods of direction finding such as using an array of antennas with scalar outputs is often impractical at the HF band because of the required spacing between the array element which increases linearly with the wavelength. An alternative approach is to use vector sensors that are capable of measuring a vector quantity, such as the three-dimensional electric field or magnetic field, instead of a scalar value. [102]. Neglecting the multi-path effects, five independent field components (e.g. three components of electric field and two components of magnetic field) are required to uniquely determine the field direction of arrival; however, in multi-path environments more field components will be needed. The electric field components can be measured using short dipoles and the magnetic field components can be measured using loop antennas. Accurate direction finding

using the field components requires all the probes to be co-located. Due to physical constraints and interference effects, co-locating loops and dipoles that are oriented in different directions is impractical.

To reduce the inaccuracies due to interference effects a two-port loop antenna configuration is proposed [81]. This antenna is configured to have two ports and is capable of simultaneously measuring one component of electric field and one component of magnetic field. Fig.6.1 shows the principle of operation of this antenna for the transmission line (loop) mode and the transverse dipole modes. It is assumed that the circumference of the loop is small compared to the wavelength. If the two ports are excited completely out of phase, the current distribution on the antenna is uniform and the antenna has the radiation patten and other characteristics of a loop antenna. If the two ports are excited in phase, symmetry of the structure can be exploited to split the antenna into two curved dipoles. Since the two dipoles are excited identically and placed close to each other, the radiation pattern of the antenna with this excitation is similar to that of a dipole antenna. In this mode, the currents on the left and right sides are symmetric with zeros at the top and bottom of the antenna. Using reciprocity, it then follows that in the receiving mode with the two ports open-circuited, the sum of the received voltages is proportional to the component of the incoming electric field that is parallel to the direction of the ports. Similarly, the difference between the received voltages is proportional to the component of the incoming magnetic field perpendicular to the plane of the loop. These relations are summarized in Fig.6.2.

The advantage that the two-port loop antenna provides is simplicity in the required antenna structure. Basically, three such probes can be placed orthogonal to each other at the same location. This configuration is shown in Fig.6.3. Each probe measures one component of the electric field and one component of the magnetic field. Therefore three orthogonal probes are sufficient to measure all six field components. Such arrangement also provides minimal mutual coupling. The direction of arrival can be estimated using

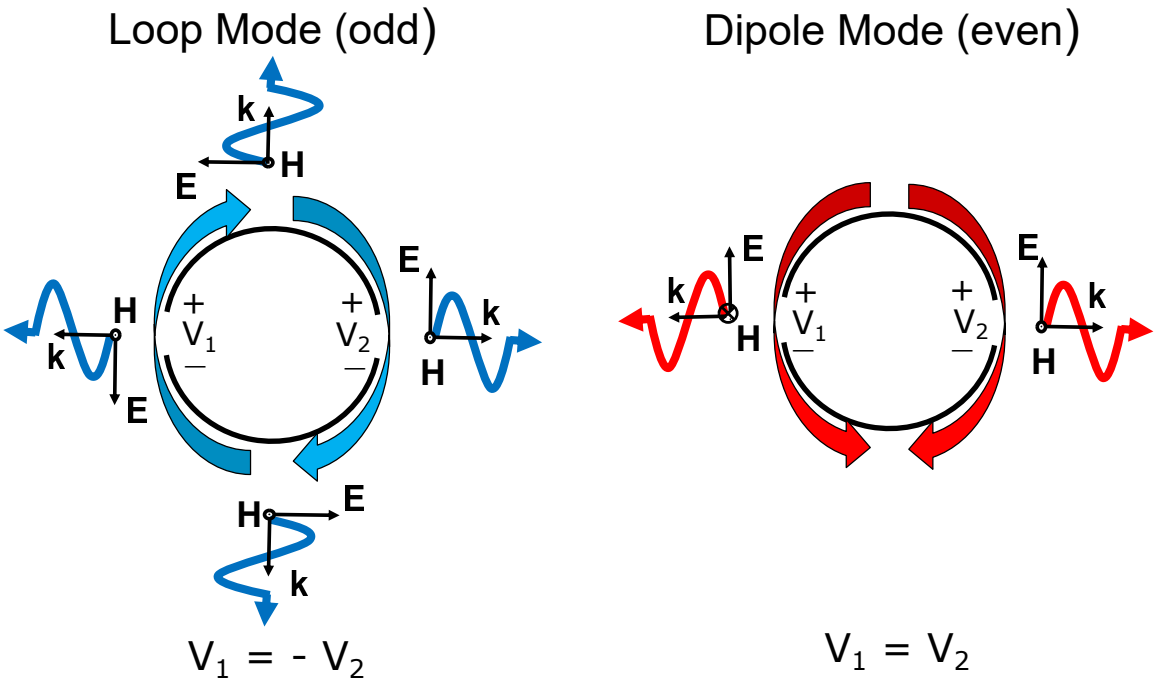

Figure 6.1: The principle of operation of the two-port loop antenna. The structure acts like a loop antenna if the two excitations are out of phase and a dipole antenna if the excitations are in phase.

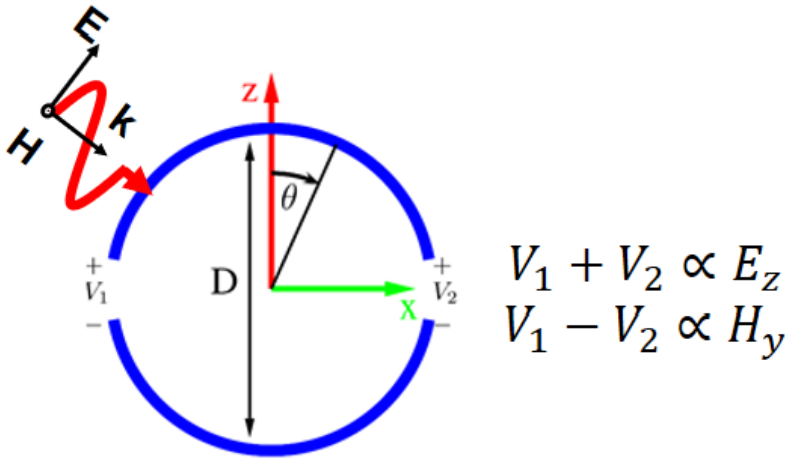

Figure 6.2: Assuming the loop circumference is much smaller than the wavelength, the received open-circuit voltages can be related to the incident electric and magnetic fields

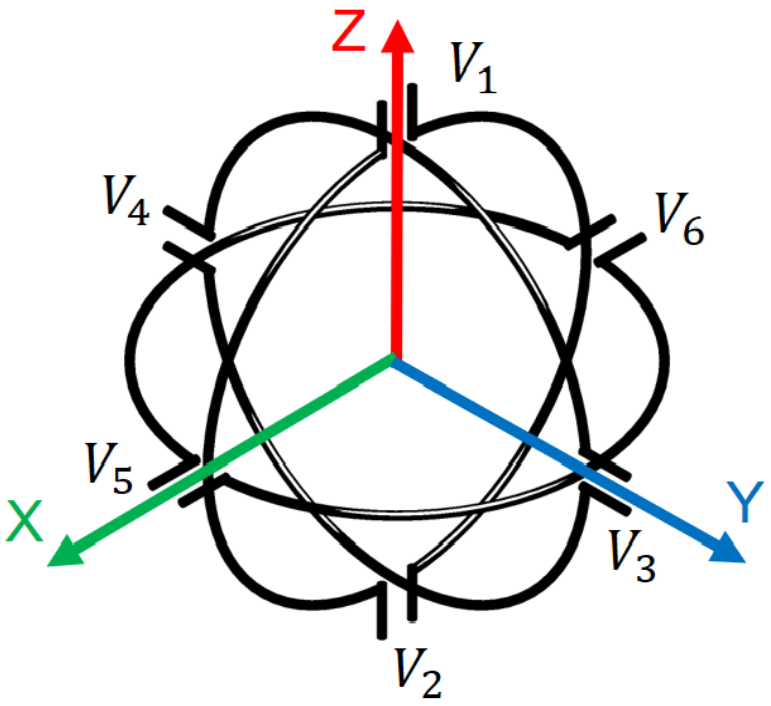

Figure 6.3: Three orthogonal two-port loops can be placed at the same position to measure all 6 components of the incident electric and magnetic fields.

the cross product of the vector electric and magnetic field. Careful study of the retrieval method shows that even in the absence of noise and other sources of interference, there is a difference between the detected direction of arrival and the actual direction of arrival. This error is due to the small loop approximation used in our analysis. Fig.6.4b shows the detected and actual direction of arrival for several arrival angles. The results are obtained by first finding the received voltages for each angle of arrival using a full-wave simulation and then estimating the direction of arrival using the voltages. The simulation setup is shown in Fig.6.4a. The error in direction of arrival estimation for loops of different sizes is plotted in Fig.6.5 as a function of the actual angle of arrival. The simulation results show that accurate results can be obtained only for extremely small loops (C = λ / 30). The disadvantage of using extremely small loops is that the received signal becomes extremely weak and hard to detect. The accuracy of direction finding can be improved using a more sophisticated model for the two-port loop antenna than the small loop assumption.

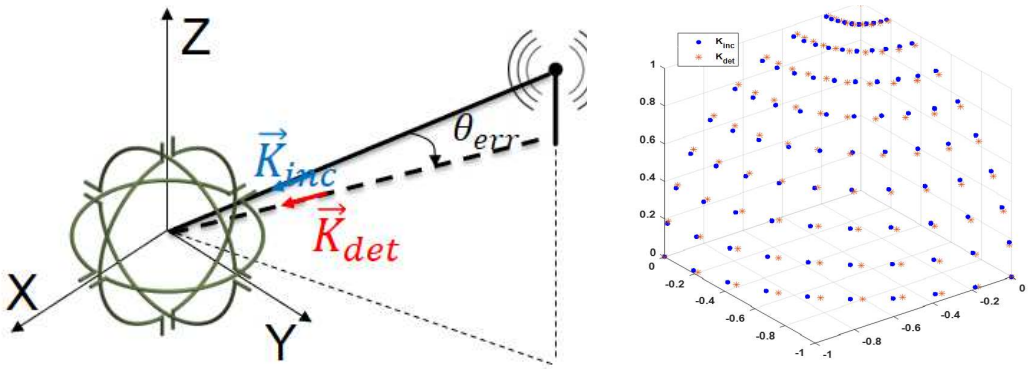

(a) simulation setup

(b) detected direction of arrival

Figure 6.4: The simulation setup and detected angle of direction of arrival compared to the actual angle of arrival. There is a small difference between the two due to the small loop approximation.

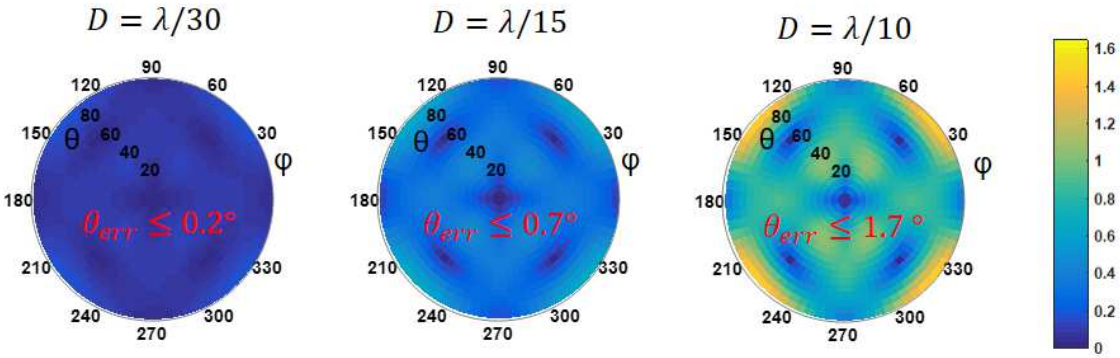

Figure 6.5: The error in retrieved direction of arrival as a function of the actual elevation angle, θ, and azimuth angle, ϕ, of the incident field.

In this chapter, a simple circuit model applicable for a wide frequency range is developed for which the values of the lumped elements are related to the physical parameters (i.e. size and shape) of the split-loop. Numeric values of the circuit components are found using a full-wave simulation of the loop's passive Z-parameters. This model also provides a more accurate lumped element circuit model for the conventional loop antennas simply by short circuiting one of the two ports of the split-loop model. The circuit model is also used to predict the gain pattern of the antenna very accurately. The received voltage due to the transverse dipole mode currents as well as the transmission line mode currents are taken into account. The accuracy of this model is examined for loops with circumferences up to 1.1λ and is compared with the commonly used parallel L-C model and the transmission line model [89]. The circuit model is then used to develop an algorithm for direction of arrival estimation based solely on the received open-circuit voltages at the antenna terminals.

6.2 The Circular Split Loop

When a conventional loop antenna is illuminated by an incident wave, both the transverse dipole mode and the transmission line modes are excited [82]. The amplitude of the dipole mode excitation is directly proportional to the incident electric field in the plane of the loop and in the direction of the feed, whereas the transmission line mode currents are proportional to the incident magnetic field perpendicular to the plane of the loop. The received voltage observed at the terminal of the small loop has contributions from both modes. To isolate the received voltage due to transmission line mode alone, a two-port loop antenna configuration can be used. Here we propose a new circuit model for this antenna that is depicted in Fig.6.6b. The two-port loop antenna can be viewed as two curved short dipoles that are connected to each other at the two ends. These short dipoles are modeled as a series LC circuit and a voltage source whose amplitude, V_{Σ} is related to the incident electric field in the direction of the dipole (the diagonal branches in Fig.6.6b). In addition to

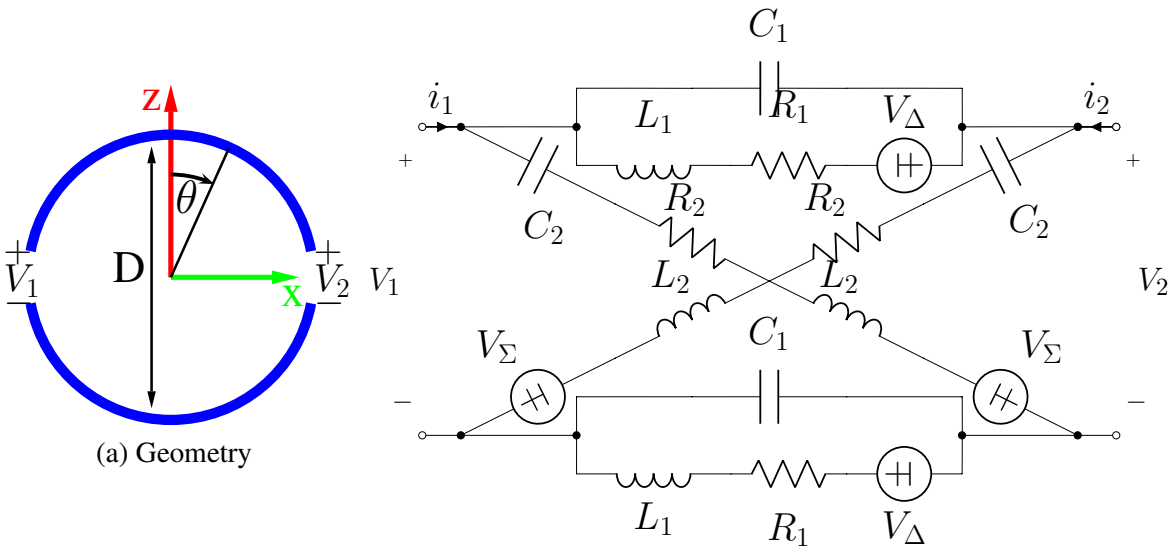

(a) Geometry

(b) Circuit model

Figure 6.6: Split loop geometry and circuit model. The dipole mode and the transmission line mode excitations are respectively proportional to the incident electric and magnetic fields.

the dipole mode, the transmission line mode can also be excited in which case the antenna acts like a small loop and can be modeled with a parallel LC circuit and a voltage source whose amplitude, V_Δ is linearly related to the magnetic field perpendicular to the plane of the loop (the horizontal branches). The radiation resistances of the transmission line and dipole modes are accounted for by R_1 and R_2 respectively. The values of the capacitors and inductors are independent of the excitation and are functions of the geometry of the loop structure. Noting the symmetry, the intrinsic equations of the two port network of Fig.6.6 can be easily derived:

$$\begin{bmatrix} V_1 \\ V_2 \end{bmatrix} = \frac{1}{2} \begin{bmatrix} Z_2 + Z_1 & Z_2 - Z_1 \\ Z_2 - Z_1 & Z_2 + Z_1 \end{bmatrix} \begin{bmatrix} i_1 \\ i_2 \end{bmatrix} + \begin{bmatrix} 1 & k_1 \\ 1 & -k_1 \end{bmatrix} \begin{bmatrix} V_\Sigma \\ V_\Delta \end{bmatrix} \tag{6.1}$$

where,

$$Z_1 = \frac{j\omega L_1 + R_1}{1 - \omega^2 L_1 C_1 + j\omega R_1 C_1} \tag{6.2}$$

$$Z_2 = \frac{1 - \omega^2 L_2 C_2 + j\omega R_2 C_2}{j\omega C_2} \tag{6.3}$$

$$k_1 = \frac{1}{1 - \omega^2 L_1 C_1 + j\omega R_1 C_1} \tag{6.4}$$

Approximate expressions for the radiation resistances of loop and dipole antennas exist in the literature [88, 103] and are, respectively, given by:

$$R_1 = \frac{1}{2} R_r^{loop} = \frac{(\omega\mu D)^2}{16\eta} \int_0^{\pi} J_1^2(\beta a sinx) sinx dx \tag{6.5}$$

$$R_2 = R_r^{dipole} = 20\pi^2 \left(\frac{L^{dipole}}{\lambda} \right)^2 \tag{6.6}$$

In this equation, R_r^{dipole} represents the radiation resistance of a straight dipole antenna with the length of L^{dipole}. Since the two dipoles that are forming the two-port loop antenna are half circles rather than straight lines, they exhibit a different radiation resistance than that of a straight dipole of the same length. An approximate solution for the radiation resistance can be found by using a different length, L^{dipole}, than the physical length of the dipole, $\pi D/2$. The relation between the open circuit voltages of the two ports, V_1^{OC} and V_2^{OC} and the voltage sources in the model, V_Σ and V_Δ can be found by setting $i_1 = i_2 = 0$ in (1):

$$V_1^{OC} + V_2^{OC} = 2V_\Sigma,\ V_1^{OC} - V_2^{OC} = 2k_1 V_\Delta \tag{6.7}$$

A very good approximation for V_Σ due to an incident field $\vec{E}^{inc}$ can be found by assuming a standing wave current distribution on the circumference of the loop when the dipole mode is excited. If θ and ϕ represent the spherical coordinates as depicted in Fig.6.6a, the dipole

mode current distribution on the loop can be expressed as follows:

$$I(\theta, \phi = 0) = I(\theta, \phi = \pi) = sin\left(\frac{kD}{2}\left(\frac{\pi}{2} - \left|\frac{\pi}{2} - \theta\right|\right)\right) \tag{6.8}$$

Using the reciprocity theorem, V_{Sigma} can be found:

$$\begin{aligned} V_\Sigma = & \frac{1}{sin(\frac{kD\pi}{4})}\int_0^\pi \frac{D}{2} I(\theta, \phi = 0)\hat{\theta}.\vec{E}^{inc}(\theta, \phi = 0)d\theta \\ & + \frac{1}{sin(\frac{kD\pi}{4})}\int_0^\pi \frac{D}{2} I(\theta, \phi = \pi)\hat{\theta}.\vec{E}^{inc}(\theta, \phi = \pi)d\theta \end{aligned} \tag{6.9}$$

The above integrals can be calculated numerically for an arbitrary incident field. Alternatively, a Taylor series expansion of the incident field in the $x - z$ plane about the center of the loop can be used to find approximate analytic solutions for the integrals. The contribution from different components of the incident field on the received voltages can then be calculated separately. The component of $\vec{E}^{inc}$ in the $x - z$ plane near the origin can be expressed as:

$$\begin{aligned} \vec{E}^{inc}(x - z) = & \hat{x}\left(E_x + x\frac{\partial E_x}{\partial x} + z\frac{\partial E_x}{\partial z}\right. \\ & \left. + \frac{1}{2}x^2\frac{\partial^2 E_x}{\partial x^2} + \frac{1}{2}z^2\frac{\partial^2 E_x}{\partial z^2} + xz\frac{\partial^2 E_x}{\partial x \partial z}\right) \\ & + \hat{z}\left(E_z + x\frac{\partial E_z}{\partial x} + z\frac{\partial E_z}{\partial z}\right. \\ & \left. + \frac{1}{2}x^2\frac{\partial^2 E_z}{\partial x^2} + \frac{1}{2}z^2\frac{\partial^2 E_z}{\partial z^2} + xz\frac{\partial^2 E_z}{\partial x \partial z}\right) \end{aligned} \tag{6.10}$$

V_Σ can be found by substituting (6.10) and (6.8) in (6.9):

$$\begin{aligned} V_\Sigma = & L_{eff}^{dipole} E_z + D^2 D_1 \frac{\partial^2 E_z}{\partial x^2} + D^2 D_2 \frac{\partial^2 E_z}{\partial z^2} \\ & + D^2 D_3 \frac{\partial^2 E_x}{\partial x \partial z} \end{aligned} \tag{6.11}$$

where L_{eff}^{dipole}, D_1, D_2 and D_3 depend on the shape of the loop as well as frequency. These parameters can be calculated analytically for circular loops using:

$$L_{eff}^{dipole} = \frac{D}{sin\left(\frac{kD\pi}{4}\right)} \int_0^{\pi/2} sin\theta sin\left(\frac{kD}{2}\theta\right) d\theta \tag{6.12}$$

$$D_1 = \frac{D}{8sin\left(\frac{kD\pi}{4}\right)} \int_0^{\pi/2} sin^3\theta sin\left(\frac{kD}{2}\theta\right) d\theta \tag{6.13}$$

$$D_2 = \frac{D}{8sin\left(\frac{kD\pi}{4}\right)} \int_0^{\pi/2} sin\theta cos^2\theta sin\left(\frac{kD}{2}\theta\right) d\theta \tag{6.14}$$

$$D_3 = 2D_2 \tag{6.15}$$

The differential voltage, V_Δ is the induced voltage on the loop due to the incident magnetic field and can be calculated using Faraday's law:

$$V_\Delta = -\frac{\pi}{8} jkD^2\eta H_y + \frac{1}{2}k^2 S_{eff} D^2 \frac{\partial E_z}{\partial x} \tag{6.16}$$

The second term in (6.16) is a higher order term in frequency and is accounting for a differential voltage generated by the near-field scattering from the loop itself. S_{eff} depends on the geometry of the loop and its value for a number of loop shapes is provided in the last section of this paper. Because of this term, the magnetic field cannot be directly recovered by measuring the open circuit voltages of the two ports. However, the second term in (6.16) is proportional to k^3 and therefore decays very rapidly as frequency decreases. This term and higher order modes in (6.11) can be neglected for small loops. Under the small loop assumption, the field components can be found in terms of the measured open circuit voltages:

$$E_z \approx \frac{V_1^{OC} + V_2^{OC}}{2L_{eff}^{dipole}},\ H_y \approx 4\pi j \frac{V_1^{OC} - V_2^{OC}}{Z_0 k_1 kD^2} \tag{6.17}$$

It is interesting to note that a more accurate circuit model for the single-port loop than what is normally considered for a small loop antenna (parallel LC) can be obtained by short

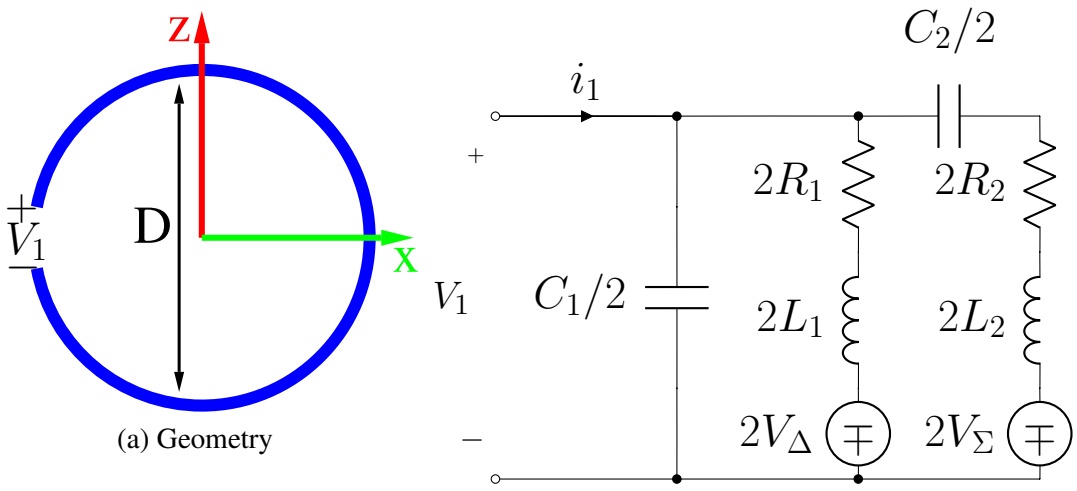

(a) Geometry

(b) Circuit model

Figure 6.7: Geometry and circuit model of a conventional one-port loop antenna. The circuit model is obtained by short-circuiting one terminal of the two-port model.

circuiting the second port of the split-loop as shown in Fig.6.7. This circuit model can be used to solve for V_1:

$$V_1 = \frac{2Z_1Z_2}{Z_1+Z_2} i_1 + \frac{2Z_1}{Z_1+Z_2} V_\Sigma + \frac{2Z_2}{Z_1+Z_2} V_\Delta \tag{6.18}$$

This equation for the open circuit voltage of the conventional loop antenna takes into account contributions from both transmission line and dipole modes. In the absence of external fields, this equation gives an expression for the input impedance of the single-port loop antenna by setting V_Σ=V_Δ=0:

$$Z_{in} = \frac{2Z_1Z_2}{Z_1+Z_2} \tag{6.19}$$

As will be shown next, this circuit model is more accurate than the commonly used models at high frequencies.

6.3 Verification

In this section the accuracy of the proposed circuit model for the two-port antenna is verified with the aid of a finite element based full-wave solver, ANSYS HFSS 2014. The two-port network is first modeled in the absence of any incident fields and its Z parameters are extracted by exciting the ports individually. The proposed model predicts that quantities $Z_1 = Z_{11} - Z_{12}$ and $Z_2 = Z_{11} + Z_{12}$ as defined in (6.2) and (6.3) are impedances of parallel and series LC circuits respectively. The circuit components can be found by basic fitting of Z_1 and Z_2 of full-wave analysis to the theoretical equations. These values for a two-port loop with diameter of $D = 2m$, wire thickness of $d = 1cm$ and terminal gap size of $g = 10cm$ are found to be: $L_1 = 3.37\mu H, C_1 = 3.95pF, L_2 = 1.14\mu H$ and $C_2 = 8.39pF$. The Z parameters calculated using the circuit and those obtained from the full-wave simulation are plotted and compared in Fig.6.8 and excellent agreement between the full-wave analysis and the circuit model is demonstrated. Equation (6.19) provides a closed form expression for the input reactance and resistance of a single port loop antenna which are compared to the full-wave analysis results in Fig.6.9 and Fig.6.10. The full-wave results are also fit to the traditional parallel LC and transmission line models which are plotted as well for comparison. As seen in the graph all models have excellent agreement for circumferences smaller than 0.45λ. However, the proposed circuit model agrees much more accurately with the full-wave analysis for larger loops with circumferences up to 1.1λ.

The circuit model is also validated using full-wave analysis when the antenna is illuminated by an incident plane wave. The source voltages for $\vec{E}^{inc} = 1V/m\hat{\theta}$ and $\hat{k} =$

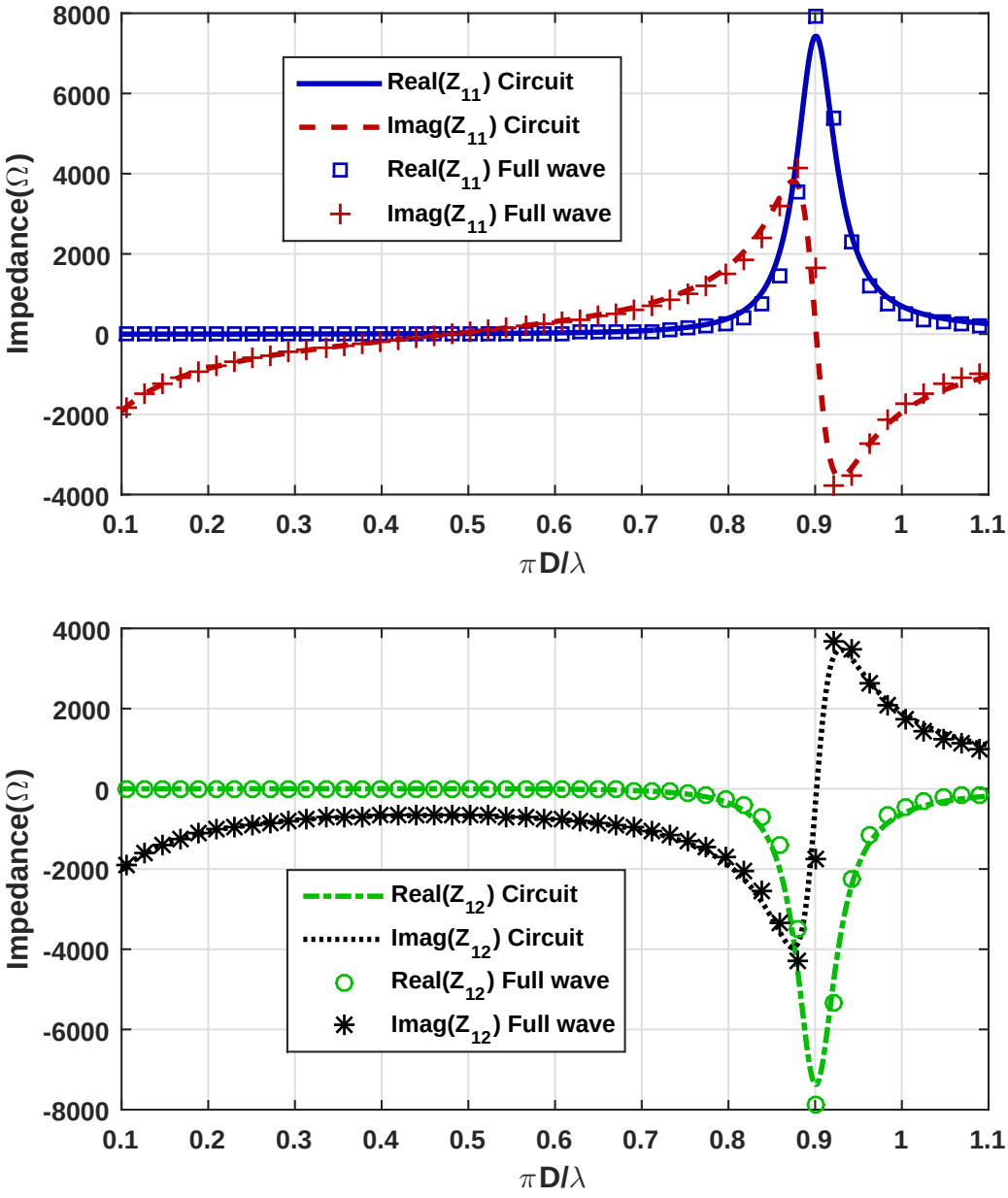

Figure 6.8: The Z matrix of the two-port loop antenna using full-wave analysis and proposed circuit model.

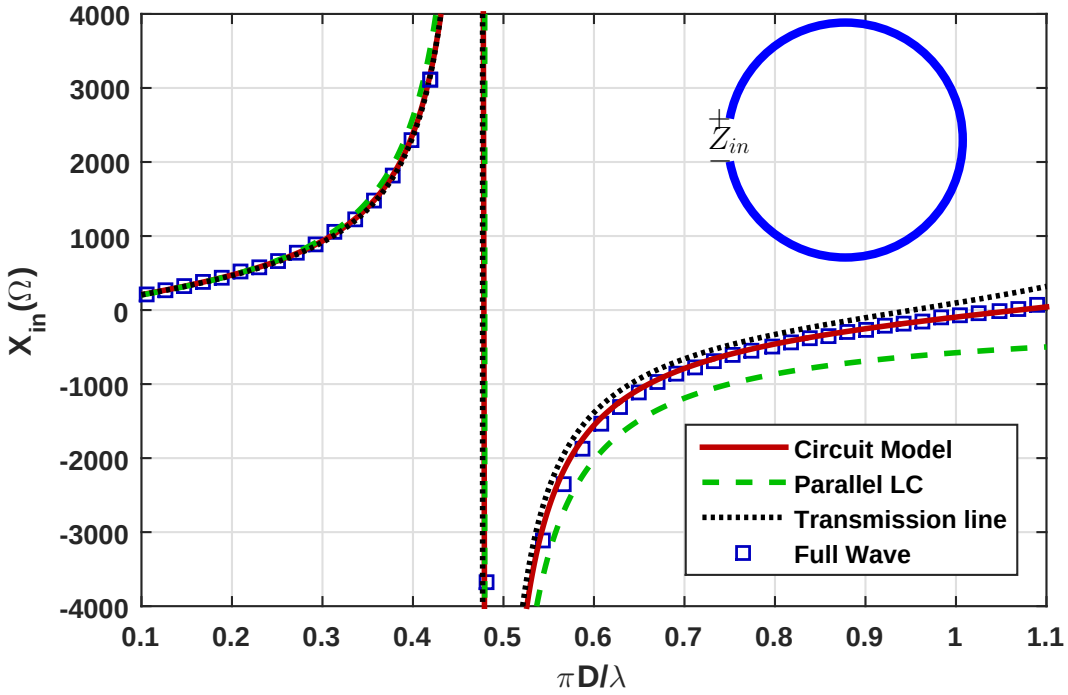

Figure 6.9: Input reactance of a single port loop antenna as predicted by full-wave analysis, our proposed method and traditional LC and transmission line methods. The proposed method provides much more accurate results for larger loops

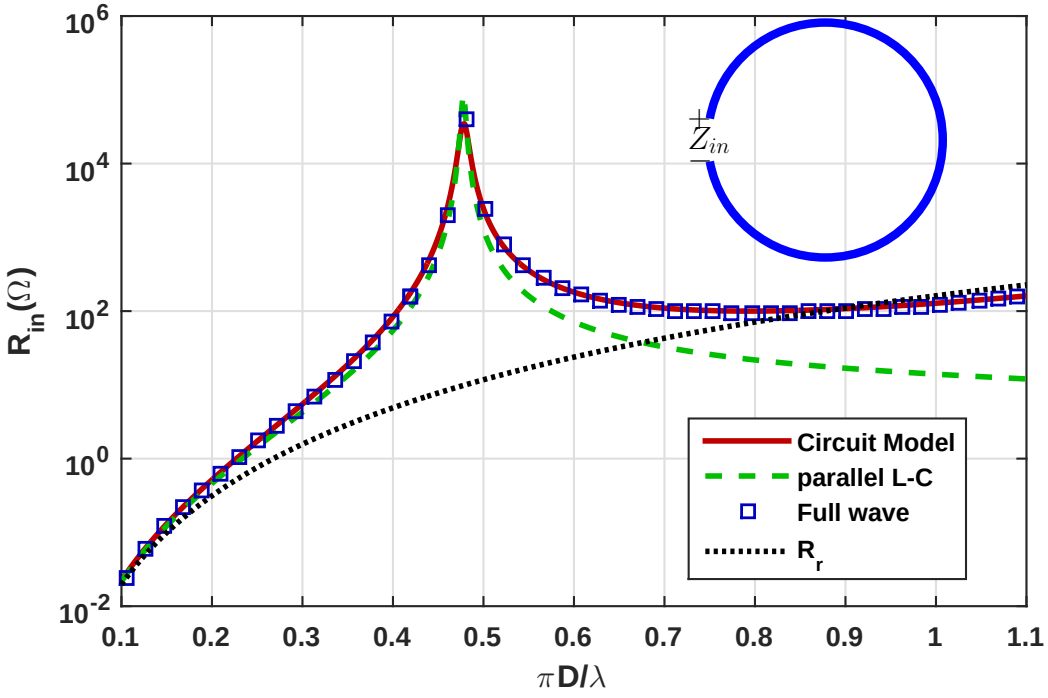

Figure 6.10: Input resistance of a single port loop antenna as predicted by full-wave analysis, our proposed method and traditional LC. The radiation resistance alone is also plotted for comparison. The proposed method provides much more accurate results for larger loops

$-\hat{r}(\theta^{inc}, \phi^{inc})$ are given by:

$$V_\Sigma = -L_{eff}^{dipole} sin\theta^{inc} + k^2 D^2 D_1 sin^3\theta^{inc} cos^2\phi^{inc} + 3k^2 D^2 D_2 sin\theta^{inc} cos^2\theta^{inc} cos^2\phi^{inc} \quad (6.20)$$

$$V_\Delta = -\frac{\pi}{8} jkD^2 \eta cos\phi^{inc} + \frac{1}{2} k^3 S_{eff} D^2 cos\phi^{inc} sin\theta^{inc} \quad (6.21)$$

Fig.6.11 shows the simulation setup and the open circuit voltages received by the single- and two-port loop antennas illuminated by a plane wave with the intensity of $\vec{E}^{inc} = 1V/m\hat{\theta}$ and wave vector direction of $(\theta^{inc}, \phi^{inc}) = (0, 0)$. The incident magnetic field is therefore perpendicular to the surface of the loop and induces a finite open circuit voltage at the terminals. The incident electric field has no $\hat{z}$ component and does not change with x which means both V_Σ and the second term of V_Δ in (6.16) vanish for this incident field. This special case is chosen to validate the performance of the circuit model when only the transmission line mode currents are excited. As seen in the graph, the circuit model closely predicts the behavior of the split-loop and single-port loop antennas for high frequencies up to a point where the circumference of the loop is 1.1λ.

In general situations, E_z and its derivatives with respect to x are not zero. Therefore the magnetic field cannot be fully retrieved using a single-port or two-port loop antenna. The contribution due to $\partial E_z/\partial x$ in (16) is proportional to $1/\lambda^3$ and decays rapidly at lower frequencies. The contribution due to E_z does not appear in the expression for $V_1 - V_2$ of a two port loop antenna as can be seen in (16). The term proportional to E_z in (18) is proportional to ω^2 at lower frequencies whereas the term proportional to H_y for this angle of incidence varies with k. As a results the loop can be used to measure the magnetic field accurately only at low frequencies. As will be shown here, the two-port probe can estimate the magnetic field much more accurately than the single-port loop and for a wider frequency range. To evaluate the circuit model when the E_z and its derivatives are not zero, the same simulation setup as before is used but with the incident field direction of $(\theta^{inc}, \phi^{inc}) =$

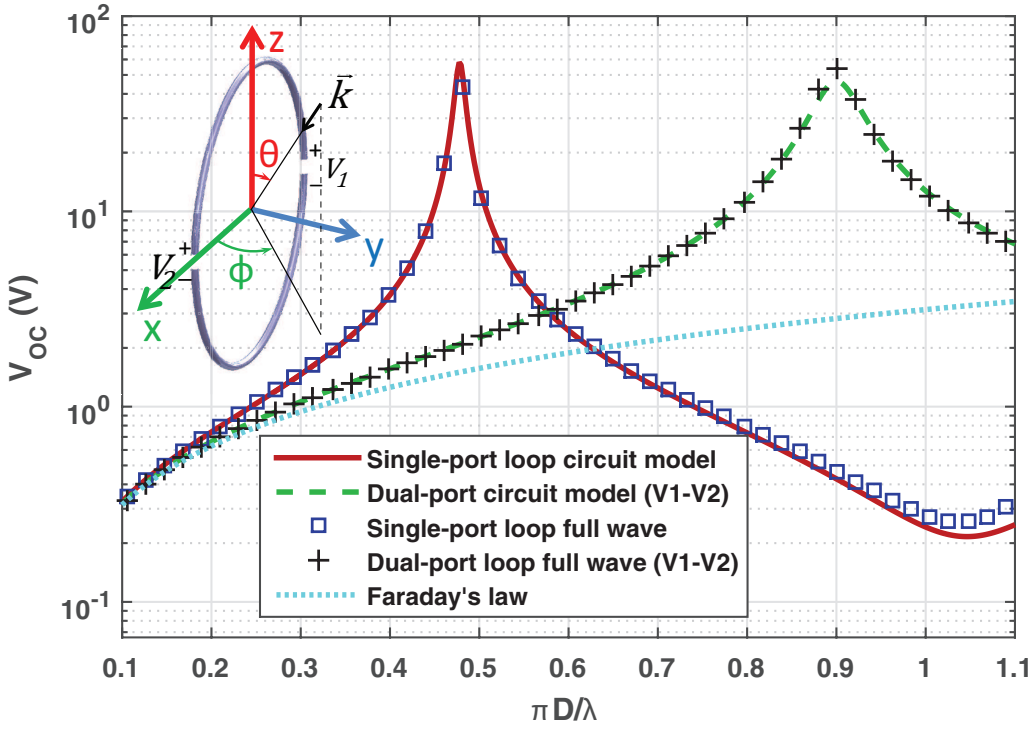

Figure 6.11: Simulated open circuit voltage obtained from the proposed circuit model, full-wave analysis, and Faraday's law. $\vec{E}^{inc} = 1V/m\hat{\theta}$ and $(\theta^{inc}, \phi^{inc}) = (0, 0)$

$(90°, 0)$. The results are depicted in Fig.6.12 and excellent agreement between the proposed circuit model and full-wave analysis is demonstrated. The error in retrieving H_y is below 1% for circumferences less than 0.3λ for the single port loop, and circumferences less than 0.45λ for the dual-port loop antenna. In practice, the error due to these terms can be significantly higher depending on the angle of incidence. In a realistic direction-finding setup, at least three probes are used that are placed perpendicular to each other. If the incident magnetic field makes a small angle with the plane of one of the probes, the main contribution to $V_1 - V_2$ for that probe is from $\partial E_z/\partial x$ which can result in notable errors in direction finding. The accuracy of direction finding can be significantly improved by using redundant probes [79].

The proposed circuit model can also be used to find the received voltage at the antenna terminals for any arbitrary termination impedance. Therefore the antenna factor and consequently the gain of the antenna can be calculated by finding the received voltage for a 50Ω

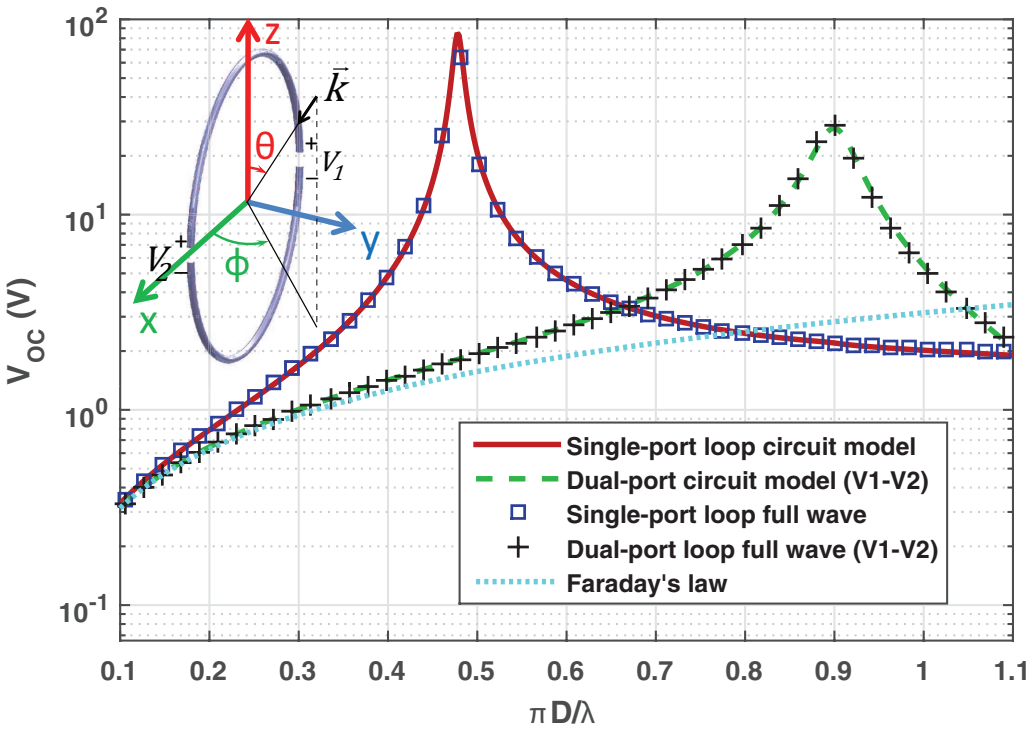

Figure 6.12: Simulated open circuit voltage obtained form the proposed circuit model, full-wave analysis, and Faraday's law. $\vec{E}^{inc} = 1V/m\hat{\theta}$ and $(\theta^{inc}, \phi^{inc}) = (90°, 0)$

load. The radiation pattern of a loop antenna at low frequencies is identical to that of a small magnetic dipole placed perpendicular to the surface of the loop. That is, a donut shaped radiation pattern with maximum radiation in the plane of the loop. It is a well known fact that as the frequency increases, the radiation pattern gradually changes and the maximum radiation shifts towards perpendicular to the surface of the loop. The reason for the shift in radiation pattern is that at lower frequencies mainly the transmission line mode is excited. As the frequency increases, the amplitude of the dipole mode currents increases and causes the radiation pattern to shift. Since the proposed circuit model is capable of estimating the contributions due to both transmission line and dipole modes and their respective magnitudes, this change in the radiation pattern is also predicted by the circuit model. Figures 8 and 9 show the gain of the antenna in $x-y$ and $x-z$ planes respectively. The radiation patterns obtained from the circuit model and the full-wave analysis closely match each other for frequencies up to a point where the circumference of the loop is around a wavelength.

6.4 Other Loop Shapes

The circuit models that are shown in Fig.6.6b and Fig.6.7b can be used to model loop antennas with different shapes and sizes. A number of commonly used shapes, side-fed square, corner-fed square and hexagonal are depicted in Fig.6.15. The effective length and other geometric parameters of the dipoles must be calculated for different shapes individually:

$$L_{eff}^{SF} = \frac{2}{sin(kD)} \int_0^{D/2} sin\left(k\left(D-z\right)\right) dz \tag{6.22}$$

$$D_1^{SF} = \frac{1}{8} L_{eff}^{SF} \tag{6.23}$$

$$D_2^{SF} = \frac{1}{D^2 sin(kD)} \int_0^{D/2} z^2 sin\left(k\left(D-z\right)\right) dz \tag{6.24}$$

$$D_3^{SF} = \frac{2}{D sin(kD)} \int_0^{D/2} x sin(kx) dx \tag{6.25}$$

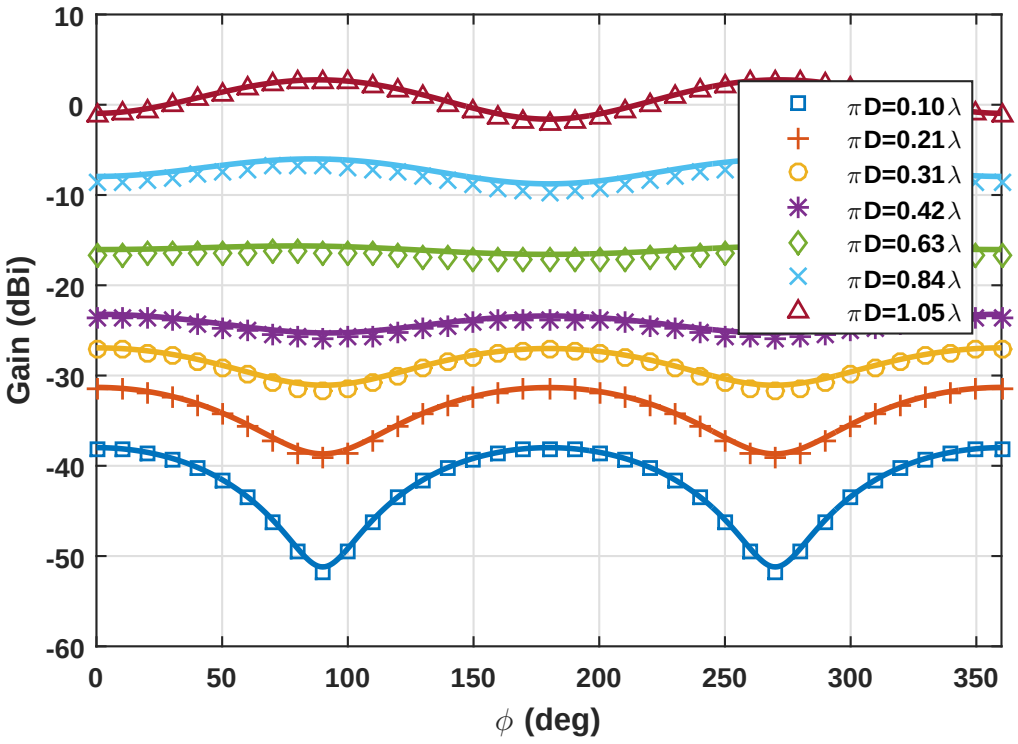

Figure 6.13: Radiation pattern of the antenna in $x-y$ plane. The circuit model (solid lines) matches closely with the full-wave analysis (markers)

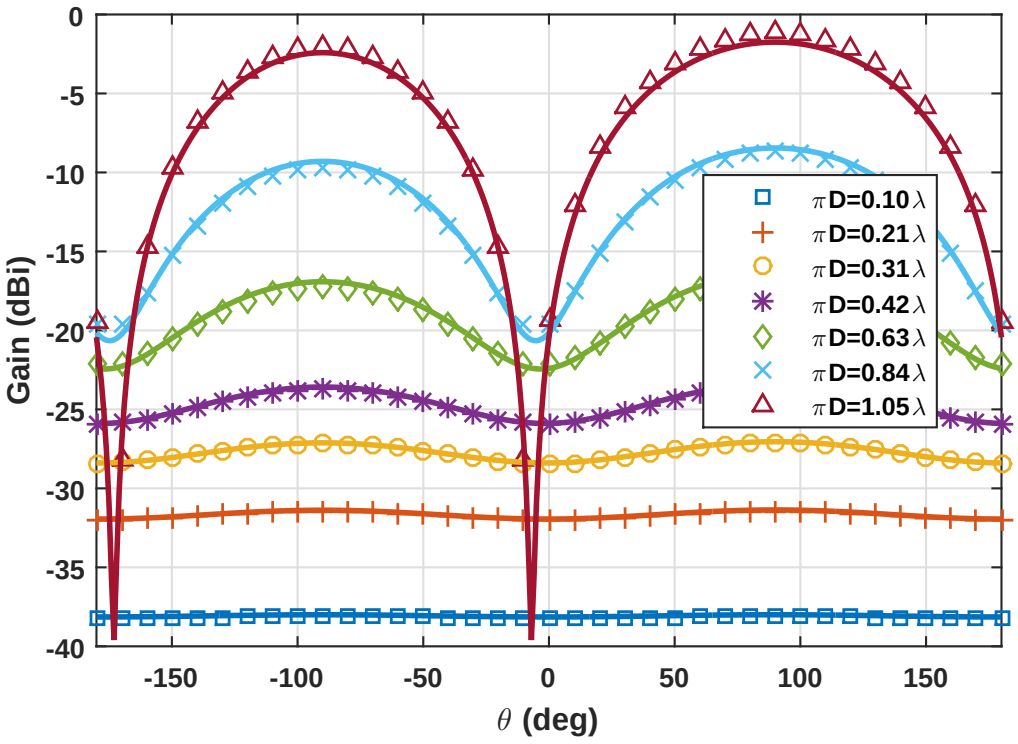

Figure 6.14: Radiation pattern of the antenna in $x-z$ plane. The circuit model (solid lines) matches closely with the full-wave analysis (markers)

$$L_{eff}^{CF} = \frac{\sqrt{2}}{sin(kD)} \int_0^D sin\left(k\left(D-z\right)\right) dz \tag{6.26}$$

$$D_1^{CF} = \frac{1}{\sqrt{2}sin(kD)} \int_0^D \left(\frac{D}{2} - z\right)^2 sin\left(k\left(D-z\right)\right) dz \tag{6.27}$$

$$D_2^{CF} = \frac{1}{\sqrt{2}sin(kD)} \int_0^D z^2 sin\left(k\left(D-z\right)\right) dz \tag{6.28}$$

$$D_3^{CF} = \frac{1}{\sqrt{2}sin(kD)} \int_0^D z\left(\frac{D}{2} - z\right) sin\left(k\left(D-z\right)\right) dz \tag{6.29}$$

$$\begin{aligned} L_{eff}^{Oct} = & \frac{1}{sin(3kh)} \left(2\int_0^h sin(k(3h-z))dz \right. \\ & \left. + \sqrt{2}\int_h^{3h} sin(k(3h-z))dz\right) \end{aligned} \tag{6.30}$$

$$\begin{aligned} D_1^{Oct} = & \frac{1}{sin(3kh)} \left(\frac{1}{4}\int_0^h sin(k(3h-z))dz \right. \\ & \left. + \frac{1}{\sqrt{2}}\int_h^{3h} \left(\frac{D}{2}+h-z\right)^2 sin(k(3h-z))dz\right) \end{aligned} \tag{6.31}$$

$$\begin{aligned} D_2^{Oct} = & \frac{1}{sin(3kh)} \left(\int_0^h z^2 sin(k(3h-z))dz \right. \\ & \left. + \frac{1}{\sqrt{2}}\int_h^{3h} z^2 sin(k(3h-z))dz\right) \end{aligned} \tag{6.32}$$

$$\begin{aligned} D_3^{Oct} = & \frac{1}{sin(3kh)} \left(D\int_{D/2-h}^{D/2} xsin(k(D/2-x))dx \right. \\ & \left. + \sqrt{2}\int_h^{3h} z\left(\frac{D}{2}+h-z\right) sin(k(3h-z))dz\right) \end{aligned} \tag{6.33}$$

$$h = \frac{D}{2(1+\sqrt{2})}$$

The lumped component values, L_1, L_2, C_1, C_2, and the geometrical parameters L^{dipole}/D and S_{eff}/A must be calculated for loops of different shapes and sizes. The geometrical parameters depend on the shape of the loop and the ratio between its size and wire thickness, D/d. The geometrical parameters as defined here are unitless and are not affected by scaling the loop. The circuit parameters vary with shape, size and D/d of the loop and can easily be scaled for a loop size of D' using $L_i' = D'L_i/D$ and $C_i' = D'C_i/D$. The circuit

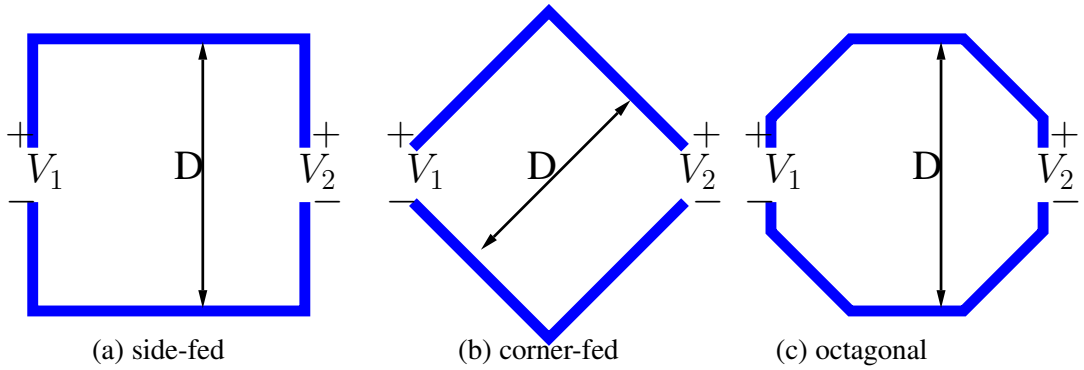

(a) side-fed (b) corner-fed (c) octagonal

Figure 6.15: Geometry of a few commonly used loop antenna configurations.

Table 6.1: Circuit parameters

Shape	L_1	L_2	C_1	C_2	S_{eff}	L^{dipole}
	μH		pF		/A	/D
○	3.34	1.17	4.07	8.35	.144	1.77
□	4.10	1.48	4.88	10.0	.270	2.11
◇	4.09	1.42	5.09	9.49	.167	2.08
⬡	3.50	1.17	4.08	8.85	.153	1.81

parameters are calculated for circular, octagonal, side-fed and corner fed square loops and are tabulated in Table.6.1. The diameter of the circular loop and the side length of the square loops are $D = 2m$ for these calculations and $D/d = 200$. The geometrical parameters for these loop shapes are also calculated and presented in Table.6.1. As an example, the input resistance of a conventional side-fed square loop is calculated using these tables and the results are compared with simulation in Fig.6.16.

The developed circuit model can be used to find the direction of arrival based on the received open-circuit voltages. The circuit model provides an accurate expression for the three-dimensional array manifold of the vector sensor consisting of three orthogonal two-port loop antennas. Several methods have been developed in recent years for direction of arrival estimation using vector sensors [104–107]. These methods are capable of separating multiple sources and mitigating multi-path and noise effects to a great extent [108]. These methods require an accurate knowledge of the three-dimensional array manifold and

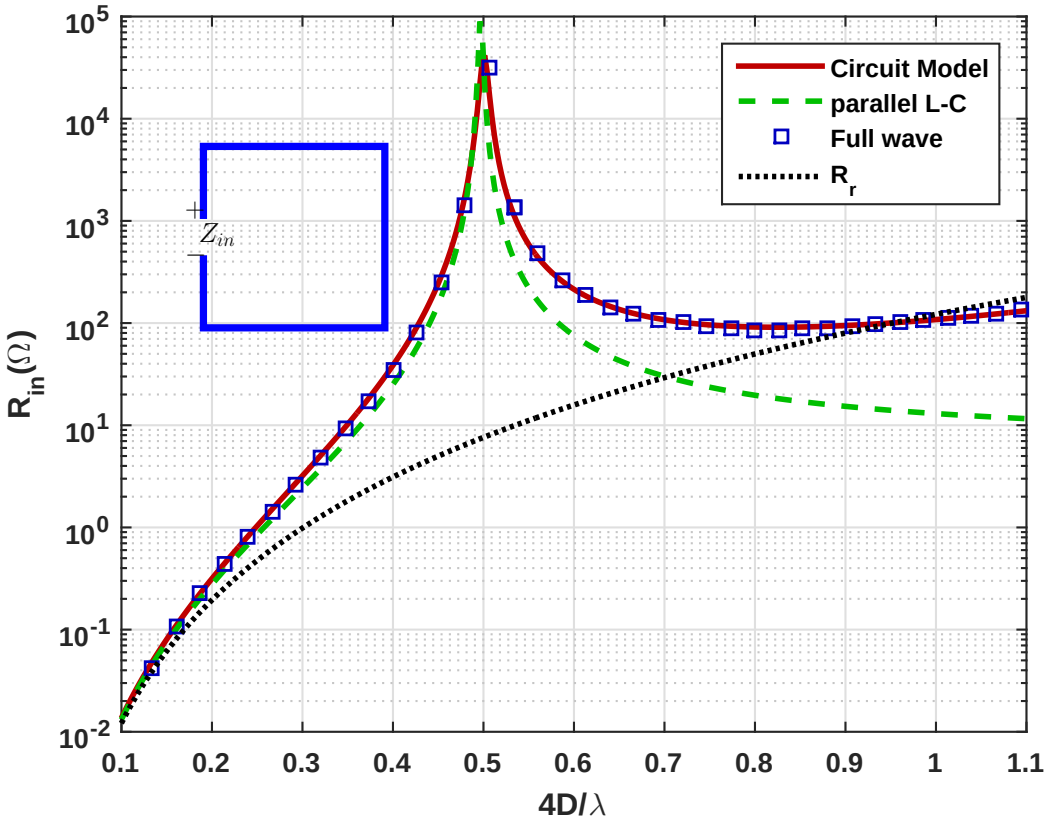

Figure 6.16: Input resistance of a single port loop antenna as predicted by full-wave analysis, our proposed method and traditional LC and transmission line methods. The proposed method provides much more accurate results for larger loops

currently rely on look-up tables populated by measurement data. Therefore a large number of measurements must be performed at different frequencies and a large database must be stored t be used by the retrieval algorithm. The presented circuit model can be used to reduce the number of parameters to a handful of parameters obtained numerically and validated by a limited number of measurements. Discussing the details of the advanced retrieval algorithms is beyond the scope of this thesis. However, a simple algorithm to retrieve the electric and magnetic fields assuming an incident plane-wave is presented to evaluate the performance of the developed circuit model.

Using equations (.6.7), (.6.11), and (6.16), the received voltages can be related to the incident field values as follows:

$$\overline{V} = \overline{\overline{L}}\overline{F} \tag{6.34}$$

where,

$$\overline{V} = \begin{bmatrix} V_1 + V_2 \\ V_3 + V_4 \\ V_5 + V_6 \\ V_1 - V_2 \\ V_3 - V_4 \\ V_5 - V_6 \end{bmatrix}, \overline{\overline{L}} = \begin{bmatrix} 2\mathfrak{f}_1 & 2\mathfrak{g}_3 & 0 & 0 & 0 & 0 \\ 2\mathfrak{g}_2 & 0 & 2\mathfrak{f}_3 & 0 & 0 & 0 \\ 0 & 2\mathfrak{f}_2 & 2\mathfrak{g}_1 & 0 & 0 & 0 \\ 2k_1\mathfrak{j}_2 & 0 & 0 & 0 & 0 & 2k_1\mathfrak{h} \\ 0 & 0 & 2k_1\mathfrak{j}_1 & 0 & 2k_1\mathfrak{h} & 0 \\ 0 & 2k_1\mathfrak{j}_3 & 0 & 2k_1\mathfrak{h} & 0 & 0 \end{bmatrix}, \overline{F} = \begin{bmatrix} E_x \\ E_y \\ E_z \\ \eta H_x \\ \eta H_y \\ \eta H_z \end{bmatrix} \tag{6.35}$$

and,

$$\mathfrak{f}_3 = L_{eff}^{dipole} + D^2 D_1 \frac{\partial^2}{\partial x^2} + D^2 D_2 \frac{\partial^2}{\partial z^2} \tag{6.36}$$

$$\mathfrak{g}_2 = D^2 D_3 \frac{\partial^2}{\partial x \partial z} \tag{6.37}$$

$$\mathfrak{j}_1 = \frac{1}{2\eta} k^2 S_{eff} D^2 \frac{\partial}{\partial x} \tag{6.38}$$

$$\mathfrak{h} = -\frac{\pi}{8} jk D^2 \tag{6.39}$$

In order to find the incident fields from the retrieved voltages, the equation (6.34) must be inverted. However, since the matrix $\overline{\overline{L}}$ is a function of the direction of arrival, $\hat{k}$, its value is not known. Therefore a simple matrix inversion cannot be used to find the field values. Assuming the received voltages are known from measurements, the incident field, $\overline{F}$, the direction of arrival, $\hat{k}$, and the effective length matrix, $\overline{\overline{L}}$ depend on the frequency, and therefore can be expressed as power series:

$$\overline{F}_n = \overline{f}_0 + \overline{f}_1 \left(\frac{D}{\lambda}\right) + \overline{f}_2 \left(\frac{D}{\lambda}\right)^2 + ... + \overline{f}_n \left(\frac{D}{\lambda}\right)^n \tag{6.40}$$

Here $\overline{F}_n$ denotes the field vector accurate to the nth order of D/λ. Similar expressions can be assumed for $\hat{k}_n$ and $\overline{\overline{L}}_n$ as well. The zeroth order quantities can be solved for by setting $D/\lambda = 0$ in (6.34). Since $\overline{\overline{L}}_0$ is not a function of the angle of arrival, the zeroth order field components and direction of arrival can be found using a simple matrix invertin:

$$\overline{F}_0 = \overline{\overline{L}}_0^{-1} \overline{V}, \hat{k}_0 = \frac{\vec{E}_0 \times \vec{H}_0^*}{\|\vec{E}_0 \times \vec{H}_0^*\|} \tag{6.41}$$

Setting $D/\lambda = 0$ means assuming the size of the loop is much smaller than the wavelength which yields the small loop approximation as is apparent from the equation (6.34).

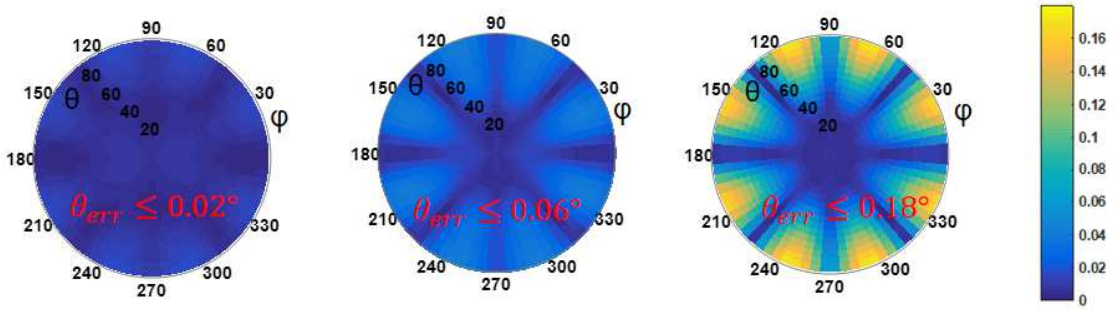

Figure 6.17: The error in retrieved direction of arrival as a function of the actual elevation angle, θ, and azimuth angle, ϕ, of the incident field.

Note that $\overline{\overline{L}}$ depends on the angle of arrival only through the incident wave vector, $\vec{k}$. Recalling the fact that $D\vec{k} = 2\pi D/\lambda \hat{k}$, the first order approximation for $\overline{\overline{L}}$ can be found knowing only the zeroth order approximation of $\hat{k}$:

$$\overline{\overline{L}}_1 = \overline{\overline{L}}\left(\frac{2\pi D}{\lambda}\hat{k}_0\right) \tag{6.42}$$

The first order approximations of all the other variables then follow:

$$\overline{F}_1 = \overline{\overline{L}}_1^{-1}\overline{V}, \hat{k}_1 = \frac{\vec{E}_1 \times \vec{H}_1^*}{\|\vec{E}_1 \times \vec{H}_1^*\|} \tag{6.43}$$

The same procedure can be carried on to obtain higher order approximation of all the variables. However, since the original circuit model is only accurate to the second order of D/λ, continuing the approximation beyond the second order does not increase the accuracy. The performance of the proposed algorithm is verified by carrying out the above procedure on received voltages obtained by full-wave simulation in a similar manner to what was reported for the small loop approximation. The results are plotted in Fig.6.17 and 6.18. The results show an improvement by a factor of 10 in the accuracy of the retrieval algorithm using the circuit model compared to the small loop approximation.

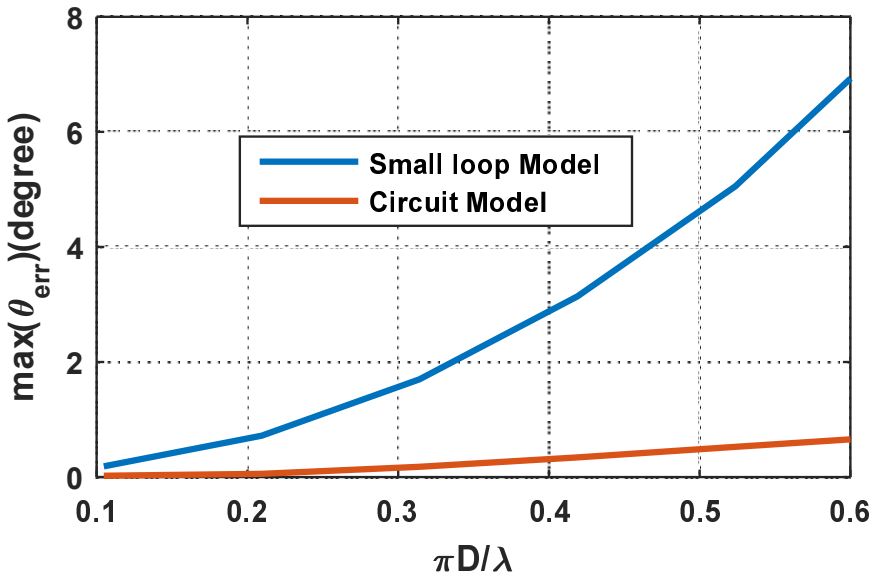

Figure 6.18: The maximum error in retrieved direction of arrival using the circuit model compared to the results obtained using the small loop approximation. The error is reduced by a factor of 10 using the circuit model.

6.5 Conclusion

A simple and accurate circuit model consisting of lumped elements for two-port (split) loop antenna was presented. The circuit was shown to accurately estimate the input impedances and received voltages of the split loop antenna as a field probe. It was demonstrated that the same circuit model can be reduced to model the behavior of a single port loop antenna and provides much higher accuracy than the existing transmission line and lumped element models for the input impedance of the single port loop. The circuit model was verified against full-wave analysis and was shown to have excellent agreement with full-wave results for loop circumferences up to a wavelength. The circuit model was used to develop an algorithm for direction of arrival estimation based on the received open-circuit voltages at the antenna terminals and an it was shown that the accuracy can be improved by a factor of 10 using the proposed circuit model compared to the small loop approximation.

CHAPTER 7

Conclusion and Future Work

7.1 Research Summary and Conclusion

This thesis presents a number of novel technologies to enhance wireless communication in harsh environments. The concepts that are presented are particularly relevant to the problem of ad hoc communication between mobile platforms. In this scheme, the network cannot rely on pre-existing infrastructure to overcome the adverse effects of the communication channel such as multipath and fading. Therefore operation at lower frequencies is desired where the shortcomings of the communication channel are less present.

Chapter 2 focuses on addressing the problem of communication between local platforms at low UHF and VHF frequencies. Because of the wavelength is longer at these frequencies, efficient radiating elements are prohibitively long. Common cases of such radiating elements include long vertical monopole and dipole antennas mounted on armored vehicles. These antennas create air-drag, are suspectable to co-cite interference and increase visibility of armored vehicles. In an effort to eliminate these unwanted effects, optically transparent window embedded antennas are proposed and several antenna geometries for different window shapes and tilt angles are presented.

First, the design of a monopole antenna placed in a sub-wavelength window is discussed and it is demonstrated that a tilted beam can be achieved exploding the inherent asymmetry of a monopole antenna above a finite ground plane. The solid surface of the antenna is then

replaced by a mesh that follows the current directions on the surface of the antenna and has a higher density in places where the surface currents are stronger. It is shown that this nonuniform mesh geometry outperforms a uniform square mesh. Following the monopole design, a dipole antenna for a slightly larger window is presented. A microstrip tapered balun was designed and the performance of the antenna was evaluated using the tapered balun and a standard balun transformer.

The same concepts were used to design a wide-band dipole antenna and a two-element array for the side window and the windshield of a commonly used armored vehicle. These windows have irregular shapes which causes the main beam of the antenna to steer in different directions unwantedly. A mode management technique was presented to suppress the unwanted beam steering. A few method of feeding the two-element array is considered and it is shown that a tilted beam can be achieved by feeding only one element of the array and using the mutual coupling between the two elements to feed the other element. All antennas are fabricated and integrated with the armored windows using a bonding method that involves stacking different layers of the window glass and placing them under high pressure and temperature. The performance of the antennas are evaluated in a number of scenarios including placing the fabricated antennas on an actual vehicle in an outdoor test facility.

In Chapter 3, design of a band-selective ground plane with better opacity and/or better frequency response than those of the traditional wire mesh is presented. The wire mesh was used as a transparent ground plane in the second chapter. A simple miniaturized element frequency selective surface based on square loop unit cells are introduced and the challenges associated with using this design as a reflector for antennas at UHF and VHF bands are presented. In particular, it was shown that the most limitation in fabrication of band-selective ground planes at these frequencies stems from the difficulties in fabricating extremely small gaps between metallic traces to create large enough capacitors. Following the basic studies, a novel design with overlapping capacitors is introduced that requires

fabrication of square loops on the opposite sides of a very thin transparent substrate. It is shown that the novel design can be used to increase the capacitance between the adjacent loops and hence the bandwidth of structure. Moreover, the same alternating pattern can be stacked multiple times to create extremely large capacitor values.

In addition to the single-pole design, a multi-pole stop-band miniaturized MEFSS is introduced that consists of multiple layers of single pole MEFSS. It is shown that the proposed method allows for achieving a wide-band multi-pole response while maintaining a relatively small thickness which renders the design to be light and independent of the angle of incidence. A three pole transparent BSGP was designed using the proposed method and a 10dB insertion loss bandwidth of 2.5 to 1 was demonstrated.

In addition to operation at lower frequencies, the challenges related to the communication channel can be overcome by intelligent use of radio repeaters. However, conventional radio repeaters require a communication protocol and also reduce the available throughput because of the half-duplex nature of these repeaters. Chapter 4 deals with the design of a directional radio repeater system with a simple architecture composed of a transmit antenna, a receive antenna and an amplifier and filter. Because of this simplicity, the repeater is energy efficient and does not require down-conversion and up-conversion with frequency translation and complicated operational protocols to manage users. These properties of the proposed repeater makes it suitable for ad hoc wireless networks since different protocols and channels can be simultaneously supported. Close to 70dB of isolation is achieved between the transmit and receive antennas that allows significant amplification of the received signal to be retransmitted in desired directions. The isolation improvement between the transmit and receive antennas is achieved using a number of techniques. The antennas are separated by a ground plane in between, a polarization mismatch is enforced between the two antennas, and a near-field cancellation technique is used to further reduce the mutual coupling. The near field cancellation is achieved using a two-element receive antenna whose elements are appropriately located with respect to the transmit antenna to cancel the

signal leakage received by each other. The repeater is fabricated and tested in different environments and significant signal coverage enhancement is demonstrated in all cases.

In Chapter 5, a different application for a full-duplex repeater structure is explored. The large isolation between the transmit and receive antennas of full-duplex repeaters enables them to receive a signal retransmit after significant amplification. If the gain of the amplifier and antennas are known with enough accuracy, this device can be used as calibration target for polarimetric radars. A single-antenna polarimetric active radar calibrator to be used with NASA's SMAP radar is introduced. It is shown that due to the large footprint of the SMAP radar, a point calibration target with an RCS of 75 dBsm or more is needed to achieve a 20 dB or better signal-to-clutter ratio for calibration. An orthomode transducer was used to isolate the transmit and receive isolation and better than 60 dB of isolation was initially achieved over the desired bandwidth. The isolation was improved further using a number of techniques including an external leakage cancellation circuit and a perturbation method. A stable-gain amplifier system with thermal stability of better 0.1 dB over the temperature range of -25°C to 40°C was fabricated and integrated with the antenna. The very large RCS of the PARC was measured using a three-stage non-intrusive measurement technique and the results were presented. The PARC was deployed during the operation period of SMAP and satisfactory performance of the PARC was verified using the data collected by the SMAP radar.

Chapter 6 addresses the problem of direction of arrival finding at the HF band (1 MHz to 30 MHz). This frequency band is of particular interest because of its ability to penetrate common obstacles and less prominent multi-path, fading and diffraction effects at these frequencies. In addition, especially towards the lower end of the band, the HF radio waves are reflected by the ionosphere, thereby extending the range of communication beyond the horizon. Direction of arrival estimation at the HF band using baseline method results in an exorbitantly large array of sensors. However, a vector sensor consisting of three orthogonal two-port loop antennas can be used. A simple and accurate circuit model consisting of

lumped elements for the two-port loop antenna was presented. The circuit was shown to accurately estimate the input impedances and received voltages of the split loop antenna as a field probe. It was demonstrated that the same circuit model can be reduced to model the behavior of a single port loop antenna and provides much higher accuracy than the existing transmission line and lumped element models for the input impedance of the single port loop. The circuit model was verified against full-wave analysis and was shown to have excellent agreement with full-wave results for loop circumferences up to a wavelength. The circuit model was used to develop an algorithm for direction of arrival estimation based on the received open-circuit voltages at the antenna terminals and an it was shown that the accuracy of direction of arrival estimation can be improved by a factor of 10 using the proposed circuit model compared to the small loop approximation.

7.2 Future Work

In Chapter 4, a radio repeater for the 2.4 GHz ISM band was introduced. The proposed repeater uses a two-element array as the receiver antenna which results in a lower mutual coupling between the transmit and receive antennas. The transmit antenna in this configuration is a single antenna to make the design and fabrication less complicated. However, the symmetry of the design and therefore the isolation between the antennas can be improved if a two-element antenna is used as the transmitter antenna.

Similarly, improvements in the fabrication procedure can be made to improve the accuracy of fabrication. The theoretical value that is predicted by the numerical simulation is better than 80 dB over the entire band. However, a better than 68 dB isolation was achieved after fabrication. The difference between these values is due to inaccuracies in fabrication, particularly in aligning the two substrates on which the antennas are fabricated. One way to achieve this is to include structure that is used to keep the two substrates together. Such structure will impact the mutual coupling and must be designed at the same time as the

antennas. In addition, a foam pedestal is used as the support structure for all our tests. In practice, a more realistic support structure is required for holding the repeater in place and/or providing power to the repeater. Simulation results show a minimal change in the mutual coupling if a vertical plastic rod, parallel to the polarization of the receive antenna is used. Nevertheless, for best performance, the repeater must be simulated and optimized in the presence of such structure.

The radar calibrator that was introduced in Chapter 5 operates at 1.25 GHz with 100 MHz of bandwidth. However, airborne and space-borne radars utilize a wide range of frequency band including P-band (250 MHz to 500 MHz) and S-band (2 GHz to 4 GHz). The ideas introduced in this thesis are suitable for applications in other frequency bands with slight modifications. For example, using our horn antenna and OMT design is impractical at the P-band (250 MHz - 500 MHz)because the size of the structure would be more quadrupled in every dimension. However, The horn antenna can be replaced by a waveguide opening to reduce the size of the antenna. In this case, further optimization is needed to compensate for the increase in the mutual coupling due to the mismatch between the waveguide opening and free space.

BIBLIOGRAPHY

[1] Q. Spencer, A. Swindlehurst, and M. Haardt, "Zero-forcing methods for downlink spatial multiplexing in multiuser MIMO channels," *IEEE Transactions on Signal Processing*, vol. 52, no. 2, 2004.

[2] D. Gesbert, M. Shafi, D.-S. Shiu, P. Smith, and A. Naguib, "From theory to practice: An overview of MIMO space-time coded wireless systems," *IEEE Journal on Selected Areas in Communications*, vol. 21, no. 3, 2003.

[3] A. Goldsmith, S. Jafar, N. Jindal, and S. Vishwanath, "Capacity limits of MIMO channels," *IEEE Journal on Selected Areas in Communications*, vol. 21, no. 5, 2003.

[4] F. Rusek, D. Persson, B. Lau, E. Larsson, T. Marzetta, O. Edfors, and F. Tufvesson, "Scaling up MIMO : Opportunities and challenges with very large arrays," *IEEE Signal Processing Magazine*, vol. 30, no. 1, 2013.

[5] A. Paulraj, D. Gore, R. Nabar, and H. Bölcskei, "An overview of MIMO communications - A key to gigabit wireless," *Proceedings of the IEEE*, vol. 92, no. 2, 2004.

[6] L. Zheng and D. Tse, "Diversity and multiplexing: A fundamental tradeoff in multiple-antenna channels," *IEEE Transactions on Information Theory*, vol. 49, no. 5, 2003.

[7] D. Benhaddou and A.-F. Ala, *Wireless sensor and mobile ad-hoc networks vehicular and space applications*. 2015. cited By 3.

[8] I. Chlamtac, M. Conti, and J.-N. Liu, "Mobile ad hoc networking: Imperatives and challenges," *Ad Hoc Networks*, vol. 1, no. 1, pp. 13–64, 2003. cited By 724.

[9] G. Zruba, S. Basagni, and I. Chlamtac, "Bluetrees - scatternet formation to enable bluetooth-based ad hoc networks," vol. 1, pp. 273–277, 2001. cited By 246.

[10] K. Bullington, "Characteristics of beyond-the-horizon radio transmission," *Proceedings of the IRE*, vol. 43, no. 10, pp. 1175–1180, 1955. cited By 9.

[11] J. Headrick and J. Thomason, "Applications of high-frequency radar," *Radio Science*, vol. 33, no. 4, 1998.

[12] J. Headrick and M. Skolnik, "Over-the-Horizon Radar in the HF Band," *Proceedings of the IEEE*, vol. 62, no. 6, 1974.

[13] A. Nehorai and E. Paldi, "Vector sensor array processing for electromagnetic source localization," *IEEE Trans. Sig. Proc.*, vol. 42, no. 2, pp. 376–398, 1994.

[14] J. Bull, "Field probe for measuring vector components of an electromagnetic field," Apr. 5 1994. US Patent 5,300,885.

[15] L. DaHan and K. Sarabandi, "Modeling and simulation of near-earth propagation in presence of a truncated vegetation layer," *Antennas and Propagation, IEEE Transactions on*, vol. 55, pp. 949 –957, March 2007.

[16] K. Sarabandi, M. Casciato, and I.-S. Koh, "Efficient calculation of the fields of a dipole radiating above an impedance surface," *Antennas and Propagation, IEEE Transactions on*, vol. 50, pp. 1222–1235, Sep 2002.

[17] M. Roo-Ons, S. Shynu, M. Ammann, S. McCormack, and B. Norton, "Transparent patch antenna on a-si thin-film glass solar module," *Electronics Letters*, vol. 47, no. 2, pp. 85–86, 2011.

[18] T. Peter, T. Rahman, S. Cheung, R. Nilavalan, H. Abutarboush, and A. Vilches, "A novel transparent uwb antenna for photovoltaic solar panel integration and rf energy harvesting," *Antennas and Propagation, IEEE Transactions on*, vol. 62, pp. 1844–1853, April 2014.

[19] A. Katsounaros, Y. Hao, N. Collings, and W. Crossland, "Optically transparent ultra-wideband antenna," *Electronics Letters*, vol. 45, pp. 722–723, July 2009.

[20] M. Gustafsson, A. Karlsson, A. Rebelo, and B. Widenberg, "Design of frequency selective windows for improved indoor outdoor communication," *Antennas and Propagation, IEEE Transactions on*, vol. 54, pp. 1897 – 1900, june 2006.

[21] C. Tsakonas, S. Liew, C. Mias, D. Koutsogeorgis, R. Ranson, W. Cranton, and M. Dudhia, "Optically transparent frequency selective window for microwave applications," *Electronics Letters*, vol. 37, pp. 1464 –1466, nov 2001.

[22] M. D'Amore, V. De Santis, and M. Feliziani, "Equivalent circuit modeling of frequency-selective surfaces based on nanostructured transparent thin films," *Magnetics, IEEE Transactions on*, vol. 48, pp. 703 –706, feb. 2012.

[23] K. Chopra, S. Major, and D. Pandya, "Transparent conductors–a status review," *Thin Solid Films*, vol. 102, no. 1, pp. 1 – 46, 1983.

[24] J. Saberin and C. Furse, "Challenges with optically transparent patch antennas," *Antennas and Propagation Magazine, IEEE*, vol. 54, pp. 10–16, June 2012.

[25] J. Hautcoeur, F. Colombel, M. Himdi, and E. Cruz, "Radiofrequency performances of transparent ultra-wideband antennas," *Progress In Electromagnetics Research C*, vol. 22, pp. 259–271, 2011.

[26] F. Colombel, X. Castel, M. Himdi, G. Legeay, S. Vigneron, and E. Cruz, "Ultrathin metal layer, ito film and ito/cu/ito multilayer towards transparent antenna," *Science, Measurement Technology, IET*, vol. 3, pp. 229–234, May 2009.

[27] T. Yasin, R. Baktur, and C. Furse, "A study on the efficiency of transparent patch antennas designed from conductive oxide films," in *Antennas and Propagation (APSURSI), 2011 IEEE International Symposium on*, pp. 3085–3087, July 2011.

[28] G. Byun, C. Seo, B.-J. Jang, and H. Choo, "Design of aircraft on-glass antennas using a coupled feed structure," *Antennas and Propagation, IEEE Transactions on*, vol. 60, pp. 2088–2093, April 2012.

[29] J. Schaffner, H. Song, A. Bekaryan, H.-P. Hsu, M. Wisnewski, and J. Graham, "The impact of vehicle structural components on radiation patterns of a window glass embedded fm antenna," *Antennas and Propagation, IEEE Transactions on*, vol. 59, pp. 3536–3543, Oct 2011.

[30] Y. Kim, Y. Noh, and H. Ling, "Design of ultra-broadband on-glass antenna with a 250 omega; system impedance for automobiles," *Electronics Letters*, vol. 40, pp. 1566–1568, Dec 2004.

[31] S. Ahn and H. Choo, "A systematic design method of on-glass antennas using mesh-grid structures," *Vehicular Technology, IEEE Transactions on*, vol. 59, pp. 3286–3293, Sept 2010.

[32] M.-S. Wu and K. Ito, "Basic study on see-through microstrip antennas constructed on a window glass," in *Antennas and Propagation Society International Symposium, 1992. AP-S. 1992 Digest. Held in Conjuction with: URSI Radio Science Meeting and Nuclear EMP Meeting., IEEE*, pp. 499–502 vol.1, June 1992.

[33] T. Turpin and R. Baktur, "Meshed patch antennas integrated on solar cells," *Antennas and Wireless Propagation Letters, IEEE*, vol. 8, pp. 693–696, 2009.

[34] Y. Rahmat-Samii and S.-W. Lee, "Vector diffraction analysis of reflector antennas with mesh surfaces.," *IEEE Transactions on Antennas and Propagation*, vol. AP-33, no. 1, pp. 76–90, 1985.

[35] J. Wait and K. Spies, "On the radiation from a vertical dipole with an inductive wire-grid ground system," *Antennas and Propagation, IEEE Transactions on*, vol. 18, pp. 558 – 560, jul 1970.

[36] B. A. Munk, *Frequency Selective Surfaces: Theory and Design*. John Wiley & Sons, Inc., 2005.

[37] R. Langley and E. Parker, "Equivalent circuit model for arrays of square loops," *Electronics Letters*, vol. 18, pp. 294 –296, 1 1982.

[38] E. A. Parker and S. M. A. Hamdy, "Rings as elements for frequency selective surfaces.," *Electronics Letters*, vol. 17, no. 17, pp. 612–614, 1981. Cited By (since 1996): 31.

[39] K. Sarabandi and N. Behdad, "A frequency selective surface with miniaturized elements," *Antennas and Propagation, IEEE Transactions on*, vol. 55, pp. 1239 –1245, may 2007.

[40] E. Parker and A. El Sheikh, "Convoluted array elements and reduced size unit cells for frequency-selective surfaces," *Microwaves, Antennas and Propagation, IEE Proceedings H*, vol. 138, pp. 19 – 22, feb 1991.

[41] F. Bayatpur and K. Sarabandi, "Multipole spatial filters using metamaterial-based miniaturized-element frequency-selective surfaces," *Microwave Theory and Techniques, IEEE Transactions on*, vol. 56, pp. 2742 –2747, dec. 2008.

[42] C. K. Toh, *Ad Hoc Wireless Networks: Protocols and Systems*. Upper Saddle River, NJ, USA: Prentice Hall PTR, 1st ed., 2001.

[43] H. Li, M. Lott, M. Weckerle, W. Zirwas, and E. Schulz, "Multihop communications in future mobile radio networks," *IEEE International Symposium on Personal, Indoor and Mobile Radio Communications, PIMRC*, vol. 1, pp. 54–58, 2002.

[44] R. Pabst, B. Walke, D. Schultz, P. Herhold, H. Yanikomeroglu, S. Mukherjee, H. Viswanathan, M. Lott, W. Zirwas, M. Dohler, H. Aghvami, D. Falconer, and G. Fettweis, "Relay-based deployment concepts for wireless and mobile broadband radio," *IEEE Communications Magazine*, vol. 42, no. 9, pp. 80–89, 2004.

[45] D. Sharp, N. Cackov, N. Laskovi, Q. Shao, and L. Trajkovi, "Analysis of public safety traffic on trunked land mobile radio systems," *IEEE Journal on Selected Areas in Communications*, vol. 22, no. 7, pp. 1197–1205, 2004.

[46] M. Merro, "An observational theory for mobile ad hoc networks (full version)," *Information and Computation*, vol. 207, no. 2, pp. 194–208, 2009.

[47] M. Lee, B. Keum, Y. Son, J.-W. Kim, and H. Lee, "A new low-complex interference cancellation scheme for wcdma indoor repeaters," *Proceedings - 2008 IEEE Region 8 International Conference on Computational Technologies in Electrical and Electronics Engineering, SIBIRCON 2008*, pp. 457–462, 2008.

[48] M. Lee, B. Keum, M. Park, Y. Shim, H. Lee, and D. Woo, "A frequency domain approach for complexity reduction in wideband radio interference cancellation repeaters," *International Conference on Signal Processing Proceedings, ICSP*, pp. 1971–1976, 2008.

[49] K. Sarabandi and Y. Song, "Subwavelength radio repeater system utilizing miniaturized antennas and metamaterial channel isolator," *IEEE Transactions on Antennas and Propagation*, vol. 59, no. 7, pp. 2683–2690, 2011.

[50] Y. J. Song and K. Sarabandi, "Miniaturized radio repeater for enhanced wireless connectivity of ad-hoc networks," *IEEE Transactions on Antennas and Propagation*, vol. 60, pp. 3913–3920, Aug 2012.

[51] A. Diallo, C. Luxey, P. Le Thuc, R. Staraj, and G. Kossiavas, "Study and reduction of the mutual coupling between two mobile phone pifas operating in the dcs1800 and umts bands," *IEEE Trans. Antennas Propag*, vol. 54, no. 11, pp. 3063–3074, 2006.

[52] A. Mak, C. Rowell, and R. Murch, "Isolation enhancement between two closely packed antennas," *IEEE Transactions on Antennas and Propagation*, vol. 56, no. 11, pp. 3411–3419, 2008.

[53] Y.-S. Wang, J.-C. Lu, and S.-J. Chung, "A miniaturized ground edge current choke-design, measurement, and applications," *IEEE Transactions on Antennas and Propagation*, vol. 57, no. 5, pp. 1360–1366, 2009.

[54] S.-W. Su, C.-T. Lee, and F.-S. Chang, "Printed mimo-antenna system using neutralization-line technique for wireless usb-dongle applications," *IEEE Transactions on Antennas and Propagation*, vol. 60, no. 2 PART 1, pp. 456–463, 2012.

[55] R. Shelby, D. Smith, S. Nemat-Nasser, and S. Schultz, "Microwave transmission through a two-dimensional, isotropic, left-handed metamaterial," *Applied Physics Letters*, vol. 78, no. 4, pp. 489–491, 2001.

[56] F. Yang and Y. Rahmat-Samii, "Microstrip antennas integrated with electromagnetic band-gap (ebg) structures: A low mutual coupling design for array applications," *IEEE Transactions on Antennas and Propagation*, vol. 51, no. 10 II, pp. 2936–2946, 2003.

[57] E. Rajo-Iglesias, O. Quevedo-Teruel, and L. Incln-Snchez, "Mutual coupling reduction in patch antenna arrays by using a planar ebg structure and a multilayer dielectric substrate," *IEEE Transactions on Antennas and Propagation*, vol. 56, no. 6, pp. 1648–1655, 2008.

[58] H. Mosallaei and K. Sarabandi, "Design and modeling of patch antenna printed on magneto-dielectric embedded-circuit metasubstrate," *IEEE Transactions on Antennas and Propagation*, vol. 55, no. 1, pp. 45–52, 2007.

[59] J. Choi, M. Jain, K. Srinivasan, P. Levis, and S. Katti, "Achieving single channel, full duplex wireless communication," *Proc. 2010 Intl. Conf. Mob. Comp. Netw*, pp. 1–12, 2010.

[60] Y. J. Song and K. Sarabandi, "A simultaneous dual-channel micro-radio-repeater for ad-hoc wireless communication," *Antennas and Propagation, IEEE Transactions on*, vol. 62, pp. 3378–3383, June 2014.

[61] D. Entekhabi, E. G. Njoku, P. E. O'Neill, K. H. Kellogg, W. T. Crow, W. N. Edelstein, J. K. Entin, S. D. Goodman, T. J. Jackson, J. Johnson, J. Kimball, J. R. Piepmeier, R. D. Koster, N. Martin, K. C. McDonald, M. Moghaddam, S. Moran, R. Reichle, J. C. Shi, M. W. Spencer, S. W. Thurman, L. Tsang, and J. V. Zyl, "The soil moisture active passive (smap) mission," *Proceedings of the IEEE*, vol. 98, pp. 704–716, May 2010.

[62] K. Sarabandi, L. E. Pierce, and F. T. Ulaby, "Calibration of a polarimetric imaging sar," *IEEE Transactions on Geoscience and Remote Sensing*, vol. 30, pp. 540–549, May 1992.

[63] K. Sarabandi and F. T. Ulaby, "A convenient technique for polarimetric calibration of single-antenna radar systems," *IEEE Transactions on Geoscience and Remote Sensing*, vol. 28, pp. 1022–1033, Nov 1990.

[64] K. Sarabandi, F. T. Ulaby, and M. A. Tassoudji, "Calibration of polarimetric radar systems with good polarization isolation," *IEEE Transactions on Geoscience and Remote Sensing*, vol. 28, pp. 70–75, Jan 1990.

[65] K. Sarabandi, L. E. Pierce, M. C. Dobson, F. T. Ulaby, J. M. Stiles, T. C. Chiu, R. D. Roo, R. Hartikka, A. Zambetti, and A. Freeman, "Polarimetric calibration of sir-c using point and distributed targets," *IEEE Transactions on Geoscience and Remote Sensing*, vol. 33, pp. 858–866, Jul 1995.

[66] K. Sarabandi, "Calibration of a polarimetric synthetic aperture radar using a known distributed target," *IEEE Transactions on Geoscience and Remote Sensing*, vol. 32, pp. 575–582, May 1994.

[67] K. Sarabandi, Y. Oh, and F. T. Ulaby, "Measurement and calibration of differential mueller matrix of distributed targets," *IEEE Transactions on Antennas and Propagation*, vol. 40, pp. 1524–1532, Dec 1992.

[68] Y. Oh, K. Sarabandi, and F. T. Ulaby, "An empirical model and an inversion technique for radar scattering from bare soil surfaces," *IEEE Transactions on Geoscience and Remote Sensing*, vol. 30, pp. 370–381, Mar 1992.

[69] J. M. Stiles, K. Sarabandi, and F. T. Ulaby, "Electromagnetic scattering from grassland. ii. measurement and modeling results," *IEEE Transactions on Geoscience and Remote Sensing*, vol. 38, pp. 349–356, Jan 2000.

[70] Y.-C. Lin and K. Sarabandi, "A monte carlo coherent scattering model for forest canopies using fractal-generated trees," *IEEE Transactions on Geoscience and Remote Sensing*, vol. 37, pp. 440–451, Jan 1999.

[71] J. R. Kendra, K. Sarabandi, and F. T. Ulaby, "Radar measurements of snow: experiment and analysis," *IEEE Transactions on Geoscience and Remote Sensing*, vol. 36, pp. 864–879, May 1998.

[72] K. Sarabandi and T.-C. Chiu, "Optimum corner reflectors for calibration of imaging radars," *IEEE Transactions on Antennas and Propagation*, vol. 44, pp. 1348–1361, Oct 1996.

[73] K. Sarabandi, Y. Oh, and F. T. Ulaby, "Performance characterization of polarimetric active radar calibrators and a new single antenna design," *IEEE Transactions on Antennas and Propagation*, vol. 40, pp. 1147–1154, Oct 1992.

[74] A. Bifot, E. Lier, and T. Schaug-Pettersen, "Simple and broadband orthomode transducer," *IEE Proceedings H (Microwaves, Antennas and Propagation)*, vol. 137, pp. 396–400(4), December 1990.

[75] G. Pisano, L. Pietranera, K. Isaak, L. Piccirillo, B. Johnson, B. Maffei, and S. Melhuish, "A broadband wr10 turnstile junction orthomode transducer," *IEEE Microwave and Wireless Components Letters*, vol. 17, pp. 286–288, April 2007.

[76] S. J. Skinner and G. L. James, "Wide-band orthomode transducers," *IEEE Transactions on Microwave Theory and Techniques*, vol. 39, pp. 294–300, Feb 1991.

[77] A. Navarrini and R. L. Plambeck, "A turnstile junction waveguide orthomode transducer," *IEEE Transactions on Microwave Theory and Techniques*, vol. 54, pp. 272–277, Jan 2006.

[78] G. Valente, G. Montisci, T. Pisanu, A. Navarrini, P. Marongiu, and G. A. Casula, "A compact l-band orthomode transducer for radio astronomical receivers at cryogenic temperature," *IEEE Transactions on Microwave Theory and Techniques*, vol. 63, pp. 3218–3227, Oct 2015.

[79] J. Li, "Direction and polarization estimation using arrays with small loops and short dipoles," *Antennas and Propagation, IEEE Transactions on*, vol. 41, pp. 379–387, Mar 1993.

[80] A. Boswell, A. J. Tyler, and A. White, "Performance of a small loop antenna in the 3-10 mhz band," *IEEE Antennas and Propagation Magazine*, vol. 47, pp. 51–56, April 2005.

[81] M. Kanda, "An electromagnetic near-field sensor for simultaneous electric and magnetic-field measurements," *IEEE Transactions on Electromagnetic Compatibility*, vol. EMC-26, pp. 102–110, Aug 1984.

[82] R. King, "The rectangular loop antenna as a dipole," *Antennas and Propagation, IRE Transactions on*, vol. 7, pp. 53–61, January 1959.

[83] H. Whiteside and R. King, "The loop antenna as a probe," *Antennas and Propagation, IEEE Transactions on*, vol. 12, pp. 291–297, May 1964.

[84] J. E. Storer, "Impedance of thin-wire loop antennas," *Transactions of the American Institute of Electrical Engineers, Part I: Communication and Electronics*, vol. 75, pp. 606–619, Nov 1956.

[85] L.-W. Li, C.-P. Lim, and M.-S. Leong, "Method of moments analysis of electrically large circular-loop antennas: non-uniform currents," in *Antennas and Propagation Society International Symposium, 1999. IEEE*, vol. 4, pp. 2542–2545 vol.4, July 1999.

[86] T. T. Wu, "Theory of the thin circular loop antenna," *Journal of Mathematical Physics*, vol. 3, no. 6, pp. 1301–1304, 1962.

[87] D. Barrick, "Miniloop antenna operation and equivalent circuit," *IEEE Transactions on Antennas and Propagation*, vol. 34, pp. 111–114, Jan 1986.

[88] C. A. Balanis, *Antenna Theory: Analysis and Design*. Wiley-Interscience, 2005.

[89] K. Awadalla and A.-E.-M. Sharshar, "A simple method to determine the impedance of a loop antenna," *Antennas and Propagation, IEEE Transactions on*, vol. 32, pp. 1248–1251, Nov 1984.

[90] M. J. Underhill and M. Harper, "Simple circuit model of small tuned loop antenna including observable environmental effects," *Electronics Letters*, vol. 38, pp. 1006–1008, Aug 2002.

[91] T. G. Tang, Q. M. Tieng, and M. W. Gunn, "Equivalent circuit of a dipole antenna using frequency-independent lumped elements," *IEEE Transactions on Antennas and Propagation*, vol. 41, pp. 100–103, Jan 1993.

[92] R. Kohno, R. Meidan, and L. Milstein, "Spread spectrum access methods for wireless communications," *IEEE Communications Magazine*, vol. 33, no. 1, pp. 58–67, 1995. cited By 194.

[93] M. Strasser, C. Ppper, and S. apkun, "Efficient uncoordinated fhss anti-jamming communication," pp. 207–217, 2009. cited By 63.

[94] D. M. Pozar, *Microwave Engineering*. John Wiley & Sons, Inc, 3nd ed., 2005.

[95] A. Thampy, M. Darak, and S. Dhamodharan, "Analysis of graphene based optically transparent patch antenna for terahertz communications," *Physica E: Low-Dimensional Systems and Nanostructures*, vol. 66, pp. 67–73, 2015. cited By 14.

[96] S. Hakimi, S. Rahim, M. Abedian, S. Noghabaei, and M. Khalily, "Cpw-fed transparent antenna for extended ultrawideband applications," *IEEE Antennas and Wireless Propagation Letters*, vol. 13, pp. 1251–1254, 2014. cited By 15.

[97] C. Lee, Y. Kim, Y. Kim, I. Kim, and C. Jung, "A flexible and transparent antenna on a polyamide substrate for laptop computers," *Microwave and Optical Technology Letters*, vol. 57, no. 5, pp. 1038–1042, 2015. cited By 6.

[98] F. Bayatpur and K. Sarabandi, "Single-layer high-order miniaturized-element frequency-selective surfaces," *IEEE Transactions on Microwave Theory and Techniques*, vol. 56, no. 4, pp. 774–781, 2008. cited By 105.

[99] F. Bayatpur and K. Sarabandi, "Multipole spatial filters using metamaterial-based miniaturized-element frequency-selective surfaces," *IEEE Transactions on Microwave Theory and Techniques*, vol. 56, no. 12, pp. 2742–2747, 2008. cited By 50.

[100] N. Behdad, M. Al-Joumayly, and M. Salehi, "A low-profile third-order bandpass frequency selective surface," *IEEE Transactions on Antennas and Propagation*, vol. 57, no. 2, pp. 460–466, 2009. cited By 70.

[101] J. Oh, M. Thiel, and K. Sarabandi, "Wave-propagation management in indoor environments using micro-radio-repeater systems," *IEEE Antennas and Propagation Magazine*, vol. 56, pp. 76–88, April 2014.

[102] A. Nehorai and E. Paldi, "Vector sensor processing for electromagnetic source localization," vol. 1, pp. 566–572, 1991. cited By 46.

[103] W. L. Stutzman and G. A. Thiele, *Antenna theory and design*. John Wiley & Sons, 2012.

[104] A. Nehorai and E. Paldi, "Vector-sensor array processing for electromagnetic source localization," *IEEE Transactions on Signal Processing*, vol. 42, no. 2, pp. 376–398, 1994. cited By 409.

[105] N. Le Bihan, S. Miron, and J. Mars, "Music algorithm for vector-sensors array using biquaternions," *IEEE Transactions on Signal Processing*, vol. 55, no. 9, pp. 4523–4533, 2007. cited By 85.

[106] K. Wong, "Direction finding/polarization estimation - dipole and/or loop triad(s)," *IEEE Transactions on Aerospace and Electronic Systems*, vol. 37, no. 2, pp. 679–684, 2001. cited By 67.

[107] K.-C. Tan, K.-C. Ho, and A. Nehorai, "Uniqueness study of measurements obtainable with arrays of electromagnetic vector sensors," *IEEE Transactions on Signal Processing*, vol. 44, no. 4, pp. 1036–1039, 1996. cited By 26.

[108] D. Rahamim, J. Tabrikian, and R. Shavit, "Source localization using vector sensor array in a multipath environment," *IEEE Transactions on Signal Processing*, vol. 52, no. 11, pp. 3096–3103, 2004. cited By 106.